DEVELOPMENT OF ADVANCED PAVEMENT MATERIALS SYSTEM FOR BLAST LOAD

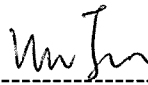## WU JUN

NATIONAL UNIVERSITY OF SINGAPORE
2012

DECLARATION

I hereby declare that this thesis is my original work and it has been written by me in its entirety. I have duly acknowledged all the sources of information which have been used in the thesis.

This thesis has also not been submitted for any degree in any university previously.

Wu Jun

DEVELOPMENT OF ADVANCED PAVEMENT MATERIALS SYSTEM FOR BLAST LOAD

WU JUN

(B.Eng., Shanghai Normal University)

(M.Eng., Tongji University)

A THESIS SUBMITTED FOR

THE DEGREE OF DOCTOR OF PHILOSOPHY

DEPARTMENT OF CIVIL & ENVIRONMENTAL

ENGINEERING

NATIONAL UNIVERSITY OF SINGAPORE

2012

DEDICATED TO

The most important person in my life ---

My Mom

My Wife

My Daughter

Acknowledgements

I want to express my sincere gratitude to my supervisor, Assistant Professor Chew Soon Hoe for his patience, support, encouragement, invaluable guidance and constructive advices throughout the entire course of this research. This research would not be completed without his supervision. Thank you, Dr. Chew.

I would also like to thank Professor Zhang Min-Hong, and Associate Professor Harry Tan Siew Ann for their valuable comments and discussions during the qualified examination. At same time, I also want to express my sincere gratitude to Assistant Professor Goh Siang Huat for valuable discussion and encouragement during my study in NUS.

My heartfelt appreciations are dedicated to Dr. Lee Siew Chin and Dr. Patria for making me be rapidly familiar with LSDYNA at the begin of this research. The most grateful appreciations are also expressed to Dr. Leonard Schwer (Schewr Engineering & Consulting Service, USA) and Mr. Joe Magallanes (Karagozian & Case, USA) for discussion on numerical problems. Special thanks are extended to Dr. Wang Shasha for discussion on the SHPB experiment and numerical problems.

During this research, I have a chance to do various tests in different laboratories at civil engineering department. Thereby, the kind assistance and support from technicians at Geotechnical, Structural and Transportation

Laboratory are gratefully acknowledged. Special thanks go to Mdm. Jamilah Bte Mohd, Mr. Loo Leong Huat, Mr. Choy Moon Nien, Mr. Foo Hee Ann, Mr. Choo Peng Kin, Mr. Koh Yian Kheng, Mr. Ang Beng Oon, Mr. Wong Kai Wai, Ms. Annie Tan, Mr. Yip Kwok Keong, and Mr. Mohd Farouk for their generous and kind support for experimental work.

Grateful thanks go to my friends and colleagues for their friendship, help and encouragement during my study life. I have a good time with you. Especially, to those from my "another family" in Singapore (you know whom I mention about), it is really a great time to live with you. I will always miss you guys no matter where I am in the future.

Lastly, I would like to express my deepest blessing and appreciations to my Mom. The great love from you is the light of my life. I owe you, Mom. Thank you mother in law and father in law for supporting my family throughout my entire study in overseas. My wife Yang Yan, I know that a man can only be strong with the support of the woman behind him. Thanks you for all your energy and patience. Your unprecedented support shows the miracle of the life. My lovely daughter Siyu, in my eyes, you are always the most wonderful gift even given to me.

Table of Contents

Summary

Runways for military and civilian airports are among the most important facilities today. It is necessary to ensure their functionality at all time not only for a nation's security but also for its economy and safety. Military airports are amongst the first targets that are easily damaged with air attacks and artillery fire during war time. Civilian airports runway are the prime target for terrorist attacks. In such time, it is extremely important to ensure that the runways are in good conditions to enable the taking-off and landing of fighters or aircraft, especially for countries like Singapore which have a limited number of airports. Furthermore for civilian airports, the emergencies such as air plane crash may destroy the runway, which will in turn affect the normal commercial function of airports , which will result in huge economic lost.

There are many aspects of runway functionality, one of which is the integrity of the runway pavement with its service life span. The functional quality of the pavement can be maintained through regular servicing. If damaged do occur on the pavement, the repair must be rapid such that disruption is minimized to the service. It will be even better if the extent of the damage on the pavement can be kept to a minimum, and then rapid repair can be carried out.

The current pavement systems are designed for normal aircraft landing and taking off and thus inadequate to provide the required resistance to impact and blast loading arising from bombing and blasting. It is observed that the existing materials used in pavement such as concrete and asphalt do not provide enough resistance against impacts and blasts. Due to their relatively brittle properties and

limited penetration resistance, conventional surface pavements are not durable and the damage by explosive may be too serious to be mitigated. Thus new pavement materials need to be developed to make the better resistance to impact and blast loading.

Thus, there is an urgent need to find a new pavement system that can withstand high impact and blast load, thereby increasing the durability of pavement and reducing the amount of repair needed. This in turn improves the operational readiness of the pavement runway.

In this study, the performance of High-Strength Concrete (HSC), Engineered Cementitious Composites (ECC) and asphalt concrete (AC) with geosynthetics (GST) subjected to impact and blast loading were investigated. This is because each of these materials has its unique characteristics of high compressive strength, high toughness and high tensile strength under impact and blast loading. However, each of these materials has its own advantages and disadvantages for blast and impact mitigation. The dynamic loading from blast and impact events requires the material to be stable under various states of stress, hence it is difficult for one single material to fully satisfy. Thus, adopting advanced composite system for the protection of runways is an attractive solution.

In this study, the concept of the multi-layers system was proposed in order to satisfy the above blast resistance requirement for pavement design. The "soft" material (AC) in the proposed multi-layers pavement system functioned as the sacrificial surface layer to absorb some portion of the dynamic energy. Thereby, the energy transmitted to the following layers was greatly reduced. With the inclusion of the high strength Geosynthetic (GST) within this AC layer, the tensile strength of this layer was increased and in turn reduced the damage to the AC

layer. Below the AC layer, HSC which was a "strong" material was used. This HSC layer served as the main body to sustain the dynamic load. Under the dynamic loading, the tensile stress tends to develop at the rear face of the material due to the reflection of the compressive stress propagating from the top face. However, it is well known that the concrete has low tensile strength. Furthermore, the HSC is very brittle and may develop cracks easily. Hence, another "soft" and ductile material (ECC) is deemed to be needed at the base of the "strong" HSC layer to absorb the energy. This ductile material can develop micro crack to dissipate and attenuate the impacted dynamic energy.

A series of large scale laboratory impact tests was carried out to prove the usefulness of this concept and showed the advantage of this proposed multi-layers pavement over other conventional pavement. Furthermore, the field blast tests were conducted to show the actual behavior of the proposed multi-layers pavement under blast load in the field condition. From the laboratory and field test, it could be concluded that combination of ECC, HSC and AC with GST could improve the impact resistance of pavements significantly. Proposed multi-layers pavement was found to perform better than conventional pavement structures (concrete rigid pavement and asphalt concrete flexible pavement). The concept of the multi-layers system was successfully used in the design of new pavement subjected to blast load. This multi-layers pavement design consisting of all 3 materials (HSC, ECC and GST) fully utilized their pronounced properties.

The interface property among the multi-layers system usually plays an important role in the pavement performance subjected to load. However, there was no well established data on the interface property in the proposed multi-layers system, that is, interface between AC, and HSC and interface between HSC and

ECC. Hence, it is necessary to conduct the test to determine the interface strength between these layers. The direct and tilt table test were conducted to determine the interface strength between these layers was conducted.

It is more productive to carry out the numerical simulation of multi-layers pavement system subjected to blast load, due to the high cost and resources needed for the field blast test. However, a reliable numerical simulation should be developed for accurate results. There are many factors that will affect the results of simulation. Among these factors, the material model plays a key role because it should reproduce the essential physical mechanisms of the material under severe dynamic loading condition. There are many material models that may be suitable to represent the static behavior of the material, but only a few material models may be relevant to the dynamic behavior of the material. Hence, the determination of the advanced material model to reflect the actual behavior of material under dynamic load condition is a challenge. In this study, the advanced material models were discussed and evaluated to simulate the dynamic behavior of materials under severe dynamic loading. The key parameters for the advanced material model were calibrated by the laboratory dynamic tests. The Dynamic Increase Factor (DIF) for AC material was first purposed and implemented into the advanced material model. Lastly, the 3D numerical model of the proposed multi-layers pavement was developed and validated based on the results from the field blast test. Then the parametric study was conducted. It was found that some methods such as increasing thickness of HSC and ECC, incorporation of steel fiber in HSC and using treated subsoil ground condition increased the blast resistance of the proposed multi-layers pavement. Finally, the design chart of the proposed multi-layers pavement under different explosive charge was developed.

Keywords: Drop Wight Impact Test, Field Blast Test, High Strength Concrete, Engineered Cementitious Composites, Geosynthetics, 3D Numerical model , Dynamic Increase Factor

List of Tables

List of Figures

List of Notations

<u>Nomenclature</u>

b_w	waveform parameter
p_s^+	peak incident overpressure
p_r	peak reflected pressure
p_0	ambient pressure
t	time
t_a	arrival time for shock front arriving at fixed point
t_0	positive phase duration of the blast wave
t_0^-	negative phase duration of the blast wave
t_d	blast loading period
T_N	natural period of the structure
I^+	positive impulse
I^-	negative impulse
α_I	the angle of incidence of the blast wave
$F(t)$	blast loading with time
$R(t)$	structure resistance with time
G_{if}	interfacial fracture energy
K_{ic}	interfacial fracture toughness
mg	weight of solid body

θ	tilt angle from the horizontal surface
μ_{static}	static friction coefficient
$\mu_{dynamic}$	dynamic friction coefficient
σ_t	tensile stress at interface
σ_s	shear stress at interface
G_I	energy release rates for tensile strength
G_{II}	energy release rates for shear strength
ρ	density
V	volume
ρ_0	reference density
V_0	reference volume
$\dot{V}$	rate of change in volume
σ_{ij}	stress tensor
σ_{ii}	hydrostatic pressure tensor
f_i	body force
$\ddot{u}$	acceleration
e	internal energy
$\dot{e}$	change in specific internal energy
$\dot{\varepsilon}_{ij}$	strain rate tensor
ε_v	volumetric strain
$\varepsilon_{v,yield}$	volumetric strain at yield
ε_{eff}^p	effective plastic strain

$d\bar{\varepsilon}^p$	effective plastic strain increment
ε_s	erosion strain
μ_{crush}	volumetric strain defining equation of state
$\Delta\mu^p$	incremental plastic volumetric strain
μ_{lock}	plastic volumetric strain for fully compacted material
$\bar{\mu}$	modified volumetric strain
s_{ij}	deviatorial stress tensor
s_i	principal deviatoric stress tensor
p	hydrostatic pressure
q	bulk viscosity
D	damage factor
$\Delta\sigma$	principal stress difference
r_t	radius of tensile meridian
r_c	radius of compressive meridian
ψ	ratio of tensile to compressive location of the current failure surface
θ_L	Lode angle
J_2	second invariant of the deviator stress tensor
J_3	third invariant of the deviator stress tensor
η	damage parameter in MAT72 R3
λ	accumulated effective plastic strain in MAT72 R3
r_f	dynamic increase factor in MAT73 R3

XXXI

δ scaled damage indicator

a_{ij} parameters defining the strength surface in MAT 72 R3

b_1 damage factor defining the softening part of unconfined

                   uniaxial compressive stress-strain curve

b_2 damage factor defining the softening part of unconfined

                   uniaxial tensile stress-strain curve

b_3 damage factor defining the softening part of triaxial tensile

G_c compressive energy

G_f fracture energy for tension

w_c localization width

k_d internal scalar multiplier

$\Delta\lambda$ incremental volumetric damage

$\Delta\sigma_y$ yield surface

$\Delta\sigma_m$ maximum strength surface

$\Delta\sigma_r$ residual strength surface

$\Delta\sigma_{me}^c$ enhanced strength due to strain rate effect

$K_{elastic}$ elastic bulk modulus defining equation of state

K_1, K_2, K_3 constants for the material is fully compressed without voids

D_c damage factor defining equation of state

α constant in Drucker-Prager model

k constants in Drucker-Prager model

c cohesion of soil

φ friction angle

ν Poisson's ratio

$\dot{\varepsilon}_s$ static compressive strain rate

$\dot{\varepsilon}_{st}$ static tensile strain rate

n safety factor in determining of time step

l the smallest mesh size

γ constant in idea gas equation

A,   empirically derived constant for explosive

B   empirically derived constant for explosive

R_1 empirically derived constant for explosive

R_2 empirically derived constant for explosive

ω empirically derived constant for explosive

σ_0 static initial yield point

β_{pk} type of plastic hardening for Plastic-Kinematic model

C_{pk} parameter considering strain rate effect for steel

P_{pk} parameter considering strain rate effect for steel

f_c compressive strength

f_t tensile strength

$f'_{c,new}$ unconfined compression strength to be modeled material

$f'_{c,old}$ unconfined compressive strength for a previously modelled

       material

r scaling factor

a_{0n}, a_{1n}, a_{2n} parameters for maximum strength surface to be determined

       from scaling law

pc_{new}	new pressure from scaling law
ku_{new}	new unloading bulk modulus from scaling law
L	length of the notched beam sample
w	width of the notched beam sample
T	depth of the notched beam sample
α_0	depth of notch
S	loaded span for notched beam
E_p	plastic modulus for steel
E	Young's modulus
E_t	Tangent modulus
Z	scaled distance

Acronyms

3D	Three Dimensional
AC	Asphalt Concrete
ALE	Arbitrary Lagrange-Euler
CBR	California Bearing Ratio
CEB-FIP	Comité Euro International du Béton-Fédération International de la Précontrainte
CFL	Courant-Friedrich-Levy condition
CH	Calcium Hydroxide
DIF	Dynamic Increase Factor
EOS	Equation of State
TNT	Trinitrotoluene (an explosive)
ITZ	Interfacial Transition Zone
HSC	High Strength Concrete

ECC   Engineered Cementitious Composites

GST   Geosynthetics

HPSFRC   High Performance Steel Fiber-Reinforced Concrete

RHSC   Reinforced High Strength Concrete

VHSC   Very High Strength Concrete

CSPC   Conventional Normal Strength Portland Concrete

SHPC   High Strength Portland Concrete

HSFR   High Strength Steel Fibre Reinforced Concrete

SFRPC   Steel Fibre Reinforced Concrete with Reactive Powder

RC   Reinforced Concrete

FRC   Fibre reinforced concrete

SNB   Single Notched Beam

Pot1, Pot2, Pot3   potentiometers in laboratory impact test

A1, A2, A3   accelerometers in laboratory impact test

V1, V2   vertical acceleration of the slab in field blast trial

H1, H2   horizontal acceleration of the slab in field blast trial

SG1, SG2, SG3, SG4   strain gauges in field blast trial

P1, P2   air pressure cell in field blast trial

TPC 1, TPC 2 ,TPC 3   total Pressure cells in field blast trial

NFLS   normal failure stress in contact model

SFLS   shear failure stress in contact model

PARAM   critical displacement at total failure in contact model

SHPB   Split Hopkinson Pressure Bar

w/c   water-to-cement ratio

w/cm   water-to-cementitious ratio

Chapter 1   Introduction

1.1 Background

Runways for military and civilian airports are among the most important facilities today. It is necessary to ensure their functionality at all time not only for a nation's security but also for its economy and safety. Military airports are amongst the first targets that are easily damaged with air attacks and artillery fire during war time. Civilian airports runway are the prime target for terrorist attacks. In such time, it is extremely important to ensure that the runways are in good conditions to enable the taking-off and landing of fighters or aircraft, especially for countries like Singapore which have a limited number of airports. Furthermore for civilian airports, the emergencies such as air plane crash may destroy the runway, which will in turn affect the normal commercial function of airports , which will result in huge economic lost. Table 1.1 summaries cases in which runway was destroyed by air crash or terrorist attack.

There are many aspects of runway functionality, one of which is the integrity of the runway pavement with its service life span. The functional quality of the pavement can be maintained through regular servicing. If the pavement is damaged, the repair must be rapid such that disruption is minimized to the service. It will be even better if the extent of the damage on the pavement can be kept to a minimum, and then rapid repair can be carried out. Figure 1.1 and 1.2 shows the crater occurred on runway and destroyed the integrity of the runway pavement.

Literature review shows that current pavement systems are inadequate in providing the required resistance to impact and blast loading. Existing materials

for typical pavements such as normal concrete and asphalt concrete do not provide enough resistance against impact and blast load. The damage caused by bombings or plane crashing is definitely too serious to allow the pavement to be functioned properly.

Thus, there is an urgent need to find a new pavement system that can withstand high impact and blast load, thereby increasing the durability of pavement and reducing the amount of repair needed. This in turn improves the operational readiness of the pavement runway.

Meanwhile, from recent studies, it was found that some materials such as High Strength Concrete (HSC) (Zhang et al. 2007) and Engineered Cementitious Composites (ECC) (Li et al. 1994; Li and Maalej 1996) and Geosynthetics (GST) (Koerner 1998), which had shown its unique characteristics of either high compressive strength, or high ductility or high tensile strength. They have some potential to be used as a new pavement material for enhanced blast and impact resistance.

Proper choice of component materials and mix proportion has been found to be able to produce concrete with very much higher strength and better toughness than conventional concrete with conventional mixing methods and at reasonable cost (Mindness et al. 2002). Recent researches (Hanchak et al. 1992; Dancygier and Yankelevsky 1996; Zhang et al. 2005) indicated that an increase in the compressive strength of concrete could reduce the penetration depth when the concrete was subjected to projectile impact. However, it was also well known that concrete with high compressive strength was too brittle for impact and blast loading (Hanchak et al. 1992).

Engineered Cementitious Composites (ECC) are composite materials using micromechanically optimized fiber reinforced cement. Unlike most of the cementitious materials, ECC is ultra-ductile under tensile and shear loading indicated by multiple micro-cracking behaviors (Li et al. 1994). These micro-cracks allow ECC to exhibit pronounced strain-hardening behavior similar to ductile metals. Besides the excellent behavior under tensile and shear loading, ECCs also possess high fracture energy and notch insensitivity (Maalej et al. 1995; Maalej et al. 2005).

Recent researches (Yong 2005; Chew and Lim 2006) also showed that inclusion of some Geosynthetics (GST) like geogrid or geotextiles in asphalt pavement not only could improve the resilience properties of the pavement but also provides some form of added ductility when it is subjected to impact load. This has the potential for blast mitigation in terms of reducing the crater size when the pavement is subjected to blast and impact load. Thus, the repair effort can be reduced to manageable scale and within shorter possible time.

However, each of these materials has its own advantages and disadvantages for blast and impact mitigation. The dynamic loading from blast and impact events requires the material to be stable under various states of stress, hence it is difficult for one single material to fully satisfy. Thus, adopting advanced composite system for the protection of runways is an attractive solution. A new pavement design consisting of all 3 materials (HSC, ECC and GST) will be considered in order to fully utilize their pronounced properties. It is expected that an optimized combination of the advantages of each material will provide a composite material system for a better impact-resistant runway pavement. Ideally,

the new pavement design should have high penetration resistance, strength, ductility and multiple resistance capability.

In this study, the concept of the multi-layers system is proposed in order to satisfy the above blast resistance requirement for pavement design. In the multi-layers system, the "soft" material will be used as the sacrifice surface layer to absorb some portion of the dynamic energy. With this consideration, the Asphalt concrete (AC) will be used as the top layer in the proposed multi-layer pavement system. Thereby the energy transmitted to the following layers will be greatly reduced. It should be noticed that the asphalt layer could be very easily repaired. With the inclusion of the high strength Geosynthetic (GST) within this AC layer, the tensile strength of this layer will be increased, and in turn reduce the crack and local failure in the AC layer when subjected to dynamic load. Below the AC layer, a "strong" material may be used and it served as the main body to sustain the dynamic load. For this purpose, the high strength concrete (HSC) may be a suitable choice due to its super high compressive strength. Under the dynamic loading, the tensile stress tends to develop at the rear face of the material due to the reflection of the compressive stress propagating from the top face. However, it is well known that the concrete has low tensile strength. Furthermore, the HSC is very brittle and may develop cracks easily. Hence, another "soft" and ductile material (ECC) is deemed to be needed at the base of the "strong" HSC layer to absorb the energy. This ductile material can develop micro crack to dissipate and attenuate the impacted dynamic energy.

The interface property among the multi-layers system usually plays an important role in the pavement performance subjected to load. However, there was no well established data on the interface property in the proposed multi-layers

4

system, that is, interface between AC, and HSC and interface between HSC and ECC. Hence, it is necessary to conduct the test to determine the interface strength between these layers.

As discussed above, the concept of multi-layers system will be studied for the design of airfield runway under dynamic load. A series of large scale laboratory impact tests will be carried out to prove the usefulness of this concept and show the advantage of this proposed multi-layers pavement over other conventional pavement. Furthermore, the field blast test will be conducted to show the behavior of the proposed multi-layers pavement under blast load in the field condition. Due to the high cost and resources needed for field trial blast test, hence, it is more productive to carry out the numerical simulation of multi-layers pavement system subjected to blast load. However, a reliable numerical simulation should be developed for accurate results. There are many factors that will affect the results of simulation. Among these factors, the material model plays a key role because it should reproduce the essential physical mechanisms of the material under severe dynamic loading condition. There are many material models that may be suitable to represent the static behavior of the material, but only a few material models may be relevant to the dynamic behavior of the material. Hence, the determination of the advanced material model to reflect the actual behavior of material under dynamic load condition is a challenge. In this study, the suitable advanced material models will be discussed, and evaluated to simulate the dynamic behavior of materials. The key parameters of this advanced material model will also be calibrated by the laboratory dynamic tests. Lastly, the 3D numerical model of the proposed multi-layers pavement is developed and validated based on the results from the field blast test. Finally, a set of the design

chart of the proposed multi-layers pavement under different explosive charge is developed.

Table 1.1 Cases for damaged runway (from http://www.airdisaster.com/cgi-bin/database.cgi)

No.	Date	Country	Target	Runway damage reason
1	1993	Georgia	Alexeyevka airport	Aircraft crash due to missile attack
2	1993	Iran	Military airport	Collision of two military aircraft
3	1994	UK	Heathrow airport	Mortar bomb
4	1994	Rwanda	Military airport	Missile attack
5	1998	Sir Lanka	Civilian airport	Aircraft crash due to missile attack
6	2000	Nairobi	Bujumbura airport	Aircraft crash due to shooting
7	2001	Sir Lanka	Civilian airport	Missile attack
8	2001	Angola	Dundo airport	Aircraft crash due to engine problem
9	2001	Colombia	Yopal airport	Aircraft crash due to fuel exhaustion
10	2002	Luxembourg	Findel airport	Aircraft crash due to fog weather
11	2003	USA	Memphis international airport	Aircraft crash due to landing gear failed
12	2006	Nigeria	Abuja airport	Aircraft crash due to poor weather condition
13	2006	Iran	Mashad airport	Aircraft crash
14	2007	Russia	Samara airport	Aircraft crash due to poor weather condition
15	2007	Brazil	Sao Paulo airport	Aircraft crash due to rainy weather
16	2008	Spain	Madrid airport	Aircraft explode
17	2009	Russia	Makhachkala airport	Collision of two aircraft
18	2009	Japan	Narita airport	Aircraft crash
19	2010	Mexico	Monterrey airport	Aircraft crash
20	2010	Libya	Tripoli international airport	Aircraft crash

1.2. Objective and Scope of Research Project

The main objective for this research is to develop and evaluate the performance of an advanced composite pavement materials for airfield runways which have better resistance to blast load.

The following items are included in this PhD thesis:

(1) Chapter 2: The concepts of blast loading and impact loading and the current pavement structure design will be reviewed. In the later part of Chapter 2, the dynamic behavior of 4 engineering materials (High strength Concrete, Engineered Cementitious Composite and High Strength Geosynthetics, Asphalt Concrete) will be discussed. Furthermore, the interface property for different components and current numerical model for pavement under impact and blast load will also be discussed.

(2) Chapter 3: The new pavement material is proposed according to the laboratory impact test. The proposed multi-layers pavement is the combination of High strength Concrete (HSC), Engineered Cementitious Composite (ECC) and High Strength Geosynthetics (GST), which has good impact resistance. The control specimens with current pavement design will also be investigated for its dynamic behavior under impact load. Results from conventional and proposed multi-layers pavement will be discussed.

(3) Chapter 4: The proposed multi-layers pavement will be tested in the full scale field trail test to evaluate its resistance against blast load. The dynamic response of the proposed multi-layers pavement under blast loading will be explored and analyzed.

(4) Chapter 5: Evaluation of the property of interface in the proposed multi-layers pavement will be conducted through laboratory test and numerical modelling.

(5) Chapters 6: The numerical analysis of the conventional pavement and the proposed multi-layers pavement under blast load will be conducted. The key results from numerical models will be discussed based on the parametric study for the proposed multi-layers pavement. The design chart for proposed multi-layer pavement under different blast energy will be further developed.

(6) Chapters 7: Conclusion will be drawn and future research will be recommended.
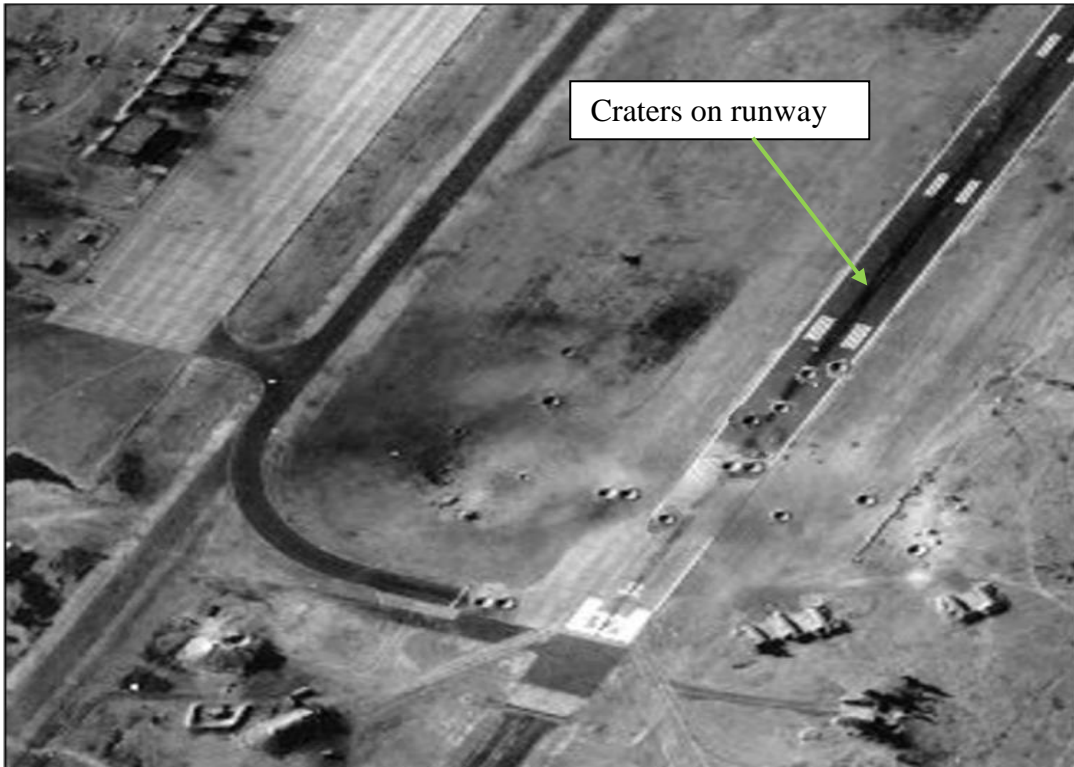
Figure 1.1 The integrity of the runway was destroyed by blast and impact load
(after Chew et al. 2009)

Figure 1.2 Runway was destroyed by the impact load (from
http://gizmodo.com/5869715/why-did-this-airplane-landing-gear-destroy-this-
concrete-runway)

Chapter 2   Literature Review

2.1 Introduction

This chapter will first review concepts of blast loading and impact loading. After which, the current pavement design will be reviewed, and the shortfall of this kind of pavement structure under impact or blast loading will be highlighted. Furthermore, the dynamic behavior of the engineering material, that is, High Strength Concrete (HSC) Engineered Cementitious (ECC) and Geosynthetics (GST), and Asphalt Concrete (AC) will be discussed. The relative strength and weakness of these materials will be highlighted. Then the interface properties in the current pavement design will be discussed. Finally, the numerical simulation of pavement under blast and impact load will be evaluated.

2.2 Blast Loading

Blast loading is generated by an explosive event, when an unconfined charge detonates in air; it gives rise to blast waves with a practically discontinuous pressure front that propagates with supersonic speed. The blast wave is initialed by the very rapid release of a large amount of energy in the surrounding medium. This rapid releasing of energy will in turn lead to a sudden increase of pressure at the front (called the shock front) followed by a gradual decrease of pressure as shown in Figure 2.1. The maximum overpressure that occurs at the shock front is called the peak incident overpressure.

The shape of the blast wave depends on the nature of the energy released. When the blast source is located on or very near to the ground surface, the blast is

considered as a surface burst, in which the incident blast wave is reflected and enhanced by the ground surface. The reflected wave then merges with the incident wave to form a hemispherical blast wave, which can be seen in Figure 2.2 (a). When the blast source is located far from the ground or any reflecting surface, the blast is considered to be an air burst with spherical shape as shown in Figure 2.2 (b) (Smith and Hetherington 1994).

The pressure time history of a blast wave at fixed distance is often described by exponential functions such as the Friedlander equation, which is given below:

$$p(t) = p_s \left[1 - \frac{t}{t_0} \right] \exp\left(-\frac{b_w t}{t_0} \right) \tag{2.1}$$

in which, b_w is the waveform parameter, p_s is the peak incident overpressure, t_0 is the positive phase duration of the blast wave and t stands for time (Smith and Hetherington 1994).

Figure 2.3 shows a typical blast pressure time history of an air burst. The arrival time for shock front arriving the fixed point is assumed as t_a. After the arrival, the blast pressure time history curve can be divided into two phases, that is, the positive and the negative phase. In the positive phase, the peak incident overpressure p_s, decays to the ambient pressure p_0, in a time period known as the positive phase duration t_0. This is followed by the negative phase, in which the blast pressure further reduces to the peak negative overpressure. The negative phase is normally weaker and has a more gradual decay with longer duration of t_0^- as compared to the positive phase, and hence it is usually ignored in design. The area under the positive phase of the pressure time curve represents the positive

impulse I^+, while the negative impulse I^-, can be obtained from the area under negative phase of the same curve.

When blast wave strikes a dense medium, such as a solid wall/door surface, the pressure of the shock front increases instantaneously because of the formation of a reflected wave, this pressure is often called peak reflected pressure p_r. The typical reflected pressure time history curve is also shown in Figure 2.3. As shown in the figure, the value of the reflected pressure was higher than that of incident pressure. The exact value of the peak reflected pressure depends on the peak incident pressure p_s, and the angle at which it strikes the surface. If the surface of target is oriented in the direction normal to the direction of propagation of the shock front (the angle of incidence of the blast wave α_I is 90°, as shown in Figure 2.4 (a)), this orientation can produce the normal reflected pressure which is a most severe loading on the target. If the target surface is oriented in the direction parallel to the direction of propagation of the shock front (the angle of incidence of the blast wave α_I is 0°, as shown in Figure 2.4 (b)), there is no reflection and the target surface is loaded by the peak pressure which is called side-on pressure which is equal to the value of incident pressure. For α_I between zero and 90°, the blast wave can undergo either the regular reflections as shown in Figure 2.4 (c).

Generally, both the blast pressure and the total load impulse determine the damage level of a structure subjected to blast loading. There are 3 cases of blast loading which based on the structure response and duration time of loading (Smith and Hetherington, 1994): Impulsive, Dynamic and Quasi-static loading. Figure 2.5 shows these 3 cases graphically, where $R(t)$ is a structure resistance with time and $F(t)$ is a blast loading with time. The first case is called Impulsive loading,

where the blast loading period t_d is much shorter than the natural period T_N of vibration of the structure ($t_d \ll T_N$). In this case, the blast loading rises to its maximum and drops to its minimum before the structure had time to respond significantly. Thus, the response of structure is determined by the impulse alone, and independent of the maximum pressure. The second case in Figure 2.5 (b) is called Quasi-static loading, where the blast loading period is much bigger than the natural period of vibration of the structure ($t_d \gg T_N$). In this case, the response of structure is solely determined by the maximum blast loading and not dependent of positive phase duration. The final case is a Dynamic loading where the blast loading period and the structure response time is quiet similar ($t_d \approx T_N$). In this case, the response of the structure depends on both maximum blast pressure and impulse.

2.3 Impact Loading

Impact is an alternative way to produce a short duration dynamic response of structure which is equivalent to certain aspects of the loading that generated by the blast event. But impact loading differs from blast loading in duration and in the form of application and they are only applied to a localized area. Impulsive blast loading propagates as a wave front, while an impact loading is caused by the force due to the collision between a moving object and a stationary target.

The layer-type of target is of interest in this study as the runway pavement is layer system. Upon impact, stresses and strains are induced in the layered-type target material. The layer of particles in the target is compressed leading to compressive stress. Via this process, the stress wave are produced which is similar

to the shock waves generated by blast loading. The stress waves propagate throughout the material at a speed which is a function of material property. When there are few layers with different density, the reflected wave will occur at the interface of these layers.

The stress wave can be classified to elastic stress wave and inelastic stress wave. Obviously, the strength of the stress wave will depend on the energy the impactor transferred to. If the energy was lower than the certain level, only elastic stress wave occurs within the target and led to elastic deformation. If the energy was higher than the certain level, the inelastic stress wave would occur which led to be failure of the target.

During impact, the response of the target may be dominated by either global response or local response based on the velocity of the impact. A global response in the target upon low velocity impact can be seen evaluated based on the deflecting of the whole target. A local response can be limited to one localized area of the target, and the deflection of the whole target may not happen. This is because during the high velocity impact, the target may not have time to response completely. Hence, the localized damage tends to occur in a small area (contact area) of the target. Bangash (1993) summarized five damaged forms due to impact for a single layer target. There are (a) penetration and scabbing, (b) spalling, (c) perforation and (d) punching shear, (e) global flexural failure, which can be seen in Figure 2.6. The former 4 damage forms are the localized damage due to the high velocity impact, while the 5th form is overall global damage. During the high velocity impact, the compressive stress due to the impact at the front face of the target passed through the material, and was reflected at the rear face. This will cause dynamic tensile wave at the rear face. Hence, if the target material is cement

15

based material, the spalling and perforation failure forms tend to occur due to its lower tensile strength compared to its compressive strength.

2.4 Current pavement structure

The pavement is designed to provide adequate support for the loads imposed by vehicles/aircrafts, and to provide a firm, stable, durable and smooth all-year, all weather surfaces. It is also used to distribute the concentrated loads so that the supporting capacity of the sub-grade soil is not exceeded. In order to achieve these objectives, the pavement must have adequate thickness and sufficient strength so that it will not fail under the imposed traffic load and could withstand the deteriorating influences from accident event. A complete pavement structural design also depends on the frequency of imposed load, the local climate and local soil property.

There are two typical pavement structures that is, rigid pavement, and flexible pavement. The following section will discuss these two types of pavement structure.

2.4.1 Flexible Pavement

Flexible pavements are made of asphalt concrete (AC). It is an asphalt aggregate mixture produced at a batch or drum mixing facility that must be mixed, spread, and compacted at an elevated temperature. In Figure 2.7, left hand side shows the cross section of a conventional flexible pavement. Starting from the top, the pavement consists of surface course, base course, compacted subbase, and natural subgrade.

The surface course is the top layer of an asphalt pavement, sometimes called the wearing course. It is usually made of dense graded AC. It must be tough to resist distortion under vehicle/aircraft and provide a smooth and skid-resistant riding surface. Typical asphalt surface course has a thickness of 75 to 100 mm. It is difficult to be compacted in one layer if the surface course was too thick, thus the surface course can be constructed as two layers: surface course and binder course. The binder course is the asphalt layer below the surface course, which usually consists of larger aggregates and less percentage of asphalt and generally has lower quality as compared to the surface course.

The base course is made of high quality crush stone or gravel necessary to ensure stability under high aircraft tire pressures.

The sub-base course is constructed with lower quality granular aggregates, and it increases the pavement strength.

The sub-grade is the natural in-situ soil material which has been cut to grade, or in a fill section, is imported common material built up over the in-situ material. It provides a stable and uniform support for the overlying pavement structure.

The asphalt pavement could be constructed as a whole piece in-situ with no joints or dowel bars. Thus for flexible pavement, times required for constructed are reduced compared to the rigid pavement and adjacent traffic flow could usually be maintained when one lane is under repair or construction.

The California Bearing Ratio (CBR) test was defined as the penetration resistance of the base, subbase and subgrade soil relative to a standard crushed rock. The higher the CBR value, the better the soil is. Hence, CBR was usually used to represent the quality of the base, subbase and subgrade material. The CBR

17

value, together with gross weight and annual departures of the aircraft can then be employed to decide the thickness of the AC layer for aircraft runway. The typical load-thickness chart for the AC layer is shown in Figure 2.8. From the figure, it can be seen that with the increase of the loading, the thickness of the AC layer is monotonic increasing.

The load from blast and impact event imposed to AC layers was much higher (i.e. about 1000 MPa from 5 kg TNT explosive detonated at pavement surface) than that from aircraft. According to Figure 2.8, it was found that in order to sustain this severe load, the thickness of AC layer needs to be very thicker (197m). However, it is not possible to construct such thicker AC layer. Thus, for the normal thickness of AC layer, it has little resistance to this severe load due to its low strength, and the whole layer may be destroyed.

Hence, it can be found that the using flexible pavement solely to sustain blast and impact may not be a good choice.

2.4.2 Rigid Pavement

Rigid pavements are made of portland cement concrete as a surface course. A typical cross section of rigid pavement was shown in the right hand side of Figure 2.7. Rigid pavements were placed either directly on the prepared subgrade or on a single layer of granular or stabilized material. Because there is only one layer of material under the concrete and above the subgrade, sometimes it is also called sub-base/base course.

In rigid pavement, due to the shrinkage and thermal expansion properties of the concrete, the concrete surface course should be cast in-situ only with a limited dimension as individual concrete slab. Dowels bars are employed to

connect the individual concrete slab sections and transfer the load between these two concrete slab sections. The joint is also used to prevent the development of transverse and longitude cracks in the concrete slab. Magnitude of wheel loads would affect the required concrete slab thickness and strength of the concrete material of this slab. The typical compressive strength of the concrete used as the surface course for runway pavements was 45 MPa. The thickness of a concrete surface course varied from 225 mm to 450 mm, depending on the sub-grade conditions.

When the explosive is detonated at the surface of the concrete slab, the crater will occur at the concrete slab. The diameter of the crater is given in Figure 2.9, which is obtained from CONWEP (1992). From the figure, it is found that the crater diameter is around 0.9 to 1.5 m for the TNT charge weight 5 to 20 kg. The crater depth is usually taken as the half of the crater diameter. Hence, for rigid pavement (i.e. the thickness of concrete slab was around 225 to 450 mm), the whole concrete slab will be penetrated even the concrete slab has higher strength compared to the AC layer in flexible pavement. Under this circumstance, the underneath subgrade will be effected and it needed to be re-compacted before placing new concrete slab.

In order to have better blast and impact resistance, the thicker concrete slab may be needed. However, thicker concrete slab will cause construction issue such as shrinkage, high wrap stress in the material as mentioned above. Hence, it is not suitable to use rigid pavement solely to sustain blast and impact load.

2.4.3 Load Distributions

For static case, an aircraft will impose to the pavement a static load equal to the gross weight of the aircraft through the landing gear. The landing gear configuration does then play a critical role in distribution the weight of the aircraft on the ground it sits on and hence affects the design of airfield pavement.

There are many types of landing gear configuration for aircrafts according to the Federal Aviation Administration (FAA). Herein, only the typical landing gear configurations were summarized in Figure 2.10. Basically, there are six configurations: (a) Single wheel, (b) Dual wheel (c) Dual (d) Double dual tandem (e) Triple tandem, and (f) Dual tandem plus triple tandem. It is observed that the heavier the aircraft, the more wheels on a landing gear.

The weight of aircraft is transmitted to the pavement though the tire connected to the wheel. The contact area between tire and pavement is usually simplified to a rectangle shape. The maximum tire pressure and gross weight for different aircraft was summarized in Table 2.1 and Table 2.2. In Table 2.1, for civilian aircraft, it is seen that the average tire pressure is 1273 kPa with the range from 1020 to 1612 kPa. For military aircraft, as seen in Table 2.2, the range of tire pressure is 861 to 2136, with an average of 1700 kPa.

Obviously, when the load generated from impact and blast event was larger than that of the design maximum tire pressure, the crater might occur in pavement. The shape of crater can be seen in Figure 2.11. From the figure, it is shown that the depth of the crater arrived at the layer of subgrade/sub-base which consisted of sand/gravel stone/ crushed stone. Thus, if the repair was carried out for this pavement, the surface course needed to be changed, and the soil underneath needed to be compacted again in order to meet the requirement of the

design tire pressure. It was postulated that this kind of repair needed a long time and was very time consuming. If the strength of the surface course was strong enough so that the depth of the crater was shallow and would not get into the sub-grade/sub-base. Under this circumstance, the rapid repair might be carried out easily.

Table 2.1 Max gross weights and tire pressure for civilian aircraft (from Boeing and Airbus official website)

Type of Plane	Max Gross Weight (kg x 10^3)	Type of Gear	Max Load on Each Main Gear (kg x 10^3)	Tire Pressure (kPa)
BOEING 707-320C	151.20	Dual-tandem	70.7	1240
BOEING 707-120B	116.10	Dual-tandem	54.0	1171
BOEING 727-100	76.50	Dual	34.6	1144
BOEING 737-100	49.50	Dual	11.6	1020
BOEING 737-200	52.20	Dual	23.8	1130
BOEING 737-300	63.00	Dual	28.6	1240
BOEING 737-400	67.95	Dual	31.8	1275
BOEING 737-500	60.30	Dual	27.8	1337
BOEING 747-100B	320.85	Double Dual-tandem in Wing Gear/Double Dual-tandem in Body Gear	74.9	1495
BOEING 747-200C	376.20	Double Dual-tandem in Wing Gear/Double Dual-tandem in Body Gear	87.3	1385
BOEING 777-200LR	345.60	Three Dual-tandem	158.4	1502
BOEING 777-300ER	349.65	Three Dual-tandem	161.6	1523
CONVAIR CV 880	83.25	Dual-tandem	39.2	1034
LOCKHEED L1011-1	184.95	Dual-tandem	87.8	1206
McDONNEL-DOUGLAS DC 10-10	185.85	Dual-tandem	87.3	1206
McDONNEL-DOUGLAS DC 8-43	143.10	Dual-tandem	66.6	1220
CONCORDE	174.60	Dual-tandem	82.9	1268
BAC 1-11-500	45.00	Dual	21.4	1199

Table 2.1 Max gross weights and tire pressure for civilian aircraft (continue)				
A330-200	232.04	Dual-tandem	109.6	1419
A340-600	378.18	Double Dual-tandem in Wing Gear/Double Dual-tandem in Body Gear	121/109.7	1612
A380-800	566.48	Double Dual-tandem in Wing Gear/Three Dual-tandem in Body Gear	101.7/161.6	1502
			Average:	1273

Table 2.2 Max gross weights and tire pressure for military aircraft (from U.S. Military aircraft, FAS Military Analysis network)

Type of Plane	Type	Max Gross Weight (kg x 10^3)	Type of Gear	Max Load on Each Main Gear (kg x 10^3)	Tire Pressure (kPa)
B-1B LANCER	Bomber	214.65	Dual	101.95	1791
B-52 STRATOFORTRESS	Bomber	219.6	Dual	109.8	1895
C-130 HERCULES	Cargo	69.75	Double Single-tandem	33	861
C-5B GALAXY	Cargo	378	Complex Dual and Quadruple	90	1171
F-4C/G PHANTOM	Fighter	27.9	Single	13.2	1826
F-15 EAGLE	Fighter	36	Single	17.1	2101
F-16 FALCON	Fighter	16.88	Single	8	2136
T-38 TALON	Trainer	5.67	Single	2.7	1826
				Average:	1710

2.5 High Strength Concrete (HSC)

2.5.1 Introduction

Concrete is a composite material composed of coarse aggregate, chemically bound and the mortar (cement + water + fine aggregate). Hence, the mechanical behavior of concrete was influenced by the coarse aggregate and mortar, as well as the interfacial transition zone (ITZ) between these two materials. A diagrammatic representation of ITZ in the normal concrete is shown in Figure 2.12. From the figure, it can be seen that the ITZ is generally more porous than the mortar. In the ITZ, the higher concentration of large Calcium Hydroxide (CH) crystals was also found than those in the mortar as shown in Figure 2.12. These made the ITZ become the weakest link in the normal concrete, and let the coarse aggregate become the strongest component in the normal concrete. Usually, with the increase of loading, the crack will first occur in the ITZ and then propagates through it (around coarse aggregate), which causes concrete failure. Hence, the compressive strength of the normal concrete is usually decided by the ITZ which is the weakest component.

In order to achieve higher compressive strength of concrete, it is necessary to improve the ITZ and increase the strength of the mortar. Adopting small size of coarse aggregates will decrease the porosity of the ITZ. Addition of silica fume will also densify the ITZ and eliminate the growth of large CH crystals in the ITZ. With adopting these measurements, the strength of the ITZ will be effectively increased. Reducing the water-to-cement ratio (w/c) will consequently enhance the strength of the mortar. Hence, for the high strength concrete, the ITZ between

the coarse aggregate and mortar may no longer be the weakest component in concrete, and cracks may go through coarse aggregates rather than around them.

When the concrete structure was subjected to dynamic loading, it was observed that the strength, stiffness and ductility (or brittleness) of the concrete could be affected or enhanced by the strain rate. It was known to be the strain-rate dependent for the concrete-based materials. This phenomenon became significance when the rate changed by more than one order of magnitude. Figure 2.13 shows the strain rate for different loading cases. It was found that under impact and blast loading, the strain rate usually reached about 10 to $10^3 \, s^{-1}$.

2.5.2 A review of Impact and Blast resistance of HSC

The protective structures such as security barriers are normally consisted of concrete. With the advancement of the research on high strength concrete technology, more and more protective structures are designed to use high strength concrete as a protective material due to its high compressive strength and economic advantage. Many researchers have investigated the impact and blast resistance of high strength concrete. The following paragraphs will highlight some of the key findings.

Clifton (1982) had reported that the volume of the crater produced when concrete was subjected to impact or impulsive loading varied approximately inversely with the square root of the concrete's compressive strength. It was also found that the dynamic tensile strength of concrete had an important effect on its impact and impulsive resistance. It was then suggested that incorporation of polymers in concrete would significantly increase the dynamic tensile strength of concrete.

Hanchak et al.(1992) carried out the perforation experiments on reinforced concrete with unconfined compressive strength of 48 MPa and 140 MPa. For impact velocities between 300 and 1100 m/s, both 48 MPa and 140 MPa concrete slabs were perforated as shown in Figure 2.14 (a) and (b). It was found that increasing in unconfined compressive strength from 48 MPa to 140 MPa did not increase the ballistic perforation resistance significantly. It was proposed that the penetration resistance in the crater regions was not sensitive to the unconfined compressive strength of concrete slab. This conclusion was different from the observation obtained by the Clifton (1982) that the crater volume was related to unconfined compressive strength. One possible reason for this different behavior is that in Hanchak's experiment, a higher impact velocity was employed which induced higher strain-rate than the impact velocity considered in the report from Clifton's. Furthermore, the high strength concrete (i.e.140 MPa concrete) showed more brittle behavior as shown in Figure 2.14. From this figure, it was observed that the higher compressive strength slab (140 MPa) had more severe cracks and slightly bigger damage region at the impact surface compared with that from 48 MPa slab.

Dancygier and Yankeleysky (1996) studied the difference in response of a normal concrete with the compressive strength of ~35MPa and high strength concrete with the compressive strength of ~110 MPa, under hard projectile impact with the velocity of about 145 m/s. It was observed that high strength concrete had smaller penetration depth than normal strength concrete. But the crater size at front face (spalling) and rear face (scabbing) was bigger for high strength concrete than for normal strength concrete, which was consistent with the finding that the high strength concrete would show higher brittleness compared to normal strength

concrete. In the experiment, it was also found that incorporation of steel fibers in the high strength concrete would arrest cracks and thus minimize the damage region.

For the function of steel fibers in the high strength concrete, Luo et al. (2000) conducted the high-velocity impact (impact velocity is between 364.9 and 378.3 m/s) experiment on a high performance steel fiber-reinforced concrete (HPSFRC) and reinforced high strength concrete (RHSC). In HPSFRC, the steel fibers were used as the reinforced material, while in RHSC the steel bars serviced as the reinforced material. The unconfined compressive strength of the HPSFRC and RHSC were 100 MPa and 80 MPa, respectively. From the test results, it was observed that under high speed projectiles impact, the RHSC targets exhibited smash failure while all the HPSFRC targets still intact with several radial cracks on the front faces and some minor cracks on the side face as shown in Figure 2.15 (a) and (b). This again showed that the addition of fibers in the brittle materials could significantly restrain the propagation of the crack.

According to the experiment study by O'Neil et al. (1999) on high strength concrete under penetration impact, it was found that penetration depth caused by impact for very high strength concrete (VHSC) with compressive strength of 157 MPa was approximately 50% less than that for conventional normal strength portland concrete (CSPC) with compressive strength of 35 MPa, and 30% less than that for high strength portland concrete (SHPC) with compressive strength of 104 MPa and high strength steel fibre reinforced concrete (HSFR) with compressive strength of 90 MPa, as shown in Figure 2.16. However, in terms of the visible crater dimension, it was observed that the SHPC concrete target was about the same as that for the CSPC concrete target, even though the depth of

penetration for HSFR was about 30% less than that of CSPC. The addition of steel fibers in the HSFR concrete resulted in a significant decrease in visible damage, and still resulted in a depth of penetration about 30% less than the CSPC concrete. The visible damage to the VHSC concrete target was larger than that to the HSFR concrete target. This was again shown that the high strength concrete would have high brittle property. The post-test photograph for these concrete targets face under high impact velocity was shown in Figure 2.17. It was also found that incorporation of fibers in the concrete did not significantly improve the penetration depth, but did minimize the damage region.

Recent research by Zhang et al. (2005, 2007) studied the impact resistance of the high strength concrete under high velocity projectile (600 – 700m/s) impact. The results showed that the penetration depth decreased with an increase in the compressive strength. However, above a certain level, further increase of the compressive strength would not make any additional contribution to the reduction of the penetration depth as shown in Figure 2.18. The impact resistance of the high strength fibre-reinforced concrete was also investigated by Zhang et al. (2007). Figure 2.18 also revealed that the penetration depth of HSC with or without steel fiber is about the same at all range of compressive strength. Hence, it can be concluded that incorporation of steel fibers in high strength concrete did not have a significant effect on penetration depth which was consistent with conclusion from O'Neil et al. (1999). However, incorporation of steel fibers in high strength concrete decreased the crater's diameter and crack significantly as shown in Figure 2.19. Figure 2.19 shows that the high strength fiber-reinforced with higher fiber concentration had significantly reduced the volume of crater compared to that with lower fiber concentration.

The effect of various type of fibers in high strength concrete or shotcrete material where investigated by Gupta et al. (2000), using low velocity impact drop test. The weight of the hammer was 578 kg. The shotcrete, compressive strength of ~54 MPa, was reinforced with different type of fibers F1 to F11 of length 18 to 35 mm and tensile strength 375 to 1115 MPa as listed in Table 2.3. In the test, the hammer was dropped from a height of 0.45m, which had a potential energy of 2551 J. The velocity of the hammer before striking the slab was about 2.97 m/s. Figure 2.20 shows the test results of shotcrete under impact load, in which the label M0 means mix without fiber, and MF1 means mix with F1 fiber and so on. From the figure, it was found that without fiber reinforcement (M0), the behavior is very brittle, with adding fiber reinforcement (except in the case of the carbon fiber reinforced shotcrete MF8 and MF9) highly effective in increasing the ductility and hence improving the fracture energy absorption. However, this improvement was highly dependent on the type and shape of the fiber, which is shown in Table 2.3. The most efficient fiber in energy absorption is the hooked-end steel fiber, followed by the flat-end steel fiber, the two polypropylene fibers, twin-cone steel fiber, and the PVA fiber, in that order.

Lok and Pei (1996; 1997) found that the steel fibre reinforced concrete panel (compressive strength was 45 MPa) under impact and air-blast loads, could significantly reduce cracking and crack propagation, and minimize spalling and retain post-peak load-carrying capacity compared to the conventional concrete. However, it was observed that the positive effect of adding fibers diminishing once the fiber concentration reached some threshold value. Concrete panel with higher fibre concentration that exceeded the threshold value will not have additional improvement in resistance (Lan et al. 2005).

Table 2.3 Properties of fibers used in drop weight test (after Gupta et al. 2000)

Fiber Shape	Fiber code	Geometry	Material	Cross section	Length (mm)	Diameter (mm)	Tensile strength (MPa)	Fiber weight (mg)	Elastic modulus (GPa)
	F1	Hooked-end	Steel	Circular	30	0.5	1115	44.74	210
	F2	Hooked-end	Steel	Circular	35	0.55	1115	63.16	210
	F3	Flat –end	Steel	Circular	30	0.73	1110	95.54	210
	F4	Straight	Polypropylene	Circular	25	0.38	375	2.75	2.6
	F5	Straight	Polypropylene	Circular	25	0.38	375	2.75	2.6
	F6	Straight	Polypropylene	Circular	38	0.63	375	10.66	2.6
	F7	Crimped	Polypropylene	Circular	30	0.76	450	21.48	3.5
	F8	Straight	Carbon	Circular	10	0.018	590	0.42	35
	F9	Straight	Carbon	Circular	18	0.017	1770	0.76	180
	F10	Flat-end	PVA	Rectangular	30	0.55x0.75	900	16.09	29
	F11	Twin-coned end	Steel	Circular	35	1.00	1115	243.90	210

31

In another experiment study on a new type of HSC by Kuznetsov et al. (2006). The blast loading using bare and fragment charge was conducted on 2 types of material: 1) SFRPC: steel fibre reinforced concrete with addition of reactive powder. 2) RC: ordinary reinforced concrete. Compressive strength of SFRPC is 170 MPa and that of RC is 50MPa. It was observed that under same bare charge, both RC and SFRPC panel did not surfer damage at the front face, while at the back face the RC panel was breached and SFRPC panel was not breached with less spalling and less scabbing as shown in Figure 2.21. The author concluded that SFRPC panels had a much larger tensile strength than the ordinary RC panel due to the presence of the steel fibers and properties of the reactive powder concrete material. However, the comparison was not so simple as the compressive strength of SFRPC and RC is not the same. In the test under fragment charge, it should be noted the fragment charge had the same charge weight as that in bare charge. It was found that SFRPC panel showed minor cracking while the RC panel was observed significant back face scabbing, which was similar to that shown in Figure 2.21. However, at the front face, the penetration was observed for SFRPC and RC. It was found that the penetration depth for SFRPC panel was less than that for the RC panel as listed in Table 2.4. It was then concluded that the loading and impulse from synergistic of fragment and blast loading was greater than that from bare charge.

Table 2.4 Depth of penetration of fragment charge into the concrete panel (after Kuznetsov et al. 2006)

Type of concrete	SFRPC	Ordinary RC
Depth of penetration (mm)	10 ±2	17 ±2

2.5.3 Remarks on Impact and Blast resistance ability of HSC

Based on above review, for the impact resistance, it could be found that the HSC had better penetration resistance compared with that of normal strength concrete. However, above a certain level, further increasing of the compressive strength would make little contribution to decrease the penetration depth. Moreover, increase of the compressive strength for the concrete would lead to more brittle behavior. For the incorporation of the steel fibers in HSC, it was found that adding steel fiber would significantly enhance the material's ductility and decrease the area of damage region and crack. However addition of the steel fiber did not have a significant effect on penetration depth resistance.

For the blast resistance, it was shown that the high strength concrete with steel fibers reinforcement would significantly decrease cracking and crack propagation, and minimize spalling and retain post-peak load-carrying capacity compared with that of the normal strength concrete. However, it was observed that the positive effect of adding steel fibers diminishing once the fiber concentration reached some threshold value. After certain threshold value, further increase of the concentration of steel fiber in concrete would not significantly improve the blast resistance of the material.

2.6 Engineered Cementitious Composites (ECC)

2.6.1 Introduction

Engineered Cementitious Composites (ECC) is micromechanically optimized fibre reinforced cement based composite materials. ECC, unlike most of the cementitious materials, is ultra-ductile under tensile and shear loading

indicated by multiple micro-cracking behaviors. These micro-cracks allow ECC to exhibit pronounced strain-hardening behavior similar to ductile metals. Figure 2.22 shows the large deformation tolerance of an ECC specimen under flexural and uniaxial tensile test. Figure 2.23 shows the stress-strain behavior of ECC showing how ductile it is compared to concrete, FRP and cement paste. From the figure, it is shown that the formation of multiple cracks in the ECC sample led to the tensile strain hardening of the material. ECC not only exhibited excellent behavior under shear, flexure and tensile loading (Li et al. 1994; Li and Maalej 1996), but also possessed high fracture energy and notch insensitivity (Maalej et al. 1995; Li and Maalej 1996). These properties made the ECC possible to be used as an ideal material for protective material.

2.6.2 A review of impact and blast resistance of ECC

The ECC is a recently developed material and so far there are little researches on the application of ECC as protective material. One of the recent studies in such application was reported by Maalej et al. (2005) which focused on the behavior of hybrid-fiber Engineered Cementitious Composites (ECC) subjected to dynamic tensile loading and projectile impact. The results from dynamic tests using different stain rates in tensile loading, it was observed that for high strain rates of up to $10^{-1}s^{-1}$, there was a substantial increase in the ultimate tensile strength with increasing strain rate. The increasing of the tensile strength for ECC was significantly higher than that for concrete under same strain rate. Further, the results from projectile impact (impact velocity was 300-750 m/s) showed that ECCs might not significantly reduce the penetration depth compared with normal concrete due to lack of coarse aggregate (as summarized in Table 2.5)

but ECC did possess other favorable characteristics against projectile impact. Especially, ECC provided increased resistance with reduced scabbing, spalling, fragmentation, and excellent ability to maintain structural integrity, and exhibits better energy absorption since micro-cracking distributing the dynamic pressure.

Table 2.5 ECC and normal concrete under high velocity impact (after Maalej et al.2005)

	ECC	Normal Concrete
Thickness (mm)	150	
Compressive Strength (MPa)	55	45
Impact Velocity (m/s)	620	670
Penetration Depth (mm)	46	48
Crater diameter (mm)	30	150

From above test results, it was shown that when ECC material was subjected to impact with small rigid projectile at high velocity, the load application was locally concentrated which would lead to local response and local damaged of the material. The tensile hardening properties for the ECC would be also important in the global response, that is the target could still have tensile and flexural strength at larger deformation.

Zhang et al. (2005) studied on the performance of Reinforced Concrete (RC), fibre reinforced concrete (FRC), and hybrid-fibre ECC panels subjected to drop weight impact at lower impact velocity. Results had shown that ECC panels had reduced crater size and penetration depth, significantly improved impact resistance and energy absorbing capacity against multiple impacts compared to both RC and FRC counterparts as shown in Figure 2.24 to 2.26. From the figures, it could be observed that both the RC and FRC specimens demonstrated brittle shear failure characterized by the formation of a large shear cone on the distal face

which was not exhibited in all ECC specimens due to the excellent shear/tensile properties of ECC material. In addition, the ECC specimens showed more ductile failure process than RC and FRC counterparts characterized by larger deformation tolerance before serious cracking/scabbing and before complete perforation. The results for number of impact till perforation for RC, FRC and ECC are summarized in Table 2.6 which shows that ECC panels could be subjected to higher number of impacts before perforation.

Table 2.6 Number of impact till perforation (after Zhang et al. 2005)

Specimen	Number of Impacts to Perforation
RC (100 mm)	3
FRC (100mm)	7
ECC (100mm)	No Perforation (> 10)
ECC (75mm)	16
ECC (50mm)	12

2.6.3 Remarks on impact and blast resistance ability of ECC

The impact test results showed that, although ECC might not significantly reduce the penetration depth compared with normal concrete, possibly due to the lack of coarse aggregate, ECC did possess other favorable characteristics against projectile impact such as excellent ability to maintain structural integrity, and better energy absorption.

From the drop weight test, it was observed that ECC can reduce damage and significantly improve impact resistance against multiple impacts and enhance energy absorption capacity and ductility compared to that of RC and FRC counterparts.

The results from above analysis about ECC under high and low impact velocity showed the great promising in using ECC material as a ductile component to suffer large deformation and absorb tensile energy without failure.

2.7 Geosynthetics (GST)

2.7.1 Introduction

ASTM (1994) defines geosynthetics as planar products manufactured from polymer materials used with soil, rock, earth and other geotechnical-related materials as an integral part of civil engineering projects. The family of geosynthetics comprises of broad range of synthetics products namely geotextiles, geogrid, geonets, geomembranes, geopipes, geowebs and geocomposites. This section would concentrate on geogrids which was normally used in the pavement engineering.

2.7.2 Geogrid

The relatively recent discovery of methods of preparing high-modulus polymer materials by tensile drawing has raised the possibility that such materials may be used in the reinforcement of a number of construction materials including soil, such as geogrid (Koerner 1998). Nowadays, the major function of geogrids was reinforcement. Geogrids are relatively high strength, high-modulus, and low-creep-sensitive polymers with apertures varying from 7 to 100mm. The holes are either elongated ellipses, near squares with rounded corners, squares, or rectangles. The key feature of geogrids is that the openings between the longitudinal and transverse ribs, called the apertures, are large enough to allow soil strike through from one side of the geogrid to the other. The ribs of the geogrids are often quite

stiff compared to the fibers of geotextiles. The strength of rib and junction is an important parameter. This is because that the soil strike-through within the apertures bore against the transverse ribs, which transmitted the forces to the longitudinal ribs via the junctions. The junctions are the point that connected the longitudinal and transverse ribs.

The use of fabrics in road pavement was first introduced by Beckham and Mills (1935). Heavy cotton fabrics were used in reinforcing the paved roads by putting them on the formation soil and before laying asphalt. It was found that the road was in good condition. There was a reduction in cracking, raveling and local failure when the fabric deteriorated. This application cited the importance of geosynthetics in modern pavement engineering, and how the reinforcement and separation functions of the geosynthetics could improve on pavement serviceability.

Research (Yong 2005) was conducted to evaluate the feasibility of using geogrid reinforcement in the middle of asphalt layer. Figure 2.27 shows geogrid installed in an asphalt layer. By placing the geogrid as close to vehicular load as possible, effectiveness of reinforcement provided by geogrid within the asphalt layer might be enhanced. The test results showed that the rutting resistance against surface rutting of geogrid-reinforced flexible pavements was significantly enhanced. Figure 2.28 shows the reduction in rutting on asphalt pavements with inclusion of geogrid in the asphalt layer.

Recent research (Chew and Lim 2006) also showed that inclusion of some polymeric material like geogrid can improve not only the resilience properties of the pavement but also provide some form of added ductility subject to impact load. This had the potential for blast mitigation in terms of reducing the crater size to a

very minimum, thus reduce or even the need of crater repair when the bomb is smaller that some charge.

2.8 Asphalt concrete (AC) under dynamic loading

Asphalt concrete is made of bitumen binder and coarse aggregate. It is usually used as the surface course for the flexible pavement as mentioned above. The dynamic load in the daily application for AC is the traffic loading which is related to strain rate less than $10^{-1}\,s^{-1}$. The tests on AC under traffic loading were conducted by some researchers. Herein, some key findings will be introduced to understand the dynamic behavior of AC.

Tan et al. (1994) and Tashman et al. (2005) conducted experiments of AC under triaxial compressive loading at the strain rate from $10^{-6}\,s^{-1}$ to $10^{-3}\,s^{-1}$. The results showed that the failure stress increased with increasing of the applied strain rate. Seibi et al. (2001) studied AC subjected to uniaxial compressive loading with strain rate from $0.064s^{-1}$ to $0.28s^{-1}$. It was found that the yield stress was significantly dependent on the strain rate. Park et al. (2005) carried out tests on AC under uniaxial and triaxial compression with the strain rate changing from $10^{-4}\,s^{-1}$ to $0.07\,s^{-1}$. The results showed that as the increase of the applied strain rates, the yield stress and failure stress increased and the strain rate dependency was clear showing up at the higher strains. It was also found that the viscous behaviour of AC decreased with the increase of strain rate.

However, all above experiments concerned about the material properties of AC under common traffic loading. When pavement structure was subjected to the impact loading from aircraft crash and the blast load from explosive device, the large deformation would occur and the corresponding strain rate would exceed the

$10^{-1}s^{-1}$. However, the literature on AC under high strain rates ($>10^{-1}s^{-1}$) was limited.

The compressive Split-Hopkinson Pressure Bar (SHPB) test on AC was studied by Tang et al. (2009). In the test, the three strain rate was applied by SHPB device, that is, $35s^{-1}$, $75s^{-1}$, and $100s^{-1}$. It was found the compressive strength had significantly increased under the high strain loading. The results showed that the dynamic compressive strength increased to 65 MPa under strain rate $100s^{-1}$ compared to the static compressive strength 3.8 MPa, which caused the dynamic increase factor (DIF) to be about 17. It was worth mentioning that the test temperature for asphalt concrete compressive SHPB test was 5°C. Under this temperature, the viscous behaviour of AC would be significantly reduced.

Tekalur et al. (2009) studied the high strain rate properties of AC which contained 30% reclaimed asphalt material. Three fundamental mechanisms were tested and measured, that is, compression, tension and fracture toughness. In their research, the SHPB configuration was modified to apply the high strain rate loading to AC. It was found that the compressive strength increased by a factor of 5 and tensile strength enhanced by a factor of 1.5 when compared to the corresponding static strength. For the fracture toughness under high strain rate, it was also shown that the fracture toughness increased by 15 times the corresponding static value. After checking the post-test specimen, it was found that under high strain rate loading, the binder and trans-aggregate failure occurred in AC, while under static loading, only binder failure occurred. However, the above experiment did not give the detailed strain rate applied by the SHPB device.

Based on above literature review, it was obvious that the strength of AC would enhance with the increase of strain rate, and the AC showed high plastic

behavior at the high strain rate. Some research had already been done on the AC under some range of strain rate loading. However, no detailed Dynamic Increase Factor (DIF) curve is available for AC under low to high strain rate loading. Hence, a proposed DIF curves for asphalt concrete under different strain rate needed to obtain better protective design principles for pavement structure.

2.9 Interface property

It was found that the interfacial bonding had a great influential on the performance of the pavement structure, especially for the interface between AC and concrete layer. The weak interface strength would induce the slippage cracking of the overlay AC or delamination of the new AC layer from old layer. In order to sustain longer service life of pavement structure, it was necessary to investigate the interface behavior between asphalt concrete and concrete. Last few decades, many researchers (Uzan et al. 1978; Tschegg and Stanzl 1991; Romanoschi 1999; Canestrari and Santagata 2005; Collop et al. 2009) had carried out the experiments on interface properties between asphalt layers or between concrete layers. Several researchers had focused on interface properties between new asphalt and old concrete, or between new concrete and old asphalt. Some findings will be presented in the following part.

A monotonic direct shear test on interface between AC overlay and concrete pavement under no normal force was conducted by Leng et al. (2008) This test checked the several factors which might affect the interface behavior such as AC type, tack coat type, tack coat application rate and surface texture at various temperatures. It was found that the AC type and tack coat type really affected the interface bonding strength. At the same time, it was also concluded

that the optimum residual tack coat application rate was 0.05gal/yd^2. For the surface texture of underlay pavement, the direction of tinning in the concrete surface had no effect on the interface shear strength at 20°C. For the temperature effect, it was observed that lower temperatures led to better bonding.

Tschegg et al. (2007) examined the interface properties between new concrete overlay and the old asphalt concrete with the different pretreatments (without an adhesive agent, with cement grout, with cement grout plus dispersion, and with dispersion as adhesive agent) at different temperatures. In their research, the new test method (wedge splitting test) to measure the tensile strength and fracture energy was proposed because of the tensile strength obtained from the traditional pullout test was strongly scatter. The measured values from wedge splitting were reliable and profitable (obtained tensile strength and fracture energy in one test). The results from the wedge splitting test showed that the interface tensile strength decreased with increasing of temperature, and the interfacial fracture energy achieved a maximum value at about 10°C. It was also found that crack resistance was higher for no pretreatment than for any chemical pretreatment. Further, it was observed that the crack resistance could be enhanced by an optimal surface roughness of the milled pavement, that is, the depth and width of the grooves should be adjusted to the maximum aggregate particle size of the concrete.

Sadd et al. (2007) investigated the static and dynamic interfacial failure between new concrete overlay and the old asphalt at the temperature 20 °C. Composite samples (new concrete and old asphalt layer) with initial man-made interface crack geometry were conducted for uniaxial quasi-static tensile test. Asphalt part with two different age groups (30 and 180-200 days old) was

fabricated in the composite specimen. It was found that the interface with older asphalt had twice interface tensile strength as that with newer asphalt. Similar trend was observed for the interfacial fracture toughness, where the interfacial fracture toughness with older asphalt was higher than that with newer asphalt. It was also found that the interfacial fracture toughness K_{ic} were less than that of asphalt and concrete materials. This result was consistent with Tschegg et al. (2007), in which the interfacial fracture energy G_{if} ($G_{if} \propto K_{ic}$) was less than that of asphalt and concrete materials at around 20°C. However, it was observed the propagation path of interfacial failure crack was closer to the asphalt side, and some asphalt binder was pullout. This phenomenon was explained as the particulate reinforced of asphalt could produce high inter-granular stresses thereby biasing crack growth into the binder component. Shear test under dynamic and static loading was conducted by using a composite lap joint specimen with no initial man-made interface crack. The SHPB apparatus was used to apply dynamic loading to shear the composite lap joint specimen. It was found that the dynamic shear strength of the composite lap joint samples had about 4 times the static strength. After checking the post-test shear interface, it was observed that some asphalt was pulled out in the static shear test while the shear surface was smooth and no pullouts of either material were found.

From above analysis, it could be concluded that the AC type, the age of AC material, the adhesive agent type, surface texture of underlay pavement and temperature at construction would affect the interface strength between asphalt and concrete.

2.10 Numerical simulation of pavement under dynamic loading

An aircraft moving over a pavement will produce a dynamic loading. The pavement layers would response differently to this load according to different strength for each layer. With the development of the high speed computer, the numerical simulation of pavement structure under wheel loading or periodic loading could be conducted with the reasonable time and financial resource. There are many researcher conducted numerical simulation of pavement structure under common traffic loading.

Zaghloul and White (1993) and Zaghloul et al. (1994; 1994) used 3D finite element program ABAQUS to model the flexible pavement, rigid pavement and composite pavement under truckloads moving at different speeds. In the model, surface, sub-base and subgrade were included, and contact algorithm was also used to describe the interface behavior between the layers. The Druck-Parger and Cam-Clay model was employed to represent granular base and clay sub-base layer, respectively. For simulation of flexible pavement, the time-dependent behavior of AC was modelled with visco-elastic behavior. For the simulation of rigid pavement, the dowel bars and longitudinal and transverse joints were considered. The concrete slab was modelled with material model three stages (elastic, plastic and after failure stages) stress-strain behavior. As for composite pavement structure, the surface layers were consisted of AC overlay and concrete, hence the materials models used for simulating flexible and rigid pavement were employed to model these two materials. The 3D FEM results from dynamic nonlinear analysis were compared with the actual field measurements, and it was shown that 3D FEM model could predict real pavement deflection very well.

Saad et al. (2005; 2006) used 3D FEM software ADINA to model the flexible pavement with geosynthetic reinforcement under pulse loading. It was aim to investigate the beneficial effects of geosynthetic reinforcement to the fatigue and rutting strain criteria. In the model, the locations of geosynthetic reinforcement were considered, that is, the base-asphalt concrete interface, the base-sub-base interface and inside the base layer at a height of 1/3 of its thickness. The interface element was used to model geosynthetic. The elastic material model was used for AC layer, and the Drucker-Prager and modified Cam-clay model were employed to represent granular base and soil sub-base, respectively. The results showed that the placing the geosynthetic at the 1/3 of the base thickness led to highest reduction of rutting and surface deflection.

In above analysis, it was assumed that the pavement surface was in the elastic range with small strain under wheel loading. However, it could be found that when pavement structure under blast or high impact load, the deformation of the pavement would not be in the elastic range, and the plastic deformation and severe damage will occur. Thus, the elastic material model was no longer suitable for simulating concrete or AC material. Hence, an advanced material model for concrete or AC material which included the strain rate effect, strain hardening, strain softening and damage for the material is urgently needed to understand the dynamic behavior of pavement under blast and impact load. However, limited researchers studied on the pavement structure under blast and impact load.

Luccioni and Luege (2006) used commercial software ABAQUS and AUTODYN3D/2D to study the dynamic behavior of the concrete pavement under blast loading. In their study, the concrete plate was directly placed on the soil, and the TNT explosive was detonated above the concrete pavement surface with

different height, which led to the scale distance was about 0.23 m/kg$^{1/3}$ to 0.31 m/kg$^{1/3}$. In ABAQUS model, the blast loading was modeled as segment pressure acting on the front face of the slab, while in the AUTODYN3D simulation, the JWL material model was employed to simulate detonation of TNT explosive in the air. In both model, the elasto-plastic material with strain rate effect had been used for concrete material, the Drucker-Prager model was used for soil material. The contact algorithm was assigned to simulate the slide behavior between concrete slab and soil. The results showed that the both numerical model approximately reproduced the deformation and the resultant failure shape of the concrete plate under blast loading. However, simple material model for concrete plate could not simulate the development of the cracking as observed in the field trial test.

Other researchers mainly focused on the structural elements (e.g. concrete slab or panel) under blast or impact loading. A few sophisticated material models had been developed and validated with experimental data. Hence, due to similar material was used for constructing concrete pavement, the concrete slab or panel under such extreme loading could be studied as a reference. Thus, the following would discuss dynamic behavior of concrete slab or panel under blast loading.

Zhou (2008) studied the dynamic behavior of concrete slab under blast loading using AUTODYN3D. The concrete slab was placed in the steel holding frame, and the TNT explosive was detonated above the concrete slab surface. The JWL material model was employed to model detonation of the TNT explosive. By adopting remap method, the blast pressure interacted with the concrete slab in 3D model. In the model, the damage-based modified piece-wise Drucker-Prager model with strain rate effect was used for concrete slab. Comparison of the

numerical results with the experimental data, it was found that the damage-based modified piece-wise Drucker-Prager model could give reliable prediction of damage pattern on the concrete slab.

Wang et al. (2008) studied the reinforced concrete slab subjected to close-in explosion using LSDYNA. The TNT explosive was detonated on the surface of the concrete slab. In the model, the reinforced concrete slab was modelled with Lagrange mesh, while the TNT and air were discretized with Arbitrary Lagrange-Euler (ALE) mesh to generate the blast pressure. The MAT72 R3 material model was used to represent the concrete material. The rebar was modelled with kinematic hardening material model. The JWL material model was assigned for simulating TNT explosive. The numerical model predicted the similar crater diameter and spalling damaged pattern compared to the experimental data. However, the development of the crack at front and back face of the concrete slab was not similar as that in field trial test. This is possible that the parameters for the advanced material model were not correctly calibrated.

2.11 Summary of Literature Review

From above discussion, the surface course was very important in the resistance to damage due to bombs as it was the part to be hit directly. However the current types of typical pavement designs are insufficient to satisfy the needs of pavements which require much higher resistance to impact and blast loading. This is especially important in pavements where damaged pavement will significantly affect the operational readiness. Thus, damage for the target pavement needs to be kept to a minimal and rapid repair has to be conducted.

Thus there is a severe need to investigate new pavement materials to satisfy these needs.

There is an urgent need to find a new pavement design that could withstand higher impact and blast loading thereby increasing the durability of pavement and reducing the amount of repair needed. This in turns improves the operational readiness of the airfield which is especially important in recent years with the prevalent terrorists' attacks.

Over the last few years, many researches have been done on various new materials that offered impact resistance (HSC and ECC) and could further improve the ductility and durability of pavements (AC layer reinforced with GST). As can be seen from the review stated in the previous sections on these new materials, all of them have potential to be used as pavement materials for the mitigation of blast loading and impact. Their general properties and characteristics are summarized in the following Table 2.7.

Table 2.7 Characteristics of ECC, HSC and GST

	Penetration Resistance	Strength	Ductility	Fracture energy	Multiple resistance
ECC	---	---	√	√	√
HSC	√	√	---	√	---
GST (reinforced AC layer)	---	√	√	---	√

Each of these materials has their own advantages and disadvantages for blast mitigation. To fully utilize all their properties, a new pavement design consisting of all 4 materials will be considered. Ideally, the new pavement design should have high penetration resistance, strength, ductility and multiple resistance capability. The configuration of these 4 materials is very important. With these standards, a new pavement design is proposed. The next chapters will discuss the proposed new pavement material based on above 4 engineering materials.

The concrete-like material shows highly non-linear response under severe loading. While it is very expensive to conduct field test to investigate the actual behavior of concrete under severe loading, the numerical method is an alternative one. With the development of the high-speed computational capabilities, it is possible to carry out the numerical simulation of concrete structures subjected to blast or impact loading. However, a reliable simulation should be developed to obtain reasonable results and reproduce the essential physical mechanisms of the material under different stress and loading conditions. The robust material model is needed and the parameters are needed to be validated before using.
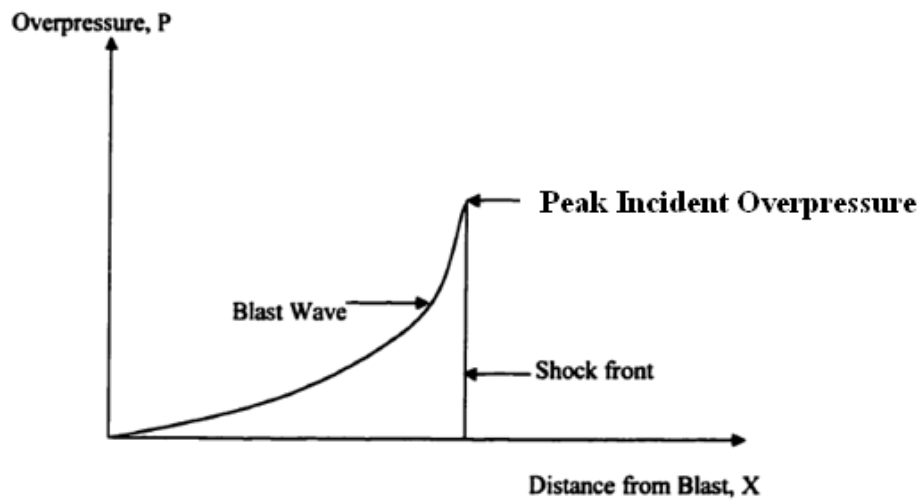
Figure 2.1 Variation of Overpressure with Distance in a Shock Wave (after Zineddin 2002)
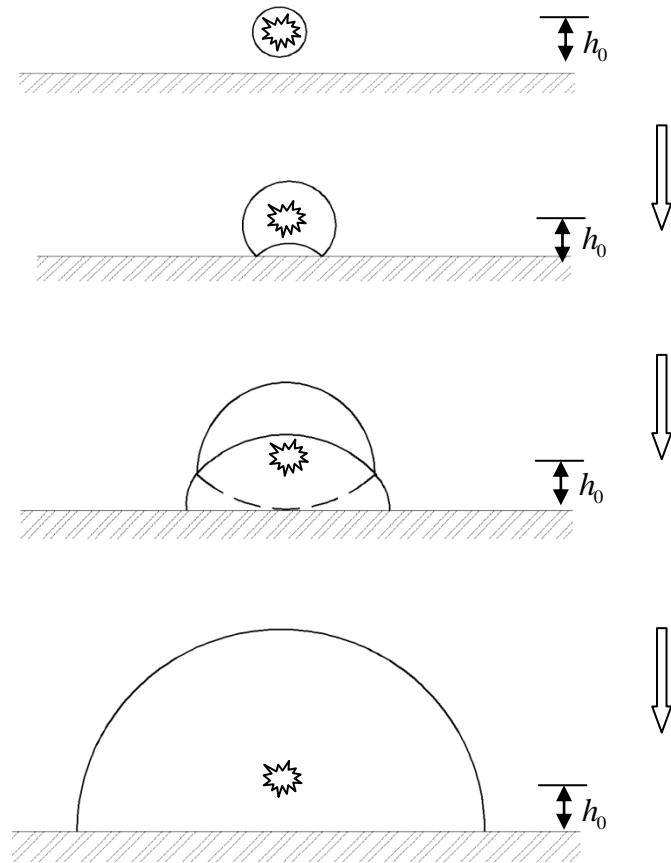
(a) Hemispherical shape of the blast wave
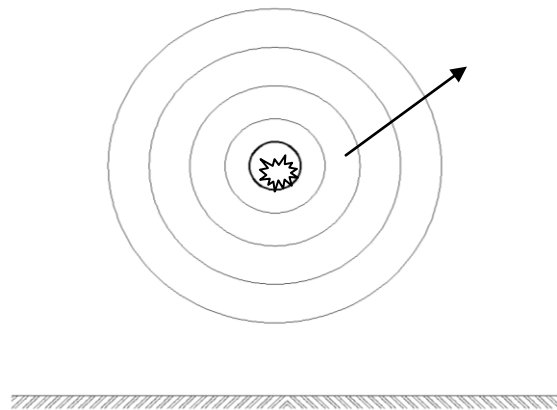
(b) Spherical shape of the blast wave

Figure 2.2 Schematic blast wave front after an explosion (a) near the surface (b) far above the surface
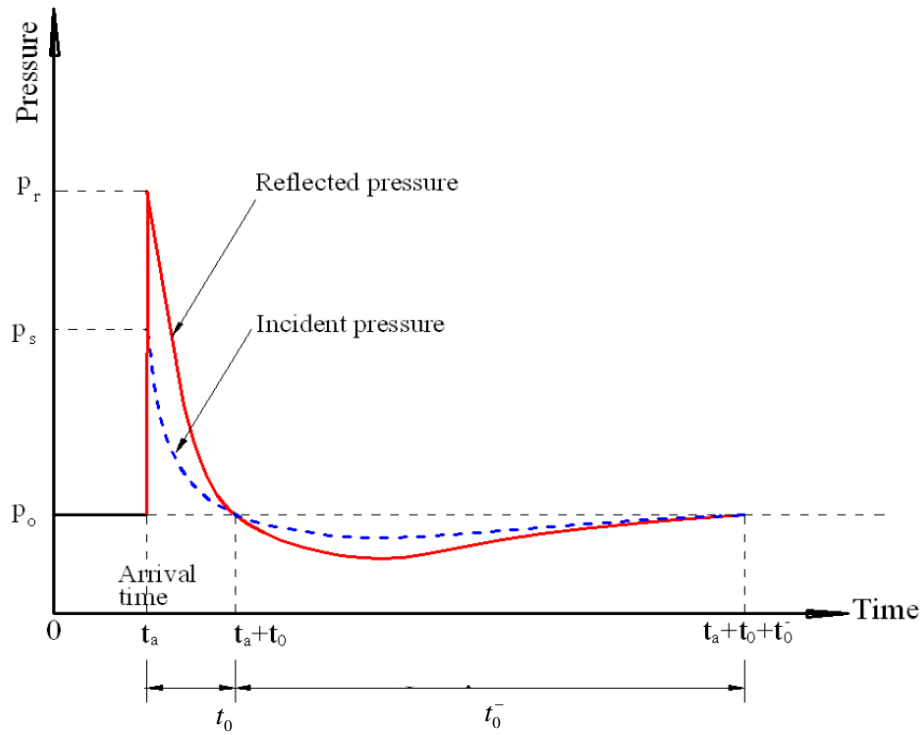
Figure 2.3 Variations of air blast pressure with time (TM5-1300)

U_i = Shock velocity of incident wave
U_r = Shock velocity of reflected wave
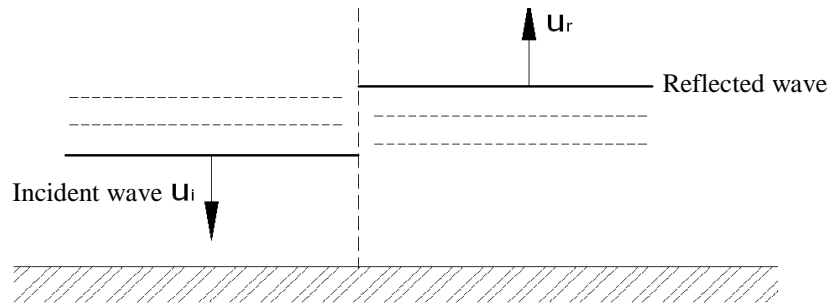
(a) Normal reflection
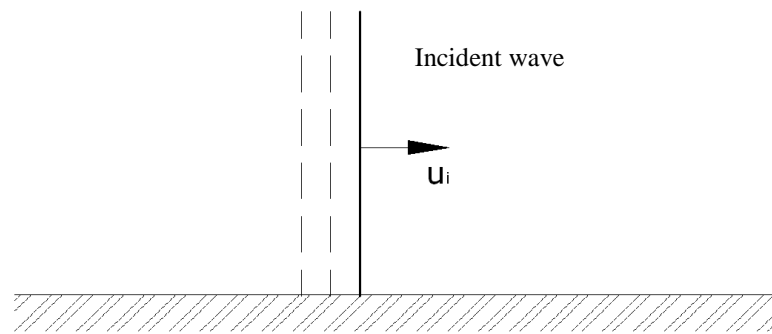
(b) Side-on reflection
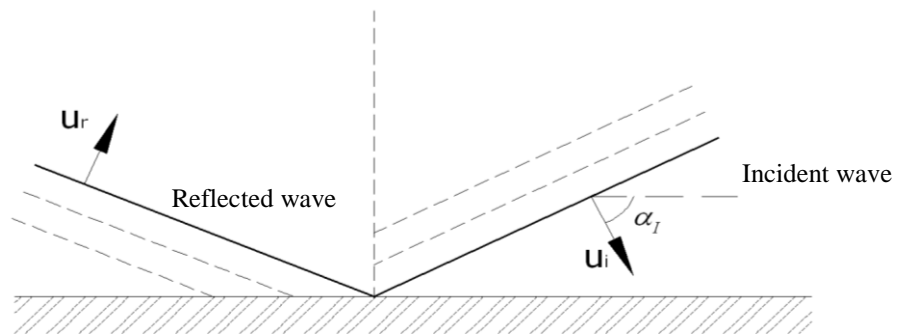
(c) Regular reflection

Figure 2.4 Different reflection at target surface

F(t) & R(t)

F(t)

R(t)

t_m

t_d

t

F (t) = Blast loading with time
R (t) = Structure resistance with time
t_d = Duration of blast load
t_m = Time to undergo maximum
        response of structure

(a) Impulsive loading

F(t) & R(t)

R(t)

F(t)

t_d

t_m

t
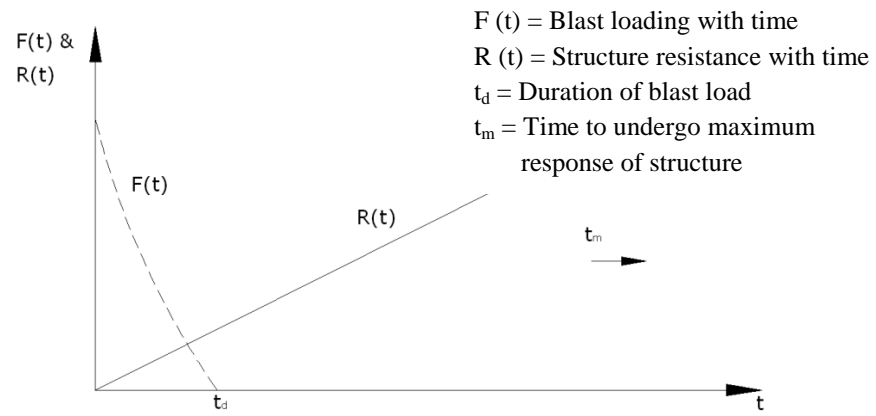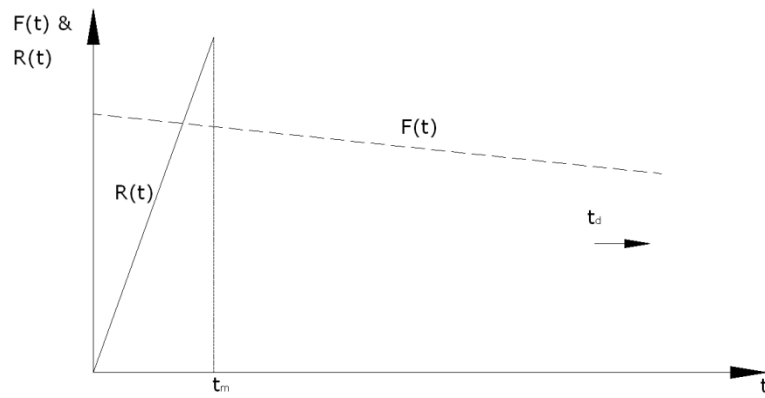
(b) Quasi-static loading

F(t) & R(t)

F(t)

R(t)

t_m   t_d

t
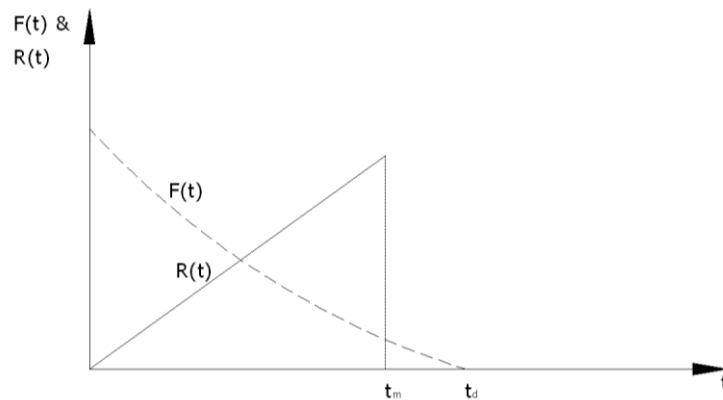
(c) Dynamic loading

Figure 2.5 Types of blast loading and structure response (after Smith and Hetherington 1994)

(a) Local effect of penetration (x) and scabbing

(b) Local effect of spalling

(c) Local effect of perforation

(d) Local effect of punching shear

(e) Overall global response
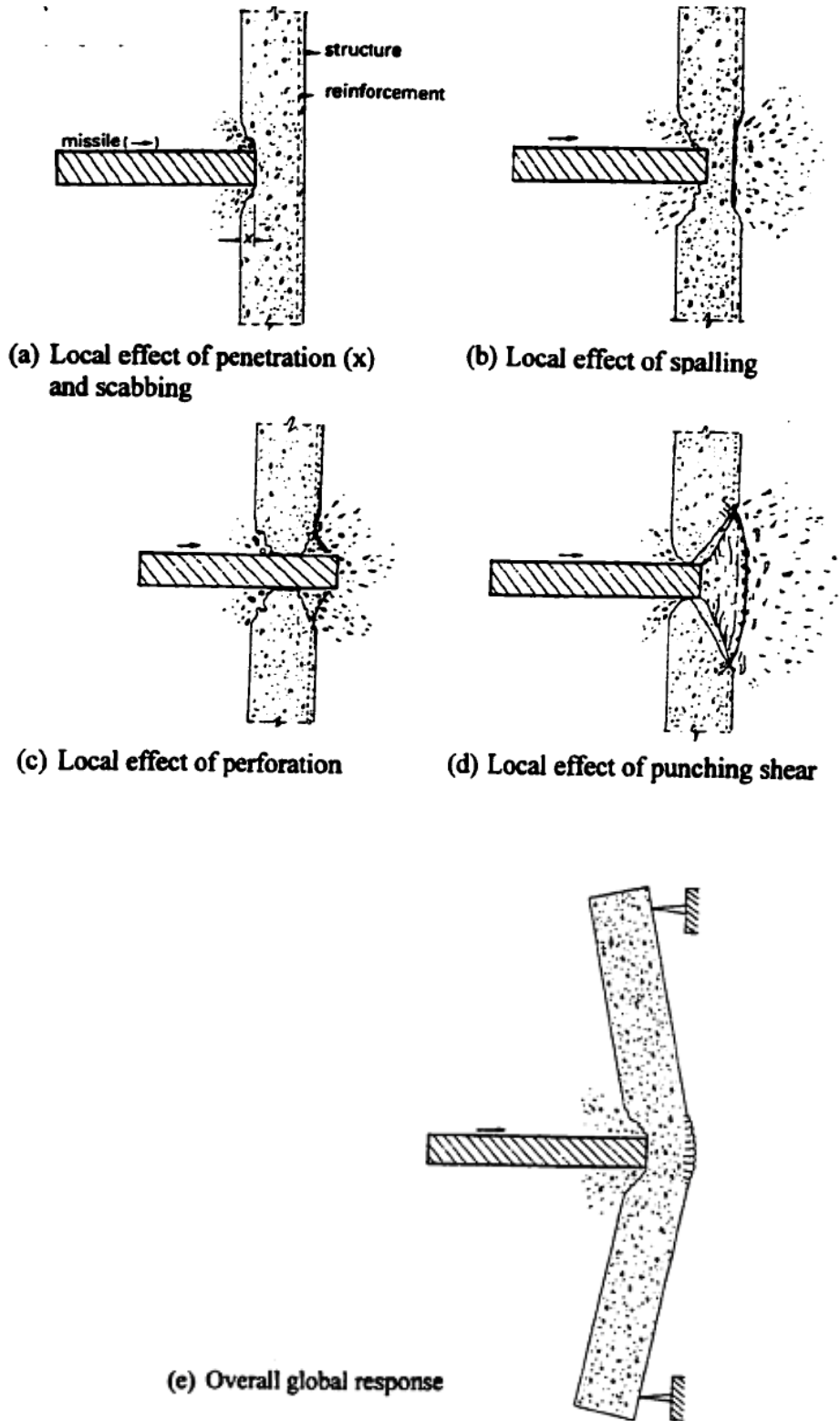
Figure 2.6 Different forms of Impact Damage (after Bangash 1993)
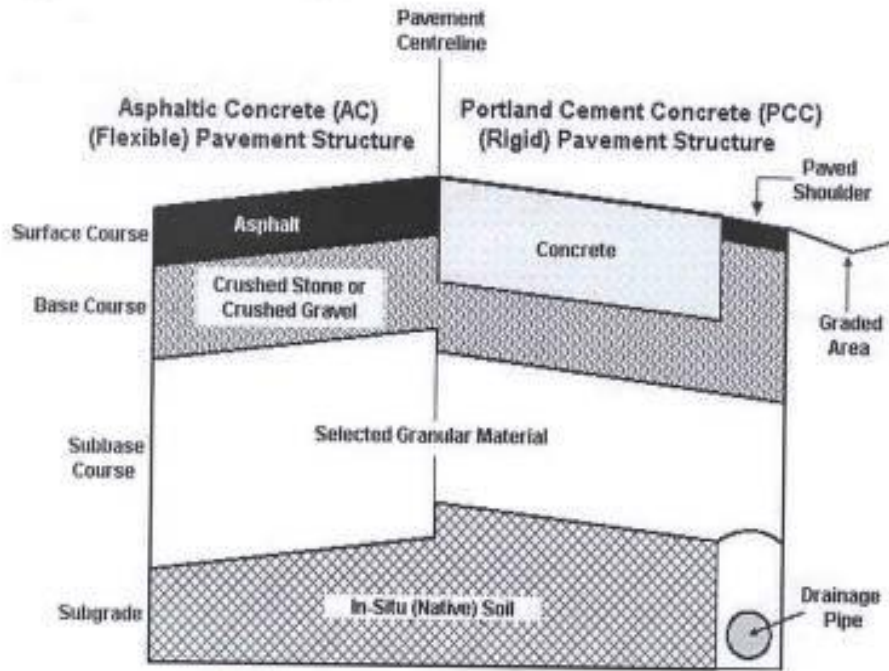
Figure 2.7 Cross section of typical pavement (after Chew et al. 2009)
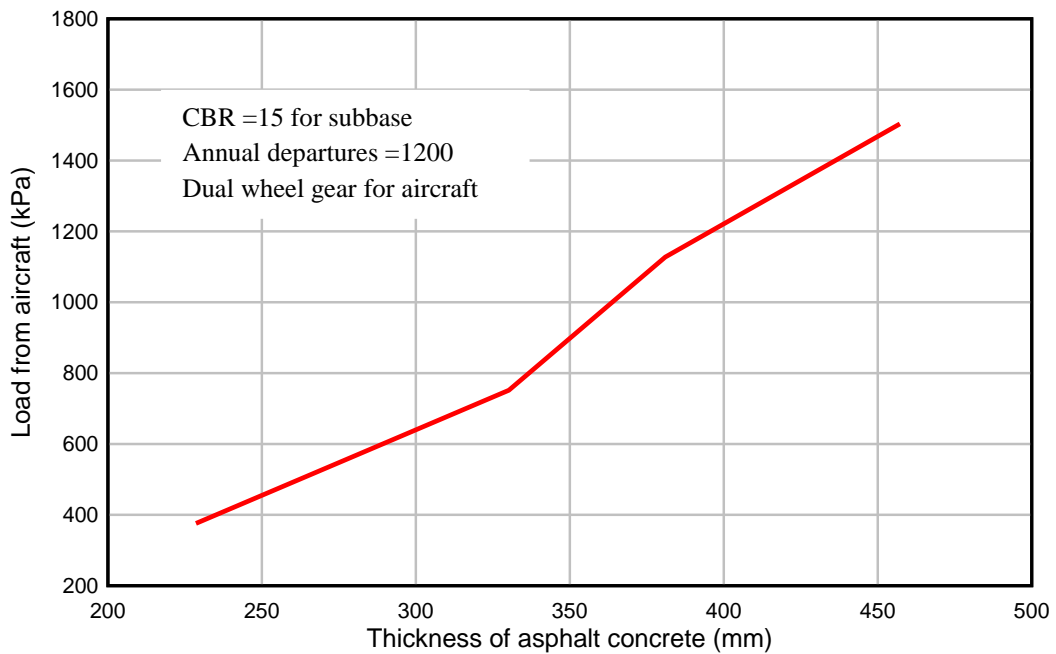
Figure 2.8 Typical load-thickness of AC layers for aircraft runway (by author)
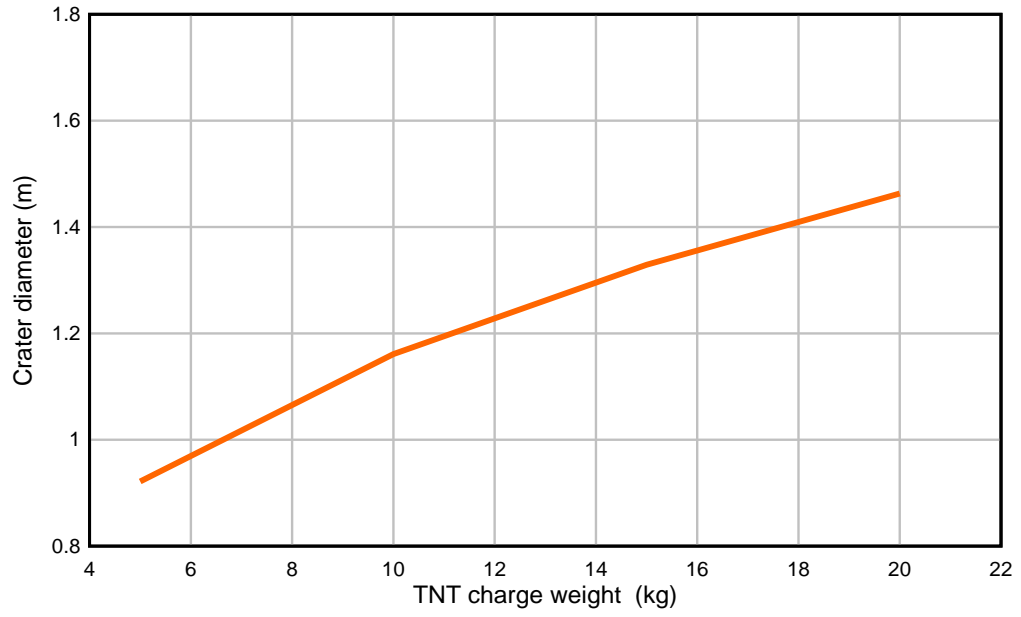
Figure 2.9 Crater diameter under different TNT charge detonated at the surface of concrete slab (by author)

"S" Single wheel

"D" Dual wheel

"2D" Dual tandem

"2D/2D2" Double dual tandem
Boeing 747

"3D" Triple tandem
Boeing 777

"2D/3D2" Dual tandem plus
triple tandem Airbus 380
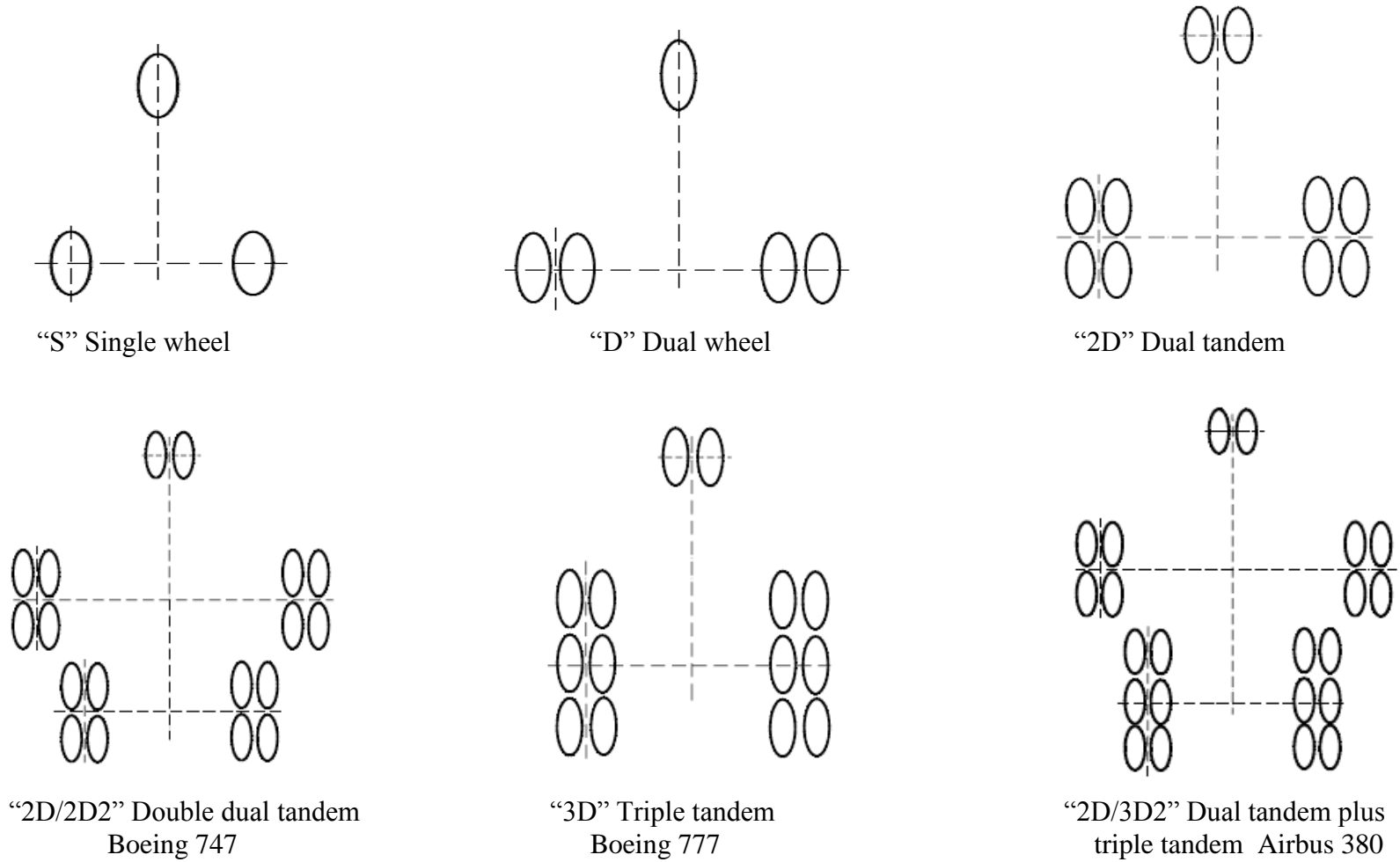
Figure 2.10 Plan view of typical aircraft landing gear configuration (from Boeing and Airbus official website)
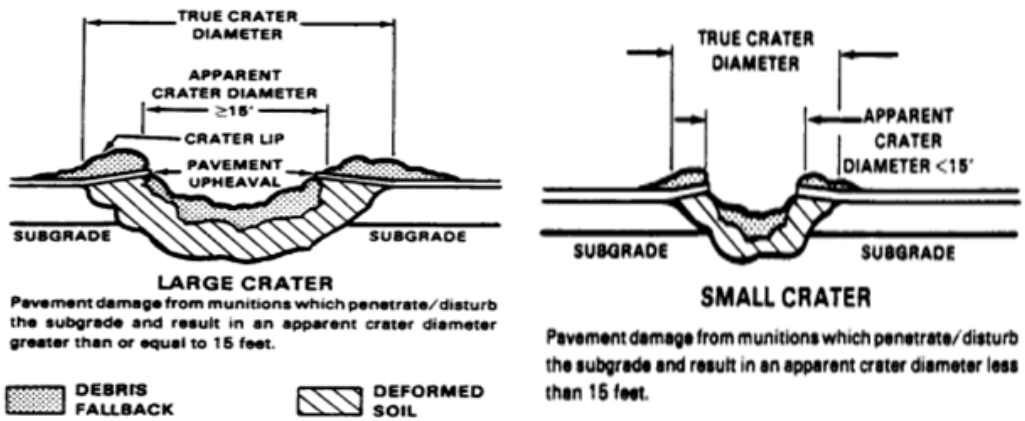
Figure 2.11 Typical crater sizes due to munitions (from US Army website)
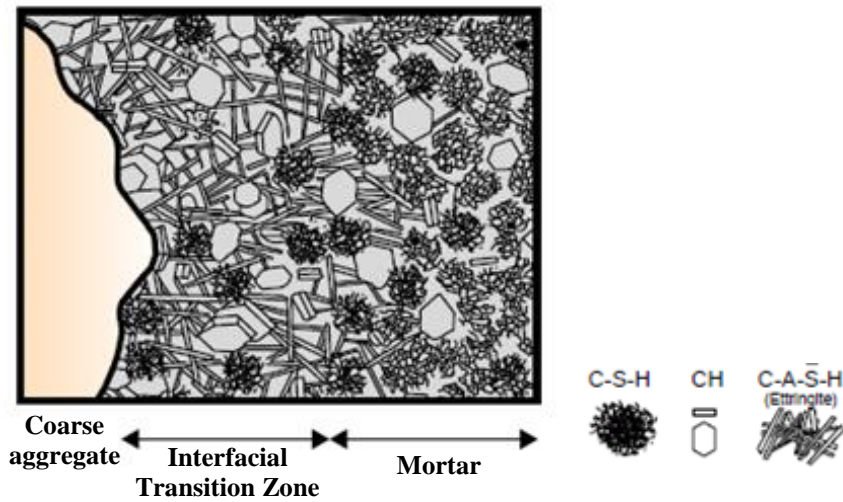
Figure 2.12 Diagrammatic representation of interfacial transition zone near coarse aggregate in normal concrete (after Methta and Monteiro 2005)
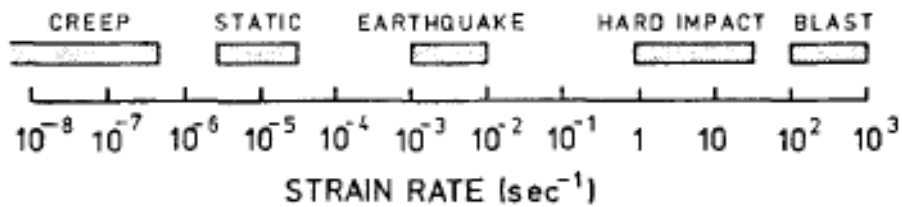
Figure 2.13 Magnitude of strain rates for different loading cases (after Bischoff 1991)
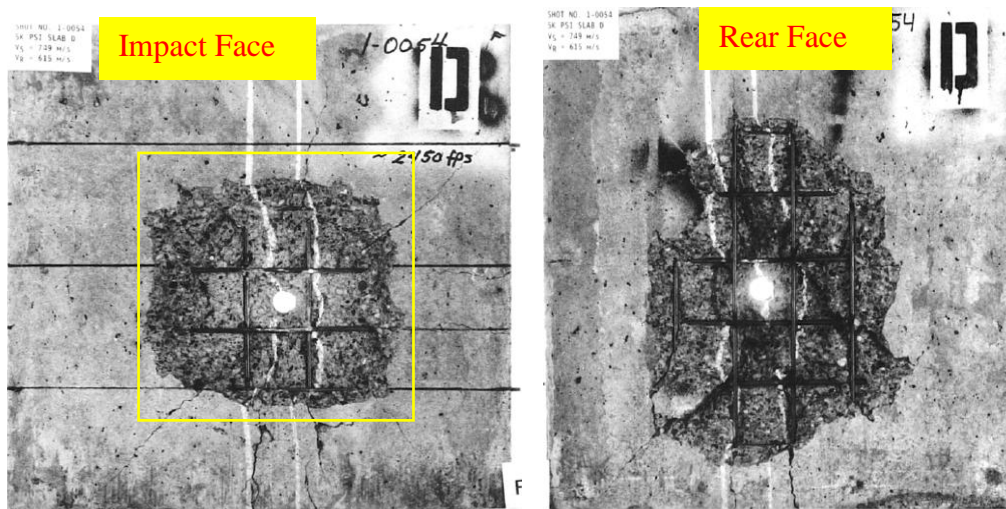
(a) Concrete slab with unconfined compressive strength of 48 MPa under impact velocity 750 m/s
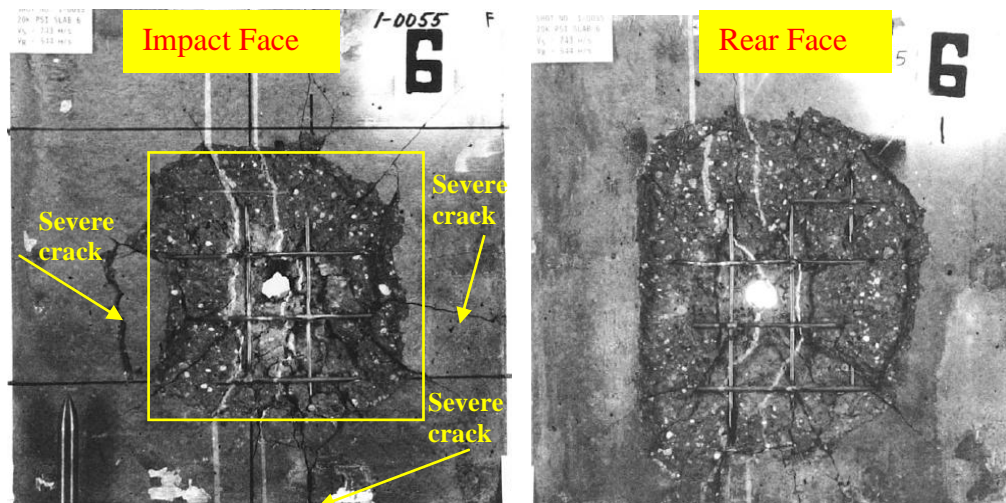
(b) Concrete slab with unconfined compressive strength of 140 MPa under impact velocity 750 m/s

Figure 2.14 Post-test photographs of impact and rear face for 48 MPa and 140 MPa concrete slabs (after Hanchak 1992)
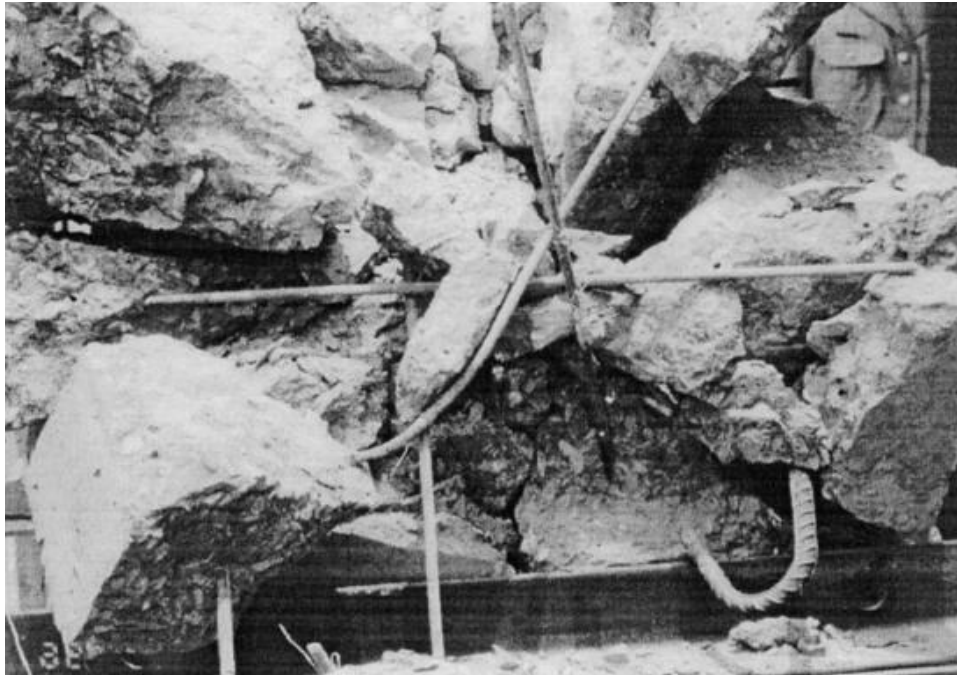
(a) RHSC target after impact test

(b) HPSFRC target after impact with projectile imbedded

Figure 2.15 Damaged situation after projectile impact on RHSC and HPSFRC
(after Luo et al. 2000)

61
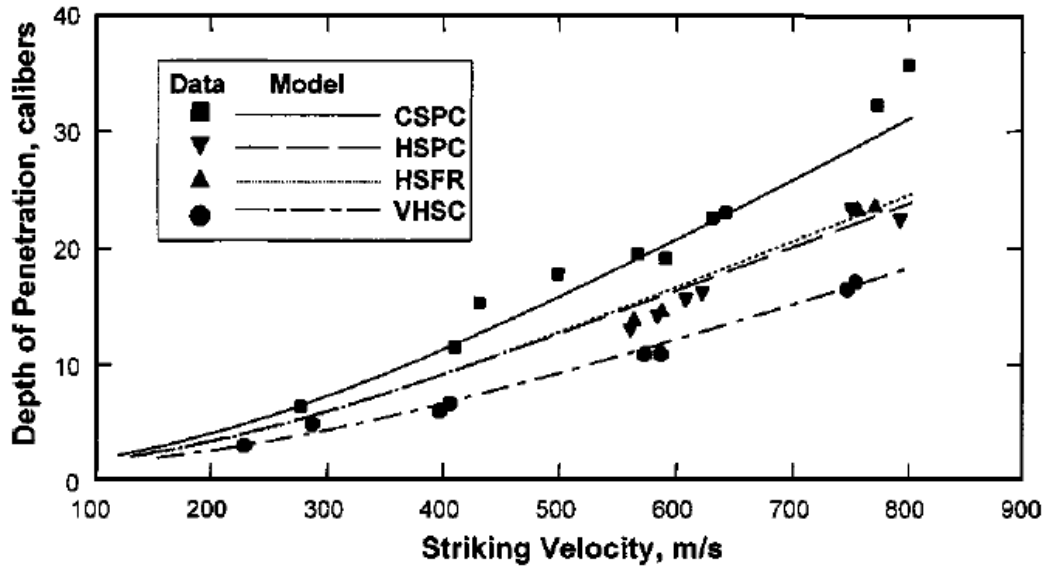
Figure 2.16 Comparison of results from penetration experiments into CSPC, HSPC, HSFR, and VHSC concretes and spherical-cavity expansion model calculations (after O'Neil et al. 1999)

(a) CSPC

(b) HSPC

(c) HSFR

(d) VHSC
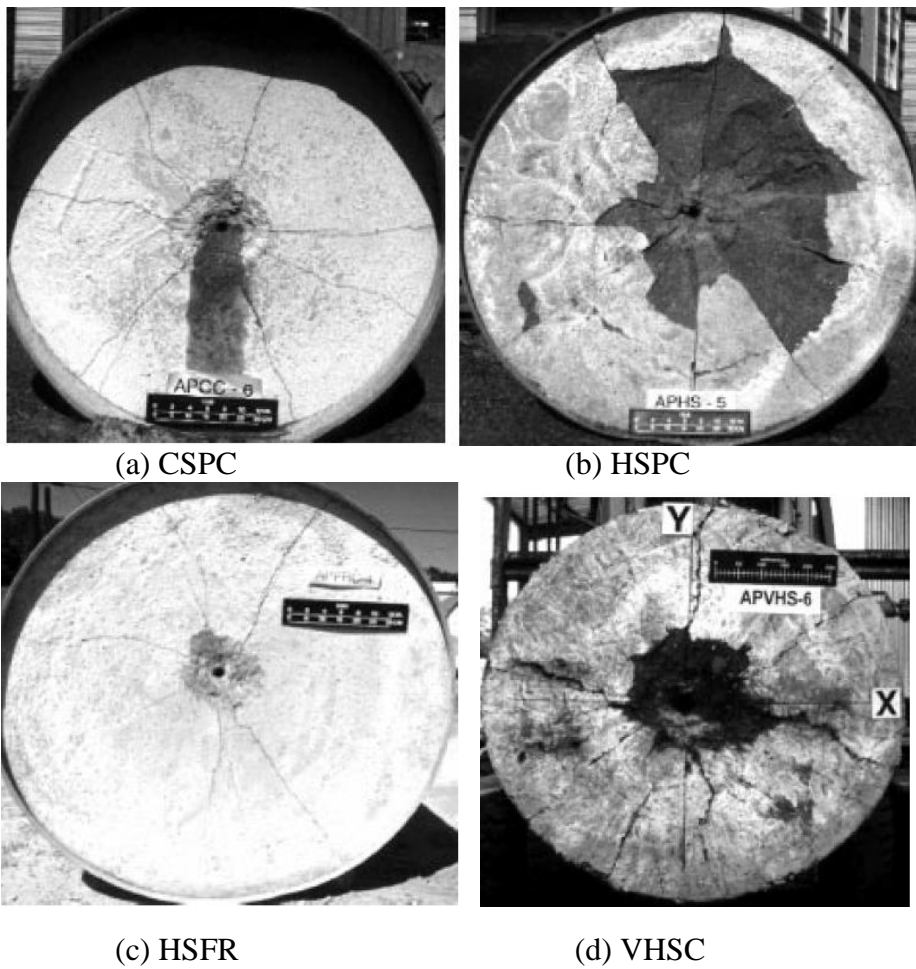
Figure 2.17 Front-face damage to targets under the impact velocity of 800 m/s (after O'Neil et al. 1999)
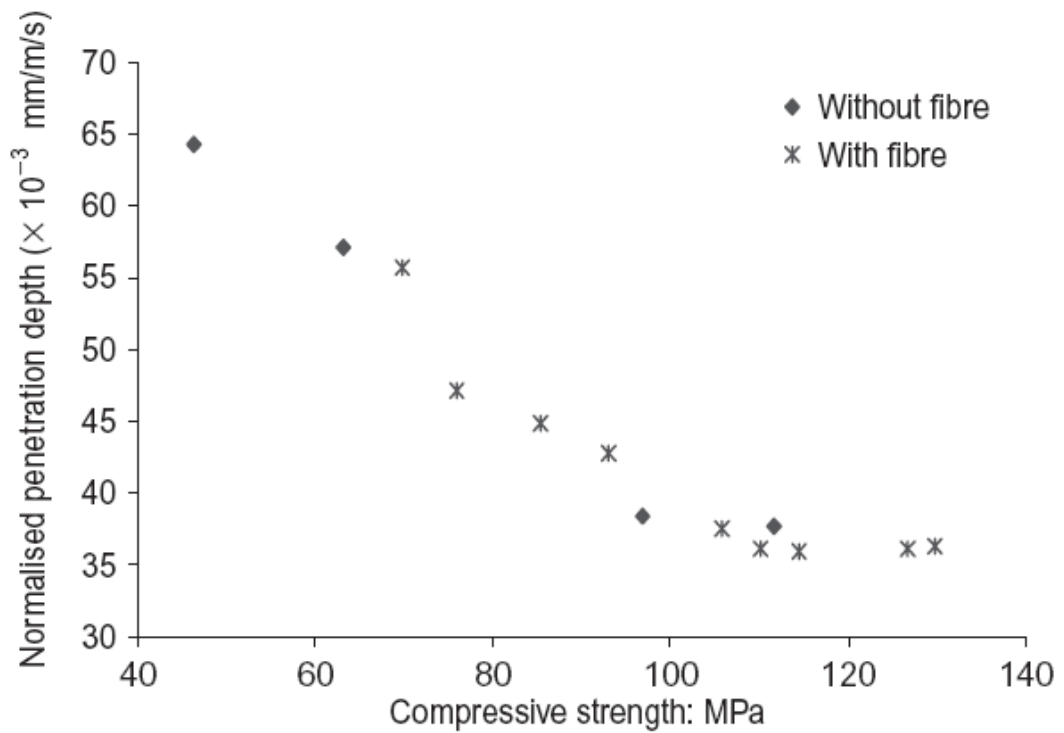
Figure 2.18 Effect of compressive strength on the penetration depth of the concrete (after Zhang et al. 2007)
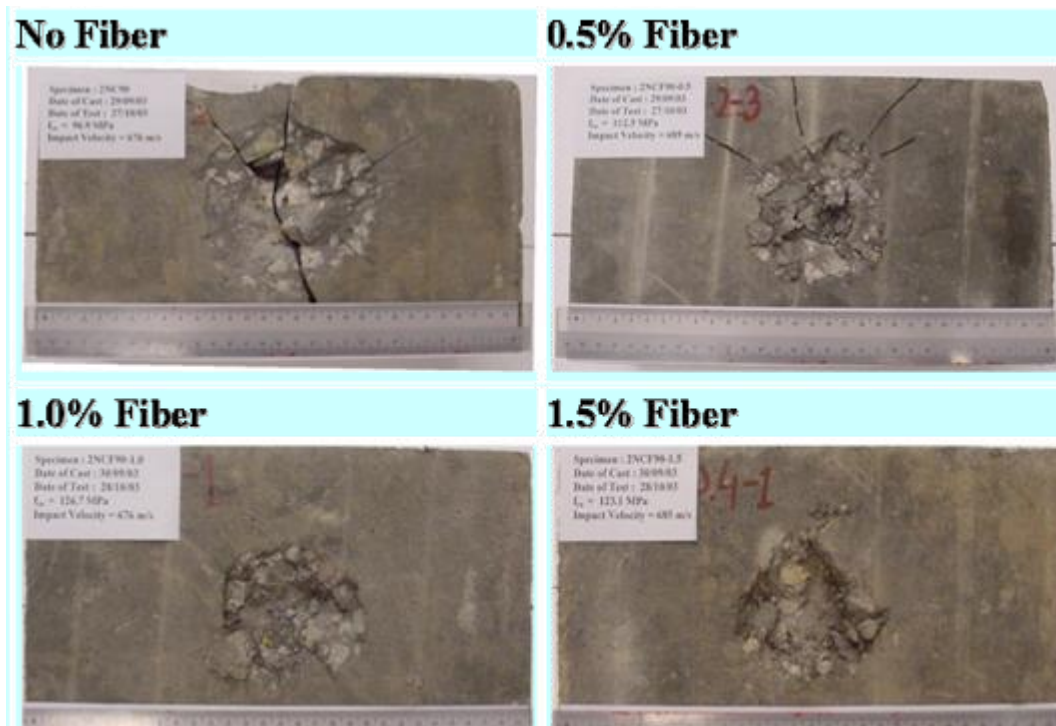
Figure 2.19 Crater Dimensions of HSC with different volume of Fibers (after Zhang et al. 2007)
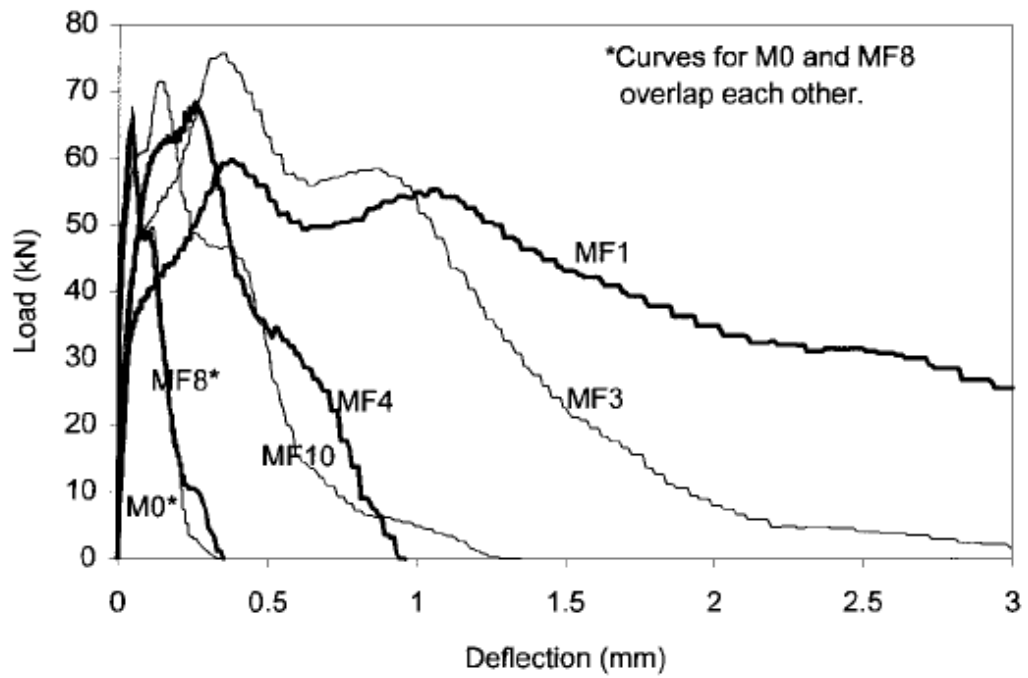
Figure 2.20 Impact load-displacement curve for shotcrete reinforced with different fibers (M0-mix with no fiber, MF1- mix with fiber F1, etc) (after Gupta et al. 2000)

Figure 2.21 Experimental results of RC and SFRPC under bare charge (bottom surface) (after kuznetsov et al. 2006)
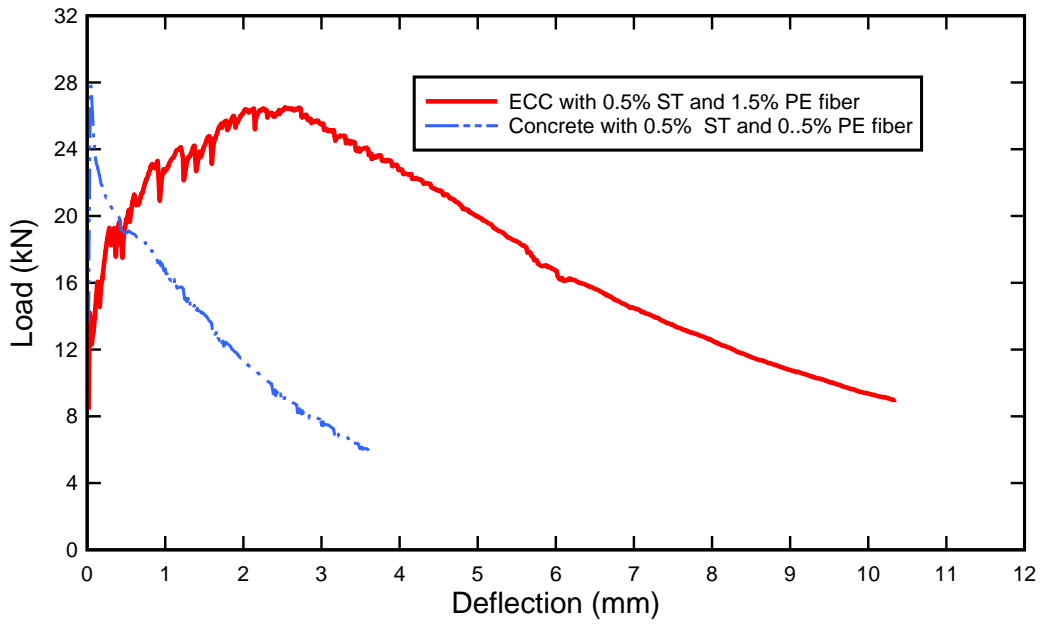
(a) three points bending test (by author)
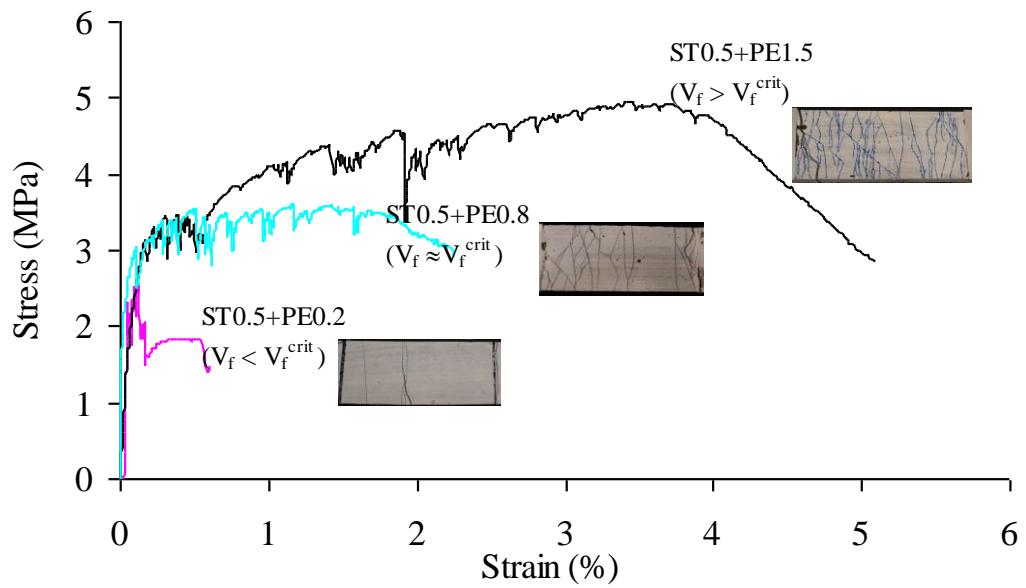
(b) Tensile stress-strain response and multiple cracking of hybrid-fibre ECC (after Maalej et al. 2006)

Figure 2.22 ECC specimen in flexure test and uniaxial tensile test

65
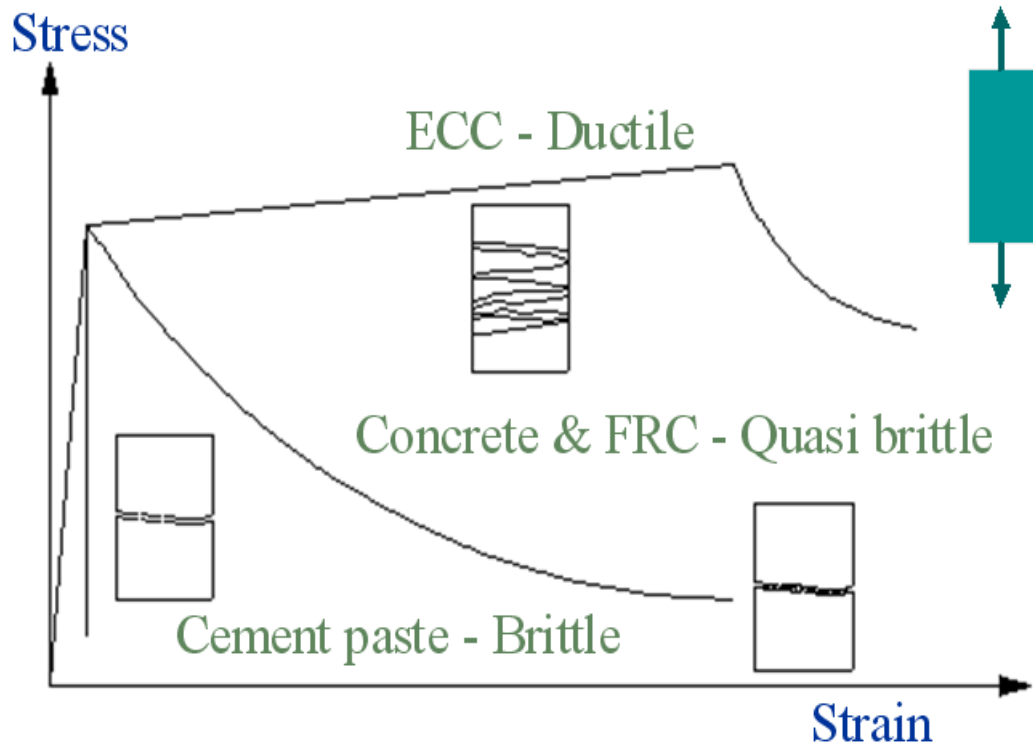
Figure 2.23 Typical Stress-Strain Curve of ECC (after Maalej et al. 2006)
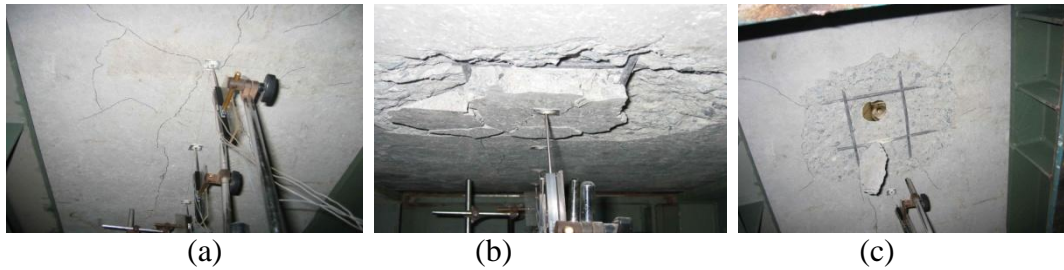
Figure 2.24 Damage development of RC100 panel on distal face: (a) 1st impact, (b) 2nd impact (serious scabbing), and (c) 3rd impact (perforated with big shear cone) (after Zhang et al. 2005)
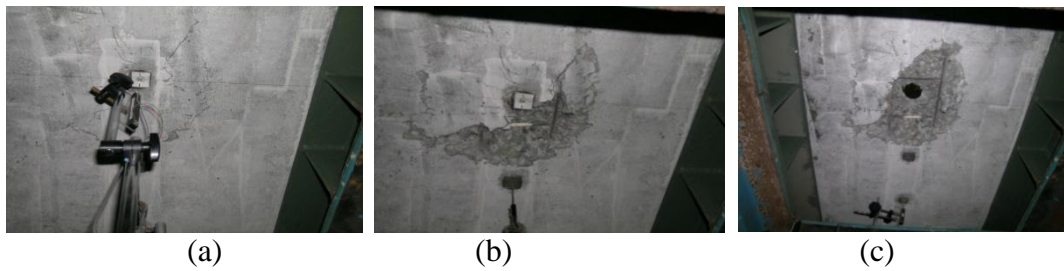
Figure 2.25 Damage development of FRC100 panel on distal face (a) 3rd impact, (b) 5th impact, and (c) perforation at 7th impact (after Zhang et al. 2005)

Figure 2.26 Damage development of ECC panels on distal face after 10 impacts (only very fine cracks developed, highlighted using a thick marker: (a) ECC100, (b) ECC75, and (c) ECC50 (after Zhang et al. 2005)

Figure 2.27 Geogrid Installed in Asphalt Layer (after Yong 2005)
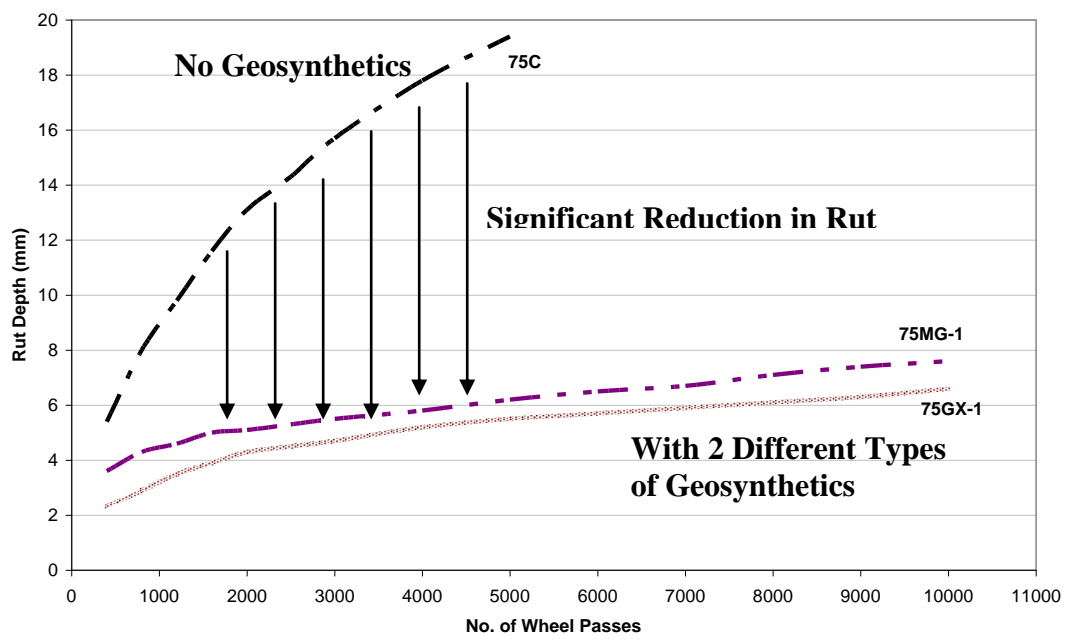
Figure 2.28 Reduction of Rut Depth with Geogrid (after Yong 2005)

68

Chapter 3 Development of New Multi-layers Pavement Material Subjected to Impact Load --- Laboratory Large Scale Drop Weight Test

3.1 Introduction

The current pavement designs are found to be inadequate in satisfying the needs of pavements that were much higher resistance to impact and blast load. Hence, there is an urgent need to develop a new pavement material that could withstand higher impact and blast load thereby increasing the durability of pavement or/and reducing the amount of repair needed when damaged.

From the literature review, it was found that some new materials could offer stronger impact resistance or/ and further improve the ductility and durability of pavements. They are High Strength Concrete (HSC), Engineered Cementitious Composite (ECC) and Asphalt concrete reinforced with Geosynthetics (GST). These 4 materials have potential to be used as components in the new pavement materials for the mitigation of blast and impact load. However, each of these materials has their own strength and weakness for blast mitigation. To fully utilize all their advantageous properties, a new pavement design consisting of all 4 materials will be considered. Ideally, the new pavement design should have high penetration resistance, high compressive and tensile strength, large ductility, and multiple resistance capability.

In this section, a multi-layers pavement system was proposed. This proposed multi-layers pavement was a combination of 4 engineering materials, namely, HSC, ECC and AC reinforced with GST of which the dynamic behavior was discussed in Chapter 2. The proposed multi-layers pavement would be conducted under the large scale drop weight test to check its impact resistance. As a comparison, tests on the existing runway pavements subjected to the same impact load, were also conducted.

3.2 Configuration for Proposed Multi-layers Pavement

Different configurations of these 4 engineering materials ECC, HSC and AC reinforced with GST under impact loading were studied with the assistance of an undergraduate researcher (OW 2008). The combined properties of these 3 materials would enable a pavement structure to minimize the crater size and penetration depth caused by impact loading with a reduction in deformation and cracking. It was found that the optimum configuration to achieve desired function was (a) the asphalt concrete (AC) reinforced with GST serviced as a first layer, and (b) followed by the HSC layer, and (c) the final layer of ECC was placed at the bottom, as shown in Figure 3.1. The reasons for the arrangement of such layers were:

1) AC

  i. AC layer above HSC so as to provide the same surface as current pavements surface such that no issue of skid resistance etc.

  ii. Due to the lower cost of AC, it is more economical to replace after being destroyed.

iii. The AC layer is "softer" compared to concrete material, however, it is able to take a significant amount of the dynamic load at the cost of being destroyed, thereby reducing energy transmitted to the following layers.

2) Geogrid

i. Geogrid had high tensile strength and can be used to increase the strength of the AC layer significantly, if it was laid within the AC layer.

ii. Used in combination with the AC layer, thereby reducing cracking and damage during impact loading.

3) HSC

i. It could be seen as the layer of defense against impact. It would take the main impact force due to its high strength.

ii. To reduce impact craters thereby decreasing repair time.

4) ECC

i. It had high ductility, thus it could absorb more deformation before failure, thereby impeding the impact propagation

ii. It had the ability to take multiple loads before failure. This in turn reduced the amount of repair needed. This increased the operational readiness of the pavement.

3.3 Evaluation of the impact resistance of proposed multi-layers pavement material

To evaluate the impact resistance of proposed multi-layers pavement material, impact drop weight test was developed. The drop height in impact test on proposed multi-layers pavement was 1.5 m. The drop weight was 1181 kg which gave rise to impact energy of about 10 kJ. For comparison, two existing runway pavements were also tested, that is, normal concrete pavement and asphalt concrete (AC) pavement. The results from these two samples would be compared with that from proposed multi-layers pavement in terms of crater diameter and penetration depth. It should be noticed that all these three samples were conducted at a constant drop weight of 1.5 m and fixed drop weight of 1181 kg. In addition, the efficiency of proposed multi-layers pavement subjected to higher energy level was to be further investigated by subjected proposed multi-layers material to higher drop height of 3 m.

Table 3.1 shows the cross section of these three configurations of pavement tested. Sample A was a standard normal concrete pavement of 275 mm thickness. Sample B was a standard asphalt concrete pavement which consists of 300mm sub-base and 150mm wearing course (AC layer). Sample C and D was the proposed multi-layers pavement. Sample C would be subjected to 1.5 m drop height, and Sample D would be subjected to 3 m drop height.

In Table 3.1, HSC was the high strength concrete without any fiber reinforcement, while ECC was a new engineered composite material which contains steel fibers and PE fibers. The detailed mix proportion is given in Table 3.2 to 3.4. The casting procedure for these materials could be referred to Ow (2008). The ASTM standard was used as a guide for testing the properties of the

normal concrete, HSC and ECC. Table 3.5 gives the properties of above materials used in drop weight test. The AC was obtained from premix plant. The information of gradation of the mix used and binder content for AC is shown in Table 3.6. The Geogrid used to reinforce the AC layer in this study was the Polyfelt Microgrid MG-100 with bi-directional tensile strength of 100 kN/m and has an aperture size of 7 mm.

Table 3.1 Cross section of Sample A, B, C and D
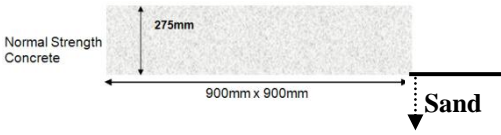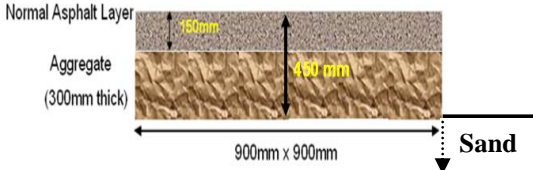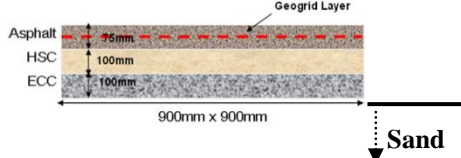
Sample	Cross Section	Impact height (m)
A (Rigid Pavement)		1.5
B (Flexible Pavement)		1.5
C/D (Proposed Multi-layers Pavement)		1.5 / 3.0

Table 3.2 Mix proportions for normal concrete in drop weight test

S/N	Material	kg/m^3
1	Cement	428
2	Silica Fume (undensified)	---
3	Superplasticizer (SP/B) (DARACEM 100)	---
4	Water	193
5	Natural Sand	671
6	Coarse Aggregates (max size of 20mm)	1,058
7	Water/Cementitious	0.45

Table 3.3 Mix proportions for HSC in drop weight test

S/N	Material	kg/m^3
1	Cement	428
2	Silica Fume (undensified)	48
3	SuperPlasticiser (SP/B) (DARACEM 100)	8.5
4	Water	162
5	Natural Sand	750
6	Coarse Aggregates (max size of 20mm)	1,000
7	Water/Cementitious	0.35

Table 3.4 Mix proportions for ECC in drop weight test

S/N	Material	kg/m^3
1	Cement	1400
2	Silica Fume (undensified)	154
3	Superplasticizer (SP/B) (DARACEM 100)	20.2
4	Water	424
5	Steel Fibers	39.1
6	PE Fibers	14.5
7	Water/Cementitous	0.28

Table 3.5 Properties of materials used in drop weight test

Material	Compressive strength (MPa)	Elastic modulus (GPa)	Poisson's ratio
HSC	90	40	0.20
ECC	80	18	0.24
Normal Concrete	54	33	0.20

Table 3.6 Aggregate gradation and binder content for AC used in drop weight test

Sieve size (mm)	% Passing
19	100
13.2	95
9.5	---
6.3	68
3.15	50
2.36	---
1.18	31
0.3	17
0.212	---
0.075	8
Binder content (Penetration grade 60/70) (% by weight of Total mix)	5.0

3.4 Large Drop Weight Impact Test

3.4.1 Setup for large drop weight impact test

The pavement slabs were subjected to impact from 1181kg drop weight. The drop weight used was a cylindrical projectile with a hemispheric head dropped from different heights within a steel frame. The drop head was 100mm diameter. Sample A, B and C would be subjected to impact at a drop height of 1.5m and Sample D would be conducted at a height of 3m drop height. Each Sample was subjected to 2 impacts from the same drop height. Figure 3.2 shows the drop weight apparatus that was used in current study.

For Sample A, C and D, the pavement slab was placed on top of compacted soil/sand in a steel strong box. Directly below the slab was the geocell which would be filled with compacted soil/sand. This was to enhance the strength of the soil/sand layer and provide a high quality subbase. The geocell used in the test was MiraCell MC-100 which consisted of expendable, polyethylene, honeycomb-like cellular structures interlinked together. Figure 3.3 and 3.4 shows the test setup and layout. A total of 1 ton of sand was used and was compacted to a density of approximately 1600 kg/m^3, with the aid of a 10 kg dead weight. The preparation of the sand layer is shown in Figures 3.5 and 3.6.

For Sample B, a standard AC pavement slab of 150 mm thick was placed on top of 300 mm thick aggregates layer. These two components cast in a small steel frame were placed on the top of the strong steel box. The small steel frame had measured 900 mm $\times$ 900 mm $\times$ 450 mm height which is shown in Figure 3.7. There was one layer of geocell to provide the confinement of the soil below the aggregates. The test setup for Sample B is shown in Figure 3.8. It should be

noticed that the small steel frame would service as the confinement boundary for the asphalt concrete pavement slab, which did not allow the AC layer to expand during impact test, and in turns would enhance the strength of the AC layer. However, this would be closer to the real site situation. Figure 3.8 and 3.9 shows the actual test setup for these samples.

3.4.2 Instrumentation

Various instruments were installed to monitor the response of the pavement during the drop weight test. These instruments include:

1. Potentiometer- to measure displacement

2. Accelerometer-to measure acceleration

3. Photo diode system -to trigger the data acquisition system during the test

4. High speed camera-to record the process of impact test

Three spring potentiometers, S13FLP100A, having a 100 mm capacity, were used to obtain the displacement profile of the tested Sample upon impact. Figure 3.10 shows the positioning of the potentiometers. The projectile was instrumented with an accelerometer of 10,000 g capacity to evaluate the acceleration of the drop weight. Two other accelerometers of 1000 g capacity were placed on the surface of each sample to measure the acceleration of the sample upon impact. The acceleration profile of each sample can be used as a check for the displacement profiles obtained from the potentiometers. Figure 3.10 also shows the positions of the accelerometers on the sample.

A photo diode system was used to trigger the data acquisition system during the test. It consisted of two photo diodes and two laser sources placed 100 mm vertically apart. The data acquisition system would be triggered when the

falling projectile crosses the top laser emitter. Impact velocity could be determined using the time interval that the projectile took to cross the second laser emitter. A schematic diagram of this system was presented in Figure 3.11.

For data acquisition, a digital oscilloscope, DL750, was used. There are two sets of laser emitter and photo diode (receiver), with a spacing of 100 mm vertically right above the specimen. During the drop test, the instant the projectile crosses the first laser emitter, it would trigger the data acquisition system and set as t=0. A short time later, the projectile would cross the second laser emitter, which was placed immediate above the pavement specimen. Hence, the impact velocity could be calculated. The data recording was set at a sampling rate of 200,000 reading per second (200 kHz). A high speed camera was also used to record the whole test. The videos and still photos were useful in helping to record the response of the slabs during the drop weight impact tests. After the test, the depth and crate size of the slab due to the impact was determined if possible.

3.5 Individual Test Results and Discussion

This part would discuss the results obtained from the drop weight impact tests conducted on the four pavement samples. This included the physical observations and instrumentation results.

3.5.1 Experimental results of Sample A

The configuration of Sample A is shown in Table 3.1. During the impact test, two belts were used to restrain the sample to reduce the rebound displacement. This was the first control test with normal strength concrete slab. The height of drop weight for Sample A was 1.5 m.

3.5.1.1 Observations of 1st impact

The velocity of the projectile in this test was found to be 5.133 m/s. Figure 3.12 shows the damage on the surface of Sample A after the first impact. The crater was about 140 mm in diameter albeit quite shallow. A high propagation of cracks (exceed the half height of the slab) was observed at the sides of the sample as shown in Figure 3.13. This was consistent with the conclusion that the concrete was a brittle material. Cracks caused by bending were able to propagate easily through Sample A. It should be noticed that there was also significant debris of the surface upon impact.

The recorded data were analyzed as follow:

a) Potentiometers

The vertical displacement of Sample A upon 1st impact is shown in Figure 3.14. From the figure, it can be seen that there were two peaks: labeled as X1 and X2. Peak X1 was the initial vertical displacement downwards when the projectile hit the sample. Peak X2 was the vertical displacement upwards of the sample. Table 3.7 summaries the peak value of these potentiometers.

Table 3.7 Peak readings of potentiometers for Sample A, 1st Impact

	Peak value at X1	Peak value at X2	Rebound
Pot1	-26.07 mm	14.81 mm	40.88 mm
Pot2	-27.06 mm	19.26 mm	46.32 mm
Pot3	-27.98 mm	15.55 mm	43.53 mm
Ave	-27.04 mm	16.54 mm	43.58 mm
(+ ve ➔ upwards, - ve ➔ downwards)			

From the table, it is observed that Pot1 (nearest to the center of the slab) suffered almost same vertical settlement as that for Pot2 and Pot3, which were located at 250 mm and 336 mm from the center of the slab respectively. It was concluded that upon the 1st impact, the whole slab was undergoing vertical

movement (rigid movement). For the rebound, it is observed that Pot2 obtained the largest rebound value as shown in Figure 3.15. It was demonstrated that the bending of the slab occurred during the rebound. Further, it is also shown that the rebound was still quite significant at an average of 43.58 mm.

b) Accelerometers

Acceleration of the impact head A1 was found to be about 2619g upon 1st impact. Acceleration of the slab at 150 mm and 250 mm radius distance (A2 and A3, as shown in Figure 3.10) were found to be 158g and 93g respectively. These values are summarized in Table 3.8.

Table 3.8 Peak readings of accelerometers for Sample A, 1st Impact

	A1	A2	A3
Peak Reading	2619 g	158 g	93 g

A1 gives the acceleration of impact head. However, this value might not represent the true impact force imposed to the target due to the strong high frequency oscillations occurred in the impactor when the accelerometers were placed on the impactor or impactor axis (Aymerich et al. 1996). During the impact test, the accelerometer A1 was placed at the 400 mm away from the drop head, and it was found that the recorded acceleration had symmetry wave to the original position which indicated that the free vibration happened in the accelerometer. From the high speed camera recording, it was also found that impactor had strong vibration after impact. Hence, the A1 value in current study could only illustrate the degree of the target stiffness. A2 and A3 measured the acceleration of the sample at various radial distances away from the center and were much lower than that for A1, which also indicated that the rebound was decreasing with the increase of the radial distance.

3.5.1.2 Observations of 2nd impact

A second impact test was conducted on Sample A. The velocity of the projectile in this test was found to be 5.168 m/s. The sample was fragmented into three segments with the projectile punching right through and stopped by the stopper of the frame upon impact. All the three major shear cracks propagated right through the sample. Sample A experienced a complete failure and sudden failure. Repair would be the replacement of the whole runway pavement section which requires more time and effort. Figure 3.16 shows the damage of the sample.

The recorded data were analyzed as follow:

a) Potentiometers

The vertical displacement of Sample A upon 2nd impact is shown in Figure 3.17. From the figure, it can be seen that there were two peaks: labeled as X1 and X2. Peak X1 was the initial vertical displacement downwards when the projectile hit the sample. Peak X2 was the vertical displacement upwards of the sample Table 3.9 summarizes the peak value of these potentiometers.

Table 3.9 Peak readings of potentiometers for Sample A, 2nd Impact

	Peak value at 1	Peak value at 2	Rebound
Pot1	-27.73 mm	-9.77 mm	17.96 mm
Pot2	-28.42 mm	-7.61 mm	20.81 mm
Pot3	-22.04 mm	5.79 mm	27.83 mm
Ave	-26.06 mm	-3.86 mm	22.20 mm
(+ ve ➔ upwards, - ve ➔ downwards)			

From Table 3.9, it is observed that the Pot1 and Pot2 (closer to the center of the slab) suffered larger vertical settlement. The Pot3 was about 336 mm away from the center. The vertical displacement was decreasing with the increase of radial distance. For the rebound, Pot1 and Pot2 recorded the almost same readings and less than that Pot3 as shown in Figure 3.18. This rebound value might not be

correctly recorded due to the Pot1 and Pot2 were dislodged after Peak X1. But P3 could still record the rebound reading, which was less than the first impact as much of the energy was dissipated through the cracking.

b) Accelerometers

Acceleration of the impact head A1 was found to be about 1897g upon 1st impact. Acceleration of the slab at 150 mm and 250 mm radius distance (A2 and A3, as shown in Figure 3.10) were found to be 342g and 195g respectively. These values are summarized in the Table 3.10.

Table 3.10 Peak readings of accelerometers for Sample A, 2nd Impact

	A1	A2	A3
Peak reading	1897 g	342 g	195 g

A1 gives the acceleration of the projectile. A2 and A3 measured the acceleration of the sample at various radial distances away from the center and were much lower than that for A1, which also indicated that the rebound is decreasing with increasing of the radial distance. Comparison with the results from 1st impact, it was found that A1 for 2nd impact were much lower than that for 1st impact, this might be that the impact energy was dissipated through the cracking and breaking occurred in the slab. At same time, the A2 and A3 from 2nd impact were bigger than that for 1st impact, this was due to the slab were broken into few piece upon 2nd impact, and each piece with small mass would vibrate strongly compared to integrity slab during the 1st impact.

3.5.2 Experimental results of Sample B

The configuration of Sample B was shown in Table 3.1. It was a standard asphalt concrete layer using as the second control test. Two belts were used to

restrain this sample to the steel strong box. The height of drop weight for Sample B was 1.5 m.

3.5.2.1 Observations of 1st impact

The velocity of the projectile in this test was found to be 4.56 m/s. Figure 3.19 shows the surface of Sample B upon 1st impact. It was found that the crater had the same diameter as the projectile head at 100 mm as the projectile went through the AC layer and right into the layer of 85 mm penetration. However, the AC layer was damaged with shear failure and no fragment occurring. This was possible that small steel frame confining the whole AC layer and did not allow the layer to expand/shift during impact. It should be noted that the confinement of small steel frame in the test simulated the real pavement boundary which was such that the top layer of pavement be confined during dynamic loading. Sample B suffered less damage than expected due to this confinement.

The recorded data were analyzed as follow:

a) Potentiometers

The vertical displacement of Sample B upon 1st impact is shown in Figure 3.20. From the figure, it can be seen that there were two peaks, labeled as X1 and X2. Peak X1 was the initial vertical displacement downwards when the projectile hitting the sample. Upon impact, there was a rebound and Peak X2 was the resulted rebound vertical displacement upwards. After that Sample B settled back to its position and the potentiometers were slightly out of their initial position after the rebound. Table 3.11 summarizes the peak value of these potentiometers.

Table 3.11 Peak readings of potentiometers for Sample B, 1st Impact

	Peak value at X1	Peak value at X2	Rebound
Pot1	-71.6 mm	-17.4 mm	54.2 mm
Pot2	-51.1 mm	27.2 mm	78.3 mm
Pot3	-47.0 mm	30.5 mm	77.5 mm
Ave	-56.6 mm	13.4 mm	70.0 mm
(+ ve ➜ upwards, - ve ➜ downwards)			

From Table 3.11, it is observed that the Pot1 (nearest to the center of the slab) suffered largest settlement and least rebound. Pot2 and Pot3 were about 250 mm and 336 mm away from the center. Thus, it can be concluded that the vertical displacement was decreasing with radial distance as shown in Figure 3.21. But the rebound value of 80 mm was "stabilized" at about 250 mm radial distance.

b) Accelerometers

Acceleration of the impact head A1 was found to be about 667 g upon 1st impact. Acceleration of the slab at 150 mm and 250 mm radius distance (A2 and A3, as shown in Figure 3.10) were found to be 135 g and 106 g, respectively. These values are summarized in the Table 3.12.

Table 3.12 Peak readings of accelerometers for Sample B, 1st Impact

	A1	A2	A3
Peak Reading	667 g	135 g	106 g

The A1 value in this test was lower than that of concrete slab, which was more rigid. A2 and A3 measured the acceleration of the sample at various distance away from the center and was much lower than A1, which indicated the extent of Sample B's rebound upon impact. It can be concluded that the rebound was decreasing with radial distance

3.5.2.2 Observations of 2nd impact

The velocity of the projectile upon impact in this test was found to be 5.21 m/s. Figure 3.22 shows the surface of Sample B upon 2nd impact. For the figure, it is shown that the crater had a bigger diameter than that in 1st impact and the depth of crater was more than 250 mm, which meant that projectile head punched through the whole AC layer and was only barely stopped by the layer of aggregates underneath. Figure 3.23 shows the crater of Sample B. Again, no fragmentation occurred. However, Sample B was considered to have failed as the AC layer was punched through, and the aggregate layer below was also disturbed. In actual field condition once the crater reached the aggregate layer, the whole pavement section needed to be replaced.

The recorded data were analyzed as follow:

a) Potentiometers

The vertical displacement of Sample B upon the 2nd impact was shown in Figure 3.24. From the figure, it could be seen that there were two peaks: labeled as X1 and X2. Peak X1 was the initial vertical displacement downwards when the projectile hitting the Sample. Upon impact, there was a rebound and Peak X2 was the resulted rebound vertical displacement upwards. After that Sample B settled back to its position and the potentiometers were slightly out of their initial position after the rebound. Table 3.13 summarizes the peak value of these potentiometers.

Table 3.13 Peak readings of potentiometers for Sample B, 2nd Impact

	Peak value at X1	Peak value at X2	Rebound
Pot1	-15.9 mm	71.6 mm	87.5 mm
Pot2	-14.4 mm	29.6 mm	44 mm
Pot3	-6.9 mm	36.5 mm	43.4 mm
Ave	-12.4 mm	45.9 mm	58.3 mm
(+ ve ➔ upwards, - ve ➔ downwards)			

From Table 3.13, it is found that Pot1 (nearest to the center of the slab) suffered largest settlement and rebound. Pot2 and Pot3 were about 250 mm and 336 mm away from the center. Thus, it can be concluded that the vertical displacement was decreasing with radial distance as shown in Figure 3.25. But the rebound was "Stabilized" at about 250 mm radial distance.

b) Accelerometers

Acceleration of the impact head A1 was found to be about 721 g upon 2nd impact. Acceleration of the slab at 150 mm and 250 mm radius distance (A2 and A3, as shown in Figure 3.8) were found to be 162 g and 106 g, respectively. These values are summarized in the Table 3.14.

Table 3.14 Peak readings of accelerometers for Sample B, 2nd Impact

	A1	A2	A3
Peak Reading	721 g	162 g	106 g

The A1 value was lower than that of concrete slab, which was more rigid than asphalt material. A2 and A3 measured the acceleration of the sample and were much lower than A1, which indicated the extent of Sample B's rebound upon impact. It can be concluded that the rebound was decreasing with the increase of radial distance.

3.5.3 Experimental results of Sample C

The configuration of Sample C was shown in Table 3.1. Two belts were used to restrain this sample to the steel strong box. The height of drop weight for Sample C was 1.5 m.

3.5.3.1 Observations of 1st impact

The velocity of the projectile in this test was 5.02 m/s. This meant that the energy caused by the projectile was about 14.9 kJ computed via the formula $E=1/2 \, mv^2$. Figure 3.26 shows the surface of Sample C upon 1st impact. The crater had the same diameter as the projectile head at 100 mm and the projectile went right through AC layer. However, the reinforced AC layer remained intact even after impact. This showed that the geogrid held the AC layer together while the soft asphalt absorbed the impact force. At the crater, it is observed that the projectile had hit the HSC layer and the geogrid was punched through. The HSC layer had impeded the projectile and prevented it from punching further due to its high compressive strength. Both the reinforced AC layer and HSC layer absorbed the impact force and a few minor cracks were observed at the AC surface of the sample which again proved that the geogrid prevented the fragmentation of the asphalt. Figure 3.27 shows the side profile of the sample which had a few visible but minor cracks in the bottom ECC layer. The micro-cracking behaviour of ECC distributed the force and prevented major cracks. The presence of only a few minor cracks also showed that most of the impact force was already absorbed by the AC layer upon impact so the bending was reduced.

The recorded data were analyzed as follow:

a) Potentiometers

The vertical displacement of Sample C upon 1st impact is shown in Figure 3.28. From the figure, it can be seen that there were two peaks: X1 and X2. Peak X1 was the initial vertical displacement downwards when the projectile hitting the sample. Peak X2 was the vertical displacement upwards (rebound) of the AC layer. After that, Sample C settled back to its position and the potentiometers were slightly out of their initial position after rebound. Table 3.15 summarizes the peak value of these potentiometers.

Table 3.15 Peak readings of potentiometers for Sample C, 1st Impact

	Peak value at X1	Peak value at X2	Rebound
Pot1	1.97 mm	36.91 mm	34.94 mm
Pot2	-1.81 mm	41.45 mm	43.26 mm
Pot3	-5.27 mm	37.71 mm	42.98 mm
Ave	-1.70 mm	38.69 mm	40.39 mm
(+ ve ➔ upwards, - ve ➔ downwards)			

From the table, it is shown that at peak X1, Pot1 went upward and Pot2 suffered the settlement which was less than that Pot3. Based on layout of the potentiometers of Sample C, it is observed that Pot1 was the nearest to the center of the slab, and Pot2 and Pot3 were at 250 mm and 336 mm away from the center of the slab. Thus, the peak X1 values seem to be unreasonable, it was possible due to that Pot1 was fully extend upon 1st impact and then could not record the vertical settlement correctly. Due to Peak X1 reading was not correctly recorded, the rebound value may not able to compute correctly. From Figure 3.28, it is shown that the potentiometers were slightly out of their initial position after the rebound after Peak X2.

b) Accelerometers

Acceleration of the impact head A1 was found to be about 574g upon 1st impact. Acceleration of the slab at 150 mm and 250 mm radius distance (A2 and A3, as shown in Figure 3.10) were found to be 49g and 61g respectively. These values are summarized in the Table 3.16.

Table 3.16 Peak readings of accelerometers for Sample C, 1st Impact

	A1	A2	A3
Peak reading	574 g	49 g	61 g

The A1 value in this test was lower than that of concrete slab, which was more rigid. A2 and A3 measured the acceleration of the sample at various radial distances away from the center. From the table, it is shown that A3 value was larger than A2, which seemed not reasonable due to the wave propagation might attenuate with the distance. Hence, the acceleration recorded by A3 might not be correct.

3.5.3.2 Observations of 2nd impact

The projectile's velocity was 4.99 m/s for the second impact. This meant that the energy caused by the projectile was kept at about 14.7 kJ. The surface of Sample C upon impact is shown in Figure 3.29. The depth of crater was about 10 mm slightly deeper compared to the first impact but the reinforced AC layer remained intact. Despite being hit at the same spot twice, Sample C could still absorb the force and maintain its structural integrity. The AC layer and HSC layers were still able to impede the projectile. More micro-cracks were observed to be propagating from the ECC layer at the sides compared to the first impact and Figure 3.30 shows the side profile of the sample. There were no major cracks and

this showed that the force was absorbed and damage was mitigated. The reinforced AC layer was also observed to have shifted slightly out of the sample as shown in Figure 3.31 and this was due to the weak bonding between AC and the underlying HSC layer. However, this would be less significant in the actual situation where the runway pavement would be much larger in scale.

The recorded data were analyzed as follow:

a) Potentiometers

The vertical displacement of Sample C upon 2nd impact was shown in Figure 3.32. From the figure, it could be seen that there were two peaks X1 and X2. Peak X1 was the initial vertical displacement downwards when the projectile hit the sample. Peak X2 was the vertical displacement upwards (rebound) of the AC layer. After that, Sample C settled back to its position and the potentiometers were slightly out of their initial position after rebound. Table 3.17 summarizes the peak value of these potentiometers.

Table 3.17 Peak readings of potentiometers for Sample C, 2nd Impact

	Peak value at 1	Peak value at 2	Rebound
Pot1	-3.62 mm	35.11 mm	38.73 mm
Pot2	-7.60 mm	42.09 mm	49.69 mm
Pot3	-5.58 mm	32.16 mm	37.74 mm
Ave	-5.60 mm	36.45 mm	42.05 mm
(+ ve ➜ upwards, - ve ➜ downwards)			

From Figure 3.32, it is shown that Pot1 was nearest to the center of the slab and Pot2 and Pot3 were about 250 mm and 336 mm away from the center. However, from Table 3.17, it can be seen that vertical displacement was almost stable with increasing radial distance as shown in Figure 3.33, and the rebound obtained large value for Pot2. This could be concluded that during impact, the bending action of the sample occurred. After Peak X2, it was shown that the potentiometers were slightly out of their initial position after the rebound.

b) Accelerometers

Acceleration of the impact head A1 was found to be about 762g upon 2nd impact. Acceleration of the slab at 150 mm and 250 mm radius distance (A2 and A3, as shown in Figure 3.10) were found to be 149g and 71g respectively. These values are summarized in the Table 3.18.

Table 3.18 Peak readings of accelerometers for Sample C, 2nd Impact

	A1	A2	A3
Peak reading	762 g	149 g	71 g

A2 and A3 measured the acceleration of the sample at various radial distances away from the center, which also indicated that the rebound was decreasing with increasing of the radial distance.

3.5.4 Experimental results of Sample D

The configuration of Sample D is shown in Table 3.1. It was a proposed multi-layers pavement which was used to evaluate the effect of higher drop energy. Two belts were used to restrain this sample to the steel strong box. It should be noted that the drop height for Sample D was 3 m.

3.5.4.1 Observations of 1st impact

The velocity of the projectile in this test was found to be 7.1 m/s. This meant the energy caused by the projectile was about 29.8 kJ computed via the formula $E=1/2\ mv^2$. Figure 3.34 shows the surface of Sample D upon 1st impact. It was found that the crater at AC layer was having diameter of 100 mm. The projectile punched through the AC layer and was stopped by the HSC layer. However, the reinforced AC layer did not fly fragment even after impact. This

was because the geogrid provided the tensile force to hold the AC layer together while the soft asphalt absorbed the impact force. At the crater, it was observed that the projectile produced a shallow crater of 5mm depth in the HSC layer and the geogrid was punched through. The HSC layer had impeded the projectile and prevented it from punching further due to its high compressive strength by absorbing the remaining impact force. Both reinforced AC and HSC layer fully absorbed the impact force. Figure 3.35 shows the side profile of Sample D which had a few visible but minor cracks in the bottom ECC layer. The micro-cracking behavior of ECC distributed the force and prevented major cracks from developing. The presence of only a few minor cracks also showed that most of the impact force was already absorbed by the AC layer upon impact. This again demonstrated the effectiveness of this proposed pavement system again impact and blast.

The recorded data were analyzed as follow:

a) Potentiometers

The vertical displacement of Sample D upon the 1st impact is shown in Figure 3.36. From the figure, it can be seen that there were two peaks, labeled as X1 and X2. Peak X1 was the initial vertical displacement downwards when the projectile hitting the sample, but these readings were not recorded due to the potentiometer fully extends in the initial condition and did not measure the settlement. Upon impact, there was a rebound and Peak X2 was the resulted rebound vertical displacement upwards. After that Sample D settled back to its position and the potentiometers were out of their initial position after the rebound. Table 3.19 summarizes the peak value of these potentiometers.

Table 3.19 Peak readings of potentiometers for Sample D, 1st Impact

	Peak value at X1	Peak value at X2	Rebound
Pot1	---	34.9 mm	---
Pot2	---	59.3 mm	---
Pot3	---	42.3 mm	---
Ave	---	45.5 mm	---

(+ ve ➜ upwards, - ve ➜ downwards)

From Table 3.19, due to peak X1 reading was not correctly recorded, the rebound value may not able to compute. However, it could be seen that for peak X2, the Pot2 went upwards at around 60 mm which was higher than other two potentiometers measured. This might indicate that the pavement suffer bending during the impact.

b) Accelerometers

Acceleration of the impact head A1 was found to be about 1214 g upon 1st impact. Acceleration of the slab at 150 mm and 250 mm radius distance (A2 and A3, as shown in Figure 3.10) were found to be 657 g and 497 g, respectively. These values are summarized in Table 3.20.

Table 3.20 Peak readings of accelerometers for Sample D, 1st Impact

	A1	A2	A3
Peak reading	1214 g	657 g	497 g

The A1 was higher than those of the previous tests which had lower drop height. A2 and A3 measured the acceleration of the sample which indicated the extent of Sample D's rebound upon impact. It could be observed that the rebound was decreasing with increasing of the radial distance.

3.5.4.2 Observations of 2nd impact

Upon 2nd impact, the AC layer was removed as it was already damaged and de-bonded/shift after 1st impact. The projectile's velocity was 7.19 m/s for 2nd

impact, thus, the energy caused by the projectile was about 30.5 kJ. The surface of Sample D upon 2nd impact is shown in Figure 3.37. It was found that the diameter crater was about 100 mm, and depth of crater was about 175 mm. Figure 3.38 shows the crater size of Sample D upon 2nd impact. From the figure, it is shown that the cracks on the surface propagated from the crater at the major axes. Majority of the cracks were found in the middle at the sides of the sample where the major axes were.

The ECC layers were penetrated through by the projectile. The stopper installed at the track of the drop weight impeded the projectile. It was observed that more cracks were propagating from the ECC layer at the sides compared to the first impact and Figure 3.39 and 3.40 shows the side profile of the Sample D. From the figure, it is found that the HSC and ECC layer were severely damaged. This was then taken as the failure limit for Sample D. Hence, thicker ECC layer or/and thicker HSC layer might be needed for larger impact and blast event.

The recorded data were analyzed as follow:

a) Potentiometers

The vertical displacement of Sample D upon the 2nd impact is shown in Figure 3.41. From the figure, it can be seen that there were two peaks, labeled as X1 and X2. Peak X1 was the initial vertical displacement downwards when the projectile hitting the Sample. Upon impact, there was a rebound and Peak X2 was the resulted rebound vertical displacement upwards. At Peak X2, the P1 dislodged when the sample became to go upward, and hence, the P1 value at X2 was not recorded. The P3 also dislodged at around 0.3s, but the peak value was still taken. Table 3.21 summarizes the peak value of these potentiometers.

Table 3.21 Peak readings of potentiometers for Sample D, 2nd Impact

	Peak value at X1	Peak value at X2	Rebound
Pot1	-13.3 mm	---	---
Pot2	-14.2 mm	14.1 mm	28.3 mm
Pot3	-10.8 mm	6.1 mm	16.9 mm
Ave	-12.8 mm	10.1 mm	22.6 mm
(+ ve ➔ upwards, - ve ➔ downwards)			

From Table 3.21, it can be observed that Pot1 (nearest to the center of the slab) and the Pot2 and Pot3 were about 250 mm and 336 mm away from the center, however, it can be seen that the vertical displacement was almost stable with radial distance. For the rebound values, due to no recording for Pot1 at peak X2, only Pot2 and Pot3 rebound were calculated. In Figure 3.38, it was found that there were four major cracks occurred in the middle of slab, which indicated that compressive and tensile failure occurred in Sample D during impact. This failure was the result of the bending of Sample D, which was the typical global behavior of concrete material under impact loading. Although the energy was higher than previously tests, it was still belong to low impact category and caused global response of the structure.

b) Accelerometers

Acceleration of the impact head A1 was found to be about 1325 g upon 2nd impact. Acceleration of the slab at 150 mm and 250 mm radius distance (A2 and A3, as shown in Figure 3.10) were found to be 375 g and 291 g, respectively. These values are summarized in the Table 3.22.

Table 3.22 Peak readings of accelerometers for Sample D, 2nd Impact

	A1	A2	A3
Peak reading	1325 g	375 g	291 g

The A1 value was slightly higher than first impact with same drop height. This was due to the impact head just directly hit the HSC surface, while for the first impact, the AC layer serviced as a first layer to absorb the energy before the head arrived HSC surface. It was also found that A2 and A3 from 2nd impact were much lower than that from 1st impact. This was probably that A2 and A3 were attached at the surface of AC layer for 1st impact, while it was attached at the surface of HSC layers for 2nd impact. During impact process, the AC layer delaminated from the HSC layer, and shifted a lot from its original position which may cause higher acceleration compared to that at HSC layer.

3.6 Comparison of 4 Test Specimens and Discussion

In this section, the response of the 4 Samples under impact will be compared and analyzed. There were rigid concrete pavements (first control sample, Sample A), flexible AC pavement (second control sample, Sample B), and the proposed multi-layers pavement (Sample C, Sample D). Sample A, B and C were subjected to the same height of drop weight (1.5m), while Sample D was subjected to higher drop height (3m). Herein, the physical observation from Sample A and B would be compared with that of Sample C and Sample D. The cross-section of these samples can be seen in Table 3.1.

3.6.1 Physical observations

A short summary of the physical observations for Samples A, B, C and D is summarized in Table 3.23 below.

Table 3.23 Summary of impact test results

Sample	Impact Height	Test Impact	Physical Observations
A (Rigid Pavement) (1st control sample)	1.5 m	1st Impact	Visible crater (140mm diameter and 5 mm depth). Higher propagation of cracks from bottom. Significant debris.
		2nd Impact	Three major shear cracks formed Sample broke into 3 pieces. Complete & sudden failure.
B (Flexible Pavement) (2nd control sample)	1.5 m	1st Impact	Visible crater (100 mm diameter and 85 mm depth). No propagation of cracks from center.
		2nd Impact	The whole asphalt layer (150 mm) & more than half of the aggregate layer was penetrated through. Visible crater (120mm diameter and 250 mm depth). Complete failure.
C (Proposed Multi-layers Pavement)	1.5 m	1st Impact	Small crater formed (100mm diameter and depth< 5mm). Asphalt layer intact and minor cracks in bottom ECC layer.
		2nd Impact	Crater depth increased by 10mm. Asphalt Layer still intact and Multiple Small Cracks propagating from ECC Layer. Performed best compared to other Samples. No complete failure.
D (Proposed Multi-layers Pavement)	3 m	1st Impact	Small crater formed (100mm diameter and asphalt layer was punched through) in the asphalt layer HSC layer was intact, minor cracks in bottom ECC layer.
		2nd Impact	Crater occurred at HSC surface (100 mm diameter and 175 mm depth). Four major compressive cracks formed and Sample broke into 4 pieces. Cracks due to tensile stress propagate from ECC. Sever Damaged under this energy.

Despite having boundary confinement provided by the belts and the strong steel box, Sample A showed a higher level of failure upon 2nd impact because Sample A was normal concrete with compressive strength of 54 MPa only. It was considered as completely failed since Sample A was broken cleanly into three distinct segments. Sample A also had significant fragmentation of the surface. The crater of Sample A after the 1st impact was large and equal to 140 mm. Concrete fragments could also cause significant damage and harm as they "fly" randomly upon impact. Hence it was better to use asphalt which was softer and less dangerous rather than concrete as the surface layer.

For Sample B, after 1st impact, the AC layer was punched through to a depth of 85 mm thickness. At 2nd impact, the whole AC layer (150 mm) was fully penetrated through, and the depth of crater was around 250 mm. The sub-base (aggregate layer) under the AC layer was disturbed due to impact, and thus the crater repair needed to be carried out in the domain of the whole AC layer and sub-base.

For Sample C, after 1st impact, Sample C had a few cracks on the AC surface and the AC layer remained intact due to the geogrid reinforcement. This demonstrated that the geogrid actually helped in preventing the tensile cracking of the AC layer. Then, the impact force was able to dissipate through the AC layer which was not fully destroyed. The geogrid reinforcement in Sample C also controlled the amount of debris on the surface upon impact. There was no debris at all for Sample C upon the two impacts.

Furthermore, Sample C did not fail under 2nd impact. Sample C still had its structural integrity even though the crater was about 10 mm deeper than the first impact and more micro-cracks appeared at the sides of the ECC layer of the

sample. Although the AC layer was still intact, it shifted slightly during 2nd impact. However, in the actual situation the AC layer would be much wider and this shift would be less significant, the test was still relatively conservative compared to that under actual site conditions. According to the test results, it was found that the configuration of Sample C met the objective the best as repair time was required only to fill up the craters or repair the asphalt layer when impacts occur.

Thus from the physical observations, it was obvious Sample C (the proposed multi-layers pavement materials) performed most satisfactory while Sample A (control test) performed the worst. Sample C still performed better than pure asphalt Sample B as Sample B failed upon 2nd impact.

For Sample D, the proposed multi-layers pavement under higher energy impact, after 1st impact, the asphalt layer was destroyed and shafted, while the HSC and ECC layer was intact. However, there was no significant fragment occurred in the AC layer. It was also observed that only small cracks occurred from the bottom ECC layer, which showed the good ductile behavior. Upon 2nd impact, the impact head penetrated through the HSC layer, and the whole pavement slab was broken into 4 pieces. However, the failure was caused by 3m drop height, compared to the Sample A and Sample B of which complete failure was caused by 1.5 m drop height. Thus, it was concluded that this proposed multi-layers pavement still performed better than the rigid concrete pavement and flexible asphalt pavement even though it was subjected to double the energy of the normal concrete and asphalt pavement.

3.6.2 Displacement of samples

As mentioned in previous section, because of the location of the accelerometer A1, the A1 value in current study could only illustrate the degree of the target stiffness. It was shown that the higher the stiffness of the impact surface, the larger the magnitude of A1. Therefore for the first impact, both Samples B and Sample C with AC as the surface layer recorded similar magnitude readings. The reading from Sample B was slightly higher than that from Sample C. This was due to that small steel frame in Sample B enhanced the strength of the asphalt layer, and in turns increased its stiffness. Both A1 readings from Sample B and Sample C were much lower than that from Sample A since Sample A was the most rigid pavement among these 3 samples. Accelerometers A2 and A3 on the surface indicated the reaction force from the sample upon impact. The AC layer was soft and had air voids compared to the rigid concrete layer of Sample A. Hence, readings of A2 and A3 for Sample A was also higher compared to that of Sample B and C. A1, A2 and A3 for Sample D were obtained from higher energy impact (3.0 m drop height), and thus, the acceleration values recorded were the highest among all the tests. Table 3.24 gives a summary of the peak readings for the accelerometers for the tests.

Table 3.24 Summary of peak readings for accelerometers and the average rebound of each sample for all tests

Sample No.	A1	A2	A3	Ave rebound
Sample A, 1st Impact	2619 g	158 g	93 g	43.58 mm
Sample B, 1st Impact	667 g	135 g	106 g	70.0 mm
Sample C, 1st Impact	574 g	49 g	61 g	40.4 mm
Sample D, 1st Impact	1214 g	657 g	497 g	---
Sample A, 2nd Impact	1897 g	342 g	195 g	22.2 mm
Sample B, 2nd Impact	721 g	162 g	106 g	58.3 mm
Sample C, 2nd Impact	762 g	149 g	71 g	42.05 mm
Sample D, 2nd Impact	1325 g	375 g	291 g	---

For the second impact, the same pattern was also observed. Sample A had the highest stiffness and thus had the highest reading for A1 at 1897g. The increase in the reading of A2 and A3 for Sample A was due to the sample itself breaking into three segments, resulting in significant displacement. Sample C also had HSC as the surface layer for the second impact because the asphalt layer had been destroyed. Hence, the reading of A1 at 762g for Sample C was slightly higher compared to Sample B.

Sample D suffered higher acceleration in A1 upon 2nd impact compared to that under 1st impact. This was due to the impact head just directly hit the HSC surface, while for the first impact, the AC layer serviced as a first layer to absorb the energy before the head reached the HSC surface. The A2 and A3 readings under 2nd impact were much lower than that under 1st impact. This was probably that A2 and A3 were attached at the surface of AC layer for 1st impact, while it was attached at the surface of HSC layers for 2nd impact. During the impact, the AC layer was delaminated from the HSC layer, and shifted a lot from its original position and then caused a larger displacement.

The rebounding of the sample upon impact was another response that indicated the amount of impact force absorbed by the sample. Table 3.24 also shows the average vertical displacement of the sample upon impact. Under the first impact, Sample A rebounded slightly more than Sample C as it had a much higher stiffness and was expected to be rebound higher than softer materials. Sample C rebounded 40.4 mm, followed by Sample B at 70 mm. Both of these samples had asphalt as their surface layer which was able absorb force better, deform and compress more due to it being softer than concrete. However, the Sample B suffered larger rebound than others two samples. This was due to that the belts had not restrained sample but small steel frame, which caused asphalt moving freely without being restricted. This could be seen from Figure 3.20, in which gap occurred between belts and sample.

Sample A, however, rebounded the least at 22.2 mm in the second impact even though it had the highest reading for A1 at 1897g. This could be explained by the large lost in energy through the shear cracks that caused the sample to break into three segments. The highest rebound of 58.3 mm was seen in Sample B. This was due to that the gap between belts and sample become narrower after 1st impact and the belt restricted the pavement slab during impact. The rebound for Sample C under 2nd impact was similar to that under 1st impact. This was demonstrated that the Sample C were not damaged under twice impact and remained integrity of the structure.

3.7 Conclusions on Laboratory Drop Weight Impact Tests

From the responses of Samples A, B and C, it could be concluded that combination of ECC, HSC and AC with GST could improve the impact resistance

of pavements significantly. Samples C which is our proposed multi-layers pavement design was found to perform better than Sample A (first control test with normal concrete layer) and Sample B (second control test with only AC layer) in drop weight test.

For Sample A (first control test with normal concrete layer), it was broken cleanly into three distinct segments under 2nd impact and seemed to be totally destroyed. Sample A also had significant fragmentation of the surface subjected to 2nd impact. The crater of Sample A after the 1st impact was large and equal to 140 mm. Concrete fragments could also cause significant damage to the surrounding human body and fixtures as they fled randomly. The results of Sample A showed that the concrete pavement had low multiple penetration resistance, and its brittleness property would also produce a large number of fragment due to impact load.

For Sample B (second control test with only AC layer), after the first impact, the asphalt layer was punched through to a depth of 85 mm thickness. At the 2nd impact, the whole AC layer (150 mm) was penetrated through, and the depth of crater was around 250 mm which was beyond the AC layer and reached the sub-base layer. The sub-base (aggregate layer) under the AC layer was loosened by the impact, thus repair is need to be carried out not only in the domain of the whole AC layer, but also the completion of sub-base, which is time consuming. Before placing the new AC layer, the sub-base needs to be re-compacted to service as a strong base. The test results of Sample B demonstrated that the flexible pavement had low penetration resistance.

The impact test for Sample C showed that the geogrid was highly effective in preventing the AC layer from being turned into fragments. The AC layer was

intact even after the 2nd impact. It can be demonstrated that the geogrid was able to improve the tensile strength of the asphalt concrete under dynamic loading. Sample C also had the correct arrangement of ECC as the bottom layer and HSC as the middle layer. The bottom ECC layer was ductile enough to bend more during impact loading thereby reducing the possibility of sudden and brittle failure. The HSC middle layer served as a 2nd layer of defense against impact loading. The geogrid-reinforced AC layer could be used a sacrificial layer by taking the majority of the impact load. It could be easily replaced or repaired upon damage. Thus the configuration of Sample C works the best in reducing the crater size when the pavement is subjected to impact loading. Thus, it could be concluded that Sample C meets the objective the best as repair time is required only to fill up the craters or repair the AC layer when impact occurs.

For Sample D, the proposed multi-layers pavement subjected to higher energy impact, it was observed that after 1st impact, the AC layer was destroyed while the HSC and ECC layer was intact, and only small cracks occurred from the bottom ECC layer. Rapid repair could be conducted to replace the damaged AC layer at this stage. Upon 2nd impact, the impact head penetrated through the HSC layer, and the whole pavement slab was broken into 4 pieces. However, there was still room for improvement as the Sample D was completely destroyed only after 2nd impact. The increase of thickness of ECC layer or/and HSC layer or increasing of strength of ECC and HSC may be needed for resistance against larger impact event. This would be discussed in the later part.

In summary, in the proposed multi-layers pavement system, the "soft" material (AC) is used as the sacrificial surface layer to absorb some portion of the dynamic energy. Thereby, the energy transmitted to the following layers was

greatly reduced. With the inclusion of the high strength Geosynthetic (GST) within this AC layer, the tensile strength of this layer was increased and in turn reduced the damage to the AC layer. Below the AC layer, HSC which was a "strong" material was used. This HSC layer served as the main body to sustain the dynamic load. Under the dynamic loading, the tensile stress tends to develop at the rear face of the material due to the reflection of the compressive stress propagating from the top face. However, it is well known that the concrete has low tensile strength. Furthermore, the HSC is very brittle and may develop cracks easily. Hence, another "soft" and ductile material (ECC) is needed at the base of the "strong" HSC layer to absorb the energy. It is because the ductile material can develop micro crack to dissipate and attenuate energy when subjected to dynamic loading. Thus, the multi-layer pavement system showed a very good impact resistance from the laboratory test.
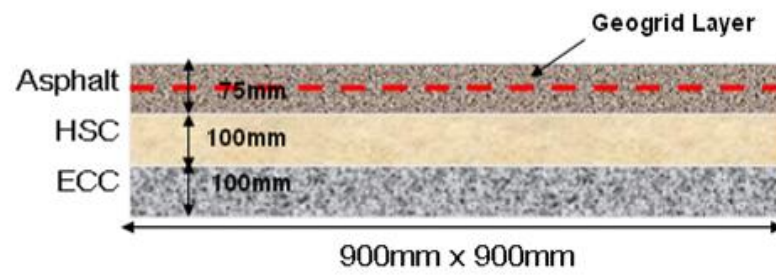
Figure 3.1 Configuration of the proposed new pavement

Figure 3.2 Drop weight test machine
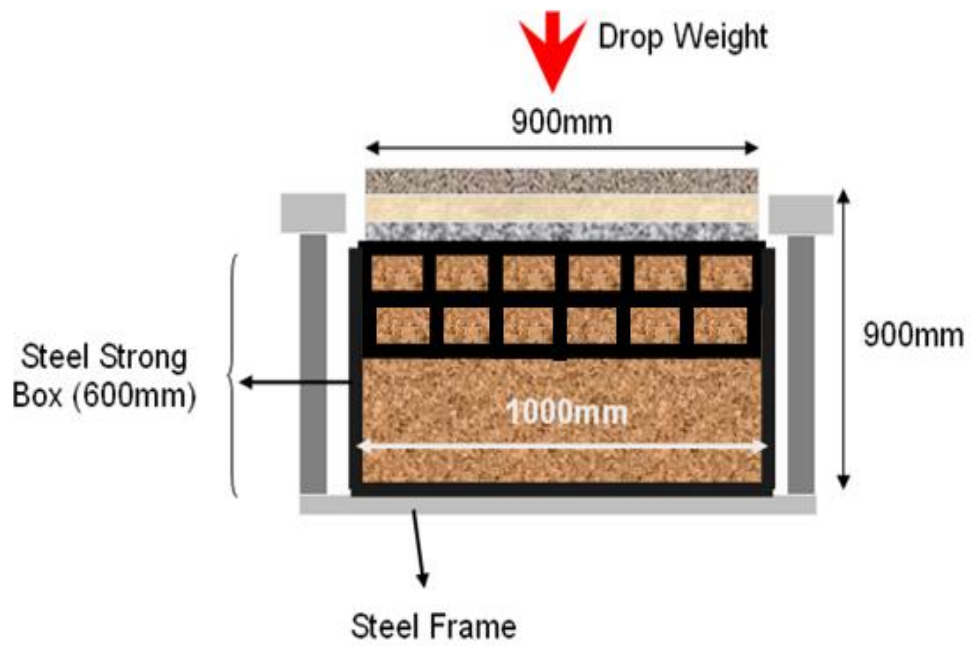
Figure 3.3 Setup for Sample A, C and D
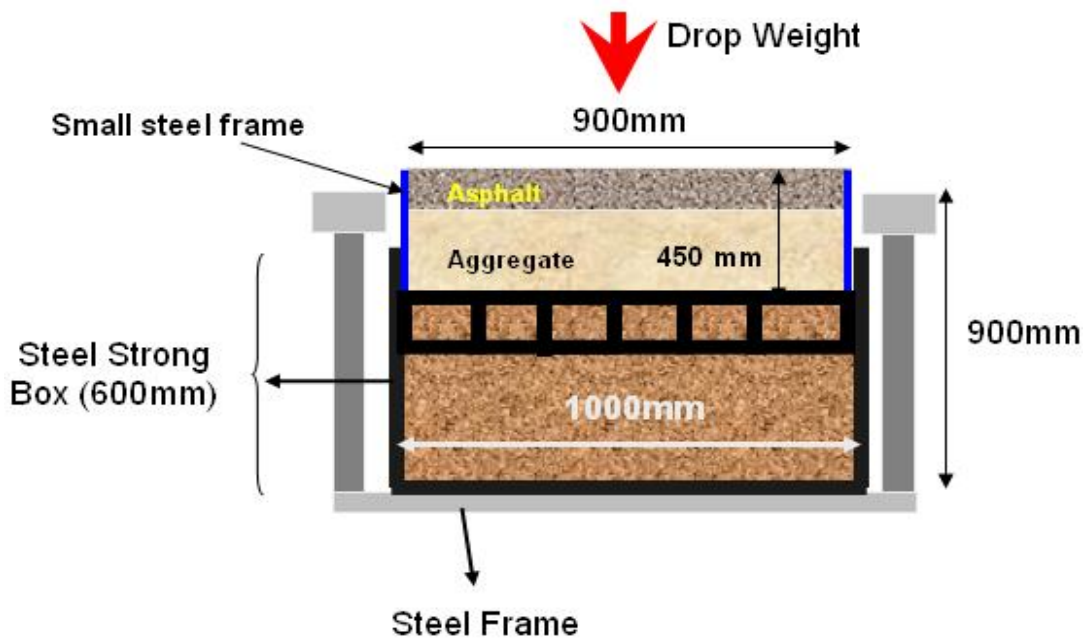
Figure 3.4 Setup for Sample B

Figure 3.5 Compacting of sand in steel strong box

Figure 3.6 Geocell used to reinforce the sand in the steel strong box
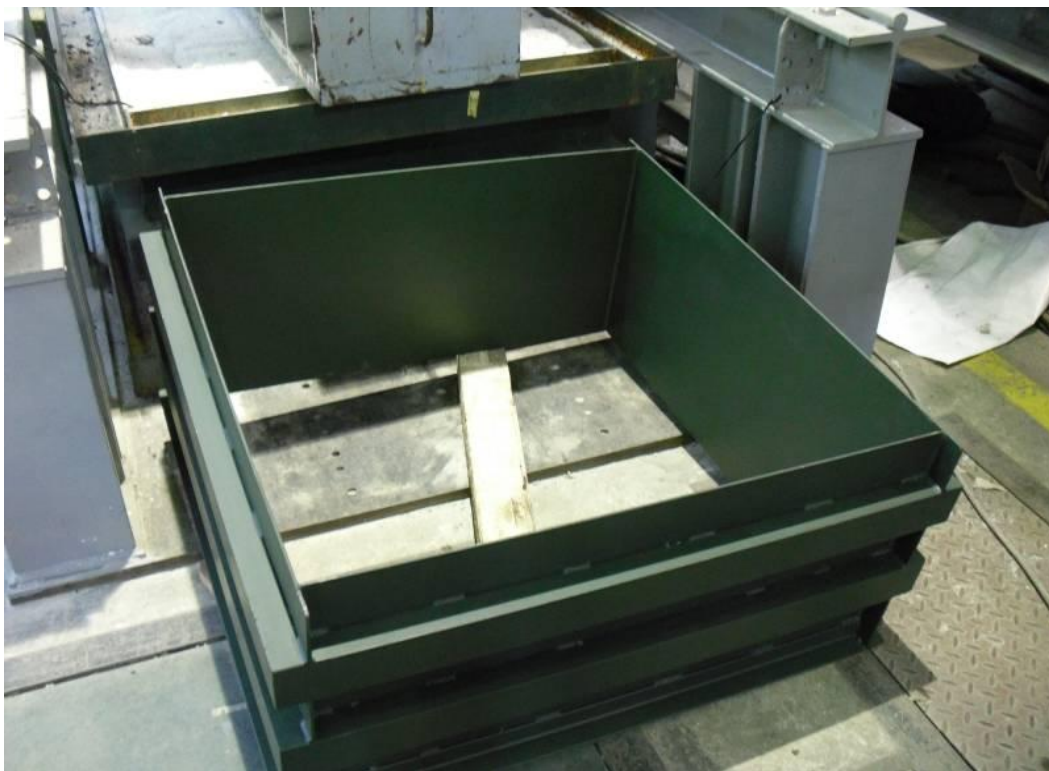
Figure 3.7 Small steel frame
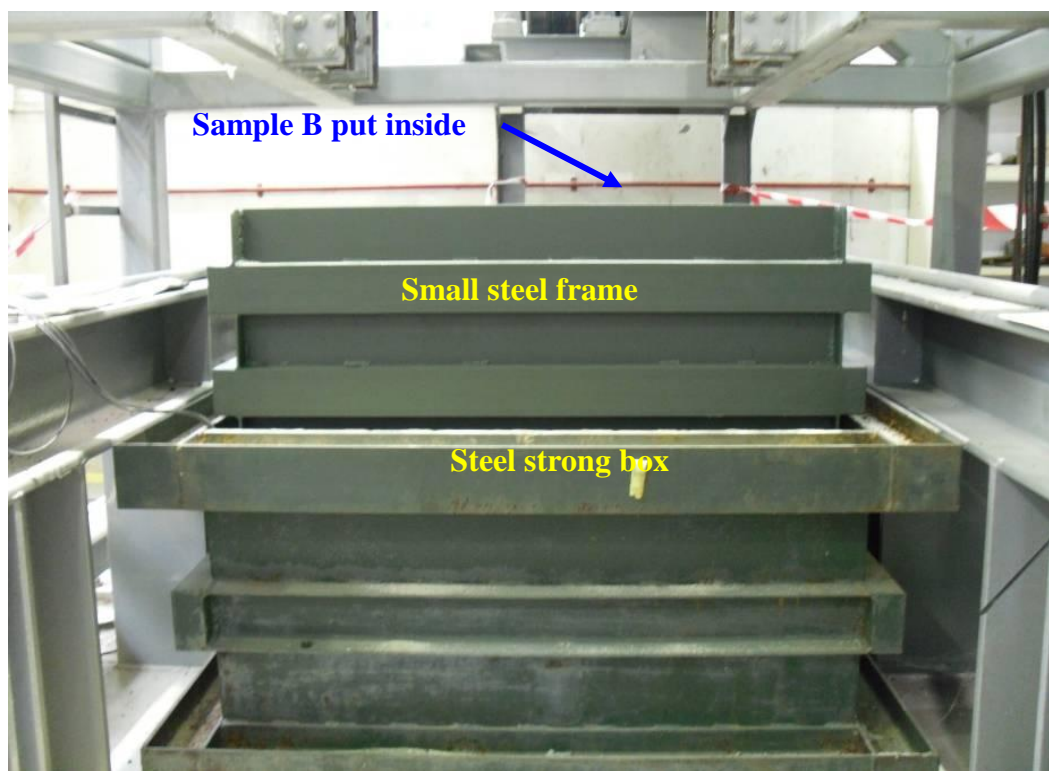
Figure 3.8 Actual test setup for Sample B

Figure 3.9 Actual test setup for Sample C
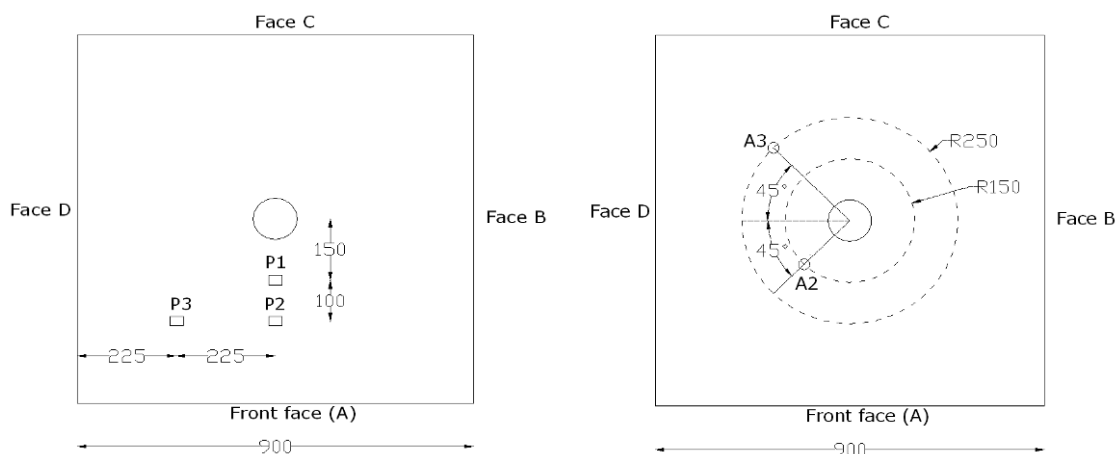
Figure 3.10 Positioning of potentiometers and accelerometer
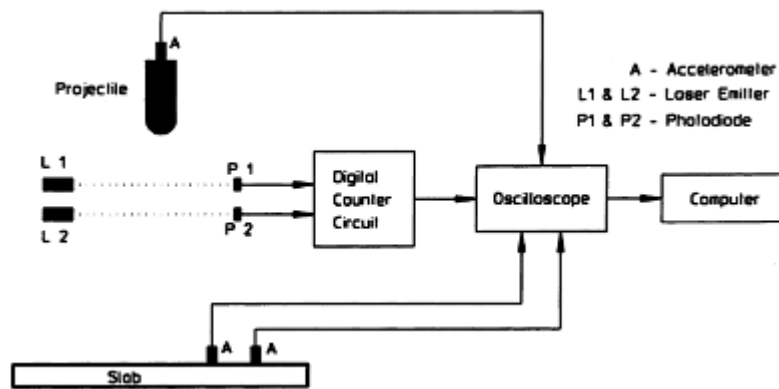
Figure 3.11 Schematic diagram of photo diode system (Ong et al. 1999)

Figure 3.12 Surface of Sample A after 1st impact

Figure 3.13 Crack Propagation in Sample A after 1st Impact
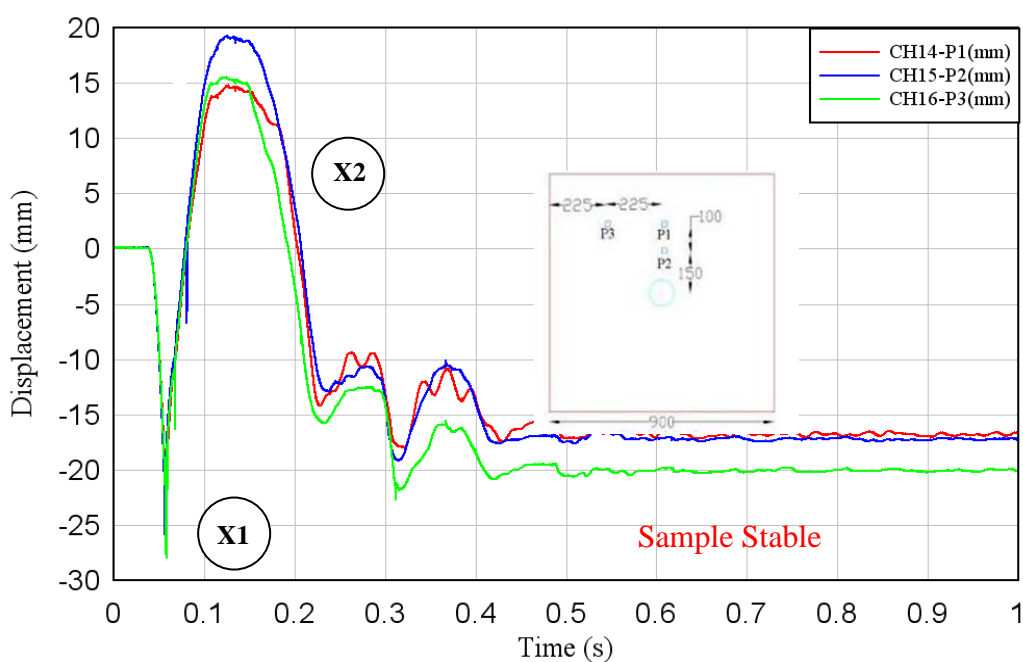
Figure 3.14 Potentiometers for Sample A upon 1st impact
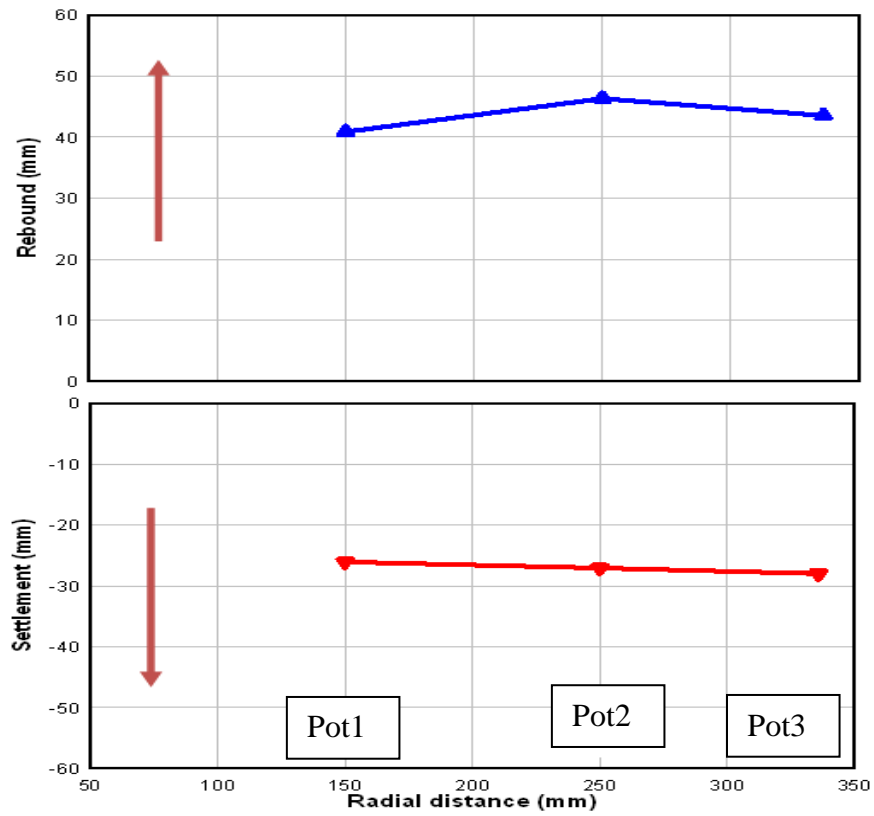
Figure 3.15 Peak displacement of Sample A upon 1st impact
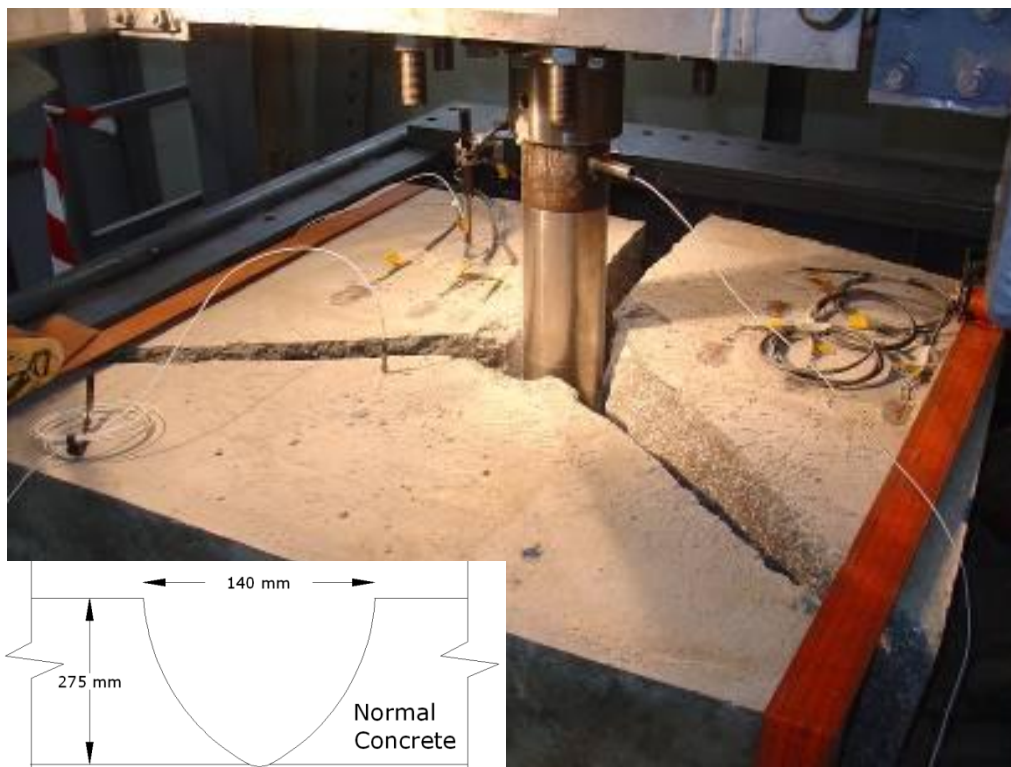
Figure 3.16 Damage on Sample A after 2nd impact
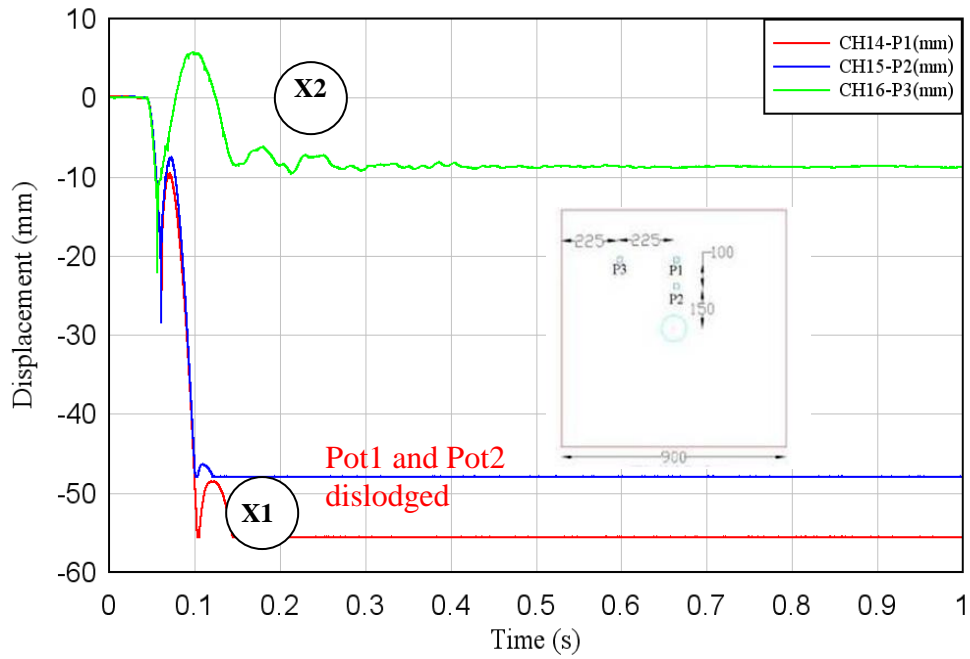
Figure 3.17 Potentiometers for Sample A upon 2nd impact
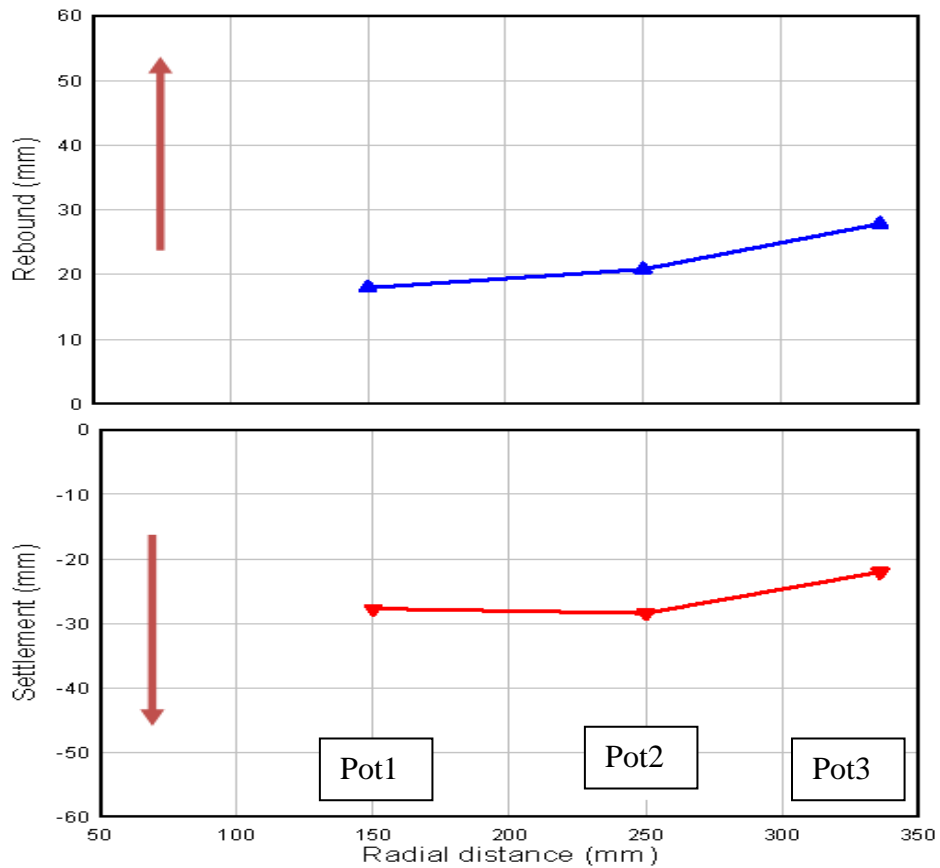
Figure 3.18 Peak displacement of Sample A upon 2nd impact
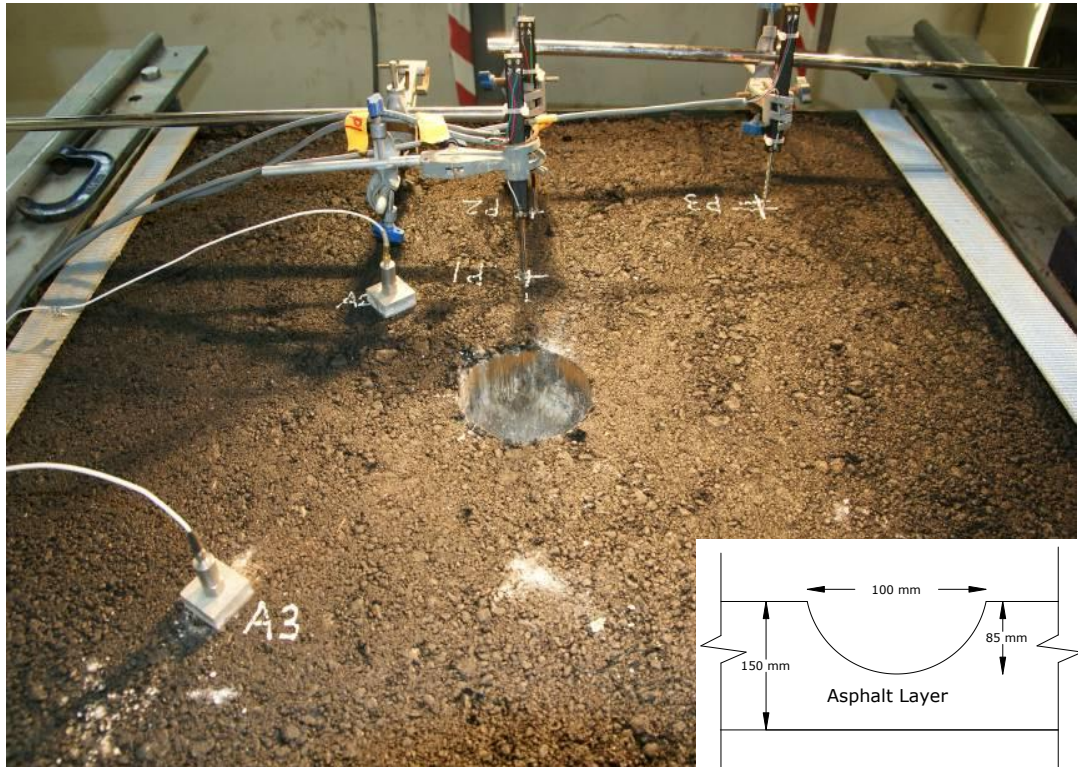
Figure 3.19 Surface of Sample B after 1st impact
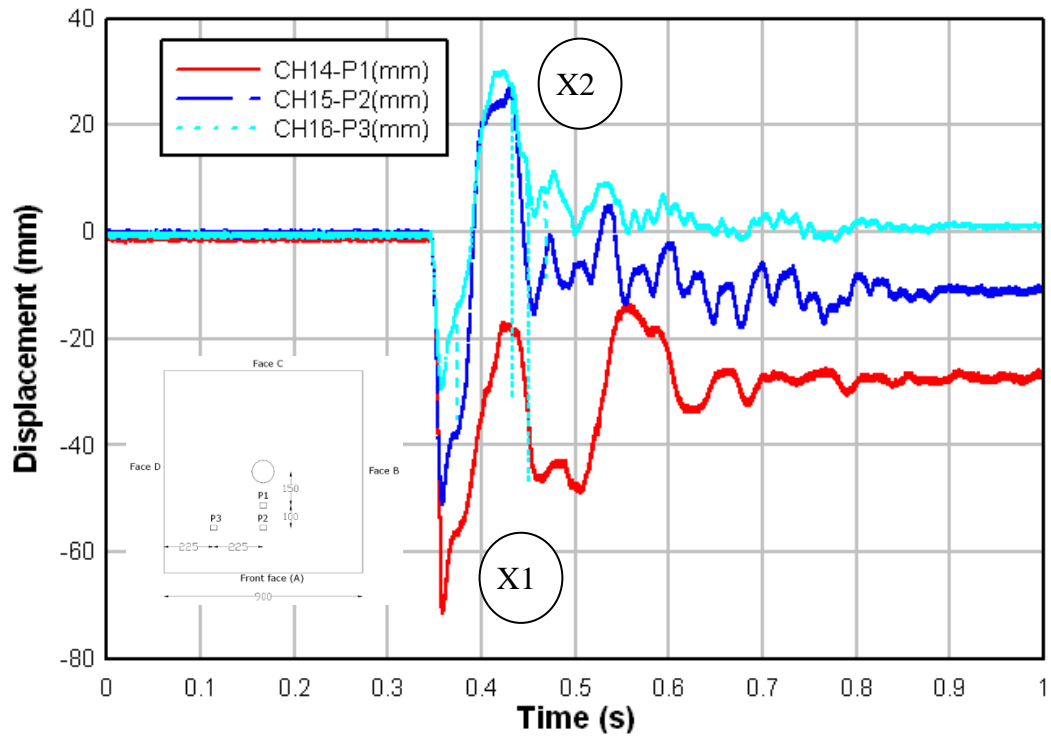
Figure 3.20 Potentiometers for Sample B upon 1st impact

114
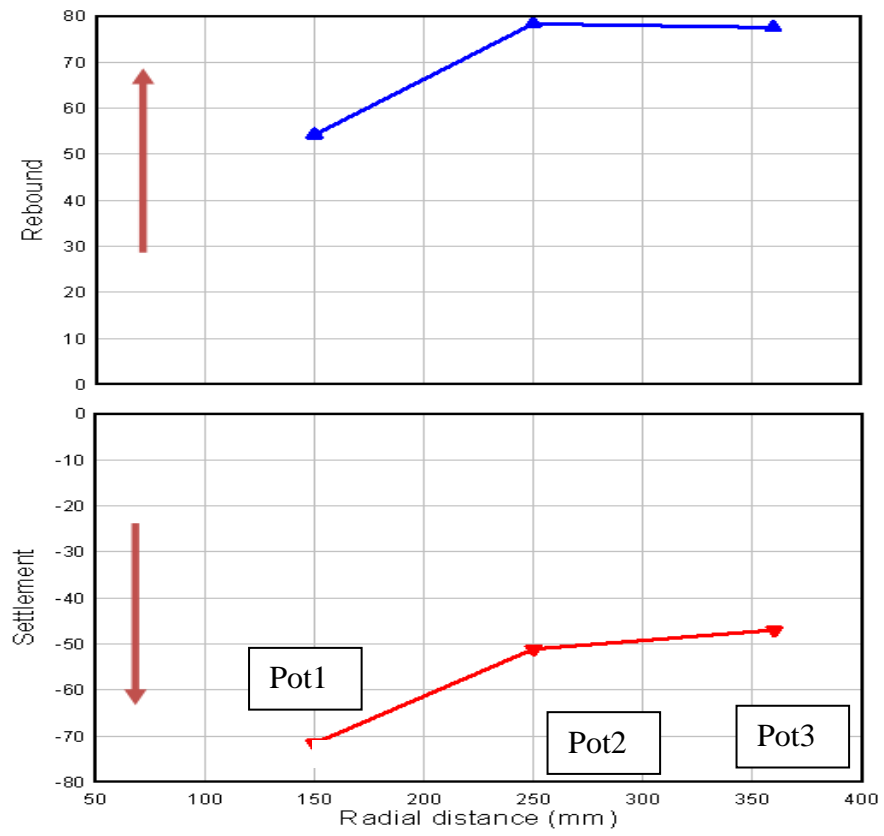
Figure 3.21 Peak displacement of Sample B upon 1st impact
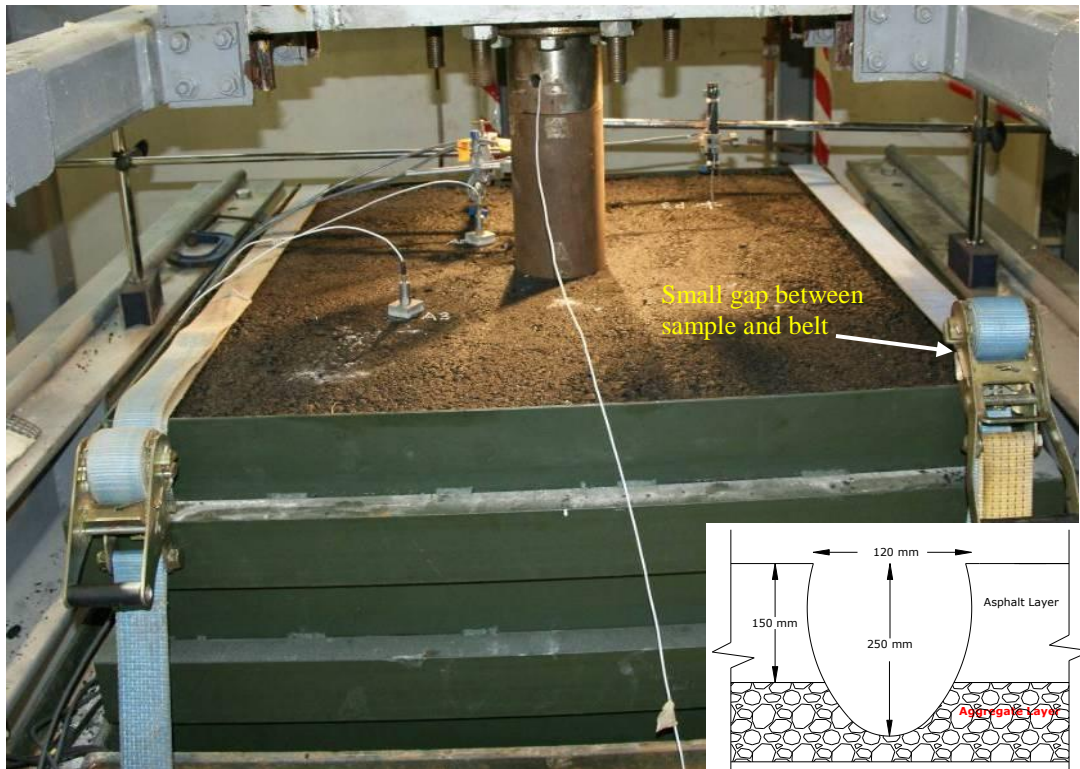
Figure 3.22 Surface of Sample B after 2nd impact

Figure 3.23 Crater of Sample B after 2nd impact
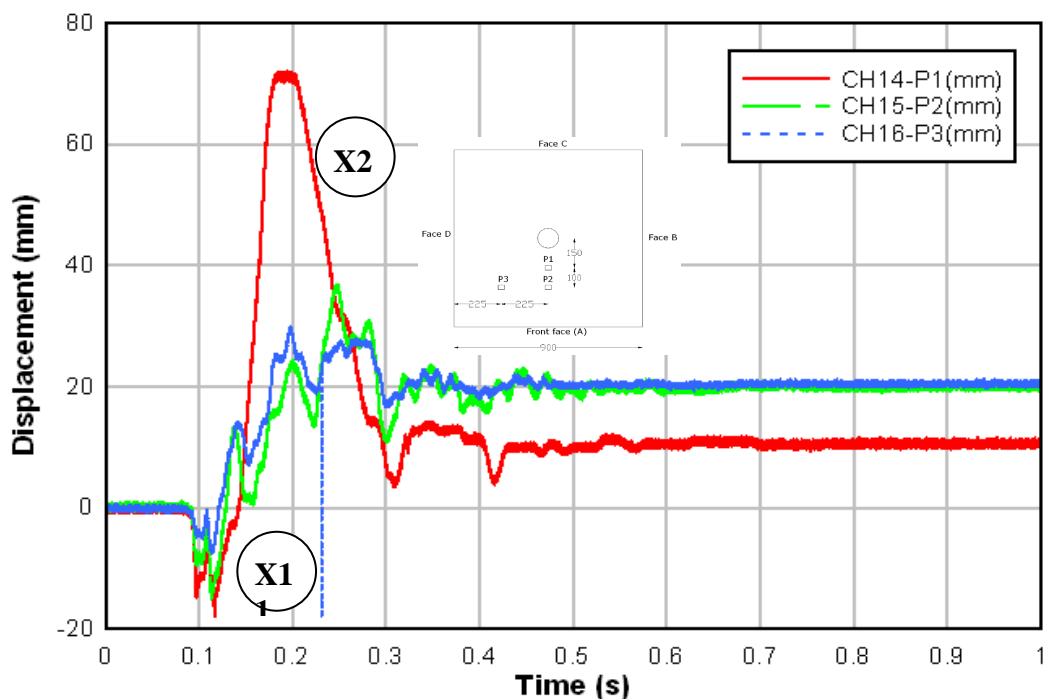
Figure 3.24 Potentiometers for Sample B upon 2nd impact
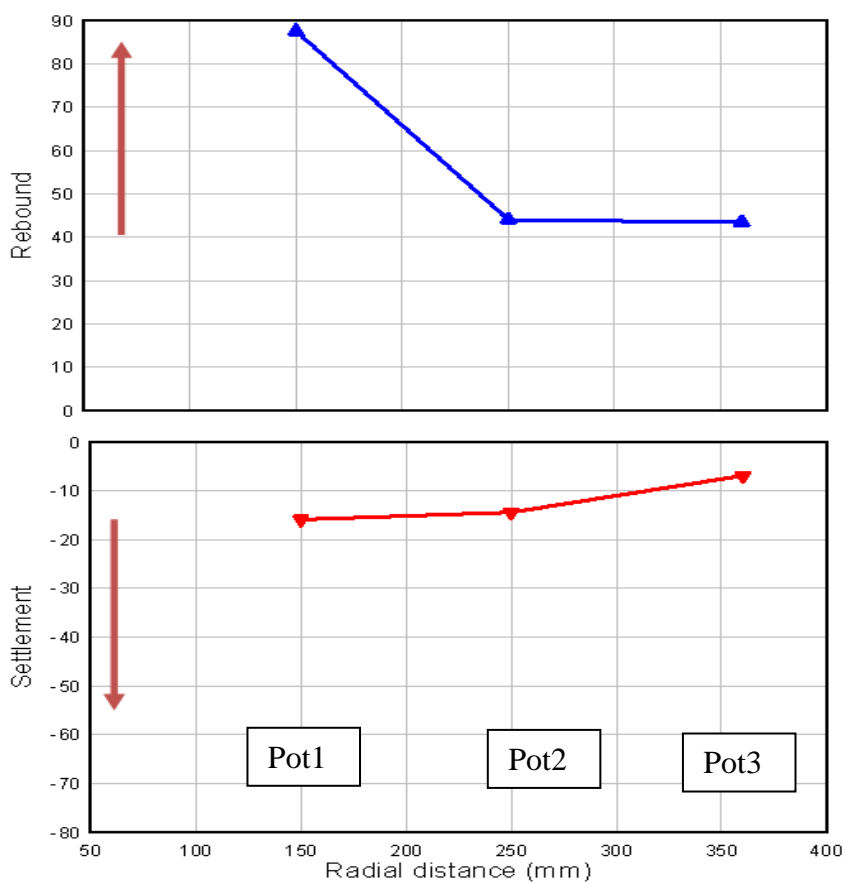
Figure 3.25 Peak displacement of Sample B upon 2nd impact
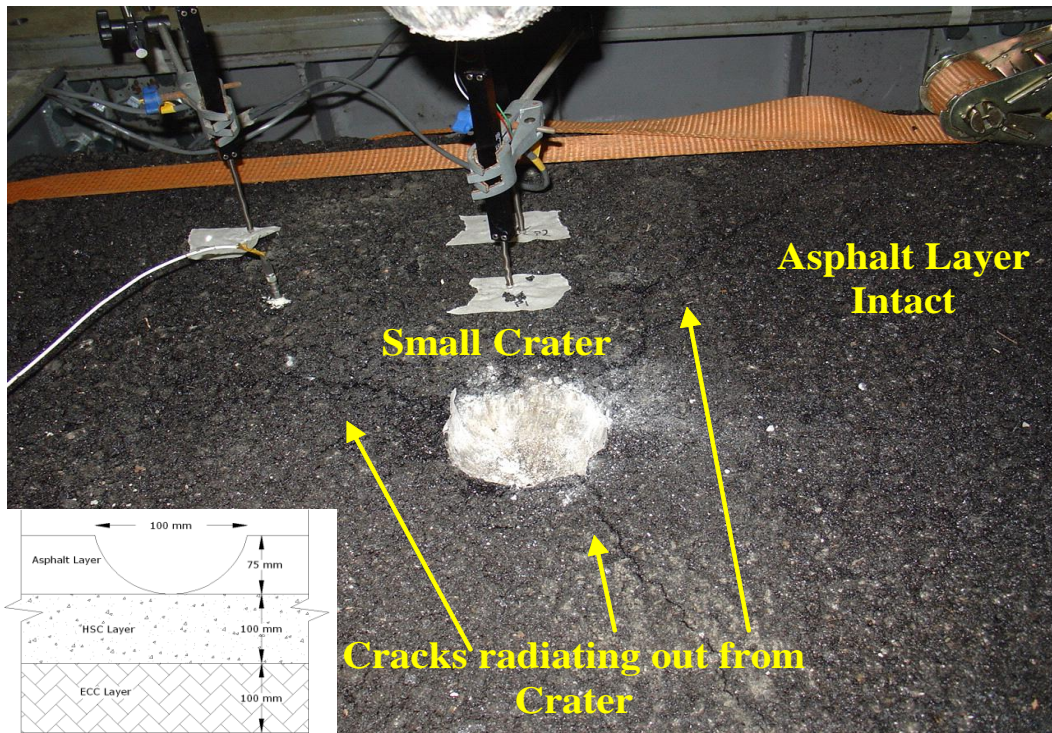
Figure 3.26 Surface of Sample C after 1st impact

Figure 3.27 Side profile of Sample C after 1st impact
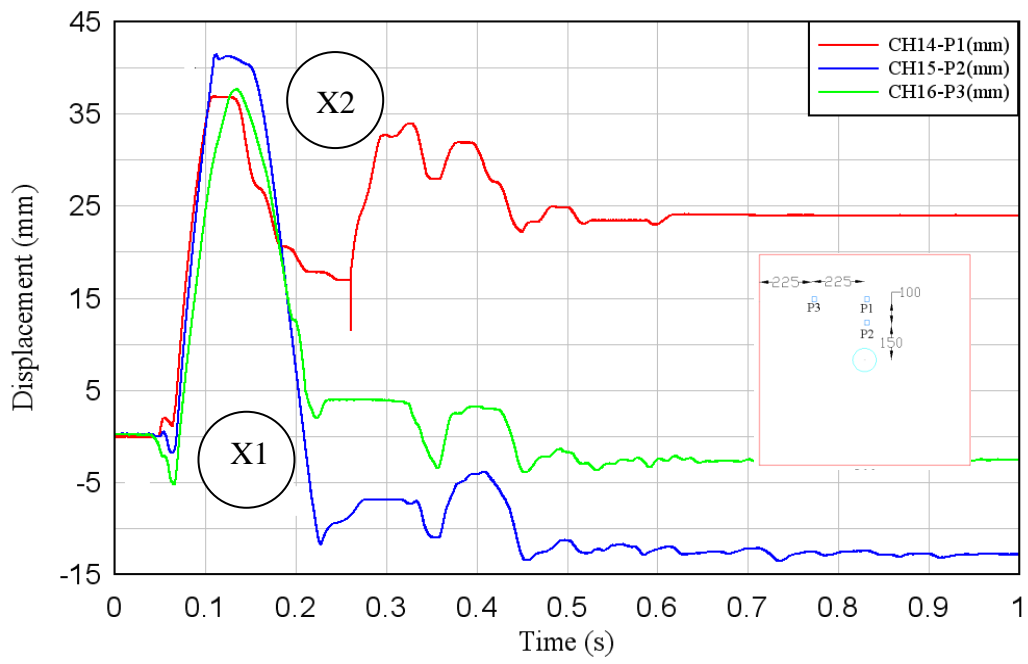
Figure 3.28 Potentiometers for Sample C upon 1st impact

Figure 3.29 Surface of Sample C after 2nd impact

Figure 3.30 Side profile of Sample C after 2nd impact
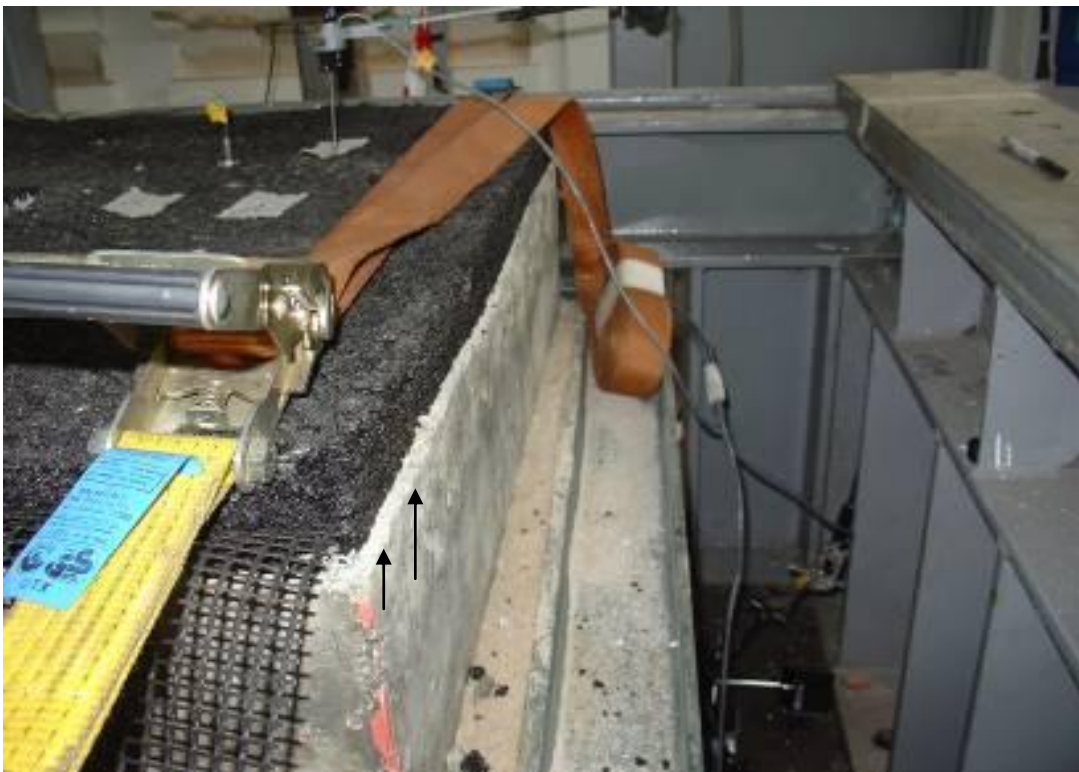
Figure 3.31 Shift of asphalt layer in Sample C after 2nd impact
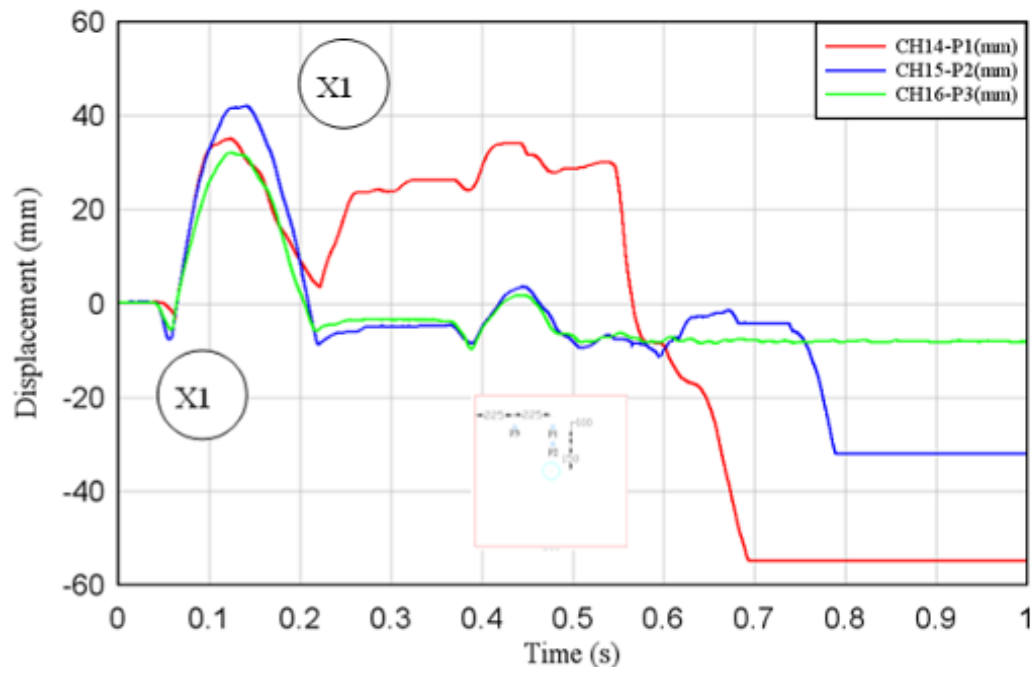
Figure 3.32 Potentiometers for Sample C upon 2nd impact
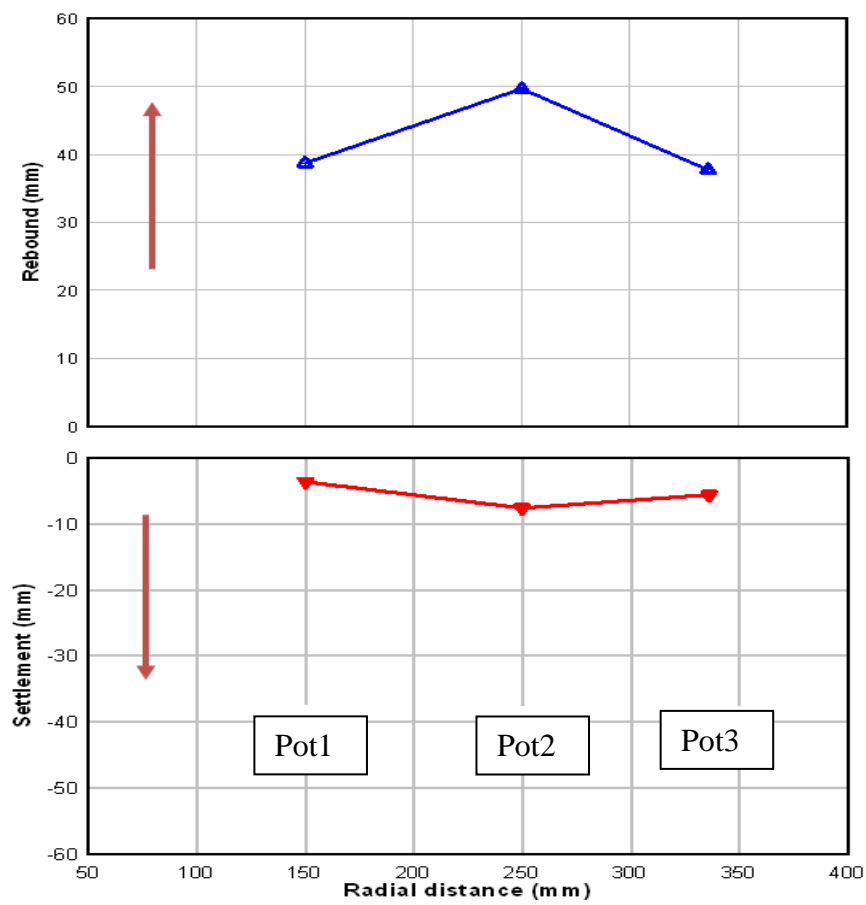
Figure 3.33 Displacement of Sample C upon 2nd impact
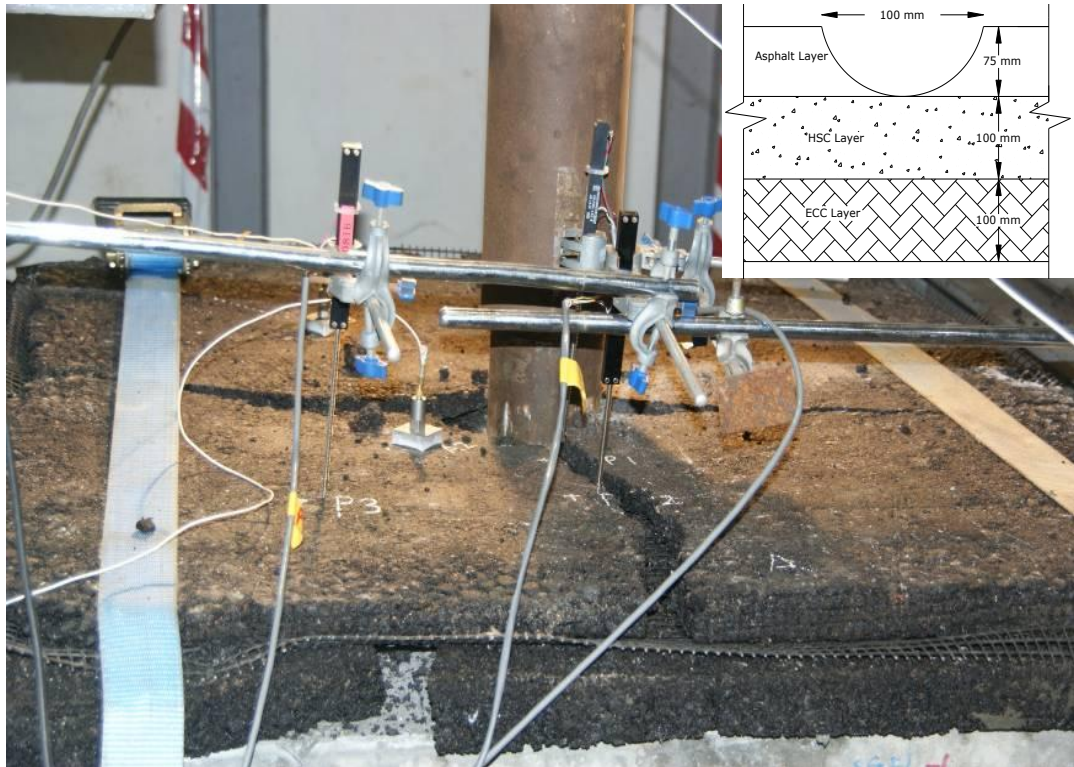
Figure 3.34 Surface of Sample D after 1st impact
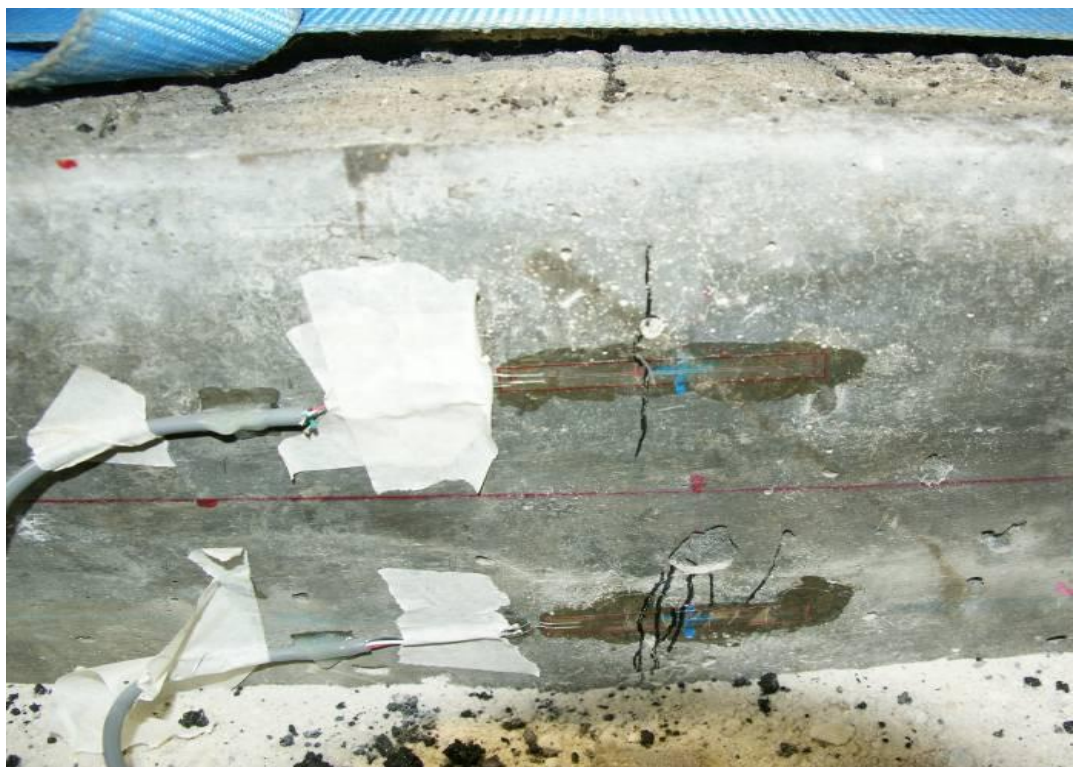
Figure 3.35 Side profile of Sample D after 1st impact (remove Asphalt layer)
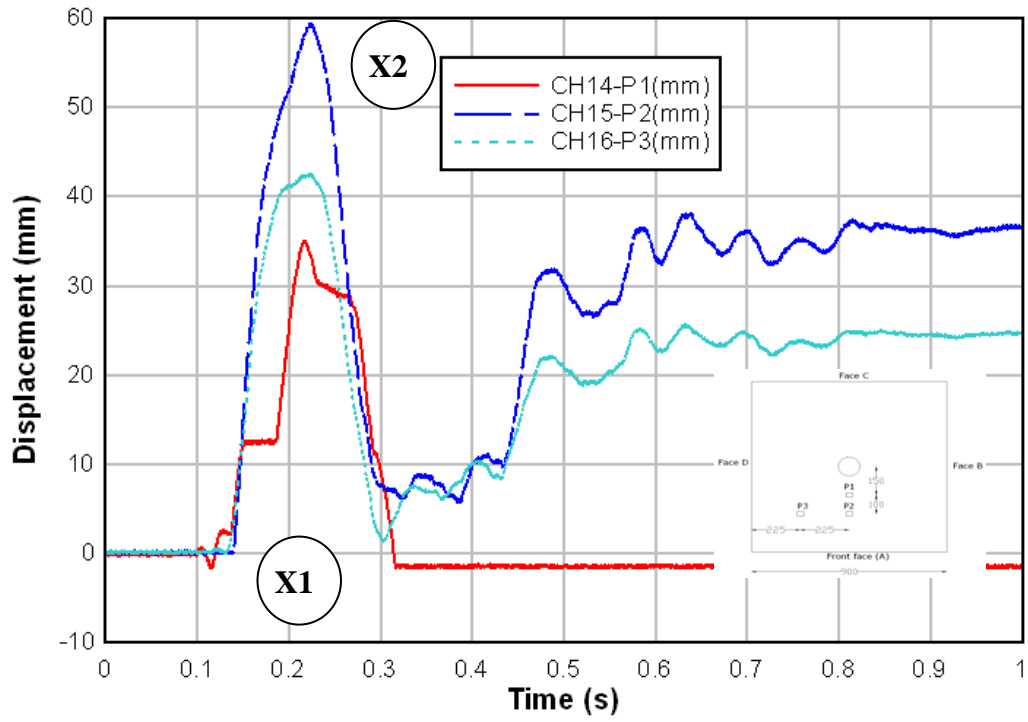
Figure 3.36 Potentiometers for Sample D upon 1st impact

Figure 3.37 Surface of Sample D after 2nd impact

123
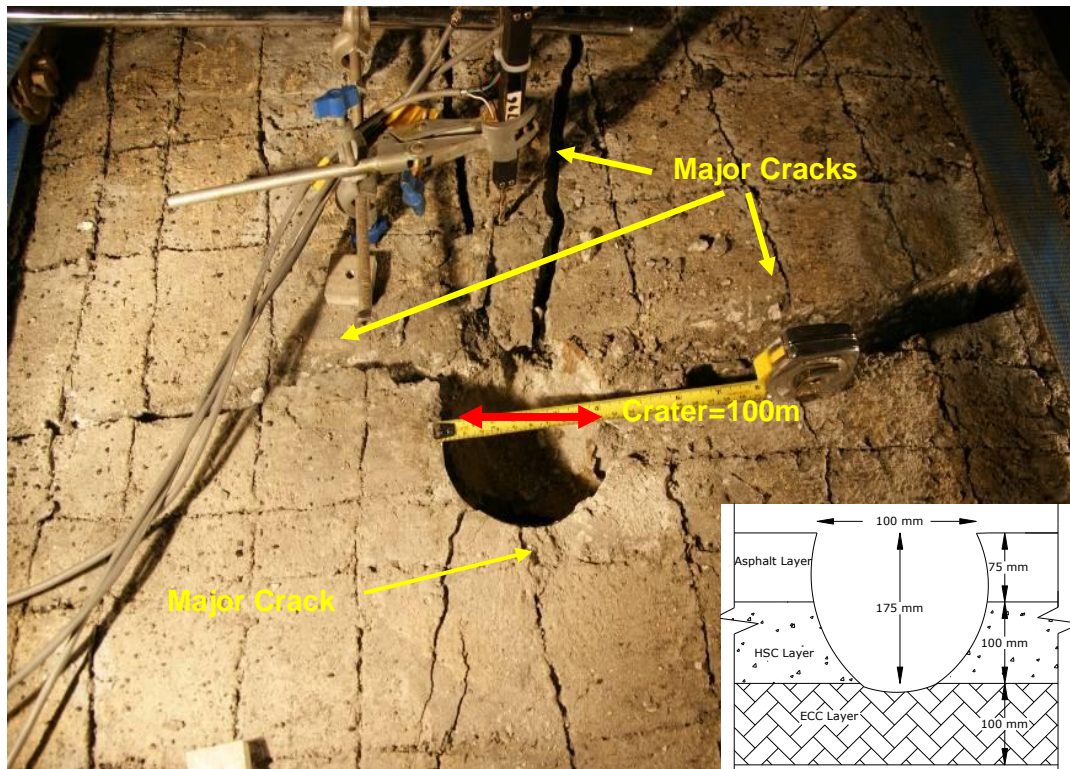
Figure 3.38 Crater size of Sample D upon 2nd impact

Figure 3.39 Side 1 profile of Sample D after 2nd impact

Figure 3.40 Side 2 profile of Sample D after 2nd impact
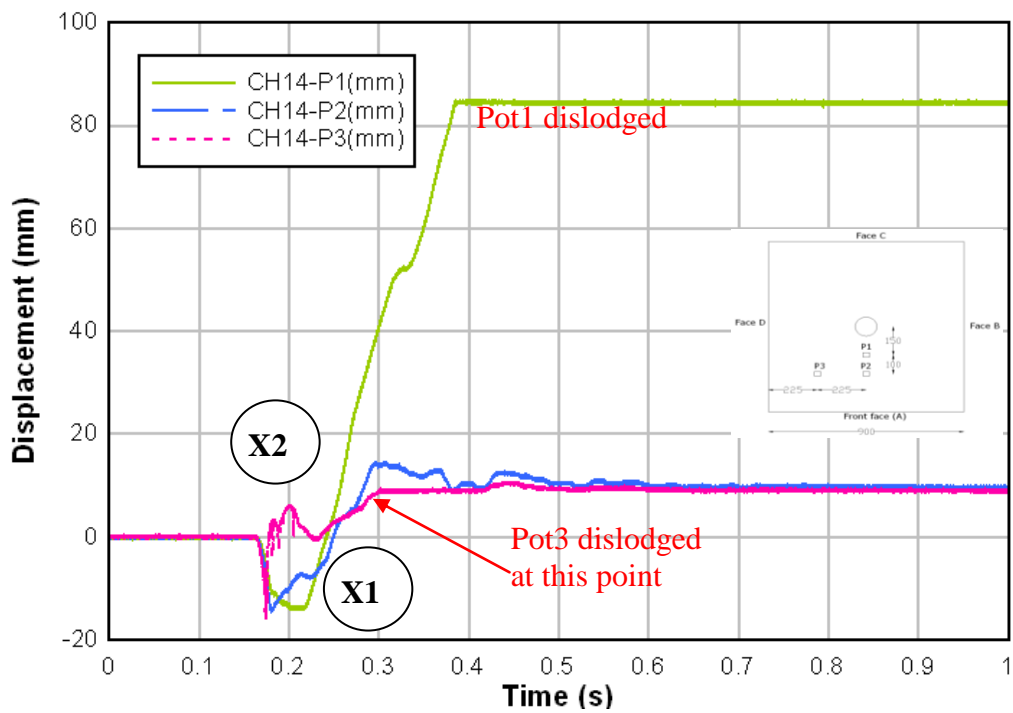
Figure 3.41 Potentiometers for Sample D upon 2nd impact

Chapter 4   Development of New Multi-layers Pavement Material Subjected to Blast Load --- Full Scale Field Blast Trial (ETSC2008)

4.1 Introduction

The results of the laboratory drop weight impact testing showed that the proposed multi-layers pavement material, (i.e. a combination of High Strength Geosynthetics [GST], High Strength Concrete [HSC] and Engineered Cementitious Composites [ECC]) suffered minimum damage when subjected to impact load. However, impact load is different from blast load in terms of the way the force is exerted and transmitted, damage area, energy level and loading rate. Impact load exerted via one solid object impacting onto another solid object, while blast load arising from load due to a series of compression wave. For the damage area, impact load generally produced on damage at a localized area, while blast load will cause damage over a large area with the propagation of the compression wave. It is also obvious that the energy level from impact and blast load can be very different. The energy level from typical drop weight impact was about 10 kJ to 10^2 kJ, while the energy level from blast load will exceed 10^4 kJ for a 10 kg of TNT. Note that the energy level from blast event is about 103 kJ per kg of the charge weight of explosive. The different loading duration of the impact and blast load will exert different strain rate onto the material. Usually, impact load will cause 1 to $10s^{-1}$ strain rate in material, while strain rate will reach 10^3s^{-1}

from blast load. Hence, due to the difference in the blast and impact load, the dynamic response of the material subjected to blast and impact load will be different. The blast load may cause more severe damage to material as compared to that from impact load due to its high energy level and high strain rate loading. Thus it is necessary to conduct a blast test to verify that the proposed multi-layers pavement material also offer good blast resistance. However, it is difficult to simulate the blast load in the lab test. Therefore, the field trial test will be conducted to evaluate the dynamic behavior of the proposed multi-layers pavement under blast load. The field trial test will also provide a means to test the performance of specimens subjected to blast load in the actual field condition.

It should be noticed that for the field trial test, limited number of tests will be conducted due to the cost limitation. Supplementation method such as numerical modelling can be employed to better understand the mechanism and dynamic behavior of the proposed multi-layers pavement subjected to blast load. However, the numerical modelling should be validated before it be used in design. The numerical modelling of the proposed multi-layers pavement subjected to blast load will be discussed in the later part of the thesis.

This section will present the full scale field blast trial for the proposed multi-layers pavement material, and as a comparison for a normal concrete pavement slab. The physical observations and instrument results of these two slabs after blast event will also be analyzed.

4.2 Test Configuration

Two samples were tested in the field blast trial. A control sample and the new pavement design sample were cast and subjected to a close-in charge. Each

slab was subjected to one blast detonation. A 155mm M107 projectile was placed at the center of each slab with the center of gravity of bomb at about 170 mm above the slab surface. Figure 4.1 shows the projectile placement on the slab.

4.3 Slabs Configuration

The two samples were cast at site with each slab 2.8m by 2.8m and 0.275m thick. The thickness of 275mm was the same as the laboratory samples so as to provide good comparison. Figure 4.2 shows the cross-sectional view of these two slabs. The configuration of Slab 2 was exactly as the same as Sample C in the laboratory impact tests.

Slab 1 was the control sample made up of normal concrete with 40MPa strength, which is obtained from the pre-mixed plant. To facilitate the lifting and transportation of the slabs to site, minimal reinforcement (T12 bars in both directions at around 350mm spacing) were installed in the bottom of each slab (concrete cover of 25mm) with four hooks installed. Figures 4.3 and 4.4 show the details of the reinforcement. The reinforcement served to prevent the slab from cracking under self weight during transportation. Minimal reinforcement was chosen so as not to affect the slabs' responses significantly. Figure 4.5 shows the completed Sample 1.

As for Slab 2, Table 4.1 and 4.2 shows the mix proportions for ECC layer and HSC layer, respectively.

Table 4.1 Mix proportions for ECC

S/N	Material	kg/m^3
1	Cement	1400
2	Silica Fume (undensified)	154
3	Superplasticizer (SP/B) (DARACEM 100)	20.2
4	Water	424
5	Steel Fibers	39.1
6	PE Fibers	14.5
7	Water/Cementitous	0.28

Table 4.2 Mix Proportions for HSC

S/N	Material	kg/m^3
1	Cement	428
2	Silica Fume (undensified)	48
3	SuperPlasticiser (SP/B) (DARACEM 100)	8.5
4	Water	162
5	Natural Sand	750
6	Coarse Aggregates (max size of 20mm)	1,000
7	Water/Cementitious	0.35

The ECC was the bottom layer of the pavement, after curing into the modules; the HSC was then poured into in order to make the interface of these two materials combined correctly. The ECC and HSC layers were allowed to cure for around one week, and then the asphalt layer was cast. The asphalt was cast in 2 layers of around 38mm each. Each layer was compacted using a small 1-tonne compactor (Figure 4.6). The geogrid layer was pulled taut and placed on top of the 1st asphalt layer. Figure 4.7 shows the completed Slab 2.

Standard tests were conducted for each material cast and Table 4.3 gives a summary of these properties.

Table 4.3 Properties of materials cast for field blast trial

Material	Compressive Strength (MPa)	Elastic Modulus (GPa)	Poisson's ratio
HSC	55	33	0.20
ECC	64	18	0.22
Normal Concrete	40	27	0.20

As seen, the compressive strength of ECC (64MPa) and HSC (55MPa) was much lower compared to that of the ECC (80MPa) and HSC (90MPa) cast in the laboratory. This was because in the laboratory, it was much easier to control the mixing, thereby resulting in a more consistent mix, whereas on site, due to the limitation of resources, the slab had to be cast in numerous batches which reduces the consistency of the mix significantly. Moreover, due to limitation of the casting site, the curing of the slabs at the site was not done perfectly.

4.4 Anchoring of Slabs

To simulate an actual pavement situation, there was a need to anchor the slabs to the ground to prevent rebound when the blast occurred. To facilitate the anchors, four small holes of diameter 70mm was pre-cast into both slabs as shown in Figure 4.4 previously. The anchors used were SkyHook SH20 from Tighter Engineering International Pte Ltd. This model used could provide an anchoring force of up to 3 tones with an average drive depth of 1.5-4m. SH20 measured 155mm in length and 50mm in width. These anchors were earth anchors and worked on the basis of a soil cone formed which provides resistance against uplifting. Figure 4.8 illustrates this concept.

Figures 4.9 and 4.10 show the anchoring process in site. First the anchors were attached to steel cables. The anchors were then placed in the precast holes and driven in by a normal air compressor (Model No: 175). Once the desired

depth was achieved (2m), the steel cables were pulled back up by around 0.5m using an excavator. This would open up the anchor and formed the soil cone which anchored the slab. Before this was done, a steel plate was slotted thru the cable. Finally, the steel cable was cut and fixed onto the surface of the slab through a washer. Figures 4.11and 4.12 show the two slabs after anchoring was done at site. As the soil in site was strong enough, no geocell layer was put below the slabs as in the laboratory drop weight tests.

4.5 Instrumentation

Various instruments were installed onto both slabs to measure the response of the slabs during the blast. The following sensors were installed for each slab

(1)   4 accelerometers

(2)   4 strain gauges

(3)   3 soil pressure cells

(4)   2 air pressure cells.

A total of 13 sensors were monitored during each blast. Figures 4.13 to 4.18 show the instrumentation installed for both slabs. Note the alignment of the instruments with respect to each other.

The accelerometers used were from PCB, Model No. 350A13. They had a range of 10,000g. The sensing element was made of quartz housed in a stainless steel body. For the accelerometers, they were mounted onto steel frames which were then cast in-situ so as to ensure the measurement is accurate. Figure 4.19 shows the steel frame that was cast in-situ while Figure 4.20 shows the pre-fabricated L-shape sections which were screwed onto to the cast in-situ steel plates. For both slabs, air pressure cells were placed at a distance of 2m (P1) and 4m (P2) from the center of the slab. The air pressure cells used were from PCB

with Model No.101A04 as well. They had a range of 12MPa. They were mounted

on a circular plate and buried at the ground surface to ensure stability during the

blast. Figure 4.21 shows the details. Table 4.4 gives the technical specifications of

the accelerometers and air pressure cells.

Table 4.4 Technical specifications of accelerometers & air pressure Cells

Name	Model No	Range	Serial No	Coefficient	Voltage Range (DC) (V)
V1	PCB 350A13	10000g	19626	0.491 mV/g	10.9
V2	PCB 350A13	10000g	19628	0.492 mV/g	11
H1	PCB 350A13	10000g	19629	0.504mV/g	11.1
H2	PCB 350A13	10000g	19630	0.5mV/g	10.7
SL1 - P1	PCB 101A04	12MPa	5715	721.0 mV/MPa	10.1
SL1 - P2	PCB 101A04	12MPa	5717	690.6 mV/MPa	9.9
SL2 - P1	PCB 101A04	12MPa	5725	723.5 mV/MPa	9.9
SL2 - P2	PCB 101A04	12MPa	5726	721.6 m V/MPa	10.1

The soil pressures were measured using total pressure cells. They are from

Tokyo Sokki Kenkyujo Co. Ltd (TML) with measurement ranging from 500kPa to

1MPa. Table 4.5 shows the technical details of the soil pressure cells used. Table

4.6 shows the technical specifications for the strain gauges installed. The strain

gauges used were specifically for concrete. They were attached onto the four sides

of each slab to measure the strain in the concrete layers during the blast.

Table 4.5 Technical specifications for soil pressure Cells

Name	Model	Range (MPa)	Rated output	Calibration coefficient	Initial Reading after Installation on Site before Blast
			$\mu V/V$	$kPa/1 \times 10^{-6}$	$\times 10^{-6}$
SL1-T1	KDE-1MPA	1	477	1.05	1980
SL1-T2	KDE-500KPA	0.5	546	0.458	763
SL1-T3	KDE-500KPA	0.5	544	0.46	635
SL2-T1	KDE-1MPA	1	475	1.05	1089
SL2-T2	KDE-500KPA	0.5	482	0.519	1687
SL2-T3	KDE-500KPA	0.5	618	0.405	1013

Table 4.6 Technical specifications for strain gauges

Name	Model	Gauge Resistance (Ω)	Gauge Factor (%)	Gauge Length (mm)	Initial Reading (με)
SL1-S1	PL-60-11	120±0.3	2.12±1	60	408
SL1-S2	PL-60-11	120±0.3	2.12±1	60	130
SL1-S3	PL-60-11	120±0.3	2.12±1	60	272
SL1-S4	PL-60-11	120±0.3	2.12±1	60	22
SL2-S1	PL-60-11	120±0.3	2.12±1	60	-40
SL2-S2	PL-60-11	120±0.3	2.12±1	60	583
SL2-S3	PL-60-11	120±0.3	2.12±1	60	356
SL2-S4	PL-60-11	120±0.3	2.12±1	60	202

4.6 Test Results and Discussion

This part will discuss the results obtained from the field trial tests. The physical observations and instrumentation results will be presented here.

4.6.1 Experimental results of normal concrete pavement slab

4.6.1.1 Physical observations for normal concrete pavement slab

Figures 4.22 and 4.23 show the damaged Slab 1 after the blast. As seen, *the slab experienced complete failure with the blast load punching through the whole slab.* Large cracks propagated from the center of the crater radiating outwards, which was caused by the compressive stress wave from blast event. The crater diameter was around 1.2m with a depth of around 300mm which was deeper than the 275mm thickness of the Slab 1. This could be witnessed by some of the soil below the slab being blown away by the blast loading. Some cracks propagated through the whole depth of the slab resulting in the slab being broken into a few pieces. The large cracks on the slab implied a sudden and brittle failure which was undesired. Various sizes of concrete fragments were also found

throughout the area surrounding the slab. These fragments could also cause damage and injury to people and equipment. The blast also destroyed one of the anchoring cables. Such severely damaged pavement would need to be extensively repaired with the entire damaged concrete portion removed. This repair might be more time consuming.

4.6.1.2 Instrumentation results for normal concrete pavement slab

The instrumentation plan and bomb location for Slab 1 is shown in Figure 4.24.

a) Accelerometers

There were 4 numbers of accelerometers installed on Slab 1, marked as H1, H2, V1 and V2. 'H' indicated the accelerometer measuring horizontal acceleration, while the 'V' indicated the accelerometer measuring vertical acceleration of the slab.

The measured results of the 4 accelerometers are summarized in Table 4.7. Table 4.7 reports the peak acceleration and its arrival time of the accelerometers. From the arrival time, it was clear that while all 4 accelerometers recording almost the same first arrival time of 47.25-47.75 ms, the slightly earlier arrival time for H2 was consistent with the position of the bomb being placed slightly close to the side of H2. From Table 4.7, it is also shown that the peak accelerometer recorded at V1 and V2 were practically the same. This was because the bomb was placed symmetrically with respect to V1 and V2, thus having the same distance to V1 and V2. It also indicated that peak acceleration at H2 was much larger than that at H1; this was probably due to the placement of the bomb where its center of gravity for the explosive part was closer to H2 than H1, as shown in Figure 4.22.

Table 4.7 Peak acceleration recorded in Slab 1

	V1	V2	H1	H2
Peak reading (m/s^2)	-21480	-22820	-14820	-60450
Arrival time (ms)	47.58	47.75	47.75	47.25
	+**ve** upward /-**ve** downward		+**ve** toward face B /-**ve** toward face A	

Figures 4.25 and 4.26 show the vertical acceleration recorded in V1 and V2. Double integration of the acceleration was done to obtain the plots of Figure 4.27 which shows the displacement of the slab during the blast. The displacement graph showed that both Face A and Face B sides moved downwards by around the same amount. It was envisaged that there were some relative displacements between the center of the slab and the edges of the slab. This relative displacement of the sides and edges might cause tensile force which would lead to transverse cracks developed from the bottom of the slab.

Figure 4.28 and 4.29 show the horizontal acceleration recorded in H1 an H2. It should be noticed that peak value of H2 was higher than that of H1. This was probably due to the arrangement of the bomb which had been mentioned previously. Double integration of the acceleration was done to obtain the plot of Figure 4.30 which shows horizontal displacement of the slab during the blast event. It was shown that there are some relative displacements among two edges, and this difference in horizontal displacement results in shear developing in the slab.

b) Strain Gauge

The instrumentation plan for Slab 1 is shown in Figure 4.24. There were 4 numbers of strain gauges installed on Slab 1, marked as SG1, SG2, SG3 and SG4. The measured peak strain recorded for the 4 strain gauges are summarized in Table 4.8. Table 4.8 reports the peak strain recorded in the test. From the table, it could be seen only 2 strain gages (SG 1 and SG 4) recorded the data, others did not have data since it might be instant damaged when the blast occurred.

Table 4.8 Peak strain recorded in Slab 1

	SG 1	SG 2	SG 3	SG 4
Peak reading (%)	-0.12	---	---	0.18
	(+ve tension **/-ve** compression**)**			

Figure 4.31 gives the detailed strain-time history for SG 1 and 4. It was observed that SG1 readings was fluctuating between the tension (+ve) and compression (-ve) phase, which indicated the propagation of wave from top to bottom and reflected from the bottom, which caused continuously change in the bending pattern of the slab. This in turns led to transverse cracks developing through the depth of slab. SG 4 started to increase at around 48ms. The rear face of the slab in Figure 4.22 showed clearly that the rear face was more significantly damaged than the other faces. It could be seen from the SG4 readings, this face was subjected to a high tensile force over a long duration. After 52ms, SG 4 suddenly increased drastically which implied it was damaged.

c) Air Pressure Cell

The layout of air pressure cell for Slab 1 is shown in Figure 4.32. There were two air pressure cells placed with the distance of 2000mm (P1) and 4000mm (P2) from the center of slab.

The measured results of these 2 air pressure cell are summarized in Table 4.9. Figure 4.33 shows the detailed air pressure-time history for these 2 air pressure cells. It was clear that the air pressure measured in the P1 was greater than that of P2 which was consistent with the typical blasting wave propagation in the air where the blast wave intensity decays with distance and time. For Slab 1, it should be noticed that this concrete material could be seen as a rigid reflector, and hence enhanced the source energy that propagates radically from the center of explosive. Arrival time of the peak air pressure also showed that the blast wave had taken around 2ms to travel a distance of 2m, giving an approximate wave propagation speed of 1000m/s in air. This was consistent with the shock front velocity estimated from CONWEP. Note that there was a 2nd peak of air pressure at about 1ms after the 1st peak for P1. This could be due to the reflection of the compression wave from the edge of the slab.

Table 4.9 Peak air pressure recorded in the test of Slab 1

	Air Pressure 1	Air Pressure 2
Peak reading (MPa)	2.2	0.4
Arrival time (ms)	48.55	50.79

d) Total Pressure Cell

The instrumentation plan for Slab 1 is shown in Figure 4.24. There were 3 numbers of total pressure cells placed under the Slab 1, marked as TPC1, TPC2 and TPC3.

The measured results of these 3 total pressure cells are summarized in Table 4.10. Table 4.10 reports the peak total pressure recorded in the test. TPC1 was no reading since it was directly under the center of the slab and might be destroyed by the blast event. The peak reading of TPC 2 was higher than that of TPC 3 as TPC3 was further from the center of explosive.

Table 4.10 Peak total pressure recorded in the Slab 1

	TPC 1	TPC 2	TPC3
Compression peak reading (kPa)	---	178	152

Figure 4.34 shows the detailed pressure-time history for TPC 2 and 3. It was also found that the reaction time of TPC 2 was earlier than that of TPC 3 as it was closer to the center of explosive. From Figure 4.34, it is seen that the peak pressure for TPC 2 was +178kPa which meant that compression pressure of 178kPa was acting on TPC 2. After the peak reading, TPC 2's reading suddenly went negative and reached -1500kPa. It should be noted that this indicated a situation where a sudden suction force was exerted on TPC 2. However, the actual suction force value might not be calibrated as the TPCs were calibrated based on compression force only. Subsequently TPC 2 showed fluctuation of the +ve and −ve values, indicating that the slab was vibrating, alternating between pressure and uplifting of the slab. The peak pressure for TPC 3 was +152kPa which meat that compression pressure of 152kPa was acting on the TPC 3. After that, vibration of the slab occurred and the pressure fluctuated around zero position.

4.6.2 Experimental results of proposed multi-layers pavement slab

4.6.2.1 Physical observations for proposed multi-layers pavement slab

Figures 4.35 to 4.38 show Slab 2 after the blast. From Figure 4.35, it can be seen that the blast loading destroyed the upper section of the asphalt layer above the geogrid reinforcement. The asphalt layer was still largely intact below the geogrid. This showed that geogrid served its purpose of increasing the tensile strength of asphalt and reducing the damage to the asphalt layer by confining it. The geogrid piece was still largely intact despite the crater created by the blast.

The center of the geogrid piece was burned off during the blast event. Figure 4.37 shows the resulting damage more clearly with the top section of asphalt removed.

The whole asphalt layer was then removed to clearly assess the damage to the bottom 2 layers of HSC & ECC. As seen in Figure 4.38, ***the crater was very shallow and did not punch through the whole layer.*** The bottom ECC layer was still intact. The cracks formed around the crater were small and evenly distributed. This showed that the high ductility of ECC enabled it to deform during the blast and thus redistributed the blast loading evenly. This could be seen as the ductile failure. Despite asphalt being much weaker compared to normal strength concrete, it was able to take a significant amount of the blast load, thereby reducing the amount of damage to the HSC layer below. Thus, the asphalt layer seemed to act as a sacrificial layer. It should be noticed that the asphalt layer could be very easily repaired and there was no need for the bottom two layers to be replaced after the blast event. A crater of around 0.7 m diameter and depth of 10 mm was formed on the HSC layer (Figure 4.38). There was also minimal debris found on site. The asphalt layer was able to reduce the amount of dangerous concrete fragments formed. Only some pieces of asphalt were found around the slab. Even so, these asphalt pieces were much softer compared to concrete. Despite the fact that the casting for Slab 2 was not consistent and the strength of the HSC and ECC obtained was lower than what was designed for, Slab 2 performed very well. This proved that the concept of this new pavement design and materials.

4.6.2.2 Instrumentation results for proposed multi-layers pavement slab

The instrumentation plan and bomb layout for Slab 2 is shown in Figure 4.39.

a) Accelerometers

There were 4 numbers of accelerometers installed on Slab 2, marked as H1, H2, V1 and V2. 'H' indicated the accelerometer measuring horizontal acceleration, while the 'V' indicated the accelerometer measuring vertical acceleration of the slab.

Table 4.11 reports the peak acceleration and its arrival time of the accelerometers. From the arrival time, it was clear that while all 4 accelerometers recording almost the same first arrival time of 31.3-31.5 ms. This indicated that the center of gravity of the bomb was right at the center of the 2.8m by 2.8m pavement slab. From Table 4.11, it is also shown that the peak accelerometer recorded at V1 and V2 are 35400m/s^2 and 29284 m/s^2 respectively. It was noted that the bomb was placed symmetrically with respect to V1 and V2. The difference peak acceleration between V1 and V2 might be due to the imperfect casting of Slab 2. It was also found that peak acceleration at H2 was much larger than that at H1; this was despite the placement of the bomb at equal distance to H2 than H1, as shown in Figure 4.39. The higher peak horizontal acceleration could be due to the imperfect compaction and casting of Slab 2 as well. The higher value at H2 was also consistent with the observation that a lot more tension cracks were found at this face (rear face) as compared to the other 3 sides as seen in Figure 4.37.

Table 4.11 Peak acceleration recorded in Slab 2

	V 1	V 2	H 1	H 2
Peak reading (m/s^2)	-35400	-29284	18690	36640
Arrival time (ms)	31.5	31.5	31.5	31.3
	+ve upward /**-ve** downward		**+ve** toward Face B /**-ve** toward Face A	

Figure 4.40 and 4.41 show vertical acceleration recorded in V1 and V2. It was noticed that the signal for V1 after 31.8ms was not considered due to damage of the connection after that point. Double integration of the acceleration V2 was done to obtain the plot of the displacement of the slabs during the blast event as shown in Figure 4.42. It could be seen that the slab was moving downward at about 0.038 m, which was slightly higher than that from Slab 1. This indicated that Slab 2, which was made up of ECC, HSC and asphalt layers, was much better in absorbing the energy of the blast compared to Slab 1. The ECC layer was able to deform more (higher ductility) and the HSC layer was able to absorb a high amount of blast energy.

Comparing with the vertical acceleration for Slab 1 and Slab 2, it was found that the vertical acceleration of Slab 2 was slight higher (29284 – 35000m/s^2) than that of Slab 1 (21000 – 22000m/s^2). This was probably due to the weight of Slab 2 being lighter than Slab 1. Table 4.12 gives the density, volume and weight of the cast materials in Slab 1 and Slab 2. The weight for Slab 2 in Table 4.12 was an overestimation as during the casting of Slab 2, no vibration was done due to the limited site resources. Thus the actual weight of Slab 2 was even lower than 4500kg. Despite the lower weight and higher acceleration of Slab 2, the damaged situation for Slab 2 was still much better that Slab 1. This again showed the good absorption of blast energy by Slab 2.

Table 4.12 Density, volume and weight for Slab 1 and Slab 2

	Components	Density (kg/m^3)	Volume (m^3)	Weight (kg)
Slab 1	Normal Concrete	2400	2.8×2.8×0.275	5174.4
Slab 2	HSC	2400	2.8×2.8×0.1	4894.1
	ECC	2080	2.8×2.8×0.1	
	Asphalt	2350	2.8×2.8×0.075	

Figure 4.43 and 4.44 show horizontal acceleration recorded in H1 and H2. It should be noticed that peak acceleration of H2 was higher than that of H1. This was probably due to the arrangement of the bomb which had been mentioned previously. Double integration of the acceleration was done to obtain the plot of Figure 4.45 which shows the displacement of the slabs during the blast event. From the figure, it is shown that the slab was first going towards Face B and then moving towards Face A by around the same amount.

Comparing with the horizontal acceleration results for Slab 1 (H1=14820 m/s^2 & H2=60450 m/s^2) and Slab 2 (H1=18690 m/s^2 & H2=36640 m/s^2), it was found that the H1 value for Slab 2 was higher than that for Slab 1. This was because for the same explosion, a lighter mass of Slab 2 had a higher acceleration than a heavier mass of Slab 1. The anchor close to H2 in Slab 1 was destroyed by blasting during the Slab 1 test which led to higher horizontal acceleration in H2 in Slab 1, than that of Slab 2, of which all four anchors were intact after the blast. Despite the higher acceleration for Slab 2, it performed significantly better since it was the new pavement material instead of normal concrete.

b) Strain Gauge

The instrumentation plan for Slab 2 is shown in Figure 4.39. There were 4 numbers of strain gauges installed on Slab 2, marked as SG1, SG2, SG3 and SG4.

The measured peak strain recorded for the 4 strain gauges are summarized in Table 4.13. The strain gauge 2 (SG 2) had no reading during the blast event. It should be noticed that all strain gages for Slab 2 were attached at the ECC layer of Slab 2 while the strain gage for Slab 1 was attached directly to the single layer of concrete. Comparing with the peak strain recorded for Slab 1 and Slab 2, it was found that strain measured for Slab 2 was higher than that for Slab 1 which was consistent with characteristics that ECC was much more ductile compared to normal concrete.

Table 4.13 Peak strain recorded in Slab 2

	SG1	SG2	SG3	SG4
Peak reading (%)	0.4	---	0.1	0.22
(+ve tension **/-ve** compression)				

Figure 4.46 shows the detailed strain-time history for SG 1, 3 and 4. From the figure, it is showed that the arrival time for these 3 strain gauges was around 31.75 ms and the tensile strains (+ve) were recorded. This implied that the faces were subjected to tension force. No compressive strain was recorded during the blast event for Slab 2, indicating that Slab 2 could absorb most of the impounding energy due to the ductile nature of the asphalt and ECC layer. Yet despite this high tensile strain in the ECC layer, Slab 2 performed better than Slab 1.

c) Air Pressure Cell

The layout of air pressure cell for Slab 2 is shown in Figure 4.48. There were 2 numbers of air pressure cell placed at a distance of 2000mm (P1) and 4000mm (P2) from the center of slab.

Table 4.14 Peak reading of air pressure for Slab 2

	Air Pressure 1	Air Pressure 2
Peak reading (MPa)	0.66	0.11
Arrival time (ms)	30.83	31.45

The measured results of these 2 air pressure cell are summarized in Table 4.14. Figure 4.49 shows the detailed air pressure-time history of these 2 air pressure cells. From the table and figure, it is obvious that air pressure measured in the P1 point was greater than that of P2 point which was consistent with the typical blasting wave propagation in the air where the blast wave intensity decayed with distance and time.

Comparing the results of P1 and P2 between Slab 1 and Slab 2, it was found that the air pressure measured in P1 and P2 for Slab 2 was much lower than that measured for Slab 1. One reason for this result was that the air pressures for Slab 2 were placed with alignment to the bomb rear part which included less charge (as shown in Figure 4.48), while for Slab 1 the air pressures were arranged with perpendicular to the bomb center part which had more charge (as shown in Figure 4.32). This might cause higher reading of the P1 and P2 from Slab 1. The blast pressure was first released with non-circular wave, and then with the increase of the distance from the detonation center became circular one. Hence, as for the P1, the values from both slabs had different magnitude, while for the P2, the value from both slab arrived same magnitude. In addition to above reason, the fact that Slab 2 was more flexible than Slab 1 might cause the P1 and P2 for Slab 2 having lower reading than that for Slab 1. The ECC component in Slab 2 was able to absorb more energy from the explosive and hence reduce the source energy which propagated radially from the center of explosive. Despite the higher absorption of the blast wave by Slab 2, the crater formed in Slab 2 was smaller and shallower than that of Slab 1. This was a combination of the positive effect of high strength concrete having high penetration resistance coupled with ECC

having high ductility. These results again demonstrated the promising application of this new pavement material.

d) Total Pressure Cell

The instrumentation plan for Slab 2 is shown in Figure 4.39. There were 3 numbers of total pressure cells placed under Slab 2, marked as TPC1, TPC2 and TPC3.

The measured results of these 3 total pressure cells are summarized in Table 4.15. TPC 1 was damaged at the instant where the blast occurs, probably due to the cutting of the connection wire. It was also observed that the peak reading of TPC2 was higher than that of TPC3 due to TPC2 being nearer to the center of explosive.

Table 4.15 Peak reading of total pressure cell for Slab 2

	TPC 1	TPC 2	TPC 3
Compression peak reading (kPa)	---	273	200

Figure 4.50 shows the detailed pressure–time history for TPC 2 and 3. From the figure, it is shown that the arrival time of TPC 2 was earlier than that of TPC 3 due to TPC 2 being closer to the center of explosive. It was shown that the peak pressure for TPC 2 was +273kPa. After peak reading, the TPC 2's reading went downward which meant the slab rebound from the ground. This trend leaded to the suction pressure about 800kPa. Subsequently TPC2 demonstrated fluctuation of the +ve and −ve values, indicating that the slab was vibrating, alternating between pressure and uplifting of the slab.

The peak pressure of TPC 3 was +200kPa. This peak reading occurred at around 32.3ms. TPC 3 then experienced the uplifting of the slab resulting in a

suction force of around. After which TPC3 readings were not logical probably due to the cutting of the connection wires.

4.6.2.3 Discussion

Based on the field trial test results, it was found that the normal concrete pavement Slab 1 was severely damaged with the whole depth being punched through. Large cracks propagated through the whole depth of the slab and significant amount of debris was found throughout. It seemed to suffer brittle and sudden failure. The crater formed had a diameter of 1.2m and 300mm depth. A pavement with this type of severe damage would need to be completely replaced as it was no longer feasible to repair.

For Slab 2, which was the proposed multi-layers pavement material, the damage was confined to the top asphalt layer and a small portion of the second layer which is the HSC layer. The crater is found to be having a diameter of 0.7 m at the plan of the top of HSC layer. The crater depth is only 10 mm in HSC layer. The asphalt acted as a sacrificial layer, taking a significant amount of the blast energy, thus reducing the amount of blast energy on the HSC layer. The geogrid within the AC layer was able to increase the tensile strength of the top layer. The debris formed from the blast mainly consisted of the softer AC rather than concrete fragments. Small cracks were evenly distributed around the crater.

The instrumentation results showed that the vertical acceleration of Slab 2 was higher than that of Slab 1 (as shown in Table 4.16). Although the higher vertical acceleration of Slab 2, the damaged situation for Slab 2 was still much better than Slab 1. This showed the good absorption of blast energy for Slab 2. Comparing with the peak strain recorded for Slab 1 and Slab 2 (as shown in Table

4.17), it was found that strain measured for Slab 2 was higher than that for Slab 1 which was consistent with characteristics that ECC was much more ductile compared to normal concrete. In addition, it was found that the air pressure P1 and P2 for Slab 2 had lower reading than that for Slab 1 (as shown in Table 4.18). This is because Slab 2 was more flexible than Slab 1. The ECC component in Slab 2 was able to absorb more energy from the explosive due to its high ductility, and then reduced the source energy which propagated radially from the center of explosive. Despite the higher absorption of the blast energy by Slab 2, the crater formed in Slab 2 was smaller and shallower than that of Slab 1. This was a combination of the positive effect of high strength concrete having high penetration resistance coupled with ECC having high ductility. The test results thus clearly demonstrated the potential of the proposed multi-layer material for blast resistance.

Table 4.16 Vertical acceleration results for Slab 1 and 2

	$V1(m/s^2)$	$V2 (m/s^2)$
Slab 1 (Normal concrete pavement slab)	-21480	-22820
Slab 2 (Proposed multi-layers pavement slab)	-35400	-29284

Table 4.17 Stain gauges recorded for Slab 1 and 2

	SG 1 (%)	SG 2 (%)	SG 3 (%)	SG 4 (%)
Slab 1 (Normal concrete pavement slab)	-0.12	---	---	0.18
Slab 2 (Proposed multi-layers pavement slab)	0.4	---	0.1	0.22

Table 4.18 Peak reading of air pressure for Slab 1 and 2

	Air pressure 1 (MPa)	Air pressure 2(MPa)
Slab 1 (Normal concrete pavement slab)	2.2	0.4
Slab 2 (Proposed multi-layers pavement slab)	0.66	0.11

4.7 Conclusions on Full Scale Field Blast Trial

From the above test results, it can be postulated that during the blast event, high peak air pressure will impact the runway pavement. The high incident pressure will destroy the top material layer (AC with the inclusion of geogrid material). It was found that the AC layer was able to take a significant amount of the dynamic load at the cost of being destroyed, thereby reduce the blast energy transmitted to the following layers. For the AC layer, it was also observed that the geogrid served its purpose of increasing the tensile strength of AC layer. Hence, the blast load completely destroyed the upper section of the AC layer above the geogrid reinforcement, while remained largely intact below the geogrid. Below the AC layer, the HSC layer with excellent dynamic properties was used as the main body to sustain the pressure from blast event with very shallow crater formed at the top of the HSC layer. Due to fact that the HSC has lower tensile strength and the HSC is very brittle, the tensile cracks easily developed with sudden failure at the bottom of the HSC layer. Hence, the ECC layer with high ductility was provided as the bottom layer in the proposed multi-layers pavement. The ductile behavior will allow material to suffer large deformation without sudden failure.

Hence, it was concluded that the proposed multi-layers pavement system has a better resistance as compared to the conventional pavement system. The

concept of the multi-layers system was successfully used in the design of new pavement subjected to blast load. This new pavement design consisting of all 4 materials (HSC, ECC and AC reinforced with GST) will fully utilize their pronounced properties. From the laboratory and field trial test, it was found that this proposed multi-layers pavement design have high penetration resistance, strength, ductility and multiple resistance capability.

However, only very limited number of the field trial test has been conducted, due to the cost and available field site limitation. In order to investigate the effect of the different parameters of this proposed system (i.e. thickness of the HSC and ECC, strength of the HSC and ECC and the interface property) on its behavior, the numerical modelling should be employed. This will be discussed in Chapter 6.

Figure 4.1 M107 Placement on Slab
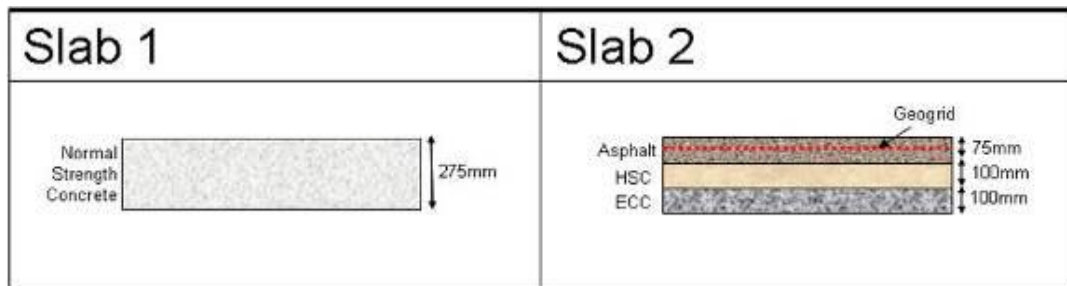
Figure 4.2 Configuration of Slabs 1 and 2
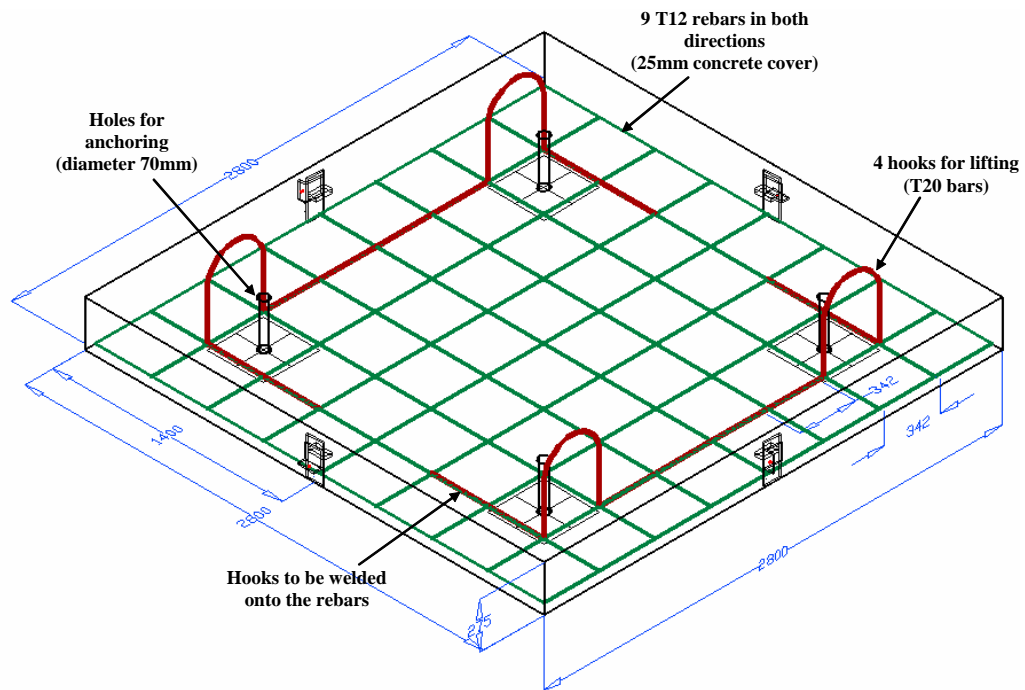
Figure 4.3 Details of reinforcement

Figure 4.4 Minimal reinforcement at bottom of slab

Figure 4.5 Completed Slab 1

Figure 4.6 Compaction of asphalt layer

Figure 4.7 Completed Slab 2
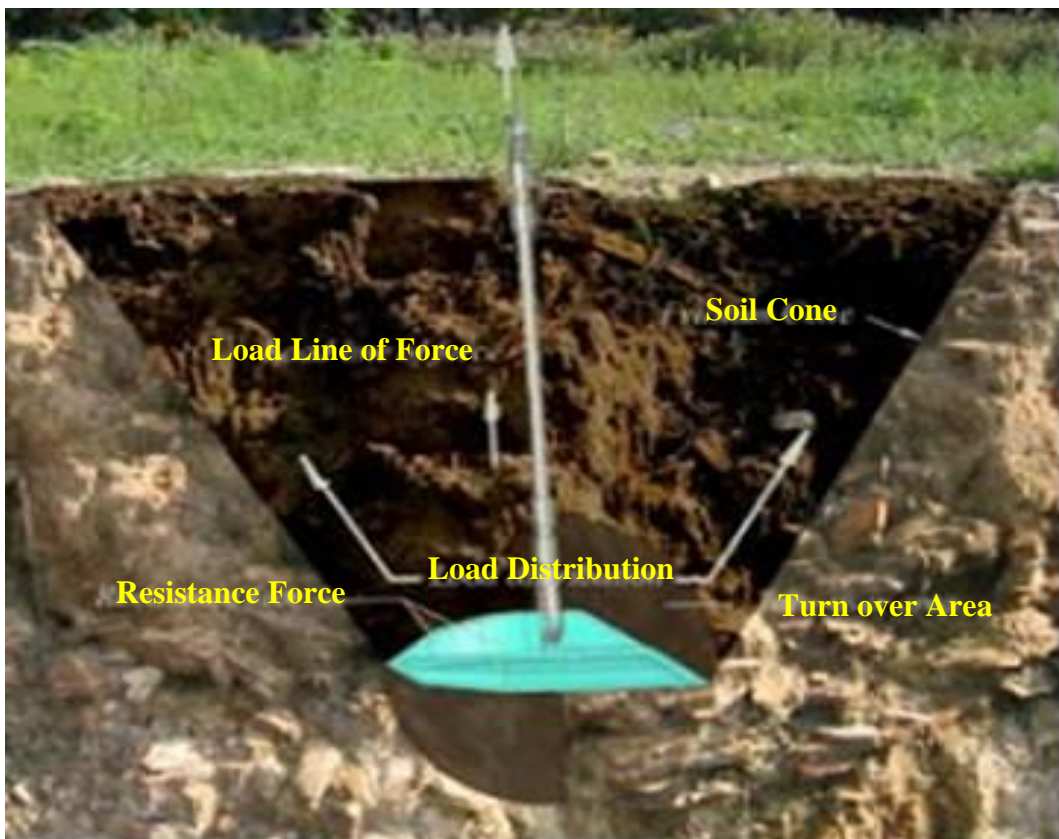
Figure 4.8 Anchoring concept

153

Figure 4.9 Attachment of steel cable to anchor & driving in of the anchor using an air compressor

Figure 4.10 Extraction of steel cable using excavator & anchoring of steel plates on surface of slab

Figure 4.11 Completed Slab 1 with anchoring at site

Figure 4.12 Completed Slab 2 with Anchoring at site
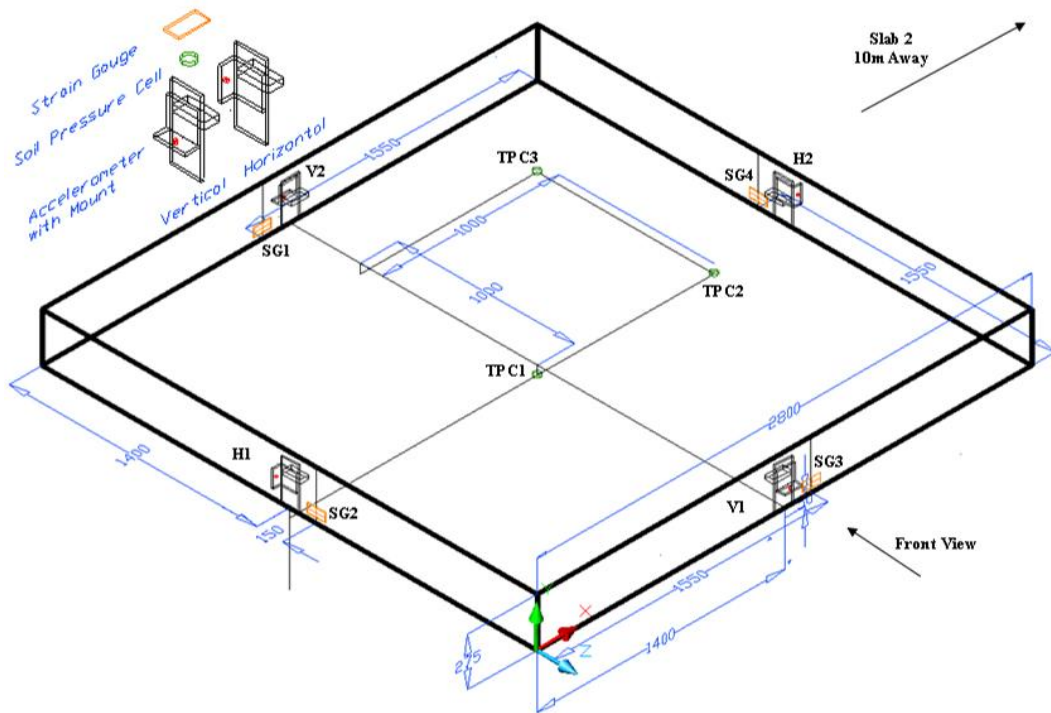
Figure 4.13 Instrumentation layout for Slab 1 (3D View)
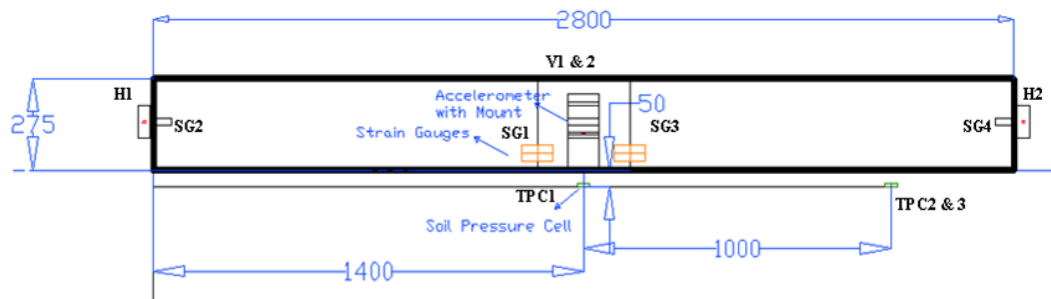
Figure 4.14 Instrumentation layout for Slab 1 (Front View)
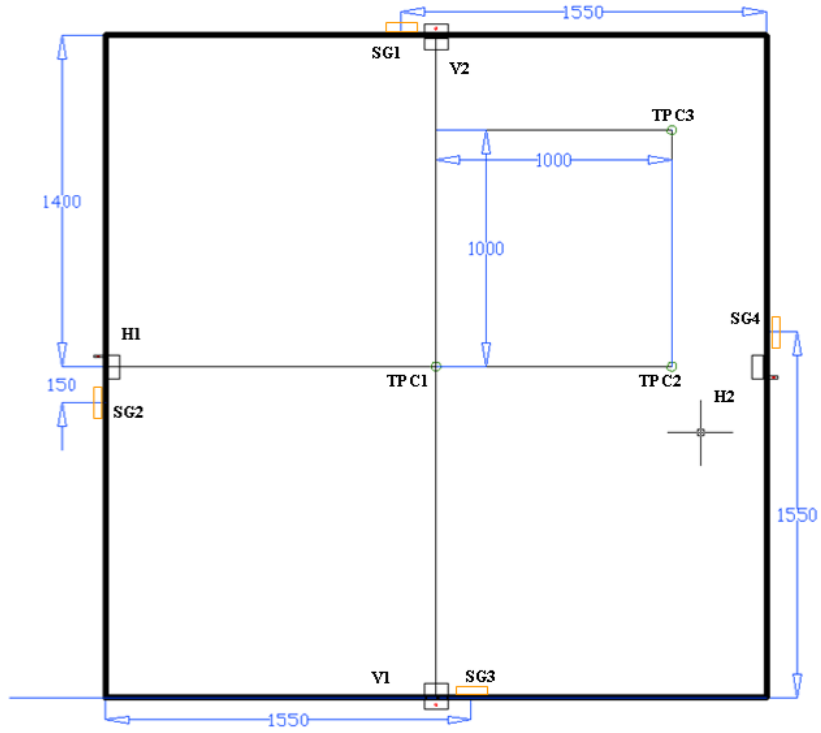
Figure 4.15 Instrumentation layout for Slab 1 (Top View)
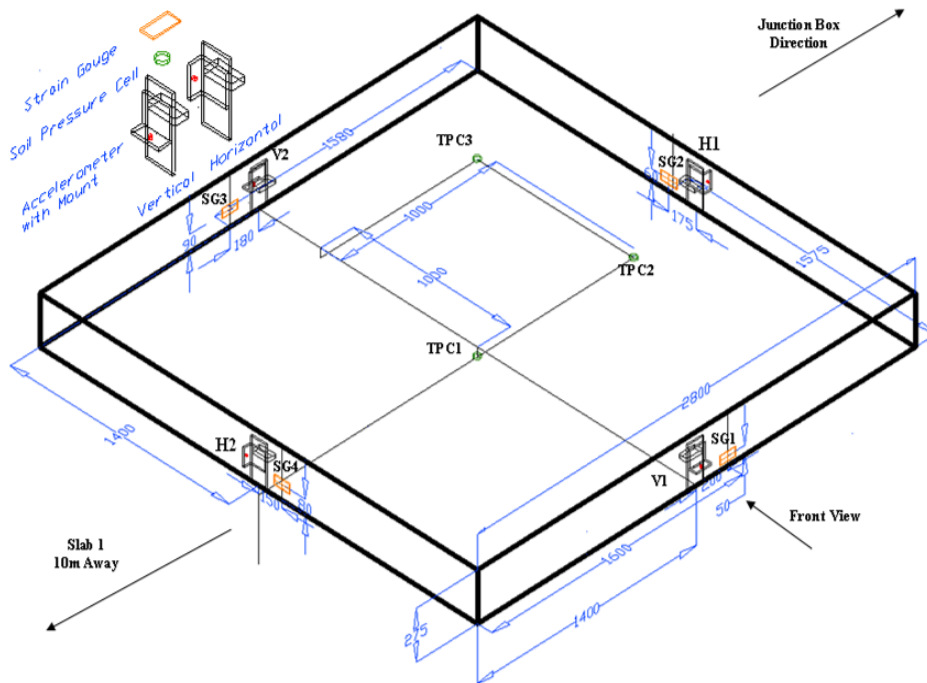
Figure 4.16 Instrumentation layout for Slab 2 (3D View)

157
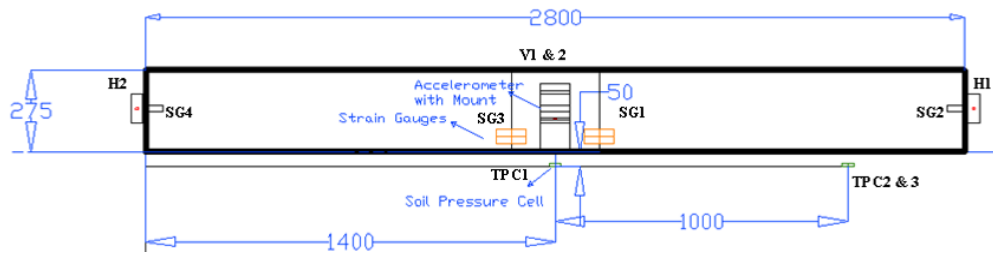
Figure 4.17 Instrumentation layout for Slab 2 (Front View)
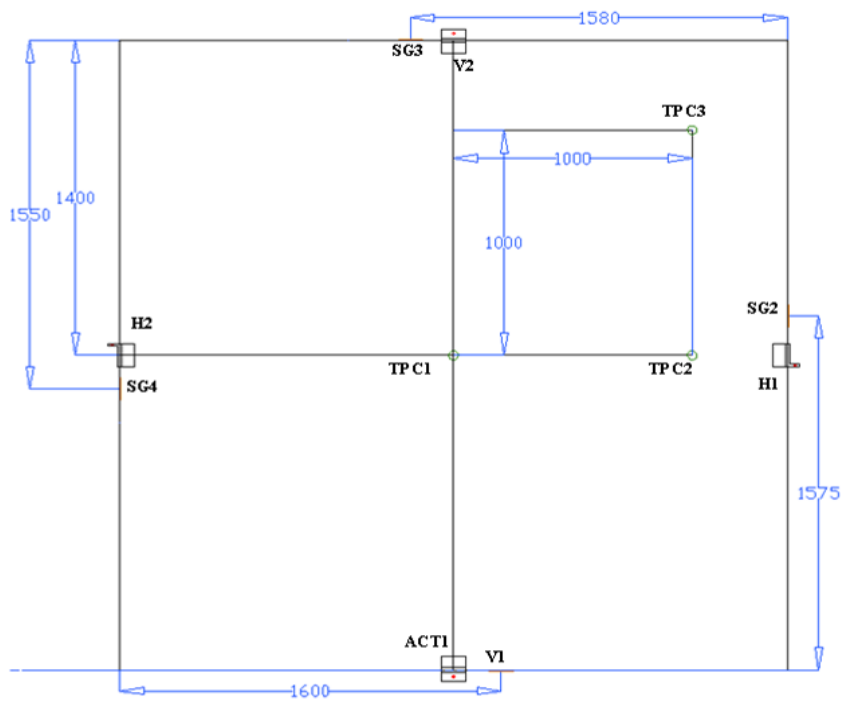
Figure 4.18 Instrumentation layout for Slab 2 (Top View)

158

Figure 4.19 Accelerometer mount cast in-situ
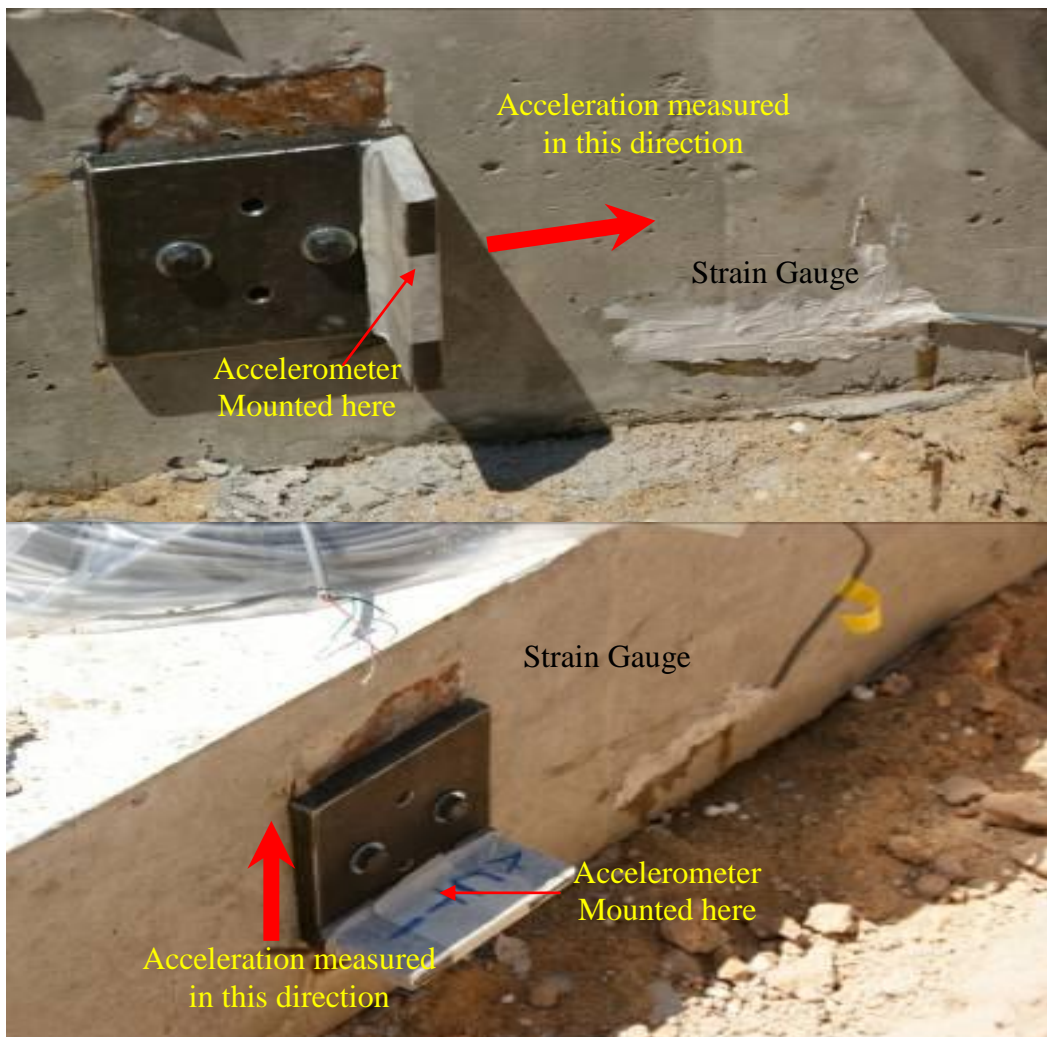
Figure 4.20 Accelerometer L-shaped plates
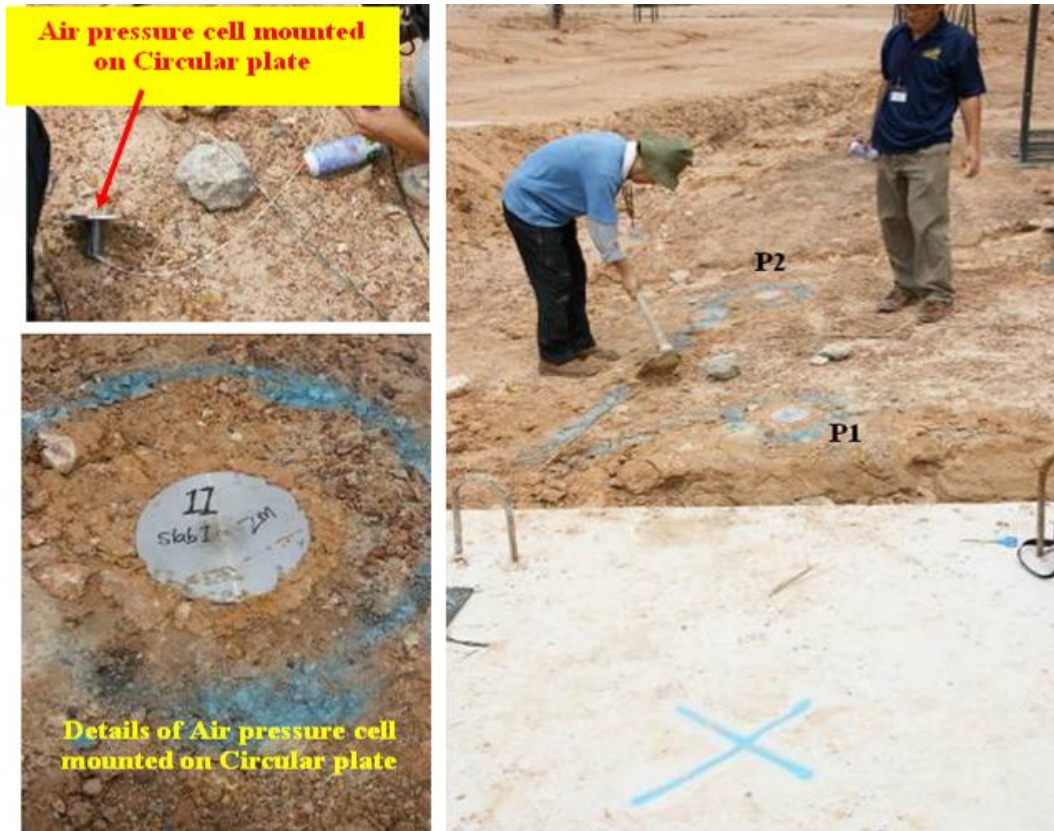
Figure 4.21 Details of installation of air pressure cells on Site

Figure 4.22 Slab 1 after blast
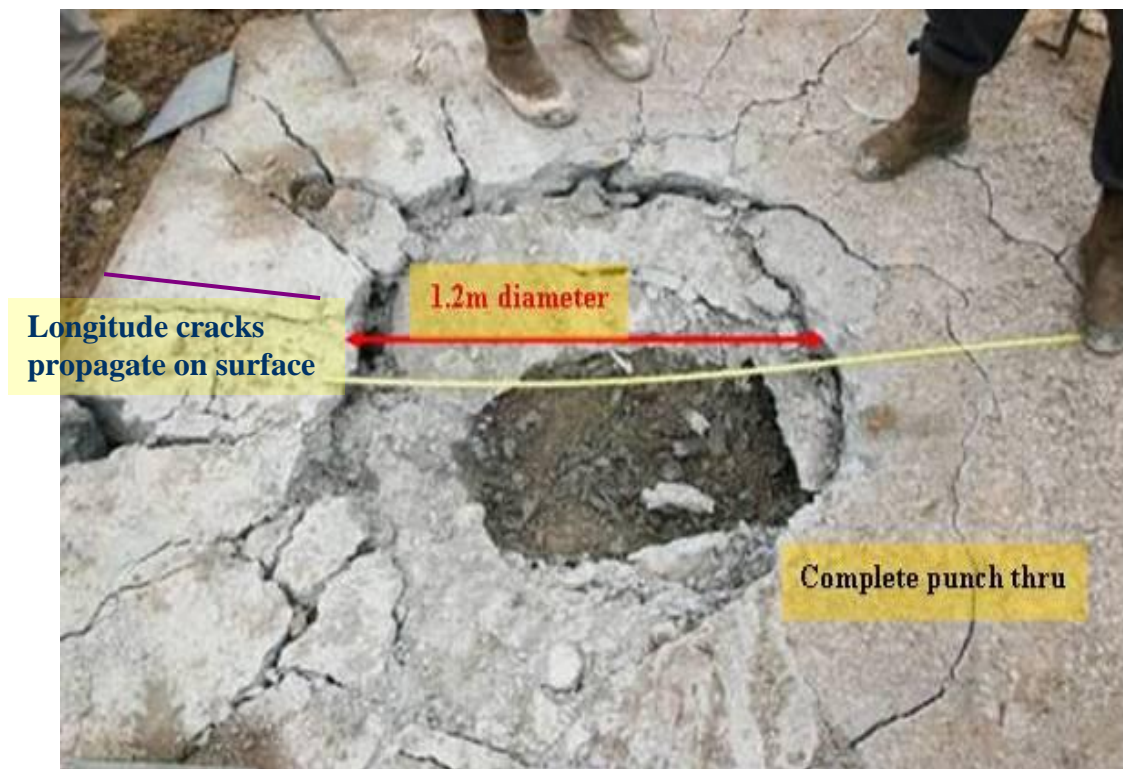
Figure 4.23 Detail of crater for slab 1
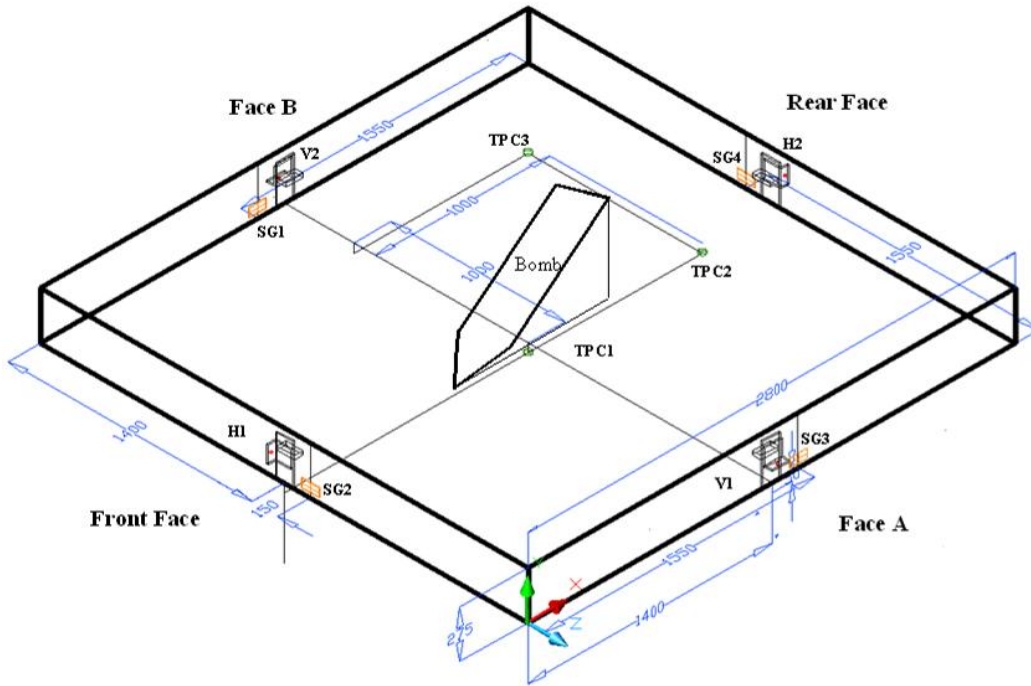
Figure 4.24 Instrumentation layout for Slab 1 (3D View)
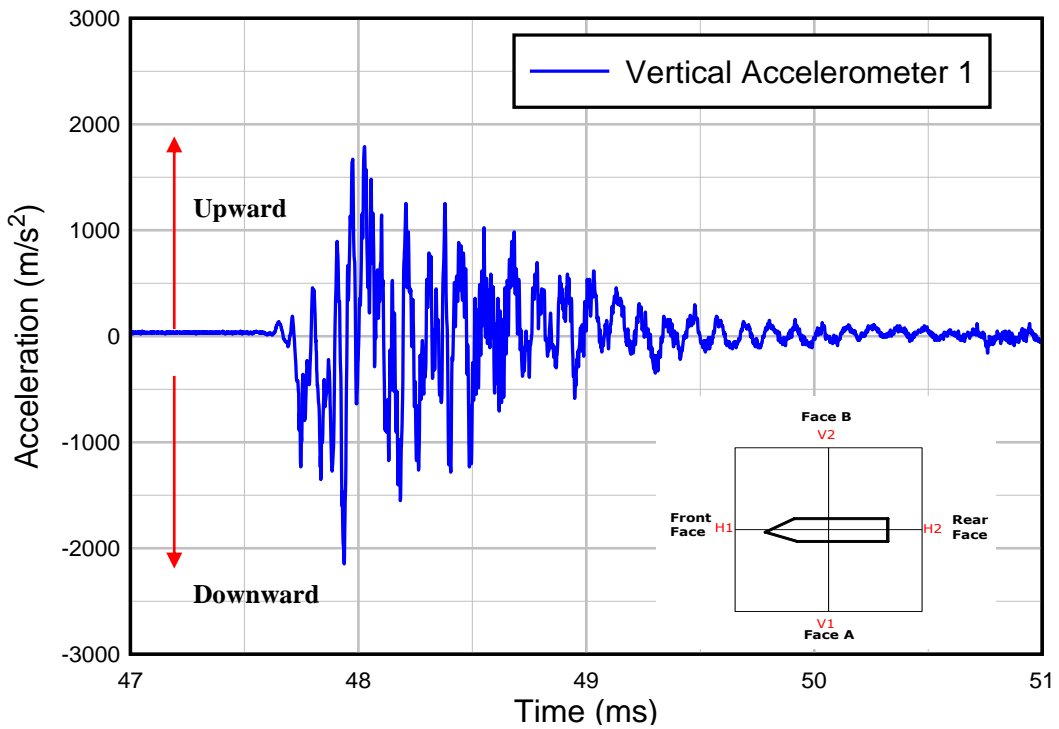
Figure 4.25 Acceleration-time history for vertical accelerometer 1 (V1)

162
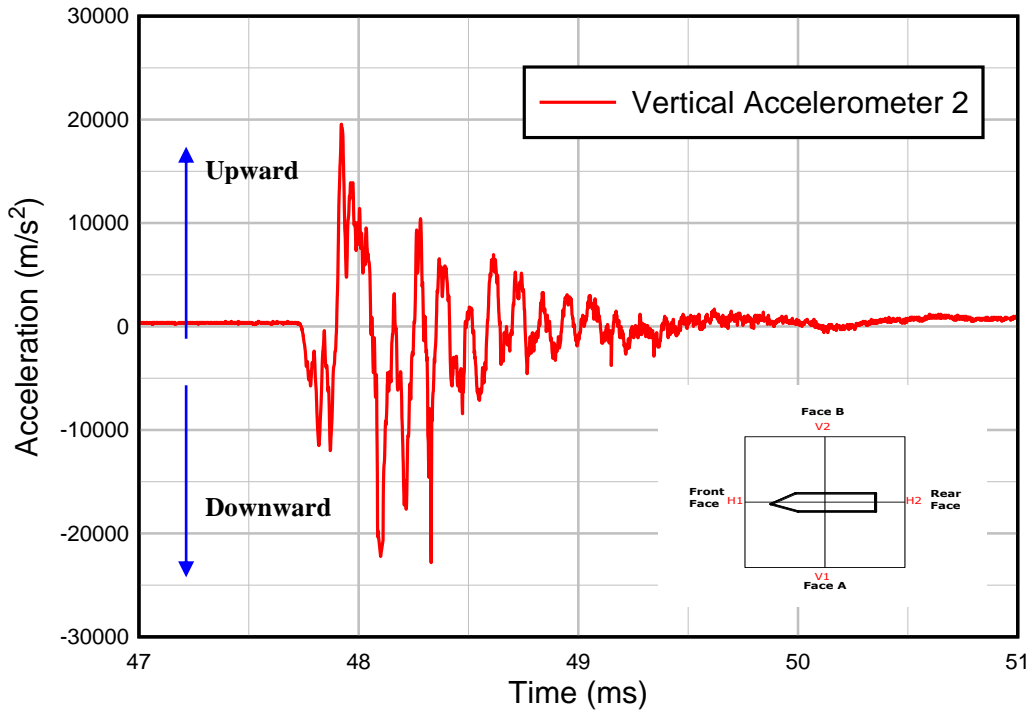
Figure 4.26 Acceleration-time history for vertical accelerometer 2 (V2)
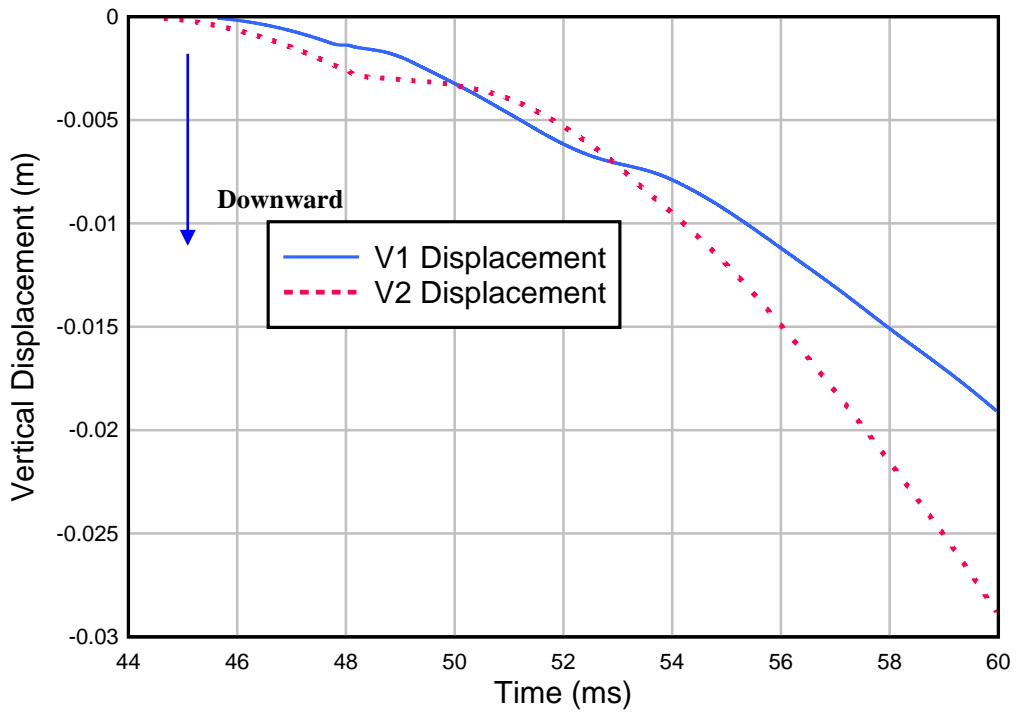
Figure 4.27 Displacement-time history for vertical accelerometers 1 & 2 (V1 & V2)

163
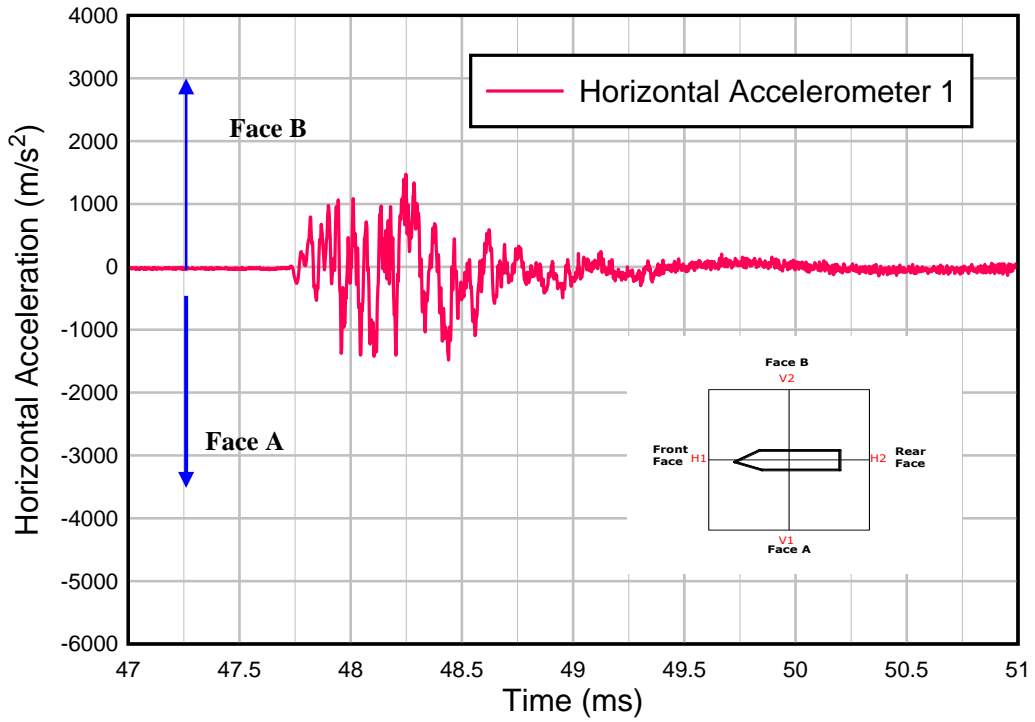
Figure 4.28 Acceleration-time history for horizontal accelerometer 1 (H1)
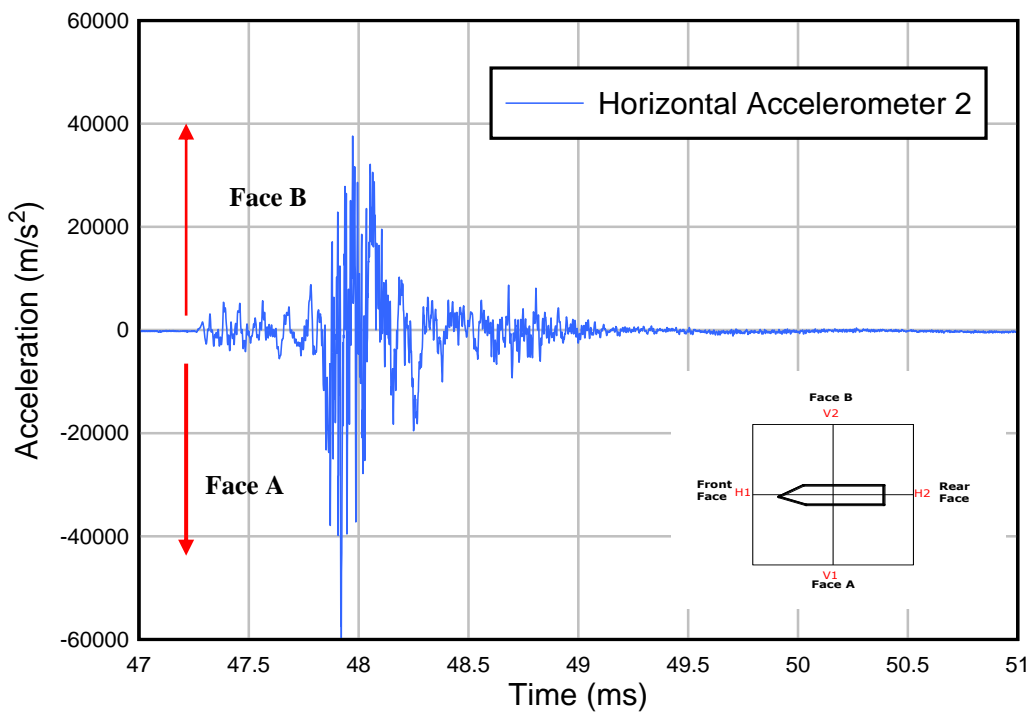
Figure 4.29 Acceleration-time history for horizontal accelerometer 2 (H2)
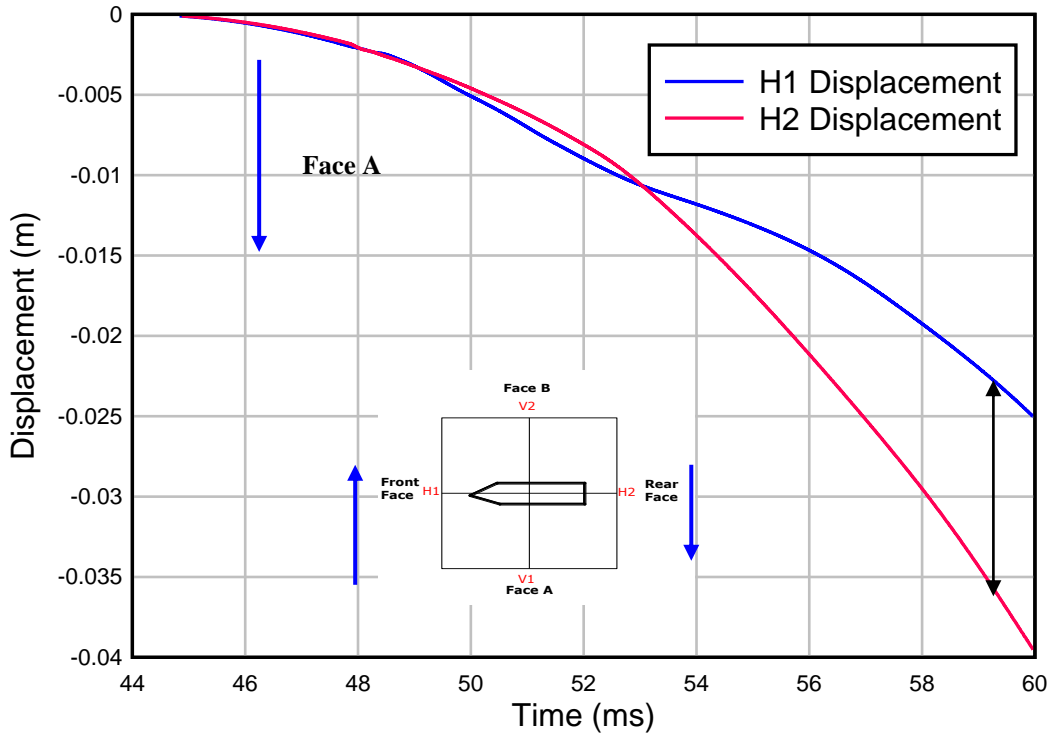
Figure 4.30 Displacement-time history for horizontal accelerometers 1 & 2 (H1 & H2)
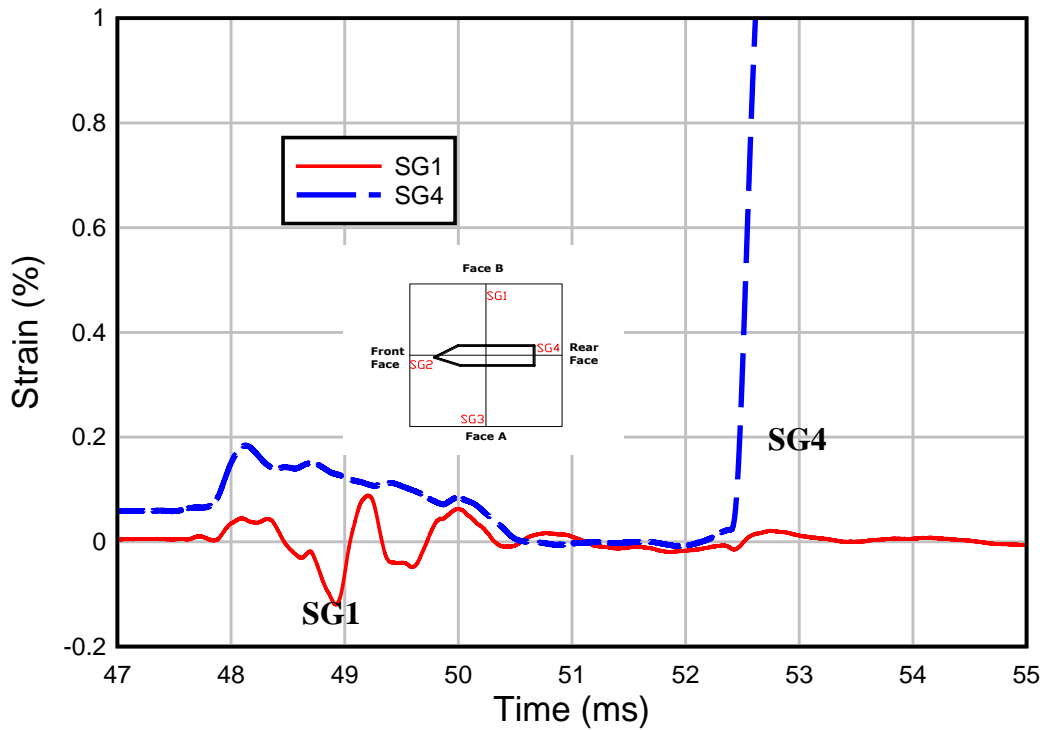
Figure 4.31 Stain-time history for strain gages (SG 1 and SG 4)
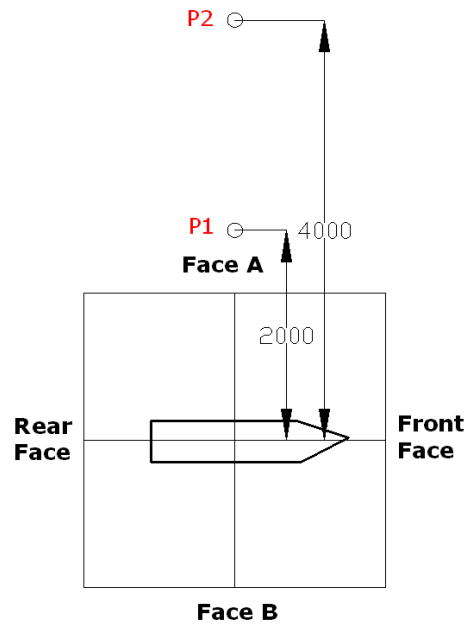
Figure 4.32 Layout of air pressure cell for Slab 1
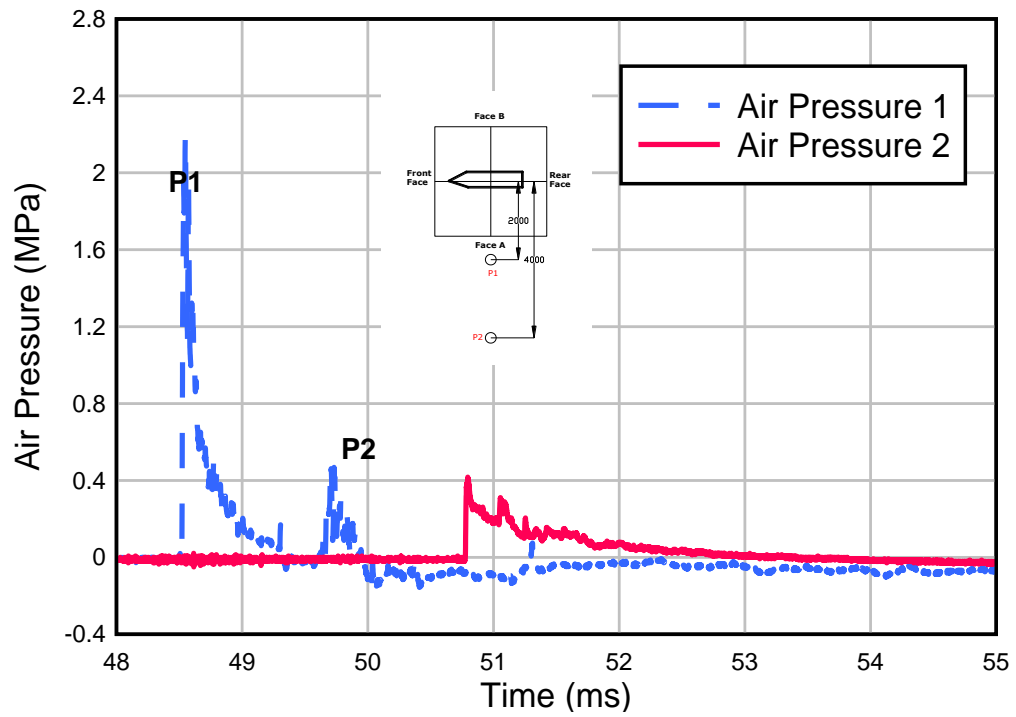
Figure 4.33 Pressure-time history for air pressure cell
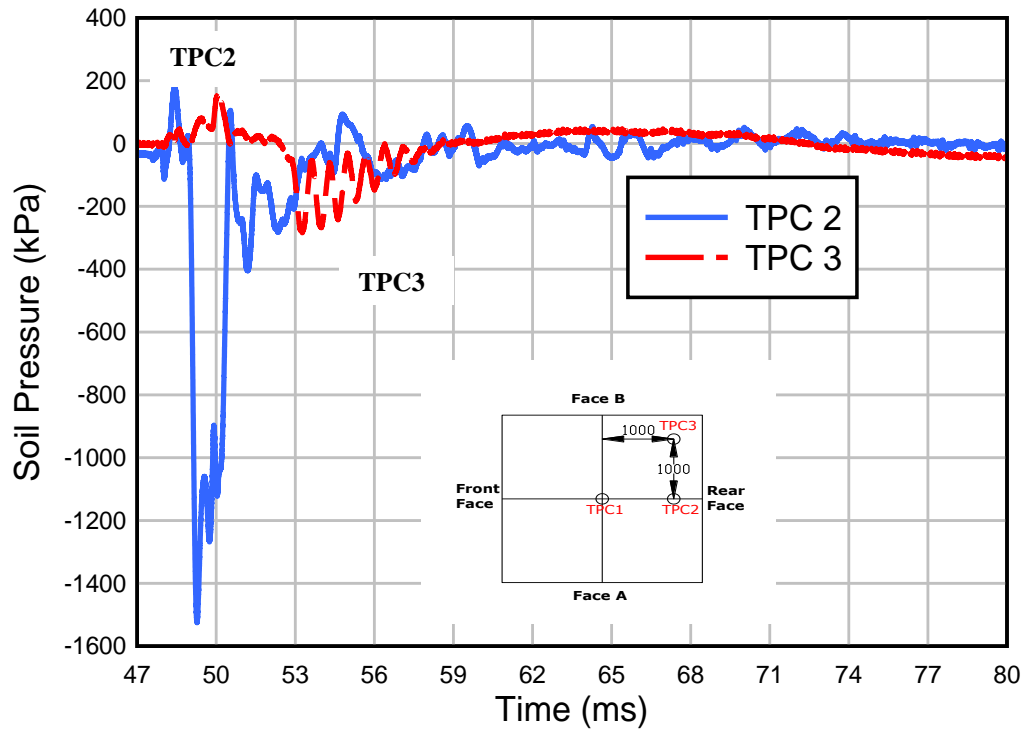
Figure 4.34 Pressure-time history for total pressure cell (TPC 2 and TPC 3)

Figure 4.35 Slab 2 after blast

167

Figure 4.36 Removal of top section of asphalt for Slab 2

Figure 4.37 Crater details for Slab 2 after removal of asphalt layer
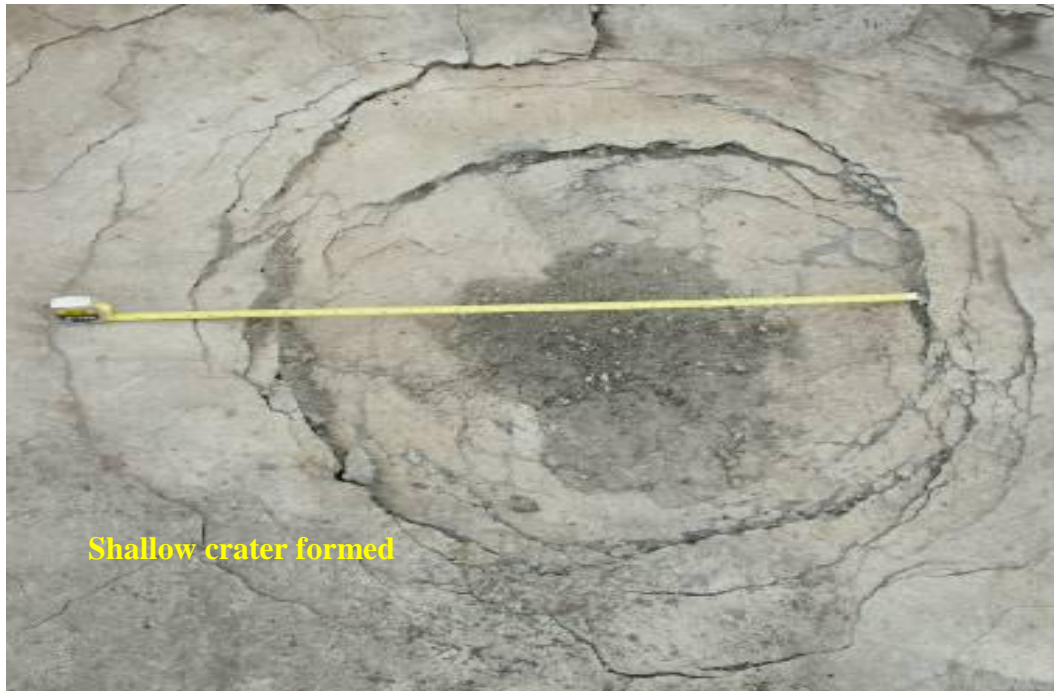
Figure 4.38 Detail of crater for Slab 2
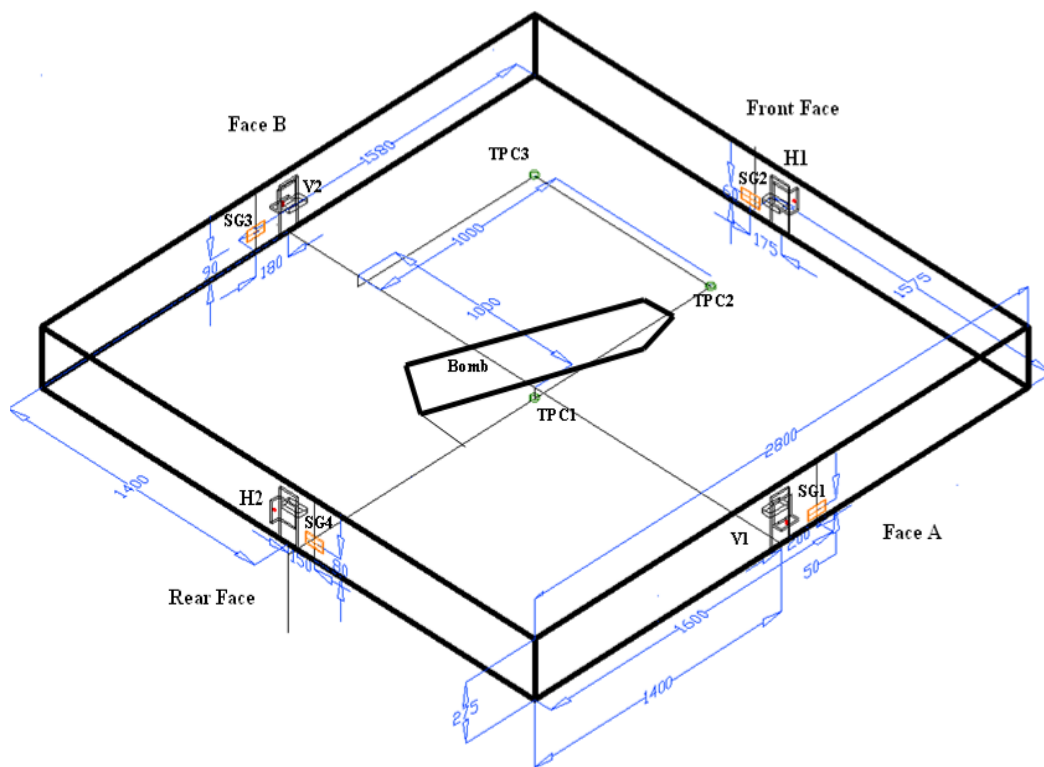
Figure 4.39 Instrumentation layout for Slab 2 (3D View)
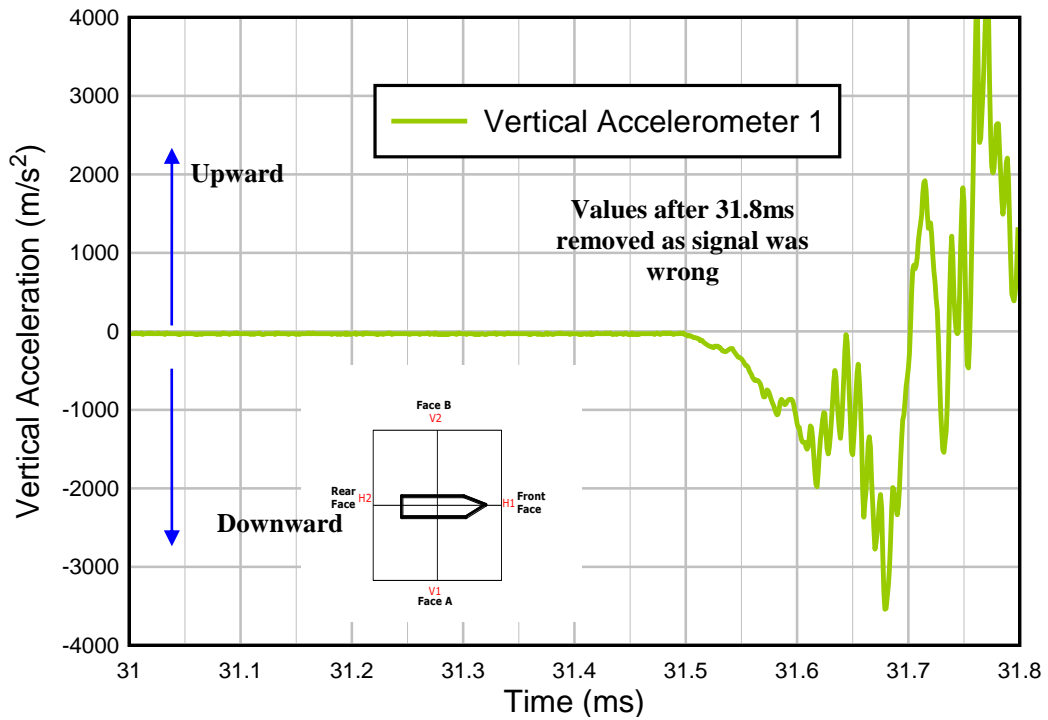
Figure 4.40 Acceleration-time history for vertical accelerometer 1 (V1)
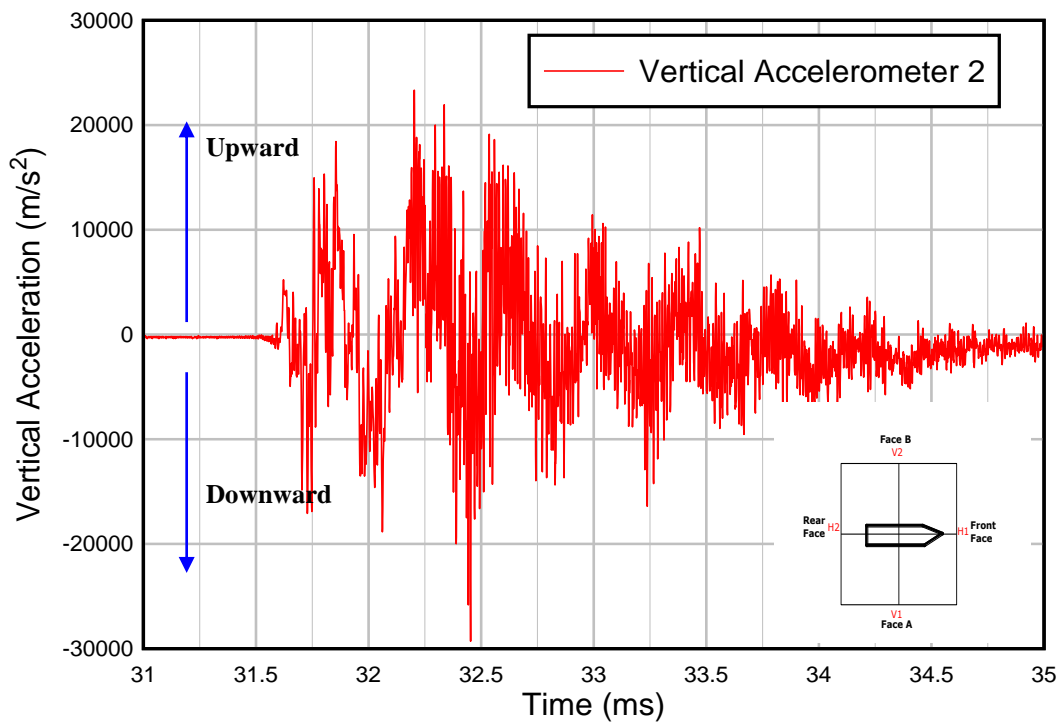
Figure 4.41 Acceleration-time history for vertical accelerometer 2 (V2)
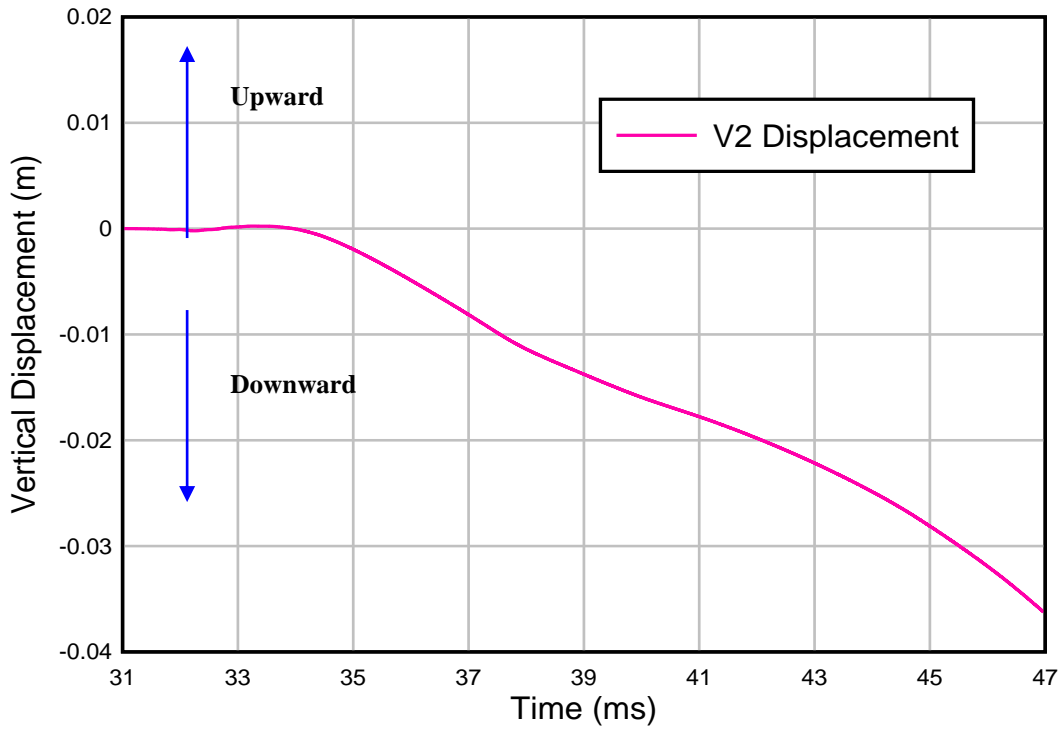
Figure 4.42 Displacement-time history for vertical accelerometers 2 (V2)
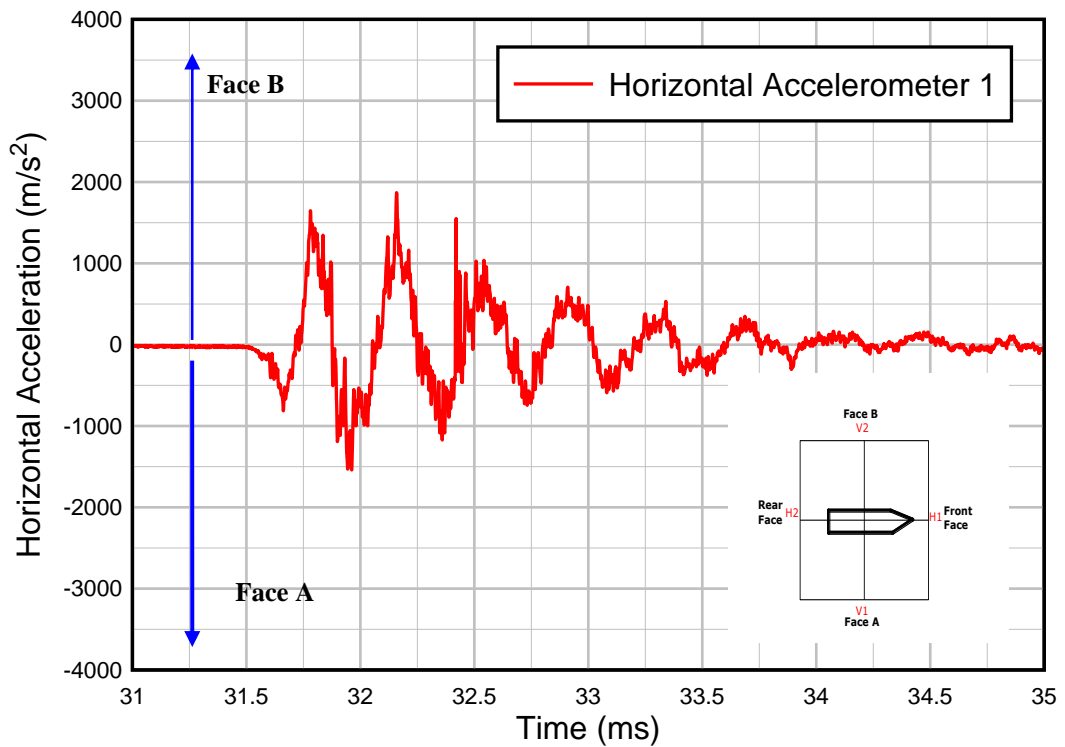
Figure 4.43 Acceleration-time history for horizontal accelerometer 1 (H1)
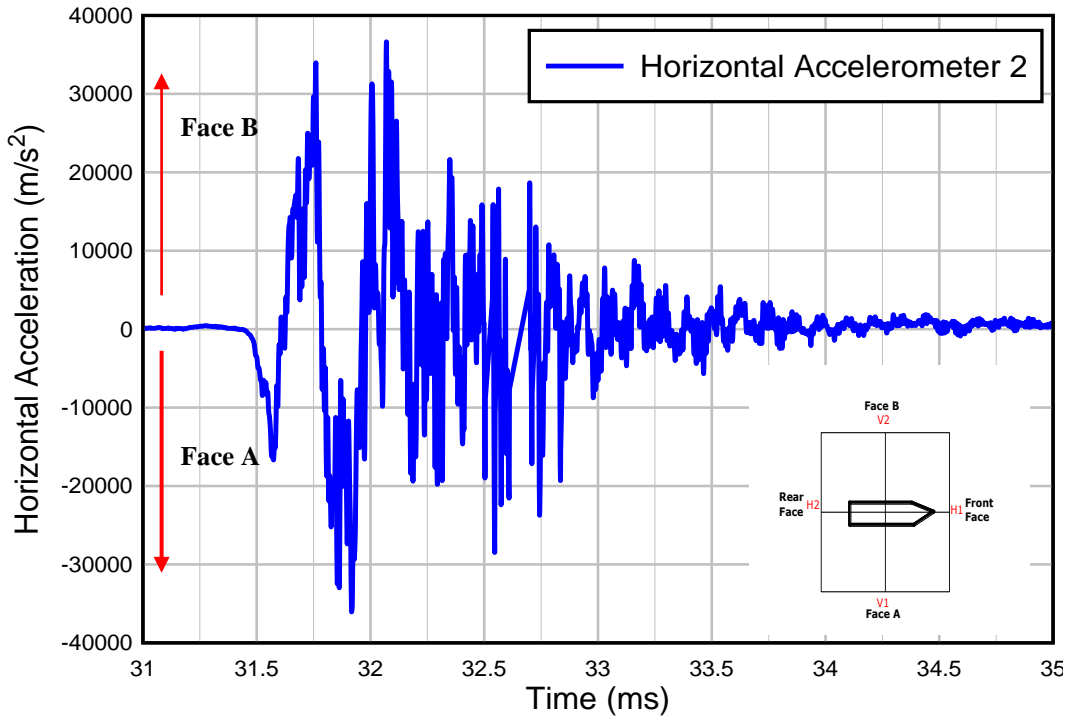
Figure 4.44 Acceleration-time history for horizontal accelerometer 2 (H2)
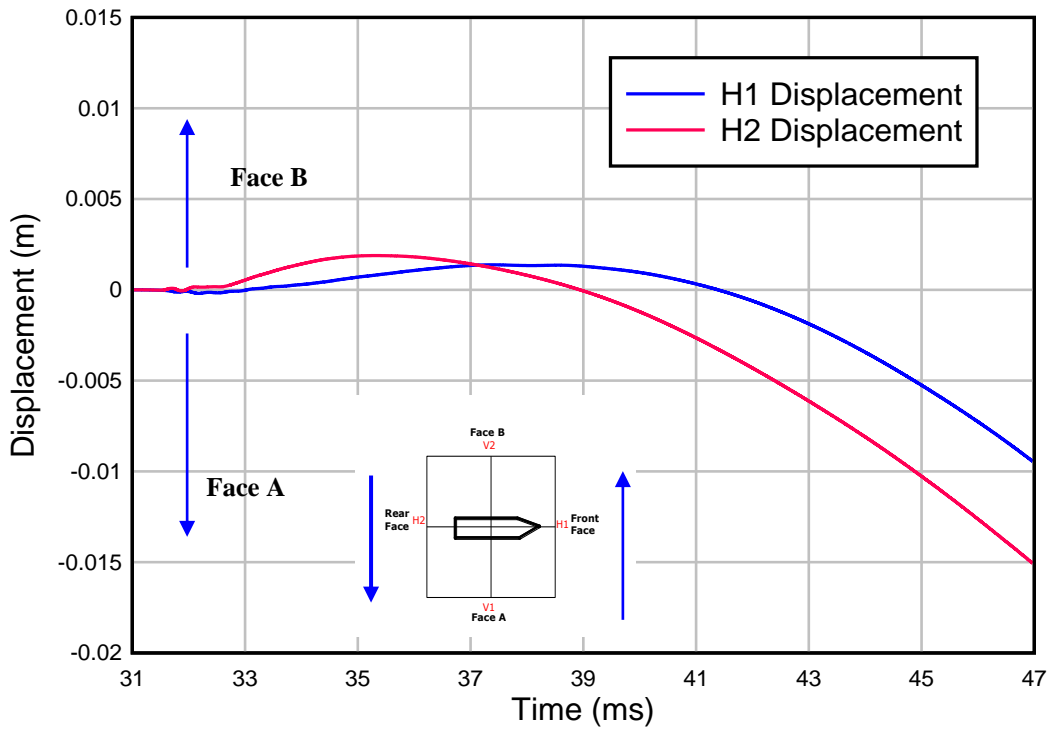
Figure 4.45 Displacement-time history for horizontal accelerometers 1 & 2 (H1 & H2)
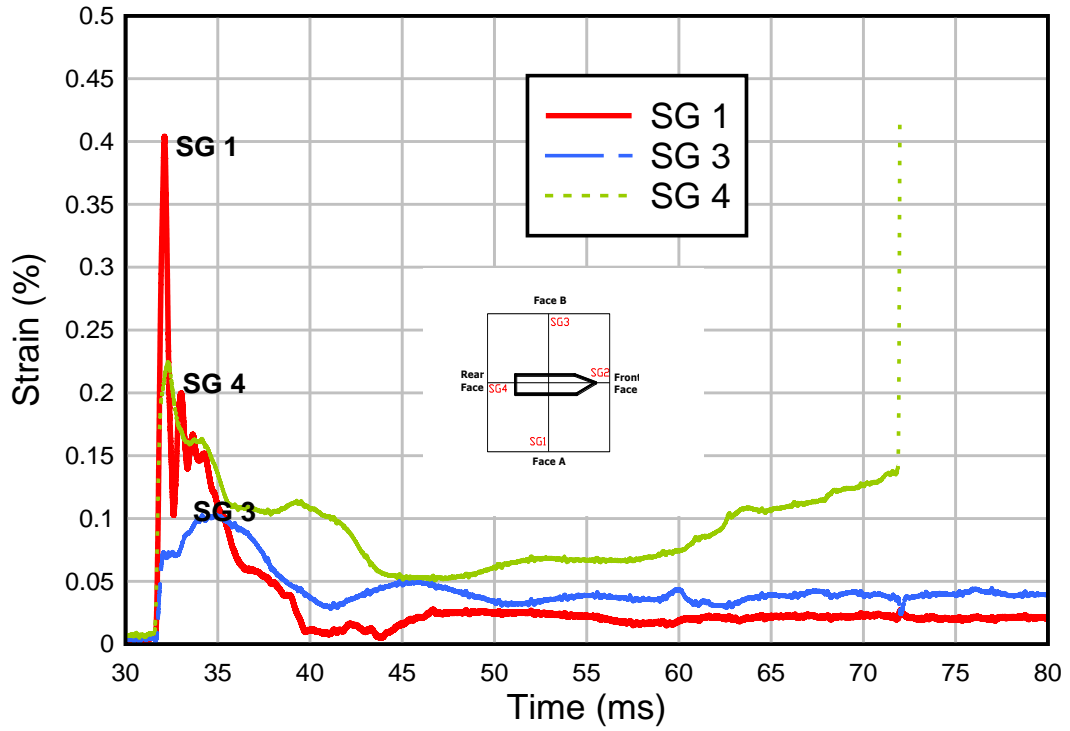
Figure 4.46 Stain-time history for strain gages (SG 1, SG 3 and SG 4)
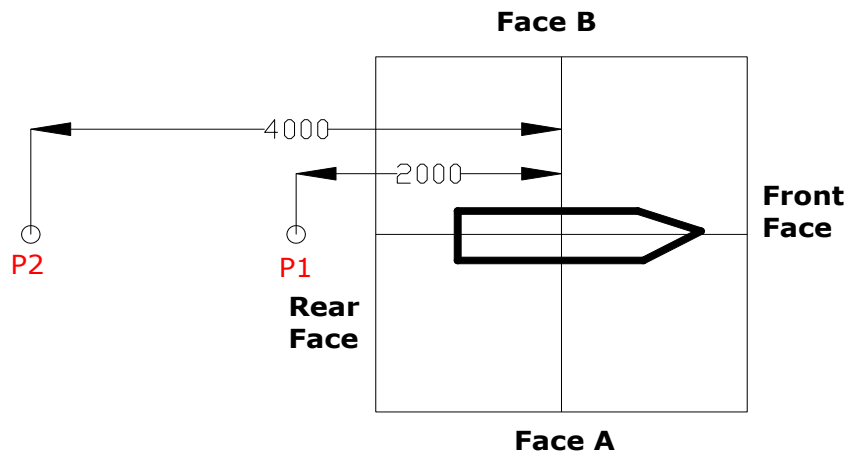
Figure 4.47 Layout of air pressure cell for Slab 2
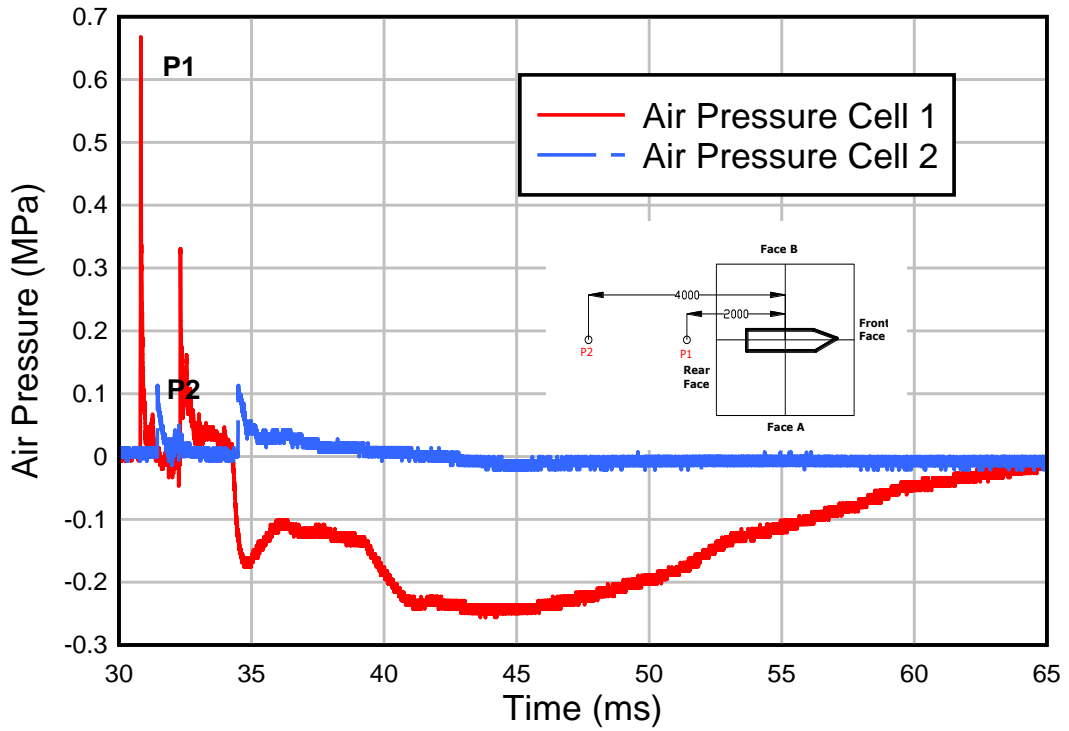
Figure 4.48 Pressure-time history for air pressure cell
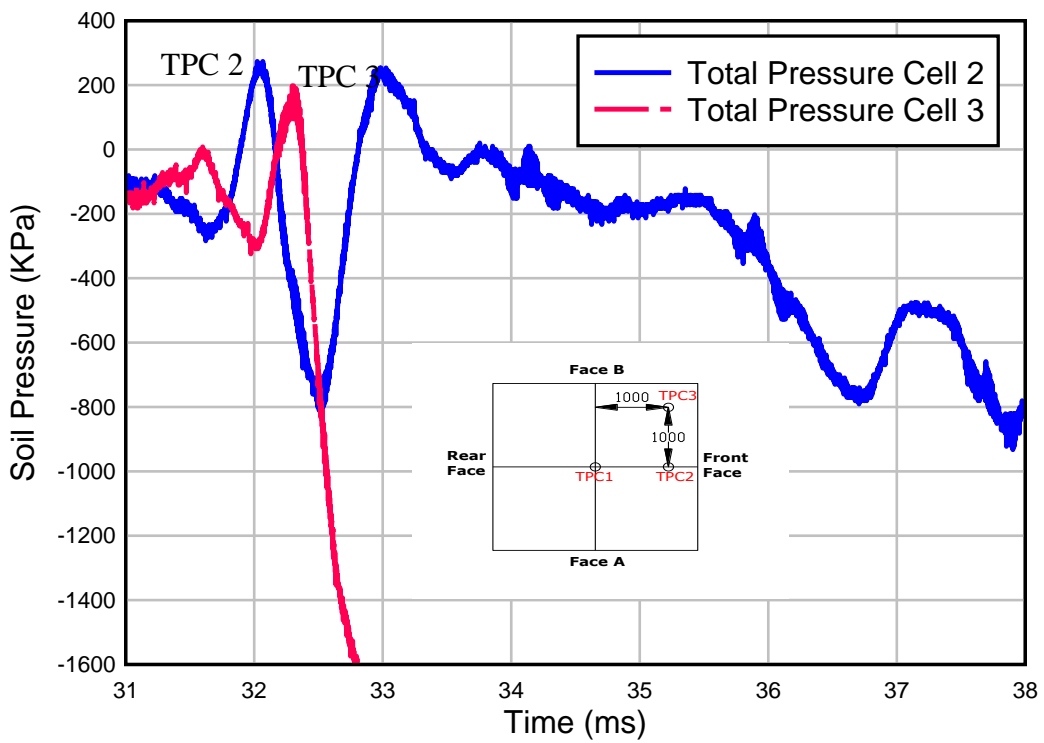
Figure 4.49 Pressure-time history for total pressure cell (TPC 2 and 3)

174

Chapter 5   Property of Interface in the New Multi-Layers Pavement System

5.1 Introduction

Like many other multilayer system, the interface condition in the proposed multi-layers pavement system plays an important role in pavement performance. There are two interfaces in the proposed multi-layers pavement, that is, the first bonding layer between high strength concrete (HSC) and Engineered Cementitious Composites (ECC) and the second bonding layer between asphalt concrete (AC) and HSC. The HSC and ECC are cast at the same time in the proposed new pavement, and thus the bonding condition between HSC and ECC can be assumed to be fully bonded, while the bonding condition between AC and HSC is weaker than that between HSC and ECC. This is because the AC layer is placed on the HSC layer few days after HSC casting and HSC has cured. Hence, there will be no direct "bonding" between HSC material and AC except surface cohesion. Thus, the interface strength between AC and HSC will not be strong, and slippage and de-bonding may occur during the application of large vertical impact and blast load. Hence, it is necessary to investigate the shear and friction coefficient of AC and HSC interface.

175

5.2 Laboratory investigation of interface property between AC and HSC layer

The strain and stress will be transferred between AC and HSC when vertical and horizontal loading is applied on AC layer. The interfacial shear strength between AC and HSC can influence the integrity of the stress/strain transfer. Hence, it is necessary to determine interfacial shear strength between AC and HSC.

Although there was no designated standard for measuring interfacial shear strength between AC and HSC, the magnitude and complexity of the stress field at the interface in relation to the mechanical properties of the adjacent materials were similar to the interface between any two cement concretes (Romanoschi 1999). Hence, this similarity could lead to the transfer of testing methodologies. In the current study, the direct shear test at constant normal loading will be conducted to investigate the shear behavior between AC and HSC.

5.2.1 Sample size

The sample size of the direct shear test was commonly controlled by the largest aggregate size used in the specimen and usually taken as 3 to 5 times the maximum aggregate size. In current study, the maximum aggregate size was 20 mm and 19 mm for HSC and AC mix, respectively. Thus, the length and width of the sample should be greater than 100 x 100 mm and the height should be greater than 60 mm. After taking into account the boundary effect and bending effect during the shear test, the length and width of sample used in this study is 150 mm x 150 mm and the height was set as 75 mm as shown in Figure 5.1.

5.2.2 Shear box setup

Due to the large size of the proposed direct shear box, it was decided to design this shear box inside of a larger box which was equipped with pulling mechanism. The sketch of the direct shear test is shown in Figure 5.2 (a). The shear box consisted of two independent half boxes. The upper half was fixed by four steel bars to connect onto the rigid wall of the large box, and was completely stationary, as shown in Figure 5.2 (b). As shown in Figure 5.2 (c), the hydraulic jack was placed at the top of box to exert vertical loading. In the lower half, the box was connected to a horizontal pulling shaft, which was connected to the hydraulic actuator in front of the large box. The hydraulic actuator exerted horizontal pulling force to shear the specimen, in which the top half remained stationary. A load cell was attached to the hydraulic actuator to measure the shear force. The roller frame below the bottom half was placed to eliminate the friction effect between box and ground. During the test, a 5 mm gap between two layer boxes was introduced to make the interface align to the shear plane.

For evaluation of interface between AC and HSC, HSC specimen was placed at the bottom half, while AC specimen was placed at the top half. During the test, the vertical load was applied on the AC layer. The relationship between shear force, horizontal and vertical displacement was recorded by the data acquisition system until the interface failed. The interface failure is defined as when shear stress reached its peak. The shear strength of interface was then calculated by dividing the maximum shear force by area of sample interface. Testing with this shear box was performed with horizontal displacement control. The rate of horizontal displacement was set as 2.5 mm/min. This rate was consistent with that used in other study (Uzan et al. 1978).

The direct shear test was conducted under constant vertical loading. Four levels of vertical loading were considered, that is 2.1 MPa, 1.5 MPa, 1 MPa and 0.5 MPa. Since the 2.1 MPa is the maximum tire pressure for the typical military and civilian runway as discussed in Chapter 2, it is set as the maximum vertical loading in the direct shear test. The equivalent normal load of 47.25 kN, 33.75 kN, 22.5 kN and 11.25 kN was applied on the AC layer via hydraulic jack which is correspond to the 2.1 MPa 1.5 MPa, 1 MPa and 0.5 MPa.

During the test, first, increasing the normal loading to the shear zone until the highest selected loading was attained. After the selected normal loading has been stabilized, the shear loading was increasing continuously via hydraulic pulling shaft using displacement control till failure. After that, remove shear loading, and apply another level of normal loading. Again, the shear loading was applied to establish a second level of peak shear strength. It should be noted that with each repeating test the situation of the AC and HSC interface would be further damaged. In order to obtain accurate static friction coefficient, another three levels of normal loading were chosen, that is 1.5 MPa, 1.0 MPa and 0.5 MPa.

In the test, a thick and rigid steel plate was placed between hydraulic jack and top surface of AC layer in order to achieve uniform loading on the AC surface. Four LVDTs were used to measure the horizontal displacement of lower shear box. Two were installed at the back of the lower shear box. Another two were installed at the track of the hydraulic actuator. Two LVDTs were installed at the top surface of AC layer to measure the vertical horizontal displacement. All samples were conducted at temperature 35°C.

5.2.3 Sample preparing

The high strength concrete (HSC) was cast first. The desired compressive strength of HSC was 90 MPa. The dimension of HSC specimen was 150 mm x 150 mm x 75 mm. In HSC specimen preparation, the steel mould and plastic plate with saw surface was designed for HSC part. Before the casting, the plastic plate with saw surface was placed at the bottom of steel mould, and then the HSC could be poured into the steel mould in order to make HSC a rough surface.

After 7 days, the strength of HSC would achieve up to 70% of its final strength, and then the AC layer could be placed above the HSC surface. The 10 kg hammer was used to compact the AC layer. In the current study, it should be noted that no bonding material such as tack coat was applied between the HSC and AC. The AC was directly placed and compacted at the top surface of HSC. The expected density of AC was around 2300 kg/m^3, which was the required density for runway in Singapore. After preparation, the specimen was brought to the test temperature by maintaining it in an over for at least 8 hours. Totally 5 specimens would be used in the direct shear test. The whole procedure of sample preparation is summarized in Figure 5.3.

5.3 Test results and discussion

5.3.1 Shear strength

Total 5 samples were conducted to investigate the shear strength between HSC and AC. The typical results could be seen in Figure 5.4. From the figure, it is clearly shown that the shear strength for interface was around 1.5 MPa for the

maximum normal loading 2.1 MPa. This value was set as the maximum shear strength for the current interface between AC and HSC.

Further checking the interface failure surface as shown in Figure 5.5, it was found that AC surface was smashed during the shear test while the HSC surface had less damaged than that of AC. This was possible that the strength of AC was much lower than that of HSC, and shear failure was mainly due to the AC failure. It might be concluded that the interface shear strength in the current study was determined by the strength of AC, and hence increasing the strength of asphalt concrete and interfacial bonding strength together might enhance the interfacial strength.

5.3.2 Static friction

Figure 5.6 shows the results for the relationship between shear stress versus normal stress under four normal loading levels for the 5 specimens. It was found that for the same normal loading the shear stress for different specimen was quite close. From the data, it was found that the static friction coefficient μ_{static} for current AC and HSC interface was around 0.71 or a friction angle of 35°. This is well within the expected range of value.

5.3.3 Dynamic friction

The dynamic friction is defined as the frictional force between two moving solid surfaces in contact with each other. Where the objects are in motion, there will still be frictional force. Usually, the dynamic friction coefficient was lower than the static friction coefficient. For the interface between steel materials, the static friction is 0.74 while the dynamic friction is 0.57 (CRC 1997) . As for the

interface between concrete and macadam, the static friction coefficient is 0.79-1.26, while the dynamic friction coefficient is 0.35-0.77(Maitra et al. 2009).

In current study, a simple "tilt table test" was used to measure the dynamic friction coefficient between HSC and AC material. The theory of the tilt table test is shown in Figure 5.7. In the figure, it is assumed that the solid body was sliding along the tilt surface with certain acceleration. The weight of solid body is mg, the tilt angle from the horizontal surface is θ. For the solid body, the force along tilt surface from its own weight is expressed as $mg\sin\theta$, the component normal to the tilt surface is $mg\cos\theta$. Considering the equilibrium of force normal to the tilt surface, the reaction force R is thus equal to $mg\sin\theta$. Thus the dynamic friction F is expressed as $\mu_{dynamic}mg\cos\theta$. The total sliding force along the tilt surface is then expressed as $(mg\sin\theta - \mu_{dynamic}mg\cos\theta)$. Hence, according to the Newton's second law $F = ma$, the acceleration of solid body can be expressed as:

$$a = g(\sin\theta - \mu_{dynamic}\cos\theta)$$

(5.1)

If the acceleration is zero, which means that the solid body is sliding along the tilt surface with constant velocity, based on the Equation 5.1, the dynamic friction coefficient can be resolved as:

$$\mu_{dynamic} = \frac{\sin\theta}{\cos\theta} = tg\theta$$

(5.2)

It can be seen that the dynamic friction coefficient can be directly obtained from the tilt angle, when the rigid body object is sliding at a constant speed down the slope.

In current study, the AC block is placed along the tilt surface which is made of HSC material. The tile angle can be adjusted to make the AC block slide along surface with constant velocity. The marked lines were drawn on the HSC surface to give the equal interval along tilt surface. The set up of tilt table test can be seen in Figure 5.8. In the test, the video camera was used to record the time when the AC body across the each marked line to check whether the velocity is constant or not. If it is not constant, then adjust the tilt angle to make another trial.

After few trials, it was found that the dynamic friction angle between AC and HSC layer is about 29° to 30°. Hence, the dynamic friction coefficient is around 0.55-057. According to the result from direct shear test, the static friction coefficient between AC and HSC is around 0.71, which corresponded to the friction angle of 35°. It can be found that the dynamic friction coefficient was about 78% of the static friction coefficient. In the current study, the dynamic friction coefficient is taken as 0.56.

5.4 Numerical modelling of interface between AC and HSC layer

Contact treatment forms an integral part of many large-deformation problems. Accurate modelling of contact interfaces between bodies is crucial to the prediction capability of the finite element simulations. LSDYNA offered a large number of contact types. Some contact types are used for specific applications such as car crashing, airbag contact and mental forming.

In LSDYNA, a contact was defined by identifying (via parts, part sets, segment sets or node sets) what locations were to be checked for potential penetration of a "slave" node through a "master" segment. A search for penetrations was made every time step. The penalty-based contact was a robust

method in handling penetration. In the case of a penalty-based contact, when a penetration was found a force proportional to the penetration depth was then applied to resist the penetration. Thus the interface force could be calculated based on the elastic spring theory.

In the current study, the contact behavior between two layers is more like sliding with little interpenetration. Hence, after checking with various contact types in LSDYNA, it was found that the TIEBREAK contact type might be most suitable to simulate the interfacial behavior between AC and HSC. This was because the AC and HSC were initially connected and with the increase of shear force, the connector between two materials broke, and then began to fail with the occurrence of the sliding. Thus in the following section, the TIEBREAK contact type would be discussed and numerical tests would be conducted to investigate the behavior of the interface using TIEBREAK contact type.

5.4.1 TIEBREAK contact type in LSDYNA

The TIEBREAK contact type allowed for the simulation of crack propagation based on the cohesive zone model. The traction-displacement law between the two materials governed the cohesive zone behavior and the energy release in the separation process. The simplest form of the traction-displacement had a linear elastic response till the crack initiation criterion was reached and then followed by a linear softening to zero traction when the damage was complete. The whole traction-displacement curve could be described as triangular shape (Praveen et al. 2008). The area under traction-displacement curve was so called the energy released rate, which described the energy dissipation during the development of crack.

In current study, the TIEBREAK contact option 6 was employed to simulate the interface behavior. The nodes were initially in contact, and failure stress needed to be defined for tiebreak to occur. The tiebreak failure stress criterion for option 6 has normal and shear components:

$$\left(\frac{|\sigma_t|}{NFLS}\right)^2 + \left(\frac{|\sigma_s|}{SFLS}\right)^2 \geq 1 \qquad (5.3)$$

in which, NFLS is the normal failure stress, and SFLS is the shear failure stress, σ_t and σ_s are the tensile stress and shear stress at interface calculated in the model respectively.

When the tiebreak criterion was met, the interface began to fail based on damage evolution. Damage was defined as a linear function of the distance between points initially in contact. When the distance exceeded the defined critical distance the interface is considered as failed completely. Thus the energy release rates G_I and G_{II} for normal and shear interface failure modes are defined as:

$$G_I = \frac{1}{2} NFLS \bullet PARAM$$

$$G_{II} = \frac{1}{2} SFLS \bullet PARAM \qquad (5.4)$$

where, PARAM is the critical displacement at total failure.

The direct tensile test (pullout test) and shear test could be conducted to obtain the energy release rate G_I and G_{II}. It should be noticed that the value SFLS and NFLS was related to the characteristic element length (square root of area). Usually, the low failure stress value was needed for coarser meshes. Hence, the SFLS and PARAM could first be numerically determined by matching load-

displacement from direct shear test, and then the NFLS could be obtained by the known value of PARAM and G_I via Equation 5.4.

After the failure criterion was met, the nodes were apart and no tensile stress was possible. The behavior of the interface was then as same as that of surface-to-surface contact type, which could transfer the shear stress and compressive stress at the interface.

5.4.2 Numerical model of direct shear test on interface between AC and HSC layer

Direct shear tests at constant normal loading had been performed on AC and HSC interface. In this section, the numerical simulation of direct shear test on AC and HSC interface will be established. The numerical parameters have been determined by matching the results from experiment as discussed in Section 5.3.

The size of model was taken as same as that in the laboratory test, that is 150 mm x 150 mm x 75 mm for AC and HSC respectively. The upper AC part was fixed and cannot move horizontally. A prescribed motion condition of 2.5 mm/min was applied to the lower HSC part. The solid element was used to model AC and HSC material. The TIEBREAK contact algorithm was employed to simulate the interface behavior. An overburden pressure of 2.1 MPa was applied and dynamic relaxation was implemented before the specimen was sheared in the numerical model. The mesh size was taken as 10 mm in the current study. Load-displacement curves from the numerical model were recorded so that the results could be directly compared to the experimental results. As mentioned above, the value of SFLS and PARAM was obtained through matching the load-displacement curve from the experimental data. In the current study, the energy

released rate G_I from tensile test was assumed to be 0.25 N/mm (referred to Section 6.3). Hence, the parameters used in the interface simulation were summarized in Table 5.1.

Table 5.1 Parameters for interface simulation

Parameters	Value
Contact type	AUTOMATIC_SURFACE_TO_SURFACE_TIEBREAK
Option	6
Friction for static	0.71
Friction for dynamic	0.56
NFLS	0.05
SFLS	1.15
PARAM	10

The load-displacement curve obtained from numerical simulation and experimental test is shown in Figure 5.9. In the figure, it was found that the peak shear force and its corresponding displacement from numerical model was very close to that obtained from experimental test. The tangent stiffness obtained from both numerical model and experiment was similar as shown in Figure 5.9. For the post-peak behavior, the numerical model could also simulate the failure behavior correctly, that meant the energy released rate G_{II} was captured. It could be concluded that the TIEBREAK contact algorithm could model the interface behavior properly. Hence, the TIEBREAK option 6 would be used in the future study.

5.5 Conclusion on interface property in the new multi-layers pavement system

For the proposed multi-layers pavement system, the interface between HSC and ECC was assumed to be fully bonded, while the interface between HSC and AC was weaker than that between HSC and ECC. This is because that the AC layer is directly placed on the HSC layer few days after HSC casting. Hence, the direct shear test with constant normal loading was carried out to investigate the shear strength and friction of the interface between HSC and AC layer.

From the direct shear test, it was found that the under the normal loading of 2.1MPa, the shear strength was 1.5 MPa. The static friction was 0.71 while it was 0.56 for dynamic friction. It can also be observed that interface between HSC and AC was initially bonded together, after peak strength the interface failed to move. At the failure surface, it was found that AC surface was smashed during the shear test while the HSC surface had less damaged than that of AC. This was possible that the strength of AC was much lower than that of HSC, and shear failure was mainly due to the AC failure. It might be concluded that the interface shear strength was determined by the strength of AC, and hence it is possible to enhance the interfacial strength by increasing the strength of AC and interfacial bonding strength.

The TIEBREAK contact algorithm was used to simulate the interface behavior between HSC and AC layers. This is because that the interface between AC and HSC layer was initially connected and with the increase of shear force, the connector between two materials broke, and then began to fail with the occurrence of the sliding. The direct shear test was used to validate the numerical model. It was found that peak shear force and the corresponding displacement at

peak shear force from numerical model was very close to that from experimental

test. Hence, it could be concluded that the TIEBREAK contact algorithm in

LSDYNA could model the interface behavior of HSC and AC properly. Hence,

this model will be used in subsequent chapters.
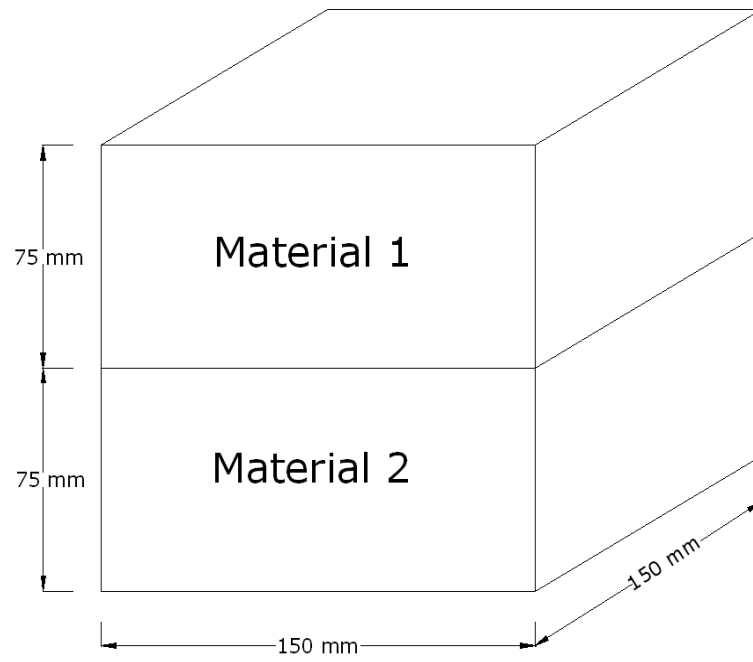
Figure 5.1 Sample size for direct shear test
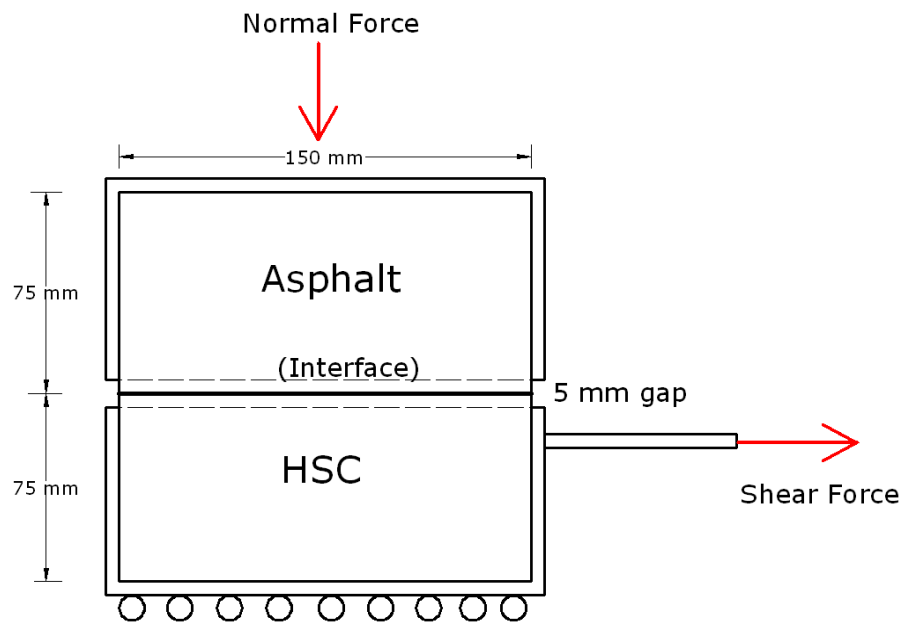
(a) Sketch of direct shear test

Figure 5.2 Configuration of direct shear test

(b) Upper box fixed by steel bar

(c) Apply normal force by hydraulic jack

Figure 5.2 Configuration of direct shear test (continue)
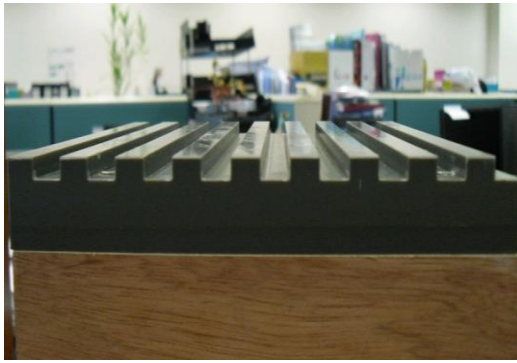
(a) Plastic plate with saw surface

(b) HSC with saw surface

(c) Put HSC as bottom layer

(d) Compact asphalt above HSC

(e) After compaction
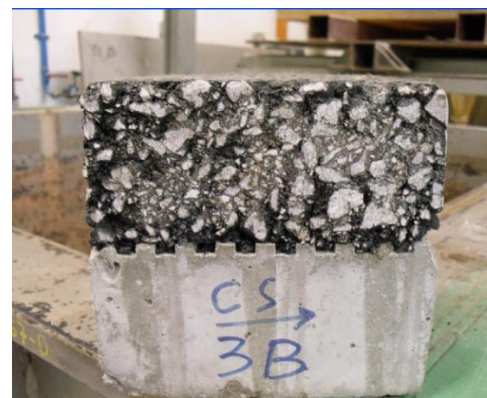
(f) Sample used in direct shear test

Figure 5.3 Process in preparation of interface sample
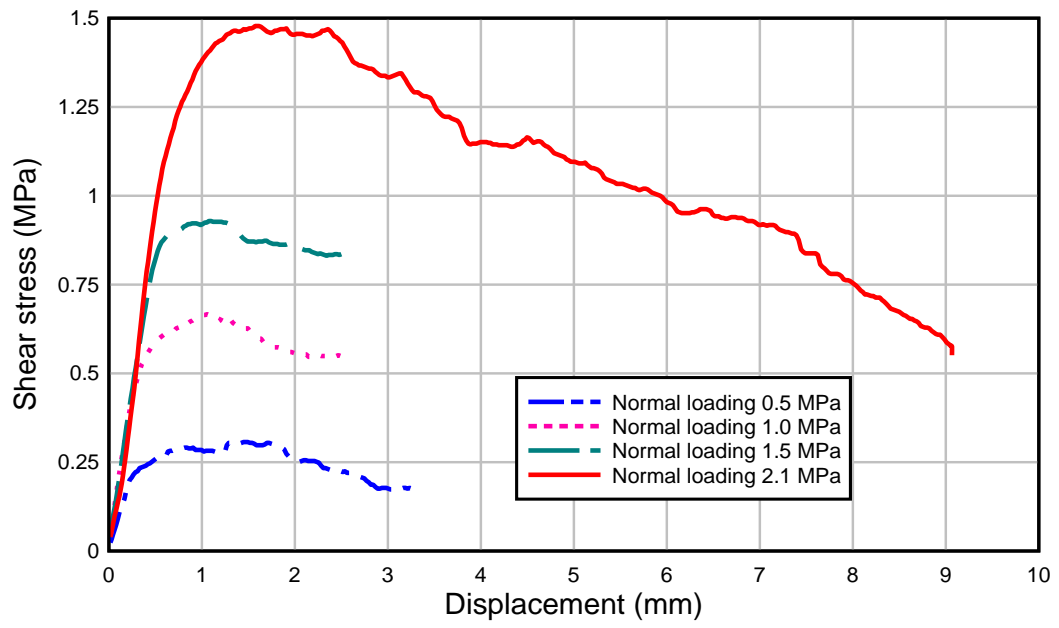
Figure 5.4 Shear stress and displacement

(a) Shear surface for asphalt

(b) Shear surface for HSC

Figure 5.5 Shear surface for asphalt and HSC after shear test
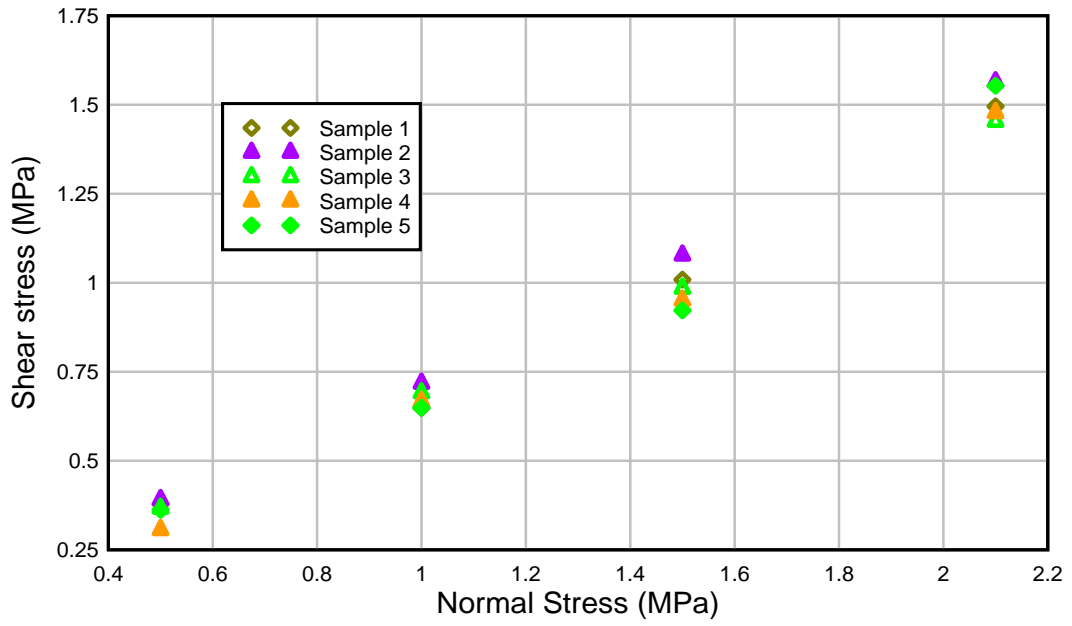
Figure 5.6 Relationship for shear stress versus normal stress
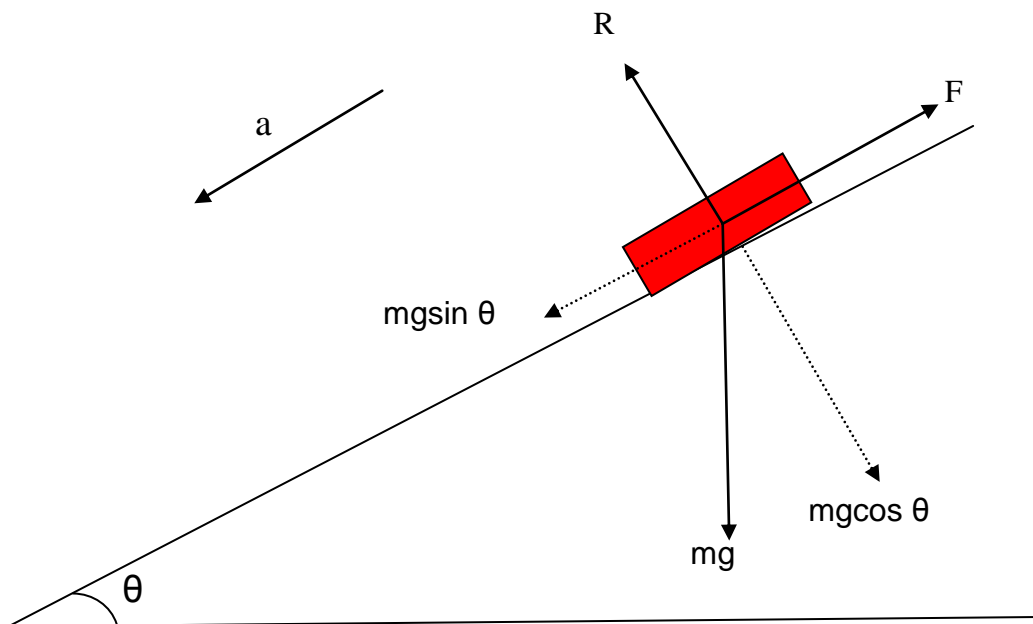
Figure 5.7 Theory of tilt table test
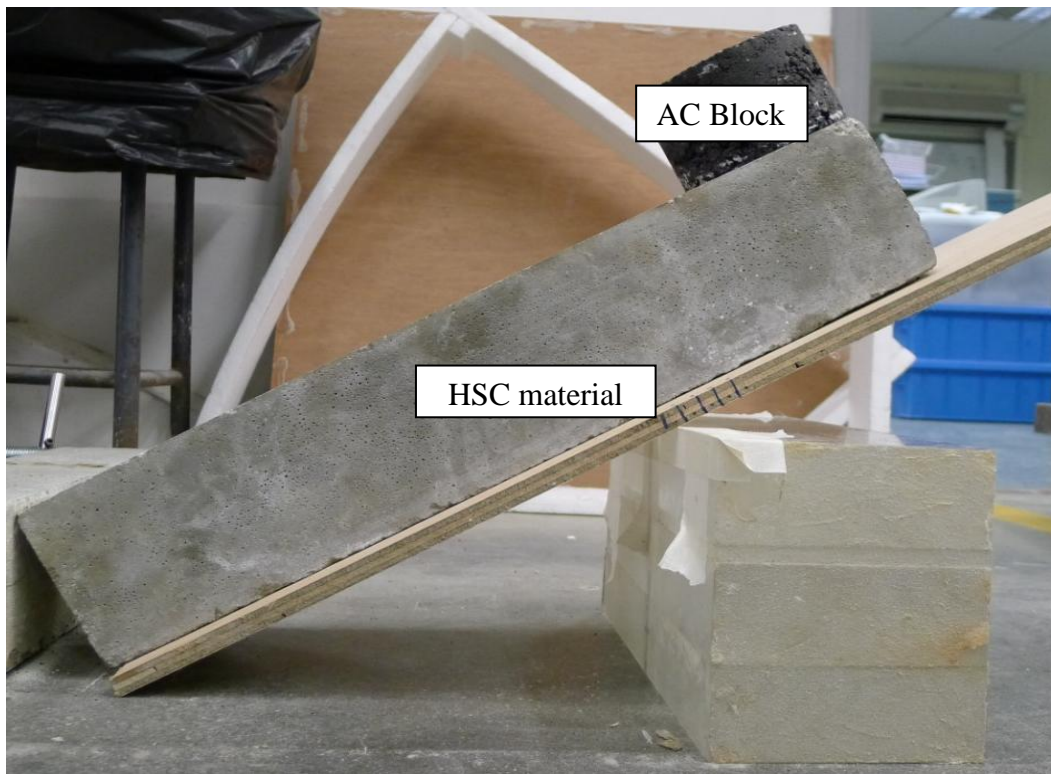
(a) Side view
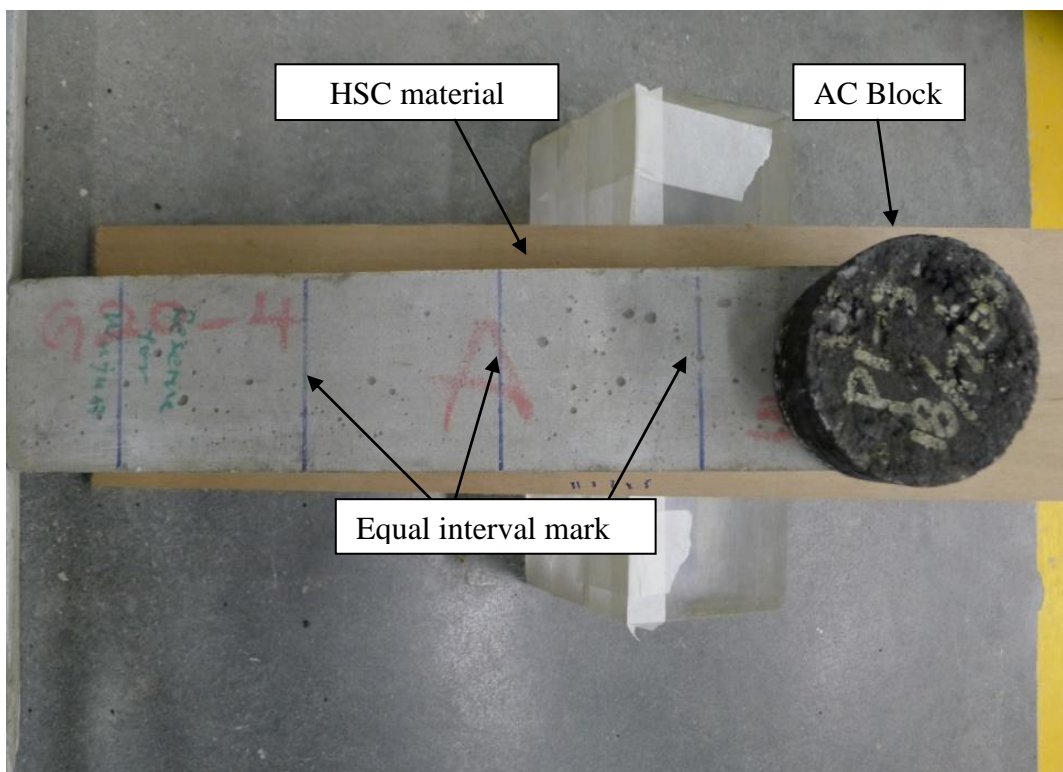
(b) Plan view

Figure 5.8 Set up for tilt table test
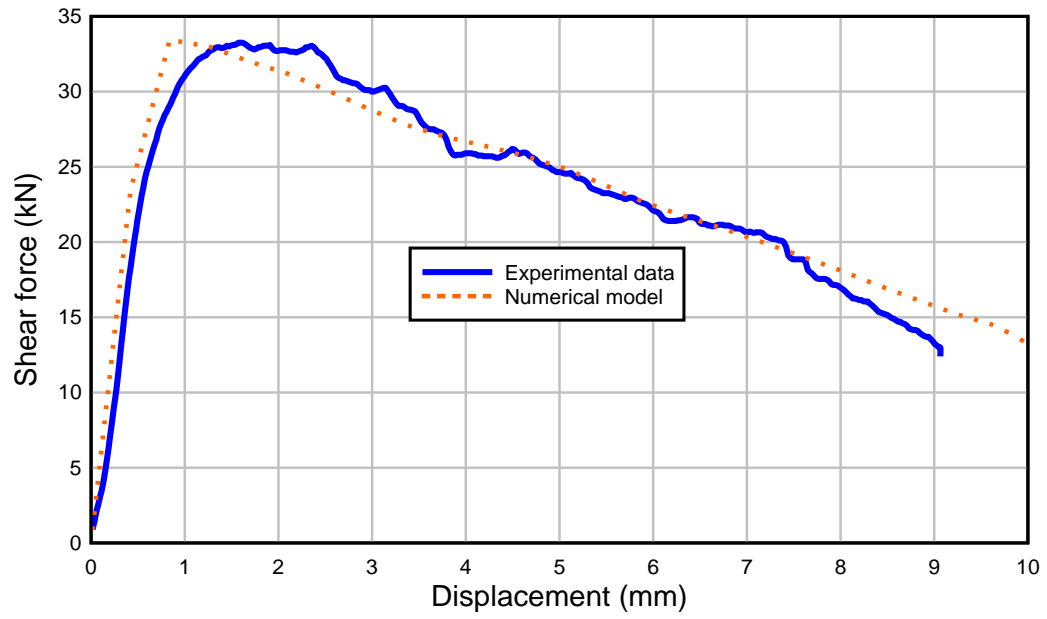
Figure 5.9 Comparison of load-displacement curve from experiment and numerical model

Chapter 6   Numerical Modelling of Pavement Slab Subjected to Blast Loading

_____

6.1 Overview

Numerical modelling is a useful tool in detailed investigation into many structural and geotechnical problems. Reasonable prediction may be provided by numerical modelling before the conducting of field test or large scale laboratory test so that greater economy can be achieved. Sometimes numerical modelling can even replace those time and money consuming tests, such as structures subjected to earthquake and blast loading. For this reason, finite element analysis was carried out for the current research project. However, numerical modelling need to be carefully calibrated before it can be used for actual design, especially for design against dynamic loadings.

6.1.1 Governing equation

In the current study, the simulation of pavement slab under blast loading will be carried out. This kind of simulation is complex as it involves material behavior under dynamic load and high strain rate. The numerical modelling of dynamic behavior can be described by a general system of differential equations. The equations are usually consisted of laws of conservation of motion, momentum and energy, constitutive model and equation of state (EOS) of the relevant materials (Malvar et al. 1996; LSDYNA 2007). The general form of laws of conservation of motion, momentum and energy can be expressed as:

Conservation of mass: $\rho V = \rho_0 V_0$ (6.1)

Conservation of momentum: $\sigma_{ij,j} + \rho f_i = \rho \ddot{u}$ (6.2)

Conservation of energy: $\dot{e} = V s_{ij} \dot{\varepsilon}_{ij} - (p - q)\dot{V}$ (6.3)

where, ρ and V are the current density and volume respectively. ρ_0 and V_0 are reference density and volume respectively. σ_{ij} is the stress tensor, the dot above the symbol represents covariant differentiation with respect to time, f_i is the body force and $\ddot{u}$ is the acceleration. $\dot{e}$ is the change in specific internal energy, $\dot{\varepsilon}_{ij}$ is the strain rate tensor. $\dot{V}$ is the rate of change in volume, s_{ij} is the deviatorial stress tensor. The subscript stands for tensor notation. p and q is the pressure and bulk viscosity respectively.

The equation of state (EOS)s describes the relationship among pressure (p), density (ρ) and internal energy (e):

$$p = p(\rho, e)$$ (6.4)

The constitutive model links stress (σ_{ij}) to strain (expressed a strain, ε_{ij} and strain rate, $\dot{\varepsilon}_{ij}$) and internal energy (e) and damage factor (D) in terms of:

$$\sigma_{ij} = g(\varepsilon_{ij}, \dot{\varepsilon}_{ij}, e, D)$$ (6.5)

The numerical method will solve the governing equations (Equation 6.1 to 6.3) with material properties' equation of 6.4 and 6.5, after discretising the problem into time (temporal) and space (spatial) domains. Temporal discretization in dynamic numerical simulation usually adopts explicit method, that is, the function values at the new time step will directly be calculated from function

values at previous time step. It should be noticed that the explicit method is conditionally stable. The restriction on time step is guaranteed by Courant-Friedrich-Levy (CFL) condition. In order to capture the important information within all the spatial elements, the CFL condition requires that the time step should be smaller than the time taken for sound to travel across the smallest elements, which can be expressed as:

$$\Delta t \leq \frac{nl}{c} \tag{6.6}$$

in which, n is the safety factor, which is 0.9 for most of the low velocity dynamic loading case and 0.6 might be suitable for blasting simulation (which is high velocity dynamic loading). l is the smallest mesh size (it is taken as for bar element for 1D problem, as square root of the area of the element for 2D elements, or cubic root of the volume of the element for 3D block elements), c is the speed of sound. The time step might also be limited by the contact algorithm, the magnitude of the shock viscosity or an explosive burn (Benson 1992).

In the current study, two spatial discretisation formations would be employed to solve the problem. One is Lagrangrian formation, another is Eulerian formation. In the Lagrangrian formation, the elements and its attached nodes moved with the material, when it was either compressed or expanded. While in Eulerian formation, the mesh is fixed and only material are allowed to flow in or out of the mesh. The Lagrangrian formation is most suitable for modelling solid materials (e.g. concrete, soil or metal), while the Eulerian formation is robust at simulating fluid or gas materials.

6.1.2 Lagrangrian versus Eulerian formation

In the Lagrangrian formation, at the beginning of the calculation, the equation of motion is employed to calculate nodal accelerations through the nodal forces which are the sum of all the internal force and external forces. Subsequently the new nodal velocity can be obtained from the integration of acceleration, and nodal displacement can be found from further integration of velocity. With the new nodal positions, the new densities and strain rates can be calculated from the conservation of mass. From the strain rate, the new stress, internal energy can be obtained from the conservation of energy and constitutive model. The internal force will be found from the new internal stress of the element using the conservation of momentum. Then, a new time step size is calculated based on the speed of sound though each of elements and their geometry and the smallest time step size will be used in the next iteration, and advanced to new computational cycle.

The main disadvantage of the Lagrangrian formation is that it might encounter severe mesh distortion problem, and in turn resulted in a small time step and stop the calculation. This problem can be solved by adopting re-zone, erosion, tunnel and local modified symmetry. The former two methods (re-zone and erosion) will be briefly discussed in this section, other two methods (tunnel and local modified symmetry) can refer to Schwer and Day (1991). The re-zone method was usually adopted in cases of moderate element distortion and mapped the current distorted mesh onto a more regular new mesh. This method would introduce some errors because the algorithm wanted to maintain a global energy balance with the old element grid during mapping and in turns cause non-conformity in the local energy distribution (Lee 2006). The erosion method could

be used for cases of severe element distortion, and it would delete the failed element from the calculation when the pre-defined erosion criteria were met. The erosion criteria were commonly defined as effective plastic strain, maximum /minimum principal strain and shear strain (LSDYNA 2007). The value of the erosion criterion would be highly dependent on mesh size. It was difficult to determine and often obtained based on comparable works. According to Bessette and Littlefield (1998), it was found that high erosion strain would cause numerically unstable energy balance while the small erosion strain might result in increasing mass loss and reducing the final material strength. Hence, erosion technology should be used with cautions.

In the Eulerian formation, it consists of two steps to obtain a solution. First it was a Lagrange step. In this step, the new node position is found based on above Lagrangrian formation. The second is the advection step, in which the deformed elements are mapped back into its original element which is fixed in space. However, the main disadvantage of the Eulerian formation is that it was difficult to track the free surface, material interfaces and history dependent material behaviors as compared to the Lagrangrian formation (Whirley and Engelmann 1992).

In this research, the software AUTODYN and LS-DYNA would be used. Eulerian formation was adopted in AUTODYN, while Lagrangrian formation was used in LS-DYNA. Herein, brief introduction of these two software would be given in this section.

6.1.3 AUTODYN

AUTODYN, produced by Century Dynamics, Inc. (2003) is a hydrocode program to solve a wide variety of non-linear problems in solid, fluid and gas dynamics. AUTODYN employs a coupled methodology to allow an optimum numerical solution for a given problem. With this approach, AUTODYN allows different solvers such as Lagrange and Euler to be used together in the same model. This capability makes AUTODYN especially suitable for the study of interaction problems involving multiple systems of structures, fluids and gases. In term of meshing, in AUTODYN, Eulerian and Lagrange grids can interact with each other (Euler-Lagrange coupling). The Lagrange subgrid imposes a geometric constraint on the Euler subgrid, while the Euler subgrid provides a pressure boundary to the Lagrange subgrid. The Euler-Lagrange coupling feature is a very powerful feature for modelling fluid-structure and gas-structure interaction problem; this extends to blast and explosive effects and interactions on structures.

In the current study, since the blast propagation might involve large displacement of gas flows, the Eulerian formation in AUTODYN would be employed. AUTODYN would model the detonation of explosive above the pavement slab, and the blast wave propagation in the air. When the blast loading reached the pavement slab, the reflected pressure (P-T curve) could be obtained. Then the P-T curves could be applied on surface of the pavement slab built by LSDYNA to explore the dynamic response of pavement structure. Another reason to use LSDYNA to model pavement structure was that the material models in LSDYNA were more robust as compared to that in AUTODYN.

6.1.4 LSDYNA

LS-DYNA (2007), is a general purpose finite element code for calculating the large deformation dynamic response of structures. LSDYNA is originally based on an explicit time integration scheme, and the implicit solution has been added gradually in recent years. In the LSDYNA explicit analysis, it was especially useful in the simulation of the cement-based material under impact and blast loading, which was verified by many other researchers (Malvar et al. 1997; Lee 2006). Furthermore, from the initial review of LSDYNA, it was found that the use of "contact algorithm", which was available in LS-DYNA, is very important and could simulate very well the interface behavior. In the current study, in addition to the simulation of normal concrete pavement slab, the proposed new material pavement with multi-components of many interfaces would be modelled. Proper modelling of interface behavior in the numerical model would enable the simulation to be closer to the real situation.

6.2 Material model

6.2.1 Air and explosive

In AUTODYN, two material models were used in current study, that is: air and TNT explosive. The air was represented an idea gas equation of state, which is in the form of:

$$p = (\gamma - 1)\rho e \tag{6.7}$$

where γ is a constant, ρ is air density and e is the specific internal energy. The parameter of air density and specific internal energy are related to the temperature, that is, the different values for air density and specific energy should be adopted

according to specific local temperature. However, for air at ordinary temperature (from $15°$ to $40°$), the deviation of density and internal energy calculated from different temperature often may be ignored without introduction of significant error. In the AUTODYN (2003), the standard constants of air, which was derived from $20°$ air, were given in the material library. Hence, these parameters could be employed in the numerical model. The parameters of idea gas used in AUTODYN are given in Table 6.1

<div align="center">Table 6.1 Parameters of idea gas (AUTODYN 2003)</div>

Parameter	Unit	Value
γ	---	1.4
ρ	(g/cm^3)	1.225×10^{-3}
Specific internal energy (under 1 atmosphere)	mJ/g	2.068×10^5

The TNT explosive was described by Jones-Wikins-Lee (JWL) equation of state which is expressed as:

$$p = A\left(1 - \frac{\omega}{R_1 V}\right)e^{-R_1 V} + B\left(1 - \frac{\omega}{R_2 V}\right)e^{-R_2 V} + \frac{\omega E}{V} \tag{6.8}$$

where A, B, R_1, R_2, and ω are empirically derived constants which are different in each explosive, V is the relative volume or the expansion of the explosive product, and E is the detonation energy per initial unit volume. Like EOS for air, the values of constants in JWL for many common explosives had been calibrated and compiled in the material library in AUTODYN. The parameters used in current study are summarized in Table 6.2.

Table 6.2 Parameters of JWL EOS for TNT explosive (AUTODYN 2003)

Parameter	Unit	Value
ω	---	0.35
A	kPa	3.738×10^8
B	kPa	3.747×10^6
R_1	---	4.15
R_2	---	0.9
E/V	kJ/m^3	6.0×10^6

The material EOS of air and TNT would be used in section 6.2.4 to generate the blast pressure in the simulation of detonation of explosive using AUTODYN.

6.2.2 Concrete model

Concrete is consisted of cement paste, coarse and fine aggregates, and admixture. It is a brittle material. The brittle behavior for concrete and other geomaterials i.e. rock and soil show obviously different strengths in compression and tension. The concrete also has the behavior of pressure hardening and strain hardening under static loading, and strain rate hardening in tension and compression under dynamic loading. When concrete begins to fail, it gradually lost its loading capacity which was also called the strain softening.

There was a number of material models for concrete materials developed in recent years. These material models could represent the typical behavior of brittle material as mentioned above. Some robust material models were capable of capturing the varying concrete material behaviors under different loading conditions. Especially, when subjected to severe loading such as blast loading or high impact loading, the concrete would show highly non-linear response. The MAT72 R3 model (Malvar et al. 1997) in LSDYNA was the one that could be

used for representing concrete behavior under such high dynamic loading. In the current study, the MAT72 R3 would be used and some outstanding features in this model would be briefly discussed in this section.

A) Strength surface of MAT72 R3 model for concrete

The MAT72 R3 model decouples stress into the hydrostatic pressure and deviatoric stress as shown in Equation 6.9:

$$\sigma_{ij} = s_{ij} + \frac{1}{3}\sigma_{ii}\delta_{ij} \tag{6.9}$$

where, σ_{ij} is stress tensor, s_{ij} is the deviatoric stress tenor and σ_{ii} is the hydrostatic pressure tensor. It should be noted that stress are positive in tension, pressure is positive in compression. The hydrostatic pressure is related to the volumetric change of material, while the deviatoric stress is related to shear resistance of the material, and is usually expressed by the second invariant of the deviatoric stress tensor, J_2:

$$J_2 = \frac{1}{2}s_{ij}s_{ji} = \frac{s_1^2 + s_2^2 + s_3^2}{2} \tag{6.10}$$

where, s_i is principal deviatoric stress.

MAT72 R3 model has three independent strength surfaces, that is, maximum failure surface, yield surface and residual failure surface, which is shown graphically in Figure 6.2 (a). The general formation of strength surfaces can be written as:

$$\Delta\sigma = \sqrt{3J_2} = f(p, J_2) \tag{6.11}$$

in which, $\Delta\sigma$ is the principal stress difference and p is the hydrostatic pressure.

Usually, the above Equation 6.11 is referred to the compressive meridian. The whole failure curve can be obtained through rotation of the compressive meridian around the hydrostatic pressure axis by multiplying $r_3(\theta_L)$, which has the formation:

$$\Delta\sigma = r_3(\theta_L) \bullet \sqrt{3J_2} = f(p, J_2, J_3) \tag{6.12}$$

$$r_3(\theta_L) = \frac{r}{r_c} = \frac{2(1-\psi^2)\cos\theta_L + (2\psi-1)\sqrt{4(1-\psi^2)\cos^2\theta_L + 5\psi^2 - 4\psi}}{4(1-\psi^2)\cos^2\theta_L + (1-2\psi)^2} \tag{6.13}$$

where, $\psi = {r_t}/{r_c}$, r_t and r_c are the radius of tensile and compressive meridian respectively as shown in Figure 6.2 (b). According to Equation 6.13, it could be found that the $r_3(\theta_L)$ depends on ψ and θ_L. The parameter ψ in turns relied on hydrostatic pressure. For the concrete material, the value of ψ varied from ½ at negative (tensile) pressures to unity at high compressive pressures and was summarized by Malvar et al. (1997):

$$\psi(p) = \begin{cases} \dfrac{1}{2} & p \leq 0 \\[2mm] \dfrac{1}{2} + 3f_t/2f_c & p = f_c/3 \\[2mm] \dfrac{1.15f_c}{a_0 + \dfrac{2.3f_c/3}{a_1 + 2.3a_2f_c/3}} & p = 2.3f_c/3 \\[2mm] 0.753 & p = 3f_c \\[1mm] 1 & p \geq 8.45f_c \end{cases} \tag{6.14}$$

The value of Lode angle θ_L can be obtained from:

$$\cos\theta_L = \frac{\sqrt{3}}{2}\frac{s_1}{\sqrt{J_2}} \quad \text{or} \quad \cos 3\theta_L = \frac{3\sqrt{3}}{2}\frac{J_3}{J_2^{3/2}} \tag{6.15}$$

From Figure 6.3 (a) and (b), it is shown that for concrete material, the shape of the deviatoric cross section would transit from triangle at low hydrostatic pressure to circle at very high hydrostatic pressure. Figure 6.3 (c) shows the tensile and compressive meridian when $\theta_L = 0°$ and $\theta_L = 60°$.

During initial increase of hydrostatic pressure P, the deviatoric stresses remain elastic until the yield surface is reached. The deviatoric stress can be further developed until the maximum strength surface is touched, then the material will begin to fail (as shown in Figure 6.4). After failure initiation, materials will gradual loss of load carrying capacity and go to residual strength surface. The compressive meridian of these three surfaces can be expressed as:

Yield surface $\Delta\sigma_y = a_{0y} + \dfrac{p}{a_{1y} + a_{2y}p}$ (6.16)

Maximum strength surface $\Delta\sigma_m = a_0 + \dfrac{p}{a_1 + a_2 p}$ (6.17)

Residual strength surface $\Delta\sigma_r = \dfrac{p}{a_{1f} + a_{2f} p}$ (6.18)

The eight parameters, namely, $a_0, a_1, a_2, a_{1f}, a_{2f}, a_{0y}, a_{1y}$ and a_{2y} for three surfaces could be obtained from the experimental data. Some parameters could be derived from the following method.

A-1: Yield surface

Available data (Malvar et al. 1997) recommended that yield surface was approximately the locus of points at $\Delta\sigma_y = 0.45\Delta\sigma_m$ on triaxial compression path, and thus from any point $(p, \Delta\sigma_m)$ on the maximum strength surface, the

corresponding point $\left(p',\Delta\sigma_y\right)$ on the yield surface was $\Delta\sigma_y = 0.45\Delta\sigma_m$ and

$P' = P - \dfrac{0.55}{3}\Delta\sigma_m$ as shown in Figure 6.5.

A-2: Maximum strength surface

Three points were used to determine the three strength parameters (a_0, a_1, a_2):

- The pure shear condition at compressive meridian, $p = 0$ kPa and $\Delta\sigma_m = 3f_t$

- Unconfined compressive strength at compressive meridian $p = \frac{1}{3}f_c$ and $\Delta\sigma_m = f_c$

- Triaxial compressive data for high confinement from Chen (1994), $p/f_c = 4.4$ and $\Delta\sigma_m/f_c = 6.025$

A-3: Residual strength surface

The residual principal stress difference $\Delta\sigma_r$ should not exceed $\Delta\sigma_m$ at high hydrostatic pressure. Hence, at high hydrostatic pressure point, the value of $\Delta\sigma_r$ would be set to $\Delta\sigma_m$. As shown in Figure 6.6, this point was the intersection of the maximum and residual failure surface, and so called brittle-ductile point. For concrete material, this point was taken at $p = 3.878f_c$ (Malvar et al. 1997).

B) Damage factor of MAT72 R3 model for concrete

After reaching the initial yield surface but before the maximum strength surface, the current surface is obtained as a linear interpolation between yield surface and Maximum strength surface:

$$\Delta\sigma = \eta(\Delta\sigma_m - \Delta\sigma_y) + \Delta\sigma_y \tag{6.19}$$

After reaching the maximum failure surface the current failure is similarly interpolated between the maximum failure surface and the residual failure surface:

$$\Delta\sigma = \eta(\Delta\sigma_m - \Delta\sigma_r) + \Delta\sigma_r \tag{6.20}$$

where η varies from 0 to 1 depending on the accumulated effective plastic strain parameter λ. In LSDYNA, the series of pairs (η, λ) was input by user. The value of η normally started at 0 and increased to unity at $\lambda = \lambda_m$ and then decreased back to 0 at some larger value of λ. The (η, λ) pairs for concrete material in the current study is plotted in Figure 6.7.

The accumulated effective plastic strain can be expressed as follows:

$$\lambda = \int_0^{\bar{\varepsilon}^p} \frac{d\bar{\varepsilon}^p}{r_f(1 + p/(r_f f_t))^{b_1}} \quad \text{for } p \geq 0 \tag{6.21a}$$

$$\lambda = \int_0^{\bar{\varepsilon}^p} \frac{d\bar{\varepsilon}^p}{r_f(1 + p/(r_f f_t))^{b_2}} \quad \text{for } p < 0 \tag{6.21b}$$

where f_t is the quais-static concrete tensile strength, $d\bar{\varepsilon}^p$ is effective plastic strain increment, and $d\bar{\varepsilon}^p = \sqrt{(\frac{2}{3})d\varepsilon_{ij}^p d\varepsilon_{ij}^p}$ with $d\varepsilon_{ij}^p$ being the plastic strain increment tensor. r_f is the dynamic increase factor (DIF) which would be discussed later.

A scaled damage indicator δ can be defined to describe the damage level of the material. The scaled damage indicator δ can be expressed as:

$$\delta = \frac{2\lambda}{\lambda + \lambda_m} \tag{6.22}$$

in which, λ is accumulated effective plastic strain as defined in Equation 6.21.

It should be noticed that there are three threshold values in Equation 6.22. (i) At yield surface, $\lambda = 0$, leading to $\delta = 0$, (ii) At maximum failure surface, $\lambda = \lambda_m$, leading to $\delta = 1$, (iii) At residual failure surface, $\lambda = \lambda_r \gg \lambda_m$, leading to $\delta = 1.99 \approx 2$. Thus the ranges of δ from 0 to 1 to 2 indicates that the failure surface migrates from "yield surface" to "maximum strength surface" to "residual strength surface" respectively, as the material being stressed.

As the research is focusing on the initiation and the degree of damage of the proposed multi-layers pavement subjected to blast load, hence, the post-peak behavior is of great interest. Thus, this post-peak behavior of the material obtained from FEM modelling would be plotted for the δ value from 1 to 2. The higher δ value would represent the higher degree of damage. In the current study, it was further assumed that the threshold δ value for the situation classified as "severe crack" is 1.8, i.e. when δ value reached 1.8 beyond, the material is taken as failed totally.

It can be seen that Equation 6.21a and 6.21b had different definitions for damage due to compression ($p \geq 0$) and tension ($p < 0$). The damage factor b_1 in Equation 6.21a determined the descending branch in the compressive stress-strain curve for concrete. Parameter b_1 was determined by adopting energy G_c (area under stress-displacement curve) obtained from uniaxial compressive test in single

element simulation. Changing iteratively the parameter b_1 until the area under stress-stain curve from single element simulation coincided with G_c / h, where h is the element size.

The damage factor b_2 in Equation 6.21b was related to material tensile softening, and also determined from experimental data. The parameter b_2 was determined by assigning fracture energy G_f obtained from uniaxial tensile test or three points notched beam test for use of single element simulation. Changing iteratively the parameter b_2 until the area under stress-stain curve from single element coincided with G_f / w_c, where w_c is the localization width, and typically w_c was taken as 1-6 times the maximum aggregate size (Malvar et al. 1997).

Based on the Equation 6.20 and 6.21b, the stress softening factor η and λ were governed by the accumulation of effective plastic strain. However, when the stress path was very close to the negative hydrostatic pressure axis, i.e. isotropic tension, wherein the hydrostatic pressure would decrease from 0 to $-f_t$, and no deviatoric stress occurred, then no damage accumulation happened. It means that the damage factor η and λ remained zero at the isotropic tension, and the hydrostatic pressure kept it at $-f_t$ even after tensile failure. It could be obviously shown that situation was not true in the real concrete behavior. To consider pressure softening after tensile failures, a volumetric damage increment was calculated and added to the total damage factor λ whenever the stress path was close to the triaxial tensile path. The volumetric damage increment $\Delta\lambda$ is expressed as:

$$\Delta\lambda = b_3 f_d k_d \left(\varepsilon_v - \varepsilon_{v,\text{yield}} \right) \tag{6.23}$$

where b_3 is the triaxial tensile softening factor, k_d is the internal scalar multiplier and ε_v is the volumetric strain, and $\varepsilon_{v,yield}$ is the volumetric strain at yield. The factor f_d restricts the effect of this change only to the paths close to the triaxial tensile path by:

$$f_d = \begin{cases} 1 - \dfrac{\left|\sqrt{3J_2}\,/\,p\right|}{0.1}, & 0 \le \left|\sqrt{3J_2}\,/\,p\right| < 0.1 \\ 0, & \left|\sqrt{3J_2}\,/\,p\right| \ge 0.1 \end{cases} \tag{6.24}$$

C) Strain rate effect

The material model considered a radial rate enhancement on the concrete failure surface. This is due to that the experimental data were typically obtained along radial paths from the origin in the principal stress difference versus hydrostatic pressure via unconfined compressive and tensile tests. Thus the enhanced strength $\Delta\sigma_{me}^{c}$ in terms of hydrostatic pressure p is expressed as:

$$\Delta\sigma_{me}^{c} = r_f \Delta\sigma_{m}^{c}\left(p\,/\,r_f\right) \tag{6.25}$$

As implied in the Equation 6.25, to get enhanced value $\Delta\sigma_{me}^{c}$, an unenhanced hydrostatic pressure $p\,/\,r_f$ was first obtained, and then the unenhanced strength $\Delta\sigma_{m}^{c}\left(p\,/\,r_f\right)$ was calculated for based on original maximum strength surface. After that, the enhanced maximum strength surface was obtained by multiplying enhancement factor r_f to the unenhanced strength. It could be found that the enhancement factor r_f (DIF) was important in Equation 6.23 for material under dynamic loading. A typical DIF-strain rate curve for concrete material was suggested by CEB (Comite Euro-International du Beton 1993). In the later part, using DIF curve in numerical modelling would be explored.

D) Equation of State (EOS)

In addition to the strength model, the equation of state was needed to describe the relationship between hydrostatic pressure and volume change. The material's equation of state could be usually decided by fly impact (i.e. for steel) test or triaxial compressive test (i.e. for concrete or geomaterials). The isotropic compression portion of the MAT72 R3 concrete model consists of pairs of hydrostatic pressure and corresponding volume strain. It is implemented as a piece-wise curve. The typical curve is illustrated in Figure 6.8. From the figure, it is shown that the pressure p was a function of the volumetric strain, in which the volumetric strain is defined as:

$$\mu = \frac{\rho}{\rho_0} - 1 \tag{6.26}$$

where ρ and ρ_0 are the current and initial densities, respectively. In compression, the hydrostatic pressure-volumetric stain response is separated into three regions. The first region is linear elastic and would terminate at (μ_{crush}, P_{crush}). In this stage, the elastic bulk modulus can be decided as:

$$K_{elastic} = P_{crush} / \mu_{crush} \tag{6.27}$$

After this stage, the second region starts, which involved crushing of the concrete and production of plastic volumetric strain, and it continued until (μ_{lock}, P_{lock}). At this stage, the loading/unloading bulk modulus for certain pressure is obtained through interpolation between elastic bulk modulus $K_{elastic}$ and fully compaction bulk modulus K_1 (to be defined later) using damage value D_c:

$$K_{av} = (1 - D_c) K_{elastic} + D_c K_1$$

$$\Delta D_c = \frac{\Delta \mu^P}{\mu_{lock}} \tag{6.28}$$

where $\Delta \mu^p$ is the incremental plastic volumetric strain, and the plastic volumetric strain for the fully compacted granular material is defined by:

$$\mu_{lock} = \frac{\rho_{grain}}{\rho_0} - 1 \tag{6.29}$$

When the air void is fully compressed out of the material, the third region steps into. In the third region, the concrete is assumed to be fully dense, and pressure volume response will act as a nonlinear elastic behavior. Under this situation, the modified volumetric strain is introduced:

$$\bar{\mu} = \frac{\mu - \mu_{lock}}{1 + \mu_{lock}} \tag{6.30}$$

where ρ_{grain} is the grain density. This was identical to the density of the material with no air voids. Usually, the grain density is set as density of coarse aggregates in the material. The behavior of material which follows a nonlinear elastic behavior can be expressed as:

$$P = K_1 \bar{\mu} + K_2 \bar{\mu}^2 + K_3 \bar{\mu}^3 \tag{6.31}$$

where, $\bar{\mu}$ is the modified volumetric strain defined in Equation 6.30. K_1, K_2 and K_3 is the constant when the material is fully compressed without voids. These values can be obtained from the curve fitting of the experiment data.

6.2.3 Plastic-Kinematic model

The Plastic-Kinematic model is an elastic-fully plastic model with kinematic hardening plasticity which is in accordance to Von Mises yield criterion. The kinematic hardening was achieved by maintaining the radius of yield surface at a fixed value by allowing the centre to move in the direction of the plastic strain.

Thus, the Von Mises yield criterion assumed that the initial yield or failure surface was independent of the hydrostatic stress and the third invariant of the deviatoric stress. Hence, it resulted in a circular shape with constant radius in deviatoric plane and similar values for uniaxial yield tensile stress and uniaxial yield compressive stress which is shown in Figure 6.9. The formula adopting the principal stress can be expressed as (Ottosen and Ristinmaa 2005):

$$\phi(J_2) = 0$$
$$\sqrt{3J_2} - \sigma_y = 0$$
$$\frac{1}{2} S_{ij} S_{ij} - \frac{\sigma_y^2}{3} = 0 \tag{6.32}$$

in which, J_2 represents the second invariant of the deviatoric stress s_{ij}, and σ_y is the yield stress.

6.2.4 Drucker-Prager model

The Drucker-Prager model was employed to model the behavior of the soil material, in which the cohesion and compaction behavior of the materials resulted in an increasing resistance to shear up to a limit value of yield strength as the pressure increase. In terms of the stress invariant I_1 and J_2, the Drucker-Prager criterion can be written in the form (Chen 1982):

$$f(I_1, J_2) = \sqrt{J_2} - \alpha I_1 - k = 0 \qquad\qquad (6.33)$$

where the two parameters α and k are positive material constants, which could be determined from laboratory test. Depending on the matched stress states, the material constants k and α may be related to the constants c and φ of the Mohr-Coulomb criterion in several ways (i.e. match along compressive meridian or tensile meridian). Figure 6.10 shows the Drucker-Prager failure criteria in meridian space.

In LS-DYNA, the soil properties was input as a series of Mohr-Coulomb parameters, and then the failure surface shape parameter was used to determine which meridian was matched along in Drucker-Prager model.

6.3 Validation I -Numerical simulation for normal concrete pavement slab and comparison with field measurement

6.3.1 Description of problem

The numerical model in this chapter was based on the full scale field blast test (ETSC2008). The simple information for the specimens would be given for understanding the numerical model, while the detailed information of the test and sample could be found in the previous Chapter 4.

In field blast trial test, two pavement slabs under blast loading were conducted, one was normal concrete pavement slab and the other was the proposed new material pavement slab, which was consisted of HSC, ECC and asphalt concrete reinforced with GST. In these two tests, an equivalent 7.3kg TNT explosive was placed at the center of the slab with the center of gravity of the charge at about 170mm above the slab. The two slabs were 2.8m by 2.8m and

0.275m thick. In the test site, four anchors were installed at 4 corners of the slab to prevent the slab rebound under blast loading. Figure 6.1 shows these two slabs placed in position before blast test.

6.3.1.1 Concrete material

The MAT72 R3 model described in section 6.2.2 was used to model the concrete in current study. The material properties for current normal concrete used in numerical simulation are summarized in Table 6.3. The EOS data used in this study is shown in Table 6.4. It should be noticed that the Equation of State for concrete with grade 40 was obtained based on scaling law. The detail information for scaling law could be found in Malvar et al. (1996).

Table 6.3 Material properties of concrete slab of grade 40

Parameters	Symbol	Units	Value
Young's modulus	E	GPa	27
Compressive strength	f_c	MPa	40
Tensile strength	f_t	MPa	3.5
Poisson's ratio	v	---	0.2
Density	ρ	kg/m^3	2400

Table 6.4 The EOS data for concrete with f_c=40 MPa

Volumetric strain	Pressure (MPa)	Unloading bulk modulus (GPa)
0	0	16.63
-0.0015	24.94	16.63
-0.0043	54.38	16.86
-0.0101	87.32	17.71
-0.0305	165.9	21.07
-0.0513	250.2	24.45
-0.0726	355	27.81
-0.0943	543	30.35
-0.174	3171	68.29
-0.208	4849	83.16

6.3.1.2 Steel material

Steel is an isotropic material having the same initial yield stress for both uniaxial tension and uniaxial compression. The Plastic-kinematic model in LS-DYNA was suitable to model isotropic and kinematic hardening plasticity with the option of including rate effects. It was a very cost effective model and available for beam and solid element. Thus for current simulation, this material model was employed to describe the behavior of the steel rebar. The steel bar was spatially discretized with beam-truss element, which was capable of sustaining only tension-compression. The material parameters of steel rebar used in this study were summarized in Table 6.5.

Table 6.5 Steel material properties

Parameters	Symbol	Units	Value
Young's modulus	E	MPa	207000
Yield stress	f_y	MPa	460
Poisson's ratio	ν	---	0.3
Density	ρ	kg/m^3	7850

6.2.2.4 Soil material

The Drucker-Prager model was used to model the soil material as mentioned in section 6.2.4. In the current study, it was assumed that the Drucker-Prager criterion matched along the compressive meridian of Mohr-Coulomb criterion. The soil parameters in the model were estimated from actual soil investigation performed on the test site (Wang et al. 2010) as shown in Table 6.6.

Table 6.6 Material properties of soil mass

Parameters	Symbol	Units	Value
Density	ρ	kg/m^3	2100
Shear modulus	G	MPa	13.8
Poisson's ratio	ν	---	0.3
Cohesion	C	kPa	62
Friction angle	φ	^{o}	26

6.3.2 Strain rate effect

6.3.2.1 Concrete DIF

The DIF versus strain rate relationship for most constitutive models were calibrated directly to peak strength data obtained using Split-Hopkinson Pressure Bar (SHPB) test. Figure 6.11 shows the compressive DIF data on different compressive strength of concrete. It was found that with the increase of the strain rate, the compressive stress of concrete would increase. The CEB recommended the DIF curve with two branches curve. The first DIF branch showed smooth increasing for compressive strength at the low strain rates, while the second DIF branch curve suddenly went up at the transit point. According to CEB, the transit point was 30s^{-1} for compression.

However, some researchers (Ross et al. 1989; Ross et al. 1996) found that the compressive DIFs obtained from SHPB should consider contribution from two

factors, one was the moisture effect at lower stain rates, and another was the lateral inertial confinement effect at higher stain rates. The moisture effect could seem as real strain rate behavior which was related to the material properties, while the inertial confinement effect was a pseudo-strain rate behavior which connected to the structural behavior.

In numerical modelling, the initial branch of the compressive DIF should be included since the constitutive model did not generally include the effects of moisture. The second phase of compressive DIF was mostly due to the inertial effect, and this inertial effect would be showing up in the numerical model (Magallanes et al. 2010). Thus, in the numerical model adopting second branch of compressive DIFs values obtained from the SHPB might duplicate the inertial effects.

In the current study, the compressive DIF curve would be modified. Only the first phase of the DIF curve would be considered. According to Li and Meng (2003), Zhou and Hao (2008), the inertial effect for the concrete-like material in numerical model would be showed up significantly after $200s^{-1}$, and thus the first phase of DIF curve would be taken until strain rate arrived at $200s^{-1}$. After then, the DIF curve was cutoff and behaved like a horizontal line.

In order to verify above concept, the validation process was employed, which was also adopted by Magallanes et al. (2010). The simulation of compressive SHPB test for plain concrete was carried out with three different input DIF curves, namely, rate-independent curve, CEB curve and modified CEB curve. The results from numerical compressive SHPB test were compared with that from real test data extracted from Wang (2011).

In the numerical model, the input bar, transmitted bar and plain concrete samples were modelled with 8-node solid element. As for the loading condition, the stress impulse was acted at one end of the input bar, which was the incident impulse measured at the incident bar during the test. The contact algorithm AUTOMATIC_SURFACE_TO_SURFACE was employed to simulate the interface between concrete and input bar, and between concrete and transmitted bar. The detailed information of model setting up could be found in Appendix A. The concrete was the plain concrete of grade 90, and thus for the DIF value, three curves were considered as shown in Figure 6.12. The results of transmitted stress history from numerical model and experimental data are summarized in Figure 6.13. From the figure, it is shown that the concrete model with rate-independent curve had the lowest stress, and concrete model with CEB curve overestimated the transmitted stress, which was due to duplicating of the inertial effects of the concrete, while for concrete with modified CEB curve showed similar increased stress. The detailed peak stress from numerical model and experimental data is listed in Table 6.7 to 6.9. It could be found that the stress from concrete model with modified CEB curve was close to that from experimental data. Hence, it could be concluded that the second branch of DIF behavior could be captured by the numerical model. In the following study, the compressive DIF for concrete-like material would adopt the modified DIF curve.

Table 6.7 Comparison with experimental data using rate-independent DIF curve

Stress level	Numerical results(MPa)	Experimental data (MPa)	Deviation
1	136	143	5%
2	152	173	12%
3	176	191	8%

Table 6.8 Comparison with experimental data using CEB DIF curve

Stress level	Numerical results(MPa)	Experimental data (MPa)	Deviation
1	163	143	14%
2	187	173	8%
3	229	191	20%

Table 6.9 Comparison with experimental data using modified CEB DIF curve

Stress level	Numerical results(MPa)	Experimental data (MPa)	Deviation
1	143	143	0%
2	170	173	2%
3	194.6	191	2%

Hence, in the current study, the dependence of DIF on strain rates for compression was determined and modified based on CEB:

$$DIF = \frac{f_{cd}}{f_{cs}} = \left(\frac{\dot{\varepsilon}}{\dot{\varepsilon}_s} \right)^{1.026\alpha_s} \qquad \text{for} \quad \dot{\varepsilon} \le 200 s^{-1} \qquad (6.34)$$

in which $\alpha_s = 1/(5 + 9 f_{cs}/10)$ and $\dot{\varepsilon}_s$ was static compressive strain rate $1 \times 10^{-5}\,\text{s}^{-1}$.

The test data for the tensile strength of concrete-like materials under a wide range of strain rates was plotted in Figure 6.14. It was found that the tensile stress increased with the increase of strain rate. The test data supported CEB formation that the tensile DIF is a two branches curve under strain rate. Malvar

and Ross (1998) further modified the CEB formation to make prediction more closer to test data at high strain rate and set the transit point at $1s^{-1}$ for the tensile DIF curve of concrete-like material. The first branch of the tensile DIF curve was due to the moisture effect in the concrete-like material (Ross et al. 1996). However, the second branch of the tensile DIF curve was seemed as the material-intrinsic behavior (Lu and Li 2011). The micro-mechanism model was developed by Lu and Li (2011) to investigate the factor contributing to the enhancement of the tensile strength under high strain rate. It was found that the micro-crack inertia was one of the mechanisms responsible for the increase of dynamic tensile strength with strain rate observed in the dynamic tensile tests on concrete-like materials. For the macroscopic level, the numerical analysis of direct dynamic test, dynamic splitting test and spalling tests by using MAT 72 R3 model with rate-independent curve were also conducted by Lu and Li (2011). It was found the numerical results from these three dynamic tests did not show any increase in tensile strength, which indicated that the strain rate enhancement of the tensile strength observed in dynamic tensile tests was a genuine material effect. Hence, in the macro-level numerical model, in order to reproduce the enhancement of the tensile strength under a wide range of strain rate, the tensile DIF curve with two branches should be considered. The tensile DIF values would adopt two branches curve as suggested by Malvar and Ross (1998) for concrete-like materials, of which the equation was expressed as:

$$DIF = \frac{f_{td}}{f_{ts}} = \left(\frac{\dot{\varepsilon}}{\dot{\varepsilon}_s}\right)^{\delta'} \qquad \text{for } \dot{\varepsilon} \leq 1s^{-1}$$

$$DIF = \frac{f_{td}}{f_{ts}} = \beta \left(\frac{\overset{\bullet}{\varepsilon}}{\overset{\bullet}{\varepsilon}_s} \right)^{1/3} \quad \text{for} \quad \overset{\bullet}{\varepsilon} > 1s^{-1} \tag{6.35}$$

where, $\delta' = 1/(1 + 8 f_c^{'}/10 MPa)$ with $\log \beta = 6\delta' - 2$ and $\overset{\bullet}{\varepsilon}_s$ is the static tensile strain rate $1 \times 10^{-6} s^{-1}$. The compressive and tensile DIF curve for concrete with grade 40 was shown in Figure 6.15

6.3.2.2 Steel rebar DIF

The strain rate effect for steel rebar was taken into account by using the Cowper and Symonds parameters into the Plastic-Kinematic model (Hallquist, 2006), as given in Equation 6.36.

$$\sigma_y = \left[1 + \left(\frac{\overset{\bullet}{\varepsilon}}{C_{pk}} \right)^{\frac{1}{P_{pk}}} \right] \left(\sigma_0 + \beta_{pk} E_P \varepsilon_{eff}^p \right) \tag{6.36}$$

in which, $\overset{\bullet}{\varepsilon}$ is the strain rate under dynamic loading, σ_0 is the static initial yield stress, E_P is the plastic modulus of the material, ε_{eff}^p is the effective plastic strain of the material. β_{pk} is a parameter that is used to determine the type of plastic hardening (Kinematic, isotropic, or a combination of kinematic and isotropic hardening). For β_{pk} equals to 0 and 1, respectively, kinematic and isotropic hardening could be chosen. For the current study, the elastic fully plastic material with kinematic hardening model was employed, and thus the additional stress of the isotropic hardening part $\beta_{pk} E_P \varepsilon_{eff}^p$ would not be considered ($\beta_{pk} = 0$). The two constants for strain rate behavior were then used: C_{pk} and P_{pk}. Due to lack of data for the C_{pk} and P_{pk} parameters, the strain rate relationship in Equation 6.37, which

was proposed by Malvar (1998) for the yield strength of steel reinforcements, was adopted as a reference in this study through curve fitting method.

$$DIF_T = \left(\frac{\dot{\varepsilon}}{10^{-4}} \right)^{\chi}$$

(6.37)

where $\dot{\varepsilon}$ is the strain rate for rebar ranging from 1 x 10^{-4} to $10s^{-1}$, $\chi = 0.074 - 0.0040(f_y / 414)$, and f_y is the rebar yield stress in MPa. It should be noted that this equation was only valid for yield stress varying from 290 to 710 MPa. For the current simulation, the yield stress of steel rebar was 460 MPa, and then via equating Equation 6.34 and 6.35, a non-linear curve fitting function was employed to obtain value C_{pk} and P_{pk} as 1080.5 and 5.48, respectively.

6.3.3 Blast loading

The LOAD_BLAST card in LS-DYNA was used to generate blast loading based on CONWEP. The CONWEP code in LS-DYNA could be used in two cases: free air detonation of a spherical charge and surface detonation of a hemispherical charge. It should be noticed that the blast pressure from CONWEP were obtained from full scale field test. The minimum scale distance in CONWEP was around 0.15 m/kg$^{1/3}$, which meant that the blast pressure would be accurate when the scale distance exceeded this certain range. However, when the scale distance was smaller than this value, the blast pressure in CONWEP was obtained through extrapolation from the blast pressure at 0.15 m/kg$^{1/3}$ scale distances, which may not be accurate.

For the current study, the charge weight of 7.3 kg was placed above slab with 170 mm height. Thus, the scale distance was 0.087 m/kg$^{1/3}$, and obviously

this scale distance should be classified into close-in range. The blast pressure obtained from CONWEP model might be no longer accurate. Hence, the blast pressure would be generated using software AUTODYN, and then applied on the surface of concrete slab as segment pressure.

In order to get correct blast pressure and impulse in this study, the parametric study was carried out. The 2D axsi-symetry model was built as shown in Figure 6.16, in which the slab was sitting on the soil and the TNT charge was detonated above the slab with the different height, which was related to different scale distance in the CONWEP. The comparison of blast pressure and impulse generated by AUTODYN and CONWEP was shown in Figure 6.17. In the figure, the dash line for the CONWEP part meant that the scale distance was out of range in CONWEP, and thus the results were obtained through extrapolation. For the close in scale distance such as 0.087 $m/kg^{1/3}$, due to the extreme conditions experienced at the target surface, the measurement of the blast pressure was not possible and in turn the direct validation of blast pressure generated from AUTODYN was also not feasible, and then an indirect method was employed to verify the blast pressure. This method could also be found in Wright and French (2008).

In the field test, one air pressure cell was placed at the 2 m away from the center of the concrete slab, and hence in the above numerical model, the one gauge point was allocated at the same location as that in the field test. Thus the blast pressure time history from gauge points in numerical model could validate against air pressure cell results in terms of peak pressure and impulse. It should be noticed that in axis-symmetry model in AUTODYN there was a circular slab instead of a rectangular shape. The total mass of the slab would be different from

227

the actual experimental model, which had a rectangular shape. One method to rectify this mass difference was adopting larger diameter of circle slab. However, based on the study by Showichen (2008) it was found that the results from both models were within 10 % deviation. Hence, in the current study, the 2D axsi-symetry model without considering mass difference was still employed to be compared with experimental data. The comparison result could be seen in Figure 6.18. From the figure, it is shown that the derivation of peak pressure between experiment and numerical model was limited to 10%. It could then be concluded that the blast pressure from current numerical model was accurate and further it could be derived that the blast pressure applied on the target surface from numerical model was almost as same as that in the field test since the incident pressure applied on air pressure cell was the result of the reflection of initial incident pressure acted on concrete slab. Thus, it could be concluded that the blast pressure generated by the AUTODYN in close-in range almost represented the real blast pressure.

Hence, the comparison of peak blast pressure and impulse generated by AUTODYN and CONWEP for different scale distance were carried out. The results are shown in Figure 6.17. In the figure, the 'E' represented the Eulerian element size used in AUTODYN simulation and the dash line represented the results for close-in blast range in CONWEP. From the figure, it can be found that for the close-in blast issues, the blast pressure might be underestimated by CONWEP while the impulse was overestimated by CONWEP. For the middle to far field blast range (solid line in Figure 6.17), both software gave the almost same results. As mentioned above, for the middle to far field range, the peak pressure and impulse from CONWEP were obtained from field tests and hence it was

demonstrated that AUTODYN could correctly replicate blast pressure using certain mesh size. Hence, in the current study the blast pressure would first be generated using software AUTODYN, and then it was applied on the surface of concrete slab as segment pressure.

6.3.4 Details of numerical model in validation I

6.3.4.1 Spatial discretization

A Lagrangrian description of the motion has been used for the model. The concrete slab and soil mass were discretized in space with one point gauss integration eight-node hexahedron elements. In current 3D numerical model, only a quarter of the concrete slab was modelling due to symmetry. Thus, the dimension of concrete slab in numerical model was taken as 1400 mm x 1400 mm x 275 mm. The concrete slab was sitting on the soil mass.

It was known that the range of soil mass would be important to the accuracy of the model. Several trials were conducted and it was found that when the thickness of soil mass was taken as 4 times of half-length concrete slab (4 x 1400 = 5600 mm) and the length of soil mass was taken as 5 times of half- length concrete slab (5 x 1400 = 7000 mm), the numerical results began to be stabilized. Thus in current study, the thickness and length of soil mass were taken as 5600 mm and 7000 mm, respectively.

The reinforcement bars were spatially discretized with beam elements. The reinforcement bars were assumed to be fully bonded with the concrete material. Thus, the concrete solid elements and reinforcement beam elements shared the

common nodes in the numerical model. The numerical model is shown in Figure 6.19.

6.3.4.2 Boundary condition

The anchor on the concrete slab was considered and simulated as the fixed points in the corresponding position in the numerical model. The soil mass was treated as a semi-infinite space. Thus, the non-reflection boundary was applied on the side and bottom of the soil mass.

The AUTOMATIC_SURFACE_TO_SURFACE contact algorithm was employed to simulate the interaction behavior of concrete slab and soil.

6.3.4.3 Mesh size

The element cells for the concrete slab had an aspect ratio of 1, which is suitable for simulating wave propagation in the concrete slab. Due to the computational time and capability, the bias mesh technology was adopted for the soil mass. In the central part of the soil mass, that is, with 1400 x 1400 mm^2, the mesh size was uniform with aspect ratio of 1, and then the mesh size gradually increased away from the center part of the soil mass. The mesh size within soil mass depth also used bias mesh technology. The mesh size was uniform in the first 600 mm depth, and then the mesh size gradually increased to the bottom part. The numerical model for mesh changing is shown in Figure 6.19.

In order to determine the adequacy of the meshes adopted in the current numerical models, two mesh sizes were considered. Mesh 1 and 2 were referred to element size 10 mm and 20 mm, respectively. The finer mesh size of 10 mm was the minimum achievable element size in current numerical model. The coarse

mesh size of 20 mm was also adopted, and the results of 20 mm mesh size were compared with that of 10 mm element size. The detail of the mesh data and computational time for the two mesh size is shown in Table 6.10.

Table 6.10 Mesh data and computing time for concrete slab

Mesh data	Mesh 1	Mesh 2
Element size	10x10x10 mm for solid elements 10 mm for beam elements	20x20x20 mm for solid elements 20 mm for beam elements
Nodes	4224607	1102623
8-node solid elements	4121490	1064190
Beam elements	1360	680
Total elements	4122850	1064870
Computational time	7 hours	1 hours 40 mins

From the mesh study on the numerical model, it was found that the model with 10 mm and 20 mm mesh sizes (geometric aspect ratio of 1:1:1 in concrete slab and central part of the soil mass) predicted similar deflection at the bottom of concrete slab as shown in Figure 6.20. However, in terms of crater diameter the results were not similar as shown in Figure 6.21. Closer examination of results for the two mesh sizes, it was found that although trend of the cracking propagation and main crack for the concrete slab were similar in both element sizes, the crater diameter predicted by 20 mm mesh size was much larger than 10 mm element size. It would be found in the later section that the crater diameter from 10 mm mesh size were closer to the experimental results. The fine mesh size would give more accurate results compared to the coarse mesh size. Hence, in the following numerical model dealing with blast loading, the mesh size of 10 mm would be employed.

6.3.5 Results and discussion of validation I

6.3.5.1 Damaged contour

Due to the non-symmetry of the charge weight, there were two obvious diameters for crater size which was perpendicular each other which are shown in Figure 6.22. The maximum diameter of the crater was about 1.2m and minimum one was around 0.4 m. Thus, the mean diameter of crater could be taken as (1.2+0.448)/2=0.844 m.

The damage contour of the concrete pavement slab under blast loading can be seen in Figure 6.23. In the figure, it is shown that the crater diameter predicted in the numerical model was 0.84 which was very close to that in the field trial test. After investigation of the bottom surface of the concrete pavement slab in the numerical model, it was found that a large piece of server cracks occurred at the center of the slab, and the whole thickness of the pavement slab was penetrated. This situation could be seen as fully damaged.

6.3.5.2 Acceleration

In the field trial test, the 4 accelerometers were installed at the mid-side of concrete slab. These accelerometers were used to measure the vertical and horizontal acceleration of concrete slab subjected to blast loading. For the Horizontal acceleration, due to the center of the charge was closer to one side of the concrete slab; there were two different horizontal acceleration readings. While in the numerical model, it was assumed that the explosive occurred in the center of the concrete slab. Thus, in this section, only the vertical acceleration from the field trial test was compared with that of numerical model. In the numerical model,

the raw nodal acceleration contained considerable numerical noise. The ELEMENT_SEATBELT_ACCELEROMETER could be used to eliminate numerical noise and obtain more accurate node acceleration. The comparison of acceleration from field trial test and numerical model is summarized in Table 6.11. From the table, it is found that the variation of vertical acceleration between field trial test and numerical model was around 5%, and the numerical model predicted higher vertical acceleration than field trial test. However, in view of the inherent uncertainties in the field trial test, prediction of 5% deviation from field trial test results in numerical model was acceptable.

Table 6.11 Vertical acceleration of the concrete slab

Item	Field trial test	Numerical result	Deviation from field trial test
Max. vertical acceleration (m/s^2)	22820	23978	5 %

6.3.5.3 Total pressure cell

Besides the crater and crack pattern, the results of total pressure cell under the slab can be compared with that from numerical model. The layout of the TPC in field trial test was showed in Figure 6.24. The stress values in the corresponding points in the numerical model were compared with pressure cell readings from field trial test, which is summarized in Table 6.12. From the table, it is seen that the pressure value from numerical model showed well agreement with that from field trial test. For the TPC1, although no pressure reading from trial test was obtained, the numerical model predicted around 10 MPa. This value seemed to exceed the maximum range of total pressure cell and destroyed the pressure cell. From above analysis, it could be concluded that the current 3D numerical model

of concrete pavement slab under blast loading could simulate the real case properly.

Table 6.12 Peak reading for total pressure cell

Item	Field trial test (kPa)	Numerical result (kPa)	Deviation from field trial test
TPC1	---	10828	---
TPC2	178	166	6.7 %
TPC3	152	156	2.6 %

6.4 Validation II - Numerical simulation for proposed multi-layers pavement slab and comparison with field measurement

6.4.1 Asphalt model

Asphalt is made of bitumen binder and coarse aggregate. It showed thermo-elasto-plastic behavior under static and dynamic loading. The compressive and tensile strength of the asphalt material was usually decreasing with the increase of temperature. According to Tan et al. (1993), the Drucker-Prager yield function could be employed to predict the behavior of asphalt mixture before failure loading. Seibi et al. (2001) and Park et al. (2005) also used the Drucker-Prager yield function to simulate the asphalt concrete under high strain loading (strain rate from $0.0001s^{-1}$ to $0.0701s^{-1}$) with implementation of strain rate sensitive feature. However, these models did not have damage factor to describe the post-peak behavior of the asphalt concrete. Tashman et al. (2005) developed a microstructure-based vsico-plastic continuum model to take into account the effect of temperature and the damage factor in asphalt concrete. It was found that the model predictions were in a good agreement with the experimental data. However, it was difficult to use due to 20 parameters needed to be determined in

order to model properly. Tang et al. (2009) adopted the Holmquist-Johnson-Cook (HJC) material model to simulate the asphalt concrete subjected to high strain rate rates ($35s^{-1}$ to $100s^{-1}$). However, it was found that HJC material model cannot simulate the tensile softening behavior of the material, and would overestimate the tensile strength of material (Loria, et al. 2008).

In the current study, MAT72 R3 model would be used to simulate asphalt concrete. This model cannot consider the temperature effect. However, during the blast event, the temperature suddenly increases to thousand degrees in few microseconds, and then drop quickly in the propagation distance. Based on field test, it could be found that only central part of asphalt was destroyed by combination of the high degree temperature and blast pressure, and with the increase of distance from the center, the asphalt was failure mainly due to blast pressure. Further, the MAT72 R3 had the damage factor to describe the material's post-peak and post-peak behavior.

6.4.1.1 Strength Surface

As mentioned in previous section, the MAT72 R3 in LSDYNA had three strength surfaces: maximum strength surface, residual strength surface and yield surface. The eight parameters for these three surfaces could be obtained through curve fitting to the experimental data. Available data was extracted from Park et al. (2005) with the compressive strength f_c=0.311 MPa. Figure 6.25 shows the determination of three surfaces by curve fitting for f_c=0.311 MPa asphalt concrete. The intersection point of maximum strength surface and residual strength surface was so called brittle to ductile point. This point should be determined by experimental data under high confining pressure. However, it was difficult to

decide this point in strength surface since no experimental data was available for asphalt concrete. Based on the experimental data for concrete material, this points was usually taken as $p/f_c=3.878$. Considering size and strength of aggregates used in asphalt concrete and concrete was almost same, hence in this study the brittle to ductile points for asphalt concrete was taken as same as that for concrete. This value may be conservative for asphalt concrete due to the higher content of coarse aggregate mixed in the asphalt concrete, however, in terms of the simulation results, this value was acceptable. The parameters for $f_c=0.311$ MPa asphalt concrete are summarized in Table 6.13:

Table 6.13 Three surface parameters for $f_c=0.311$ MPa asphalt concrete

Parameters	Value
a_0	0.14
a_1	0.60
a_2	0.20
a_{0y}	0.08
a_{1y}	2.00
a_{2y}	0.70
a_{1f}	0.70
a_{2f}	0.0055

6.4.1.2 Scaling of strength surface

If new asphalt concrete with known unconfined compression strength $f'_{c,new}$ was to be modeled, but its strength surfaces were otherwise unknown, then one way of scaling data from a known material is proposed as follows (Malvar et al. 1996):

$$r = \frac{f'_{c,new}}{f'_{c,old}} \tag{6.38}$$

where $f'_{c,old}$ is the unconfined compressive strength for a previously modelled

asphalt concrete. Then the new material strength surface can then be taken as:

$$\Delta\sigma_n = a_{0n} + \frac{p}{a_{1n} + a_{2n}p}$$ (6.39)

in which $a_{0n} = a_0 r, a_{1n} = a_1, a_{2n} = a_2/r$.

The new asphalt concrete with unconfined compressive strength f_c=0.8

MPa (Tashman et al. 2005) was used to validate the parameters obtained from

scaling method. Figure 6.26 shows the maximum strength surface determined by

scaling method. It can be seen that the maximum strength surface fitted very well

with the experimental data, and thus it could be concluded that the parameters for

asphalt concrete with different compressive strength could be obtained by scaling

method.

In current study, the unconfined compressive strength for asphalt concrete

was 4.6 MPa and the tensile strength was 0.7 MPa at 35°C. Hence, by using

scaling method, the strength parameters could be obtained, which is shown in

Table 6.14. The three strength surface is plotted in Figure 6.27.

Table 6.14 Parameters for f_c=4.6 MPa asphalt concrete

Parameter	Value
a_0	2.071
a_1	0.6
a_2	0.0135
a_{0y}	1.183
a_{1y}	2.00
a_{2y}	0.0473
a_{1f}	0.70
a_{2f}	0.0037

6.4.1.3 Damage factor

The stress hardening and softening pairs (η, λ) in the Equations 6.20 and 6.21 described the concrete material behavior transmitted from the yield surface to the maximum strength surface and from maximum strength surface to the residual strength surface respectively. The parameter η would vary from 0 to 1 depending on the accumulated effective plastic strain parameter λ as mentioned in section 6.2.2. However, it was found that the original damage factor pairs (η, λ) in MAT72 R3 model was only suitable for concrete and not for the asphalt concrete. This is because the asphalt concrete would have higher plastic failure strain. Thus, for the current study the input accumulated effective plastic strain λ was modified. Based on the uniaxial compressive test for asphalt concrete, it was shown that at peak stress the corresponding strain was approximately 0.023 and the final failure strain was about 0.1. While for the normal concrete material, the corresponding strain at the peak stress was around 0.0022. Hence, the λ should be modified to give the high failure strain for asphalt concrete. After few trials, it was found that when the modified λ was adjusted to 10 times of original λ the numerical results

238

seemed to show well agreement with experimental results of unconfined compressive test for asphalt concrete. Figure 6.28 shows the modified and original series of (η, λ) pairs. From the figure, it could be seen that the modified damage factor made smoother descending than original damage factor, and had a higher failure strain.

6.4.1.4 Equation of state

The Equation of State (EOS) data for concrete materials was usually obtained by triaxial compressive test (Hansson et al. 2001) and flyer-plate-impact test (Gebbeken et al. 2006). There were few EOS data for asphalt concrete. The available EOS data is for asphalt concrete with compressive strength f_c=3.8 MPa (Tang et al., 2009). The parameters are summarized in Table 6.12.

In MAT72 R3 model, the EOS data was input as tabulated curve of pressure-volume pairs. Hence, according to Table 6.15, the input data could be obtained for f_c=3.8 MPa asphalt concrete and summarized in Table 6.16.

Table 6.15 EOS parameters for f_c=3.8 MPa asphalt concrete (Tang et al. 2009)

Parameters	Value
Density ρ_0 (g/cm^3)	2.47
Young's modulus E (MPa)	553
Poisson's ratio	0.39
Elastic bulk modulus $K_{elastic}$ (MPa)	838
P_{crush} (MPa)	1.26
μ_{crush}	0.0015
P_{lock} (MPa)	60
ρ_{grain} (g/cm^3)	2.7
μ_{lock}	0.093
K_1 (MPa)	27000
K_2 (MPa)	154000
K_3 (MPa)	690000

Table 6.16 EOS input data in MAT72R3 for f_c=3.8 MPa

Volumetric strain	Pressure (MPa)	Unloading bulk modulus (MPa)
0	0	838
-0.0015	1.2666	838
-0.0043	3.5	1833
-0.0101	6.75	3280
-0.0305	19.5	8960
-0.0513	33	14973
-0.0726	48	21655
-0.0943	179	27000
-0.174	4091	27000
-0.208	7162	27000

For the current study, the compressive strength for asphalt concrete was f_c=4.6 MPa. Thus, the tabulated curve of pressure-volume pairs could be calculated according to scaling method (Malvar et al. 1996). In this method, assuming that new data would be obtained at the same volumetric strains, and thus the new data corresponding pressure (pc_{new}) would be:

$$pc_{new} = pc_{old} \sqrt{r} \tag{6.40}$$

and the new corresponding unloading bulk modulus (ku_{new}) would be:

$$ku_{new} = ku_{old}\sqrt{r}$$

(6.41)

The parameter r is the scaling factor which is the same as defined in Equation 6.38. Hence, the parameters of the EOS data for f_c=4.6 MPa are listed as follows:

Table 6.17 EOS input data in MAT72R3 for f_c=4.6 MPa

Volumetric strain	Pressure (MPa)	Unloading bulk modulus (MPa)
0	0.00	922
-0.0015	1.39	922
-0.0043	3.85	2016
-0.0101	7.43	3609
-0.0305	21.45	9858
-0.0513	36.31	16474
-0.0726	52.81	23825
-0.0943	196.94	29706
-0.174	4501.08	29706
-0.208	7879.91	29706

6.4.1.5 Softening parameter b1, b2 and b3

The softening parameters controlled the concrete softening behavior after peak stress in uniaxial compression, uniaxial tension and triaxial tension. These parameters could be obtained through curve fitting from the available experimental data.

A) b_1 from uniaxial compressive test

The uniaxial compressive test was conducted according to ASTM 1074. The asphalt concrete was stored in oven with 35°C for at least 8 hours before test. The stain gages and LVDTs were employed to measure the Young's modulus,

axial strain and axial displacement during the uniaxial compressive test. The test results are shown in Figure 6.29. From the figure, it is shown that the corresponding strain at peak stress was about 0.023 and the final failure strain was about 0.1, which was higher than that for concrete material. It was also shown that asphalt material was more ductile than concrete with short descending part. The average compressive strength from the test was 4.6 MPa. The Young's modulus was obtained from stain gauge attached at the middle height of sample, and measured as 598 MPa.

Thus, the compressive energy G_c for current asphalt material could be obtained through integrating of stress-displacement curve. The typical strain-displacement curve is shown in Figure 6.30. From the figure, it can be calculated that the compressive energy G_c in the current study was 15.1 MPa mm. Hence, the b_1 for different element size were obtained through single element simulation as suggested in section 6.2.2. The b_1 values for 20 mm and 10 mm mesh size are then summarized as follows:

Table 6.18 b1 value for different mesh size

Mesh size E (mm)	G_c/E	b_1
20	0.76	3.45
10	1.51	4.20

B) b_2 from fractural test

The parameter b_2 was determined using fracture energy G_f, which was obtained from uniaxial tensile test or three points Single-edge Notched Beam test (SNB). In the current study, the SNB test was employed to determine G_f. This method was often used to investigate the fracture energy for concrete material. In the SNB test, the fracture toughness K_{IC} needed to be firstly decided. The Effect Crack Model (ECM) as suggested by Karihaloo and Nallathambi (1990) was used

to calculate K_{IC}, which reflected the non-linear load-deflection behavior prior to the attainment of the peak load. The detailed description of the ECM could be referred to Karihaloo and Nallathambi (1990), and Kim and Hussein (1997).

The SNB test was carried out in the current study. The compacted asphalt concrete beam was fabricated with the dimensions of 400 mm length by 100 mm wide by 100 mm depth. A mechanical notch was saw to depth of 20 mm, which had a ratio of notch to beam depth (a_0/W) 0.2. The sample was loaded under a simply supported with a span length of 340 mm in the temperature 35°C. The dimensions for the sample are summarized as:

Table 6.19 Sample size for SNB test

Parameters	Value
L (mm)	400
W (mm)	100
T (mm)	100
S (mm)	340
α_0(mm)	20

The typical load-deflection curve from the SNB test is shown in Figure 6.31. The average fracture toughness K_{IC} for 3 samples was 12.2 $MPa\sqrt{mm}$. Therefore, the fracture energy G_f could be obtained through:

$$G_f = \frac{(1-v^2)K_{IC}^2}{E} \tag{6.42}$$

where, E is the elastic modulus and v is the possion's ratio.

The parameter b_2 was further determined by assigning fracture energy G_f in the use of single element simulation. Changing the parameter b_2 iteratively until the area under stress-stain curve from single element simulation coincided with

G_f / w_c. The parameters obtained from SNB and single element simulation for

f_c=4.6 MPa asphalt concrete are summarized in Table 6.20.

Table 6.20 Parameters from SNB and single element simulation

Parameters	Value
K_{IC} (MPa • mm ^{½})	12.2
v	0.35
E (MPa)	598
G_f (MPa • mm)	0.221
w_c (mm)	40
G_f/w_c	0.00554
f_t (MPa)	0.7
b_2	0.2

The b_3 parameter adopted the default value in MAT72 R3 model due to the

lack of test data. However, it was found that this value seem to be acceptable for

the simulation of asphalt concrete.

6.4.2 Strain rate effect for asphalt material

6.4.2.1 Dynamic increase factor for compression

The dynamic compressive strength of asphalt concrete under different

strain rates could be obtained by using Servo hydraulic machine and Split

Hopkinson Pressure Bar (SHPB). The strain rate produced by servo hydraulic

machine was about 10^{-5} to 10^{0} s^{-1}, and the higher strain rate could be generated by

SHPB test. The theory and test configuration for compressive SHPB test for

asphalt concrete could be referred to the Appendix A. Herein only the results of

dynamic increase factor (DIF) under different strain rate from SHPB and servo

hydraulic machine would be presented and discussed. The dependence of DIF on

strain rate is illustrated in Figure 6.32. From the figure, it can be found that the

DIF was increasing with the increase of strain rates. Compared with DIF curves for normal concrete (Figure 6.12), it is found that the enhancement of DIF values for asphalt concrete was higher than that of concrete-like materials at the same strain rate. This might be due to the asphalt concrete had higher content of coarse aggregates compared to concrete material. The aggregate would rearrange under dynamic loading. However, it is also shown that the DIF value increased sharply at the certain strain rate, which was same as the behavior of the concrete-like material. This was because that the inertial effect stepped in. After curve fitting for current asphalt concrete DIF data, two branches curve was obtained as shown in Figure 6.32. The transmit point was found at $100s^{-1}$. Hence, the dependence of DIF on strain rate for asphalt concrete under compression was proposed as following:

$$DIF = \frac{f_d}{f_s} = 3.18 + 1.098 \log_{10}(\dot{\varepsilon}) + 0.1397 \log_{10}^{2}(\dot{\varepsilon}) \quad \text{for } \dot{\varepsilon} \leq 100s^{-1}$$

$$DIF = \frac{f_d}{f_s} = 21.39 \log_{10}(\dot{\varepsilon}) - 36.76 \qquad \text{for } 100s^{-1} < \dot{\varepsilon} \leq 200s^{-1} \qquad (6.43)$$

As analyzed above, when concrete-like material subjected to dynamic loading, the enhancement of DIF values was due to the combination of structural inertial effect and material property. The numerical model would capture the material property such as moisture and rearrangement of aggregate through inputting DIF curve. The inertial effect could be simulated by using adequate mesh without the second branch DIF curve. To deicide the input DIF curve for the asphalt concrete in the numerical model, the compressive SHPB test was simulated using MAT72 R3 model. The test configuration could be referred to Appendix A. Three DIF curves were considered in the numerical model. Curve 1,

which used the rate-dependent curve. Curve 2 which used above proposed DIF curve with two branches. Curve 3, which used the modified proposed DIF curve with only the first branch as shown in Figure 6.33.

The results of transmitting pulse from transmit bar in numerical model and experiment are shown in Figure 6.34. From the figure, it is shown that the asphalt concrete with modified DIF had similar increased strength value compared to the experimental data. This phenomenon was as same as concrete material under high strain loading, in which the second branch of DIF behavior could be captured by the numerical model. The detailed peak stress from the experimental data and numerical model is listed in the Table 6.21 to 6.23. It could be observed that the stress obtained from material model with modified DIF curve had smallest deviation from that from the experimental data. Hence, the modified DIF curves for asphalt concrete would be implemented in the numerical model, and is expressed as:

$$DIF = \frac{f_d}{f_s} = 3.18 + 1.098\log_{10}(\dot{\varepsilon}) + 0.1397\log_{10}^2(\dot{\varepsilon}) \quad \text{for } \dot{\varepsilon} \leq 200 s^{-1} \tag{6.44}$$

Table 6.21 Comparison with experimental data using rate-independent DIF curve

Stress level	Numerical results(MPa)	Experimental data (MPa)	Deviation
1	7.6	30	75%
2	7.9	37	78%

Table 6.22 Comparison with experimental data using two branches DIF curve

Stress level	Numerical results(MPa)	Experimental data (MPa)	Deviation
1	50	30	66%
2	56	37	51%

Table 6.23 Comparison with experimental data using modified DIF curve

Stress level	Numerical results(MPa)	Experimental data (MPa)	Deviation
1	31	30	3%
2	37.2	37	1%

6.4.2.2 Dynamic increase factor for tension

The splitting tensile test was used to determine the splitting tensile strength for the concrete-like materials under quasi-static loading. In the current study, for the high strain loading, the SHPB setting up was employed for conducting the dynamic splitting tensile test. The configuration of the test and sample information could be seen in Appendix A. The test results for dynamic tensile strength of asphalt concrete are shown in Figure 6.35. From the figure, it can be seen that the splitting tension strength enhanced with the increase of the strain rates with two branch enhancement curves. After curve fitting from the test data, the transition point was found to locate at $15s^{-1}$. The post-experimental picture revealed that the binder failure and trans-aggregate failure had occurred during the dynamic loading, which was consistent with observation from Tekalur et al. (2009). The stress wave within the specimen would go through the aggregated or binder material under dynamic loading while under the static loading, the failure usually occurred at the weakest component (interfacial zone) within the specimen. Thus the dynamic strength of the asphalt concrete under high strain rate would enhance due to the tensile strength of aggregate and binder. The dependence of DIF on strain rate for asphalt concrete under tension was proposed based on experimental data:

$$DIF = \frac{f_d}{f_s} = 1.86 + 0.1432 \log_{10}(\dot{\varepsilon}) \quad \text{for } \dot{\varepsilon} \leq 15s^{-1}$$

$$DIF = \frac{f_d}{f_s} = 6.06\log_{10}(\dot{\varepsilon}) - 5.024 \quad \text{for } 15s^{-1} \le \dot{\varepsilon} \le 100s^{-1} \tag{6.45}$$

From the experimental results, it was found that the strain rate dependency of the asphalt concrete was the material properties. For the macro-level numerical model, since the MAT 72 R3 material model cannot capture the aggregate interlocking that propagates the micro-cracking and energy dissipation beyond the localization zone (Magallanes et al. 2010; Lu and Li 2011), the tensile DIF curve with two branches should be considered. Thus, the tensile and compressive DIF curves of asphalt concrete used in numerical model are summarized in Figure 6.36.

6.4.3 Geogrid model

From the lab test, it was found that the geogrid reinforcement would enhance the tensile strength of the asphalt concrete layer. Thus, in the numerical model, it was necessary to consider the function of the geogrid material. One method was to implement of geogrid into the asphalt pavement. Another method was that using higher value of tensile strength for asphalt material. In the current study, the first method was adopted. The geogrid reinforcements were simulated with 4-node Belytschko-Tsay shell element formulation in LS-DYNA due to its computational efficiency. One integration point was assigned in the shell element that allowed no bending resistance, which was appropriate assumption for the geogrid material. The thickness of the shell element was taken as the average between the rib and the junction thickness, which was 2.4 mm for MG-100 geogrid.

Since the geogrid material showed the bilinear stress-strain behavior, in which had hardening behavior after initial yield point (as shown in Figure 6.37),

the Plastic-Kinematic model was employed to simulate the behavior of geogrid. Although Plastic-Kinematic model could not fully describe the nonlinear behavior of geogrid material, the bilinear aspect of the model could in part consider the strain hardening phenomenon observed in geogrid tensile load test. The parameters for geogrid in plastic-kinematic model were determined by fitting the bilinear curve with experimental load strain curve, which is shown in Figure 6.37. The parameters for geogrid used in simulation are summarized in Table 6.24.

Table 6.24 Parameters for Geogrid MG-100 using Plastic-Kinematic model

Parameters	Symbol	Units	Value
Density	ρ	kg/m^3	1030
Young's modulus	E	MPa	500
Poisson's ratio	ν	---	0.3
Yield stress	σ_y	MPa	7.5
Tangent modulus	E_t	MPa	333
Thickness	t	mm	2.4
Erosion strain	ε_s	---	0.038

6.4.4 High strength concrete and ECC model

The MAT72 R3 model would be used to simulate high strength concrete (HSC) and ECC material. For the HSC, the procedure to decide parameters was same as that for normal concrete. The energy G_c and G_f for compression and tension were obtained from strain-stress curve recommended by CEB. The parameters for high strength concrete are illustrated in Table 6.25.

Table 6.25 Material properties of high strength concrete

Parameters	Symbol	Units	Value
Young's modulus	E	GPa	33
Compressive strength	f_c	MPa	55
Tensile strength	f_t	MPa	4.35
Poisson's ratio	v	---	0.2
Density	ρ	kg/m^3	2400

The dependence of DIF on strain rate adopted the equation recommended by CEB. However, as mentioned above, the first branch of compressive DIF curve would be suitable for numerical modelling the effects of moisture for concrete under high strain rate. The second branch of compressive DIF values could be captured by the numerical model if the adequate mesh was adopted. Adopting second branch of compressive DIF curve may duplicate the inertial effects. Hence, only the first branch of compressive DIF curve would be employed in the numerical model for high strength concrete. The tensile and compressive DIF curves used in numerical model was shown in Figure 6.38.

The ECC material was first simulated by Lee (2006) and it was shown that the MAT72 R3 was very suitable for modelling ECC material under dynamic loading such as impact and blast loading. Hence, the MAT72 R3 would be employed in the current study to simulate the ECC. The material property of ECC in current study was given in Table 6.26.

Table 6.26 Material properties of ECC

Parameters	Symbol	Units	Value
Young's modulus	E	GPa	18
Compressive strength	f_c	MPa	64
Tensile strength	f_t	MPa	5
Poisson's ratio	v	---	0.22
Density	ρ	kg/m^3	2080

The strain rate equation was recommended by Lee (2006), and hence the compressive DIF equations for ECC material could be described as follows:

$$DIF_{ECC.compression} = \frac{f_{cd}}{f_{cs}} = \left(\frac{\dot{\varepsilon}}{\dot{\varepsilon}_s}\right)^{1.026\alpha_s} \quad \text{for } \dot{\varepsilon} \le 30S^{-1}$$

$$DIF_{ECC.compression} = \frac{f_{cd}}{f_{cs}} = \gamma_s \left(\frac{\dot{\varepsilon}}{\dot{\varepsilon}_s}\right)^{1/3} \quad \text{for } \dot{\varepsilon} > 30S^{-1} \tag{6.46}$$

with $\alpha_s = 1/(5 + 9 f_{cs}/10MPa)$ and $\log \gamma_s = 6.15\alpha_s - 2$

where $\dot{\varepsilon}$ is compressive strain rate ranging from $30 \times 10^{-6} \text{s}^{-1}$ to 300 s^{-1}, and $\dot{\varepsilon}_s$ is the static compressive strain rate $30 \times 10^{-6} \text{ s}^{-1}$. From the above equation, it is showed that there were two branches behavior for ECC material. Since the second branch were mostly due to the inertial effects as mentioned in previous section, and would be automatically showed up in the numerical model given sufficient mesh, only the first branch would be adopted in the numerical model. Then the dependence of DIF on strain rate for ECC material was modified and expressed as:

$$DIF_{ECC.compression} = \frac{f_{cd}}{f_{cs}} = \left(\frac{\dot{\varepsilon}}{\dot{\varepsilon}_s}\right)^{1.026\alpha_s} \quad \text{for } \dot{\varepsilon} \le 200s^{-1} \tag{6.47}$$

in which $\alpha_s = 1/(5 + 9 f_{cs}/10MPa)$

The dynamic tensile behavior of ECC under different strain rate ranging from 2×10^{-6} to 0.2s^{-1} was studied by Maalej et al. (2005), and the tensile DIF curve was proposed as follows:

$$DIF_{ECC(tension)} = 2.0213 \times \dot{\varepsilon}^{0.0576} \quad \text{for } \dot{\varepsilon} \le 1s^{-1}$$

$$DIF_{ECC(tension)} = \beta(\dot{\varepsilon}/\dot{\varepsilon}_{st})^{1/3} \quad \text{for } \dot{\varepsilon} > 1s^{-1} \tag{6.48}$$

251

with $\beta = 1/(1+8f_c^{'}/10MPa)$

where $\dot{\varepsilon}_{st}$ was the static tensile strain rate $1\times10^{-6}s^{-1}$.

Hence, the tensile and compressive DIF curves used in numerical model are shown in Figure 6.39.

6.4.5 Interface between asphalt concrete and HSC

As discussed in Chapter 5, the TIEBREAK contact algorithm was suitable to simulate the shear and tensile behavior of interface between the asphalt concrete and HSC in the proposed new material pavement.

The interface of asphalt concrete and HSC would bear dynamic loading. Based on Sadd et al. (2007), it was found that the dynamic shear strength of the interface would be 4 times the static shear strength. However, it should be noticed that in their study, the concrete was directly cast on the top surface of asphalt which had a better micro-structural connection between asphalt and concrete compared to current interface which was fabricated by applying asphalt on the cured concrete surface without tack coat. Hence, the dynamic shear strength in current interface might not enhance too much. In the current study, it was assumed that there was no enhancement of shear strength for the interface between asphalt concrete and HSC.

As for the interfacial tensile strength, it was much lower than interfacial shear strength. Current data on tensile strength of asphalt and concrete was studied by Sadd et al. (2007). It was found that the tensile strength was 0.14 MPa for 30 days old asphalt and 0.3 MPa for 180-200 days old asphalt, which made tensile energy released rate G_I range from 0.3 N/mm to 0.4 N/mm. It should be noted that in their experiment, the concrete was directly cast on the top surface of asphalt

which obviously enhanced the interfacial tensile strength and that was why the tensile strength would increase with the day. In current study, no tack coat was applied on the interface, and only the bitumen binder severed as connecter between the asphalt and HSC. It could be postulated that the value of interfacial tensile strength and tensile energy released rate might be much smaller compared to that in Sadd, et al. (2007)'s test. Hence, the tensile energy released rate G_I for the interface between asphalt concrete and HSC was assumed to be 0.25 N/mm in this study. The parameters for interface simulation could be referred in Table 5. 1.

6.4.6 Details of numerical model in validation II

A Lagrangrian description of the motion was used for the model. The proposed new material pavement slab and soil mass were discretized in space with one point gauss integration eight-node hexahedron element. In current 3D numerical model, only a quarter of the concrete slab was modelling due to symmetry. Thus, the dimension of concrete slab in numerical model was taken as 1400 mm x 1400 mm x 275 mm. The proposed new material pavement was sitting on the soil mass.

For the soil domain, the size was taken as same as that in the simulation of concrete pavement slab, in which the thickness and length of soil mass, were taken as 5600 mm and 7000 mm, respectively.

Like the case of the simulation of concrete pavement slab, the reinforcement bars were spatially discretized with beam elements and assumed to be fully bonded with the ECC material (in the field trial test, the rebar was placed in the layer of ECC).Thus, the ECC solid elements and reinforcement beam elements shared the common nodes in the numerical model.

The element cells for the proposed new material pavement slab had an aspect ratio of 1, and the bias mesh technology was also adopted for simulation of the soil mass, which was same as that used in the simulation of concrete pavement slab discussed in Section 6.2. The mesh size for proposed new material pavement slab was taken 10 mm which was suitable for modelling the pavement slab under blast loading as mentioned in Section 6.3. The numerical model is shown in Figure 6.40.

The anchor on the proposed new material pavement slab was considered and simulated as the fixed points in the corresponding position in the numerical model. The soil mass was treated as a semi-infinite space. Thus, the non-reflection boundary was applied on the side and bottom of the soil mass. The AUTOMATIC_SURFACE_TO_SURFACE contact algorithm was employed to simulate the interaction between the pavement slab and the soil mass.

6.4.7 Results and discussion of validation II

6.4.7.1 Damaged contour

The damaged situation for proposed multi-layers pavement in field trial test is given in Figure 6.41 and 6.42. In Figure 6.41, it is shown that the blast pressure destroyed the upper section of the asphalt layer above the geogrid reinforcement and only center of the geogrid piece was burned off during the blast event. Figure 6.42 shows the resulting damage more clearly with the top section of asphalt removed. From the figure, it can be seen that the crater was very shallow and did not punch through the whole layer and a crater of around 0.7m diameter and depth of 100mm was formed on the HSC layer

The damaged pattern for asphalt concrete layer is shown in Figure 6.43(a). From the figure, it is observed that the damage pattern for asphalt surface was not similar as compared with that from field trial test. This was because the bomb was placed at the center of the slab in the field test, and thus one side of the asphalt was server damaged. However, the shear cracking related to anchor point was found in the numerical model, which was similar to that in field trial test. It could be concluded that the basic failure mechanism was similar from both results. Since the proposed multi-layers pavement was a composite material system, it was necessary to look into each layer to check the integrity of the pavement slab. Damage patterns for the each layer are illustrated in Figure 6.43 (b) and (c).

Figure 6.43 (b) shows the damage pattern for HSC layer. From the figure, it is shown that the damaged pattern was similar with that in field trial test (Figure 6.42). The diameter of crater was about 0.75 m in numerical model which was quiet close to that in field trial test. As shown in Figure 6.43 (b), the shear cracks were also found at the anchor points. Based on damaged pattern in field trial test, the crater on the HSC top face was seemed to be shallow one. However, after checking the bottom face of HSC layer in numerical model, it was found that most of the bottom face shows a large piece of severe cracks.. This might be due to combination of the bending of the HSC layer under blast load and the reflection of stress wave at the interface. In the numerical model, the interface between HSC and ECC was assumed to be fully bonded. The ECC was more flexible than HSC, and thus it would cause the tensile stress at the bottom face of HSC layer when deformed together. The compression stress wave from the top face would also travel within the HSC layer and reflect as a tension stress at the interface which is

so called spalling phenomenon. Hence, based on the damage pattern in the numerical model, the HSC layer was taken as failure.

Figure 6.43 (c) shows the damage pattern for ECC layer. From the figure, only a small part of moderate cracks was found at the center of top face. Some severe cracks were found at the bottom face. The most of the severe cracks concentrated at the center part of the bottom face. The bending behavior happened in the ECC layer subjected to blast loading; however, due to high ductility, the bottom face suffered less damaged compared to that in the normal concrete (Figure 6.23) and high strength concrete pavement slab (Figure 6.43 (b)). It could be concluded that the proposed multi-layers pavement slab kept its integrity under blast loading. Only asphalt concrete and HSC layers need to be repaired or replaced.

6.4.7.2 Acceleration

The ELEMENT_SEATBELT_ACCELEROMETER was used to obtain accurate node acceleration. The vertical acceleration from the field trial test was compared with that of numerical model Table 6.27 lists vertical acceleration from field trial test and numerical model. From the table, it is found that the variation of vertical acceleration between field trial test and numerical model was around 10%, and the numerical model predicted higher vertical acceleration than field trial test. This was due to the ECC and HSC layers were not well compacted in the field test which cause not even density distribution, while in the numerical model the ECC and HSC was assumed to be well compacted and the density was kept constant within the layers.

Table 6.27 Vertical acceleration of the proposed new material pavement slab

Item	Field trial test	Numerical result	Deviation from field trial test
Max. vertical acceleration (m/s^2)	35400	38870	10 %

6.4.7.3 Total pressure cell

The stress values in the corresponding points in the numerical model were compared with pressure cell readings from field trial test, which is summarized in Table 6.28. From the table, it is seen that the pressure value from numerical model showed to be close to that from field trial test for TPC2, while for TPC3, the deviation was about 20% from the field trial test. This might be possible that not well compaction of pavement slab in the field test and soil situation was not same as that under Slab1. However, in view of the inherent uncertainties in the field trial test, prediction of 20% deviation from field trial test results in numerical model was still acceptable.

For the TPC1, although no pressure reading was taken from the field trial test, the numerical model predicted around 13 MPa. This value seemed to exceed the maximum range of total pressure cell and would destroy the pressure cell.

From above analysis, it could be concluded that the current 3D numerical model could simulate actual dynamic behavior of proposed new material pavement slab under blast loading in terms of the crater diameter and the propagation of crack. The acceleration and pressure from numerical model showed well agreement to that from field trial test.

Table 6.28 Peak reading for total pressure cell

Item	Field trial test (kPa)	Numerical result (kPa)	Deviation from field trial test
TPC1	---	13393	---
TPC2	273	267	2 %
TPC3	200	241	20 %

6.5 Parametric study for proposed multi-layers pavement slab

In above section, the numerical model for proposed multi-layers pavement slab under blast loading was validated based on measurement from the field trial test. It could be concluded that the 3D numerical model using AUTODYN plus LS-DYNA with advanced material model MAT 72 R3 could simulate or model the real behavior at site properly. Hence, in this section, the parametric study will be carried out to further investigate the factors that might enhance the capability of blast resistance of the proposed multi-layers pavement slab, subjected to various blast loads. This will enable the development of a design chart as discuss in the next section.

6.5.1 Effect of property of HSC layer

The HSC layer in the field trial test (ETSC 2008) and numerical model was seemed as the key component to resist the blast loading. This is because the asphalt surface functions as a sacrifice surface to dissipate a fraction of the total blast energy, while most of blast energy was passed on to the HSC layer immediately below. Hence, it was important to enhance the performance of HSC layer under blast loading, so as the overall performance of the proposed multi-layers pavement, under blast loading, can be enhanced effectively.

6.5.1.1 Compressive strength

Blast resistance of a pavement material is a function of its compressive strength. Herein, one of the key parameters for evaluating the blast resistance of pavement material is the compressive strength of the HSC layer. A parametric study was conducted with f_c of 90 MPa and 110 MPa. As a comparison, a normal concrete with f_c of 40 MPa was also included in this parametric study. The key input for f_c=40 MPa concrete were showed in Table 6.3. For the high strength concrete HSC with f_c=90 and 110 MPa compressive strength, the key parameters are listed in Table 6.29.

Table 6.29 Material properties of HSC used in parametric study

Parameters	Symbol	Units	f_c=90 MPa	f_c=110 MPa*
Young's modulus	E	GPa	40	46.7
Compressive strength	f_c	MPa	90	110
Tensile strength	f_t	MPa	6.04	6.06
Poisson's ratio	v	---	0.2	0.2
Density	ρ	kg/m^3	2500	2500

* Data adopted from CEB-FIP (2008)

The parametric study was considered with three varying HSC properties, while the other materials (asphalt, ECC and foundation soil), its thickness and the blast loading remained the same as that mentioned in section 6.4. It simulated the field trial test ETSC 2008.

(i) Results

The result of this study is discussed here. The damage pattern for the proposed multi-layers pavement with different HSC grade was plotted from Figure 6.44 to 6.45. In these figures, the damage pattern for HSC and ECC were illustrated, while the damage pattern for asphalt concrete was not included. This is because that the behavior of the HSC and ECC layer was the key components to

the blast resistance of the proposed multi-layers pavement, and it is more meaningful to show the post-failure behavior HSC and ECC.

From the figure, it is shown that the HSC layers in three cases were penetrated through under blast loading, while the integrity of the ECC layer was remained. According to Figure 6.44, it is found that for HSC layers with the increase of the compressive strength, the amount of cracks increased. This is because for the plain concrete material (with no additional fibers), the higher compressive strength would induce more brittle behavior. The brittle behavior of the plain concrete material could be considered in the numerical simulation.

(ii) Discussion

In numerical simulation of the concrete material, the stress-displacement of uniaxial compression and uniaxial tension would be used to determine the b_1 and b_2 value which was shown in Figure 6.46 and 6.47. The stress-displacement of uniaxial compression was employed to decide the energy absorption of crack due to compression, while the stress-displacement of uniaxial tension was used to determine the energy absorption of crack due to tensile (tensile fracture energy). The area under stress-displacement curve represented the energy absorption of the crack. The higher value meant the larger energy was needed to develop crack. It should be noticed that the only the post-peak stress-displacement was used to calculate the energy absorption. In Figure 6.46, the arrow pointed out the peak stress for each concrete grade. It can be found that the energy absorption of the crack due to compression for the concrete with grade 40 was larger than that of grade 90 and 110. At the same time, it was also shown the ultimate displacement after peak stress for the concrete with grade 40 was larger than that of grade 90 and 110. Combination of the energy absorption and ultimate displacement, it

could be observed that the concrete with higher compressive strength tended to brittle failure with less deformation, while the concrete with low compressive strength would more ductile with much deformation. Figure 6.47 shows the tensile fracture energy (energy absorption of the crack due to tension) used in numerical simulation for the concrete with different grade. It was clear that the concrete with grade 90 had higher tensile fracture energy. This could explain the phenomenon that the outer sides of the HSC (grade 90) top face and the bottom face of the HSC (grade 90) in Figure 6.44 showed less damage area compared with other two concrete materials. The tensile failure occurred at the outer side and the bottom of the HSC due to the reflection of the tensile stress at the free boundary. Hence, the higher fracture energy would lead to less tensile failure. The tensile fracture energy for the concrete with grade 110 was higher than that of grade 40, while the ultimate displacement for the concrete of grade 40 was larger than that of grade 110. From Figure 6.44, it is shown that the outer side of the HSC top surface for the grade 40 suffered less damage than that for grade 110. Thus, it could be deduced that the ultimate displacement after peak stress would be one of the key factor to determine the extent of the damage level for the material. Since the concrete of grade 40 had larger ultimate displacement for the tensile failure, the amount of the severe crack due to the tensile stress was less than that of grade 110.

It was also found that in Figure 6.44, the center part for the HSC layer with grade 90 and 110 had larger damage area than that of grade 40. This might be due to the damage factor b_1 governing issue. The material at the periphery of the center part (highlighted by black circle in Figure 6.44) would fail due to the tension force. For the material in the center part, at the initial loading, the material was under triaxial compression state ($\sigma_1 < \sigma_2 < \sigma_3 < 0$). Then the blast pressure

decayed to zero within very short duration, and this would cause unloading state of the material and thus lead to the biaxial compression state ($\sigma_2 < \sigma_3 < \sigma_1 = 0$). With the failure of the material at the periphery of the center part, the material in the center part would suffer the unloading state in one direction, and cause the shear failure of the material (biaxial compression). In this biaxial stress state, the damage factor b_1 would govern damage level due to the positive hydrostatic pressure (p>0 in Equation 6.21a). Based on Figure 6.46, the higher grade of concrete would have low energy absorption of crack under compression. Hence, the concrete of grade 40 would have larger failure strain after the peak state than that of the concrete of grade 90 and 110, which showed sudden failure after peak state. Under this circumstance, for the concrete of grade 90 and 110, the material at the center part would show fast progressive failure from the outer to inner once the peripheral material failed. While for the concrete of grade 40, since the material could bear large failure stain, and the speed of the material failure would be lower than that of grade 90 and 110. Hence, the concrete of grade 40 would show less damage.

The analysis of the proposed multi-layers pavement under different blast loading was conducted to illustrate the trend of the crack propagation in the HSC layer. In this analysis, the HSC was taken as grade 110, while other materials (asphalt concrete, ECC and soil foundation) remained same as that in section 6.4. The blast pressure acted on the pavement surface was scaled based on the blast pressure from 0.018 m/kg$^{1/3}$ scale distance. Four scaled blast pressure were used, that is, 20%, 40%, 60% and 80%. The results are summarized in Figure 6.48. From the figure, it was shown when the pressure was low, the center part of the pavement suffered less damage due to its high strength, while the outer part

suffered less damage due to its higher tensile fracture energy. With the increase of the blast pressure, the severe cracking first developed in the anchor point and then propagated inward. The progressive failure of the outer part caused the occurrence of damage at the center part.

(iii) Summary

As seen from the above analysis, it was found that the bottom of the HSC layer failed due to the tensile stress, and all the HSC layers was penetrated through regardless of the compressive strength. For the design purpose, it was not recommended to use HSC layers with higher compressive strength. This was due to that the HSC with higher compressive strength was more brittle. It was then concluded that for the blast resistance, further increasing of the compressive strength of the material would make little contribution to decrease the penetration depth. As for HSC of grade 90, although the whole HSC layer needed to be repaired, the ECC layer suffered light damage. Hence, for the current study the optimum compressive strength for HSC layers was around 90 MPa in the proposed multi-layer pavement.

6.5.1.2 Fracture energy

According to the numerical results in section 6.4.7, it was shown that the bottom face of HSC layer had large part of severe damage area due to the occurrence of the tensile wave. From the literature review, it was found that the incorporation of steel fiber in the concrete material would significantly decrease cracking and crack propagation, and minimize spalling and retain post-peak load-carrying capacity. The implementation of steel fiber into the plain concrete would increase the fracture energy of the material and in turns minimize the amount of

crack. Hence, in this parametric study, the fracture energy of the HSC was considered to be a parameter. According to Nyström and Gylltoft (2011), the fracture energy of the plain concrete would reach 2, 4, 6 N/mm for different volume of fiber added into concrete mixture.

The parametric study was considered with three fracture energy for HSC layer, while the other materials (asphalt, ECC and foundation soil), its compressive strength and thickness and the blast loading remained the same as that mentioned in section 6.4. It simulated the field trial test ETSC 2008. The fracture energy for HSC layer is listed in Table 6.30.

Table 6.30 Fracture energy for HSC layer in proposed multi-layer pavement

Case No.	Fracture energy G_f (N/mm)	Related steel fiber content (%)
1	2	0.2
2	4	0.5
3	6	0.75

(i) Results and discussion

The results for HSC layer with different fracture energy are shown in Figure 6.49. From Figure 6.49, it is shown that the top face of the HSC layer had less severe damage area compared to that without steel fibers (Figure 6.43). Although the tensile failure still occurred at the bottom face of the HSC layer, the severe damage area was smaller than that without steel fibers (Figure 6.43). Figure 6.50 showed the damage pattern of the cross section of the HSC layer, it is observed that for all the three cases, the severe cracks occurred in the center part at the bottom of the HSC layer, and this severe crack did not propagate through the whole thickness. Thus, it could be concluded that whole HSC layer was not penetrated through and thus the integrity of the HSC layer was retained. According to Figure 6.49, it could be concluded that the implementation of steel

fiber in the HSC significantly decreased the damage area and cracking at the top surface. This conclusion was consistent with the finding (Lok and Pei 1997) that the high strength concrete with reinforced steel fibers would significantly decrease cracking and crack propagation, and minimize spalling and retain post-peak load-carrying capacity compared with that of the normal strength concrete. However, it was also observed that with the increase of concentration of the steel fiber (higher fracture energy), the damage pattern of the HSC layer did not change so much, which was also consistent with conclusion of Lok and Pei (1997). In this study, after 0.5% steel fiber, no significant blast resistance was obtained.

Figure 6.51 shows the damage pattern of ECC layers overlaid by HSC with different fracture energy. From the figure, it is observed that some severe cracks occurred at the top and bottom face of the ECC layer, but the amount of the severe cracks was small. The integrity of the ECC was still kept since the whole layer was not penetrated through. It is also found that with the various fracture energy of the HSC layer, the damage pattern for the ECC layer was almost same. It was then deduced that the energy transmitted from the HSC layer might be same. For the proposed multi-layers pavement, it was found that when the amount of steel fibers in HSC layers exceeded certain values, further increasing the steel fibers would not enhance the blast resistance of the proposed multi-layer pavement significantly.

(ii) Summary

From above analysis, it can be concluded that the implementation of the steel fibers in the plain concrete would increase the fracture energy of the material. With the increase of the fracture energy, the amount of cracks due to tension decreased significantly. The higher fracture energy also minimized the amount of

the tensile crack at the top surface of the HSC layer, and this would in turns remain the confinement stress for the center part material, which caused less damage. Although the tensile failure still occurred at the rear face, the damage area was much smaller than that without steel fibers. The integrity of the HSC layer was retained since the whole HSC layer was not penetrated through. Hence, there was no need to repair this layer after blast loading, and only refilling the asphalt concrete would be needed.

6.5.1.3 Thickness of HSC layer

The increased thickness of the pavement would increase the stiffness of the pavement structures and in turns increase the bending resistance subjected to blast. However, the thickness of the pavement slab cannot increase without limit. Thicker pavement slab would bring larger additional bending stress due to thermal expansion in the concrete-like materials. Usually, the thickness of the concrete slab in rigid pavement design was about 200 to 300 mm. Hence, in the current parametric study, the thickness of the HSC and ECC layer was to be investigated for its effect to the performance of pavement under blast loading.

The parametric study was considered with various thickness of the HSC and ECC layer, while the other materials (asphalt, and foundation soil), compressive strength of HSC and ECC, and the blast loading remained the same as that mentioned in section 6.4. Two sets of the thickness were considered. Set 1 is that the thickness of the ECC was kept constant at 100 mm and the thickness of the HSC layer was changed to make the total thickness of the HSC and ECC layer to about 220 mm to 300 mm. Set 2 run was done with both HSC and ECC thickness, divided equally and the total thickness of the HSC and ECC layer was

kept to the same as that in Set 1. The detailed dimensions of these two sets of experiment are listed in Table 6.31.

Table 6.31 Thickness of HSC and ECC layer used in the parametric study

No.	ECC thickness (mm)	HSC thickness (mm)	Total thickness (mm)
Set 1	100	120	220
		140	240
		200	300
Set 2	110	110	220
	120	120	240
	150	150	300

The numerical results of these two sets were summarized below:

i) Results of Set 1

The results for the parametric study of Set 1 are summarized in Figure 6.52 to 6.55. For Set 1, the thickness of the HSC layer was changing while the thickness of the ECC layer was kept constant. From Figure 6.52, it is shown that for the HSC layer varied from thickness of 120 mm to 140 mm, the damage pattern at the top face of the HSC layer slightly changed. The results also revealed that the HSC layer of 200mm thickness showed significantly reduced severe cracks and less damage area. It was observed that the severe cracks within the center part (area highlighted by black circle line) reduced with the increase of the thickness of the HSC layer. This was because the stiffness of the HSC layer increased with the thickness of the layer, and in turns reduced the relative displacement at the both side, which led to be less tensile cracks. However, it could be found that most of the bottom face of the HSC layer was severely damaged regardless of the thickness. This is due to the occurrence of the tensile wave at the bottom face. Figure 6.53 plots the damage pattern of the cross section

of the HSC with different thickness. According to the figure, it was observed that for all the three cases, the severe tensile crack occurred at the bottom and propagated upwards. For the HSC layer with 120 mm thickness, the severe tensile cracks connected to the compressive crack at the top face, and induced the penetration of the HSC layer. For the HSC layer with 140 mm thickness, the severe tensile cracks propagated upwards, and the only thin layer at the top remained undamaged. For the HSC layer with 200 mm thickness, the severe tensile cracks propagated upwards to almost ¾ of the whole thickness. It was deduced that with the thicker layer of the HSC, the phenomenon of the penetration for the HSC layer could be overcome. However, it should be noticed that with the increase of the thickness of HSC layer, the improvement of the blast resistance for the HSC layer was not significant even the thickness increased to 2 times the original thickness.

Figure 6.54 shows the damage pattern of the ECC layer. It was observed that with the increase of the overlaid HSC thickness, the damage pattern of the ECC layer showed reduced amount of cracks. For the top face of the ECC layer, only small amount of severe cracks were found with a number of lighter and moderate cracks. For the bottom face of the ECC layer, the severe cracks were found at the center part for the first 2 cases. With the increase of the overlaid HSC thickness, the severe cracks were reduced. This is due to less amount of blast energy being transmitted by the thicker HSC layer. Figure 6.55 plots the cross section of ECC layer after blast loading. It is observed that the some tensile cracks occurred at the center part and propagated upwards, however, these cracks were stopped at the half height of the thickness due to the excellent ductile behavior of the ECC materials. With the increase of the overlaid HSC thickness, the severe

tensile cracks reduced. The ECC layer was not penetrated through under these three cases, and hence the integrity of the ECC layer was remained. The damage level of the ECC layer was belong to light damage, and thus could be further used without being repaired.

ii) Results of Set 2

The results for the parametric study of Set 2 are summarized in Figure 6.56 to 6.59. From Figure 6.56, it was found that the most of the bottom face of the HSC layer was in severe damaged due to the tensile wave. This same trend was found earlier for the HSC layer in Set 1, that is, the severe cracks at the center part (area highlighted by black circle line) reduced with the increase of the thickness of the HSC layer. Furthermore, the damage pattern and the damaged area at the top face of the HSC layer was reduced with the increase of the HSC layer. The damage pattern of cross section of the HSC layer is given in Figure 6.57. From the figure, it was observed that for HSC with 110 and 120 mm thickness, the whole HSC layer was penetrated through at the center part due to the propagation of the tensile wave. For the HSC with 150 mm thickness, the severe tensile cracks were stopped at certain depth, and the HSC layer was not penetrated through at the center part.

Figure 6.58 summarizes the damage pattern of the ECC layer for Set 2. In the figure, it is shown that for ECC layer with all these three thickness, some cracks to different degree. It should be noticed that in Set 2, the damaged pattern of the ECC layer was slightly better than that in Set 1. The comparison between Set 1 and Set 2 can be illustrated by comparing Figure 6.55 and 6.59, which is reproduced in Figure 6.60 as three pairs. From Figure 6.60 of three pairs of comparison, it is clearly that:

1) Comparing pair #1 between (120 mm HSC + 100 mm ECC in Set 1) and (110 mm HSC + 110 mm ECC in Set 2): Since the thickness of both HSC and ECC in Set 1 and 2 are about the same, the response of crack pattern is almost the same.

2) Comparing pair #2 between (140 mm HSC + 100 mm ECC in Set 1) and (120 mm HSC + 120 mm ECC in Set 2): It is clear that the thicker HSC in Set 1 reduced the area of tension damage in bottom of ECC as marked in X. However, at the center portion, marked as Y, the Set 1 which has thinner ECC will have larger cracked region as compared to Set 2.

3) Comparing pair #3 between (200 mm HSC + 100 mm ECC in Set 1) and (150 mm HSC + 150 mm ECC in Set 2): The effect of thicker HSC , thus reducing the reflected tension crack at the bottom of ECC is obvious shown. It can be concluded that with at least 150 mm thickness of HSC, the ECC (with thickness at least 100 mm) will not have tension crack at the bottom face. At the center portion, the damage is limited to a lot smaller region.

From above analysis, it could be found that the thicker HSC is used to reduce the bottom reflect tension in ECC due to high bending capacity of thicker HSC. In addition, thicker ECC will help to reduce the crack at the center portion due to its high ductility. Thus the optimum thickness of HSC and ECC seem to be about 150 – 200 mm and 150 mm respectively.

iii) Summary

In the proposed multi-layer pavement, the HSC was designed to sustain high compressive stress of the blast loading due to its high compressive strength, while the ECC layer was used to bear bending force due to its high ductility. The

thicker ECC layer would have better bending resistance. For the increase of the thickness of the HSC layer, it was found that the tensile wave could still propagate upwards and arrived about ¾ of the height. Based on two sets of parametric study, it was found that the increasing of the HSC thickness would make little contribution to prevent being penetrated though for the HSC layers, but significantly reduced the tension cracks at the bottom of ECC layer. The equal thickness for the HSC and ECC layer might be better configuration for blast loading, since the bending resistance of the ECC layer would be enhanced.

6.5.2 Interface strength between asphalt concrete and HSC

It is well known that the interface strength would affect the behavior of the composite material significantly. In the current research, the proposed multi-layers pavement was a composite system which was consisted of asphalt concrete, HSC and ECC layers. The interfacial properties between the asphalt concrete layer and HSC layer had been explored in this research. The asphalt concrete layer was directly placed on the top of the HSC layers without application of bonding materials. However, in the practice, it was common to apply the bonding material in order to achieve better performance of the pavement structure. Hence, in this section, the investigation will be conducted on the effect of interface strength on the performance of the proposed multi-layers pavement subjected to blast loading.

The parametric study was considered with various interfacial properties between asphalt concrete and HSC layer, while the other materials (asphalt concrete, HSC, ECC and foundation soil), and the blast loading remained the same as that mentioned in section 6.4. In summary, the top layer is 75 mm thick of

asphalt concrete, followed by 100 mm thick of HSC, at then 100 mm thick of ECC.

The fracture released energy G_I and G_{II} were used as parameters to assess the tensile strength and shear strength for the interface, respectively. From the laboratory direct shear test, the G_{II} was found to be 5.75 N/mm under the constant normal pressure 2.1 MPa. In the parametric study, to study the effects of fracture released energy G_I and G_{II}, two sets of test were considered: Set 1 with tensile fracture released energy G_I of 0.5, 1.0 and 1.5 N/mm under the constant G_{II} of 5.75 N/mm; Set 2 with constant G_I at 0.25 N/mm with the varying G_{II} of 10, 20 and 30 N/mm. It should be noticed that for the fracture released energy $\underline{G_I=1.5}$ $\underline{\text{N/mm}}$, its corresponding <u>tensile strength</u> was about 0.3 MPa and for the fracture released energy $\underline{G_{II}=30 \text{ N/mm}}$, its corresponding <u>shear strength</u> was about 6 MPa. The parameters for interface comparison are summarized in Table 6.32.

Table 6.32 Interface properties used in parametric study

Case No.	G_I (N/mm)	G_{II} (N/mm)
	0.5	5.75
Set 1	1.0	5.75
	1.5	5.75
	0.25	10
Set 2	0.25	20
	0.25	30

The numerical results of these two sets were summarized below:

<u>i) Effect of G_I</u> :

The damage pattern of the upper surface of HSC layer for different tensile fracture energy G_I is illustrated in Figure 6.61. In the figure, it is found that the damage pattern of the HSC layer was similar for different G_I values. The dimension of the crater was also found to be about the same under these three

cases. For the bottom face, it is shown that the damage area was the same for these three cases. The whole HSC layer was completely penetrated under the blast loading.

The damage patterns of the ECC layers for different tensile fracture energy G_I are given in Figure 6.62. According to the figure, it is shown that the damage pattern at the top and bottom face of the ECC layer was almost same under these three cases. Hence, it could be deduced that increasing tensile fracture energy G_I could not enhance the blast resistance of the proposed multi-layers pavement significantly.

ii) Effect of G_{II} :

The damage patterns for the HSC layer under different shear fracture energy G_{II} are shown in Figure 6.63. From the figure, it is shown that the crater diameter was found to be about the same for the different G_{II} values. The whole HSC layers were penetrated through under the blast loading. However, for the top surface, it is also shown that the crack-lines were found to be more concentrate at the center with higher density with increasing shear fracture released energy G_{II}. This was because that increasing the G_{II} would enhance the interfacial shear strength correspondingly, which might exceed the shear strength of HSC and asphalt concrete layer. Under this circumstance, the shear failure would occur at the surface asphalt concrete layer but not the interface. For the bottom face of the HSC layer, the damage pattern was almost the same irrespective to G_I and G_{II} (Figure 6.41 and 6.43), which indicates tensile failure due to weak tensile strength.

Figure 6.64 shows the damage patterns of the ECC layers under different shear fracture energy G_{II}. Based on the figure, it is shown that the damage pattern

and damage area at the top and bottom face of the ECC layer was similar under these three cases.

iii) Summary

From the parametric study, it could be concluded that the increase of the released energy G_I and G_{II} might not enhance the blast resistance of the proposal multi-layers pavement significantly. The HSC layer was still penetrated through irrespective to G_I and G_{II} values. This might be due to the magnitude of the tensile and shear strength of the interface material was much lower than that of blast loading. Thus, the increase of the G_I and G_{II} did not show higher blast resistance of the proposed multi-layers pavement under severe blast load.

6.5.3 Strength of subgrade soil foundation

During the conventional pavement design, the strength of the subgrade soil foundation was seemed as the key parameters to acquire the well performance of the pavement under normal aircraft and vehicle loading. As for the weak subgrade soil foundation, the settlement of the pavement would be larger under static loading and it may be difficult for aircraft to taxi. Hence, in this section, the effect of the subgrade soil foundation to the pavement behavior will be further explored for dynamic blast event.

In recent years, the cement treated soil was mostly used in the many ground improvement projects. Addition of the cement to the soft soil would significantly enhance the shear strength of the soil foundation and thus have higher bearing capacity. The parametric study was considered with various stiffness of the soil, while the other materials (asphalt concrete, HSC and ECC material), and the blast loading remained the same as that mentioned in section 6.4.

The assumption of the soil parameters used in parametric study is listed in Table 6.33.

Table 6.33 Material properties of treated and untreated soil

Parameters	Symbol	Units	Treated soil*	Untreated soil
Density	ρ	kg/m^3	2100	2100
Shear modulus	G	MPa	61.5	13.8
Poisson's ratio	ν	---	0.3	0.3
Cohesion	C	kPa	239	62
Friction angle	φ	$^{\mathrm{o}}$	41.5	26

* Data adopted from Xiao (2009)

The results of the parametric study using numercial model for treated soil foundation are shown in Figure 6.65 to 6.70. For comprison, the results for the proposed multi-layers pavement with untreated soil foundation are also included in the figure. As shown in Figure 6.65, the asphalt concrete layer showed similar damage pattern in those two different soil foundations. For the asphalt concrete layer under cement treated soil foundation, the damage level mark in red in some areas was slightly lower than that under untreated soil foundation. However, the whole piece of asphalt concerte layer for both cases was totally penetrated through and destroied,

For the HSC layer, as shown in Figure 6.66, it is found that the damage pattern under cement treated soil foundation was better than that under untreated soil foundation in terms of the amount of cracks at top face and damage area at bottom surface. This might be due to the stiffer soil foundation makes the HSC layer deform less, and hence less tensile stress developed. Figure 6.67 shows the cross section of the HSC layer. It is observed that for both cases, the whole HSC layer was penetrated through at the center part.

For the ECC layer as shown in Figure 6.68, it is seen that the damage level for cement treated soil foundation was slightly higher than that for untreated soil

foundation. This is possible due to the higher stiffness of the cement treated soil foundation and providing a strong supprot to restrict the deformation of the pavement structure. Hence, the ECC layer could not deform too much to dissipate its energy. As seen in Figure 6.68, for the bottom face of the ECC layer under cement treated soil foundation, the severe cracks was concertrated in the center part, and the damage area was slightly smaller than that for untreated soil foundation but with intensity at the center. However, according to the cross section view of the ECC layer as shown in Figure 6.69, it was found that the whole ECC layer was not penetrated through. This could be attributed to the high ductile property of the ECC material. Figure 6.70 shows the enlarged picture of these cross-sections.

The settlement for the center part of the pavement is shown in Figure 6.71, it is expected that the settlement of pavement with cement treated soil foundation is found to be 50% lower than that with untreated soil foundation. It should be pointed out that although the aim of the proposed multi-layers pavment was to reduce the stress disturbation to the soil foundation when pavment structure subjected to blast loading, the settlement of the pavement structure was also the key factor. The results of less amount of settlment in the pavement structure would be considered as a positive point to maintain the integrity of the runway. Moreover, the cement treated soil foudantion would have higher bearing capacity which could sustain high energy from the overlaid pavement structures. Based on this idea, it was suggested that for the proposed multi-layers pamvent system, the sub-soil condition needed to be improved (e.g. using cement treament) to achieve higher bearing capacity.

6.5.4 Effect of blast loading from different burst height

In the current study, the burst height of 170 mm above the top of pavement slab was considered. With the increase of the burst height, the blast pressure and impulse would change. The damage pattern for the proposed multi-layers pavement under different burst height was investigated. In this section, the proposed multi-layers pavement under different burst height of blast loading was studied, while other materials (i.e. asphalt concrete, HSC and ECC) and TNT charge weight remained the same as that stated in section 6.4.

The three burst heights were considered, that is, 200, 300 and 400 mm above the top of the pavement slab at the center, and the charge weight was kept at 7.3 kg equivalent TNT. Hence, the corresponding scaled distance was 0.1, 0.15, 0.2 $m/kg^{1/3}$. As mentioned section 6.3.3, the COWEP method was used to conjugate the blast pressure, and then imported onto LSDYNA. This method was considered as accurate when the scaled distance is above 0.15 $m/kg^{1/3}$.

The COWEP method in LSDYNA assumed the planar blast wave front when blast wave reached the target, which meant that the whole piece of target sustained same magnitude blast pressure as shown in Figure 6.72 (a). This simplified is correct when the target is relatively small. However, in the current study, the target is a large piece of the pavement and cannot seem as the small area. During the blast event, the blast pressure would decrease in terms of distance and time when acting at the target as indicated in Figure 6.72 (b). Hence, in this study, the blast pressure was extracted from AUTODYN software and then applied as segment pressure in LSDYNA. The different area in the target would have blast pressure with different magnitude. The results were summarized below.

i) Burst height of 200 mm

The results for different burst heights are shown in Figure 6.73 to 6.77. For the burst height of 200 mm, the asphalt concrete was in severe damage as shown in Figure 6.73 (a). Figure 6.74 (a) shows that the HSC layer for H=200 mm suffered severe damage, which was similar to that under burst height of 170 mm as in baseline case. The cross section view of the HSC is shown in Figure 6.76 (a). It was found that the whole HSC layer was totally penetrated through at the center part. Then, it could be concluded that with burst height of 200 mm, the asphalt concrete layer and HSC layer needed to be repaired for subsequent use. However, For the ECC layers, it was shown that only a few severe cracks developed at the top and bottom face from Figure 6.75 (a). Checking with the cross section view of the ECC layer as shown in Figure 6.77 (a), it was found the severe cracks did not propagate through the thickness and the integrity of the layer was kept. Hence, the ECC layer could be regarded as moderate damage.

ii) Burst height of 300 mm

For the burst height of 300 mm, it could be seen that the asphalt concrete layer suffered moderate damage as shown in Figure 6.73 (b). The whole layer was partially destroyed at the center part under this blast loading. From Figure 6.74 (b), it is found that only a few severe cracks occurred at the top surface of the HSC layer. At the bottom face, the severe cracks occupied most of the area. Figure 6.76 (b) illustrates the cross section view of the HSC layer. It is found that the severe cracks propagated from the bottom face at the center part, but was stopped at the mid-height, and the whole HSC layer did not penetrated through. For the ECC layer as shown in Figure 6.75 (b), only a few moderate cracks were found at the center part of the top face. The light and moderate cracks developed at the bottom

face and the damage area occupied about one quarter of the total bottom surface. The cross section view of the ECC layer (Figure 6.77 (b)) showed that few severe cracks occurred. The whole ECC layer was not penetrated through. Under this circumstance, only the asphalt concrete layer needed to be repaired, the HSC and ECC layer was assessed to be suitable for subsequent used without being repaired.

iii) Burst height of 400 mm

For the burst height of 400 mm, Figure 6.73 (c) shows that the asphalt concrete layers kept its perfect integrity and only few cracking was found near the boundary, which was due to the stress reflection at the free boundary in the numerical model. The severe cracks were also found at the anchor point. However, this anchored is needed in this case because only a small piece of pavement material was constructed. In practice, a much larger piece of the asphalt concrete will be constructed with sufficient lateral restraint. Hence no anchor points are needed. For the HSC layer as shown in Figure 6.74 (c), the top face showed some severe shear cracks near the anchor point, which might not be found in the practice. The bottom face showed severe damage at the center part and the damage area was about one quarter of the total bottom face. Figure 6.76 (c) shows the cross section of the HSC layer. It is observed that the severe tensile cracks propagated upward to about half height of the thickness. The HSC layer was not penetrated through. Hence, the HSC layer could be considered as intact, and can be subjected to subsequent use after some repair.

According to Figure 6.76 (c) and 6.76 (c), the integrity of the HSC and the ECC layer was maintained without having any severe cracks. Thus, for the 400 mm burst height, the proposed multi-layers pavement could be repeatedly used after blast loading.

iv) Summary

From the above analysis, it could be seen that for the burst height of 200 mm, the HSC layer was still in the range of severe to moderate damage, and the integrity was destroyed. Under this circumstance, the HSC and asphalt concrete layer needed to be repaired before further use. For the burst height of 300 mm and 400 mm, the damage situation for three layers was in the range of moderate to light damage. Only minor repair needed to be conducted on the proposed multi-layers pavement structure. Hence, the burst height of 200 mm could be seen as the threshold for severe damage of the proposed multi-layers pavement. When the burst height was smaller than 200 mm, the asphalt concrete and HSC layer needed to be repaired. The burst height of 400 mm was set as the threshold for light damage. After this range, the whole pavement could be used without being repaired. From the burst height 200 mm to 400 mm, the range of moderate damage stepped into, in which the asphalt concrete layer needed to be replaced, the HSC layers could be rapidly repaired without being replaced whole piece.

The damaged pattern chart was developed, based on the scaled distance for burst height of 200 to 400 mm, in Figure 6.78. In the figure, the horizontal and vertical line represented the standoff and TNT equivalent charge weight respectively. Three threshold lines were listed in the figure to represent the damage pattern of the proposed multi-layers pavement under blast loading. Pink line was the contact detonation. If the point located at the left side of this line, it meant that the whole pavement slab would be destroyed and the repair needed for whole pavement, sometimes the underneath soil will also needed to be re-compacted. The red dotted line is for scaled distance $Z=0.1$ m/kg$^{1/3}$, corresponding to 200 mm burst height. If the point is located at the region between the contact

detonation line and Z=0.1 m/kg$^{1/3}$, the proposed multi-layers pavement slab would suffer moderate to severe damage, in which HSC layer and asphalt concrete have to be replaced to further use. The blue dotted line is for scaled distance Z=0.2 m/kg$^{1/3}$, corresponding to 400 mm burst height. If the point is located at the region between the Z=0.1 m/kg$^{1/3}$ and Z=0.2 m/kg$^{1/3}$, the pavement slab would suffer moderate damage, in which the HSC layer only need to be repaired instead of replaced, but asphalt concrete layer should be replaced to further use. If the point is located at the right hand side of the Z=0.2 m/kg$^{1/3}$, the pavement slab would be in the range of light damage, in which no repair is needed for the HSC and ECC layer.

6.6 Conclusion

In this chapter, the numerical simulation of concrete pavement slab and the proposed multi-layers pavement under blast loading was conducted. It was shown there were well agreement between the numerical results and field blast trial test result in terms of damage pattern, crater diameter and instrument readings. Hence, it could be concluded that the current 3D numerical model using AUTODYN and LSDYNA could model the real behavior of the pavement slab with interface under blast loading. A modified DIF curve for asphalt concrete was proposed based on the SHPB and servo hydraulic test. The MAT72 R3 model with implementation of DIF was found to be suitable for simulating asphalt material under high strain rated loading.

After validation of the numerical model for the proposed multi-layers pavement, the parametric study was conducted for the following factors:

1) Effect of steel fiber (Fracture energy): It was found that incorporation of steel fibers in the HSC would significantly increase the fracture energy and then reduce the damaged area of the HSC layer. However, it was shown further increasing of the steel fibers in the HSC would not significantly increase the blast resistant of the HSC. In this study, after 0.5% steel fiber, no significant blast resistance was obtained.

2) Effect of higher compressive strength of HSC layer: It was shown the increase of the compressive strength of the HSC layer did not enhance the blast resistant of the material beyond certain compressive strength. In the current study, the optimum compressive strength value was 90 MPa. Further increasing the compressive strength, the HSC would show brittle behavior with a lots of crack lines.

3) Effect of HSC thickness and ECC thickness: It was shown that the thicker ECC layer would have stronger bending resistance. It was found that the tensile wave could still propagate upwards and arrived about ¾ of the height. Based on the parametric study, it was found that the increasing of HSC thickness would make little contribution to prevent the pavement layer being penetrated though under blast load. However, the tension cracks at the bottom of ECC layer were significantly reduced. The equal thickness for the HSC and ECC layer might be better configuration for blast loading, since the bending resistance of the ECC layer would be enhanced.

4) Interface strength: It could be concluded that the increase of the released energy G_I and G_{II} might not enhance the blast resistance of the proposal multi-layers pavement significantly. The HSC layer was still penetrated

through irrespective to G_I and G_{II} values. This might be due to the magnitude of the tensile and shear strength of the interface material was much lower than that of blast loading. Thus, the increase of the G_I and G_{II} did not show higher blast resistance of the proposed multi-layers pavement under severe blast load.

5) Effect of subsoil: In order to reduce the settlement of the proposed multi-layers pavement under blast loading, the underneath soil could be improved to increase its stiffness and shear strength such as geosynthetic reinforced soil foundation or cement treated soil foundation. Moreover, the cement treated soil foudantion would have higher bearing capacity which could sustain high energy from the overlaid pavement structures.

6) Effect of blast loading from different burst of height: It was shown that with the increase of the burst height, the damage pattern of the proposed multi-layers pavement is changing. Beyond 300 mm burst of height, the HSC and ECC would suffer less damage, and then can be further used.

Based on the parametric study from numerical modelling, according to the dynamic behavior of the proposed multi-layers pavement under blast load from different burst height, the damaged pattern chart was developed. In this chart, the blast resistance of the proposed multi-layers pavement structure can be quickly assessed under different blast event. According to different damage situation, the repair for the pavement structure can be carried out. At same time, in order to enhance the blast resistance of the proposed multi-layers pavement structure, it the method such as increasing thickness of HSC and ECC, incorporation of steel fiber in HSC and using treated subsoil ground condition are strongly recommended.

(a) Normal concrete pavement slab before blast event

(b) Proposed new material pavement slab before blast event

Figure 6.1 Slabs placed in position before blast test

$\Delta\sigma > 0$

Maximum strength surface

Yield surface

Residual strength surface

$-f_t$

p

(a) 3D view of the strength surface

σ_1

θ

r_t

r_c

σ_2

σ_3

(b) Deviatoric cross section
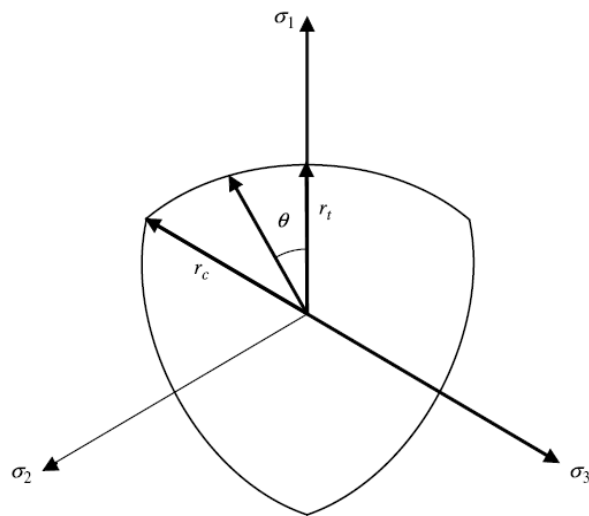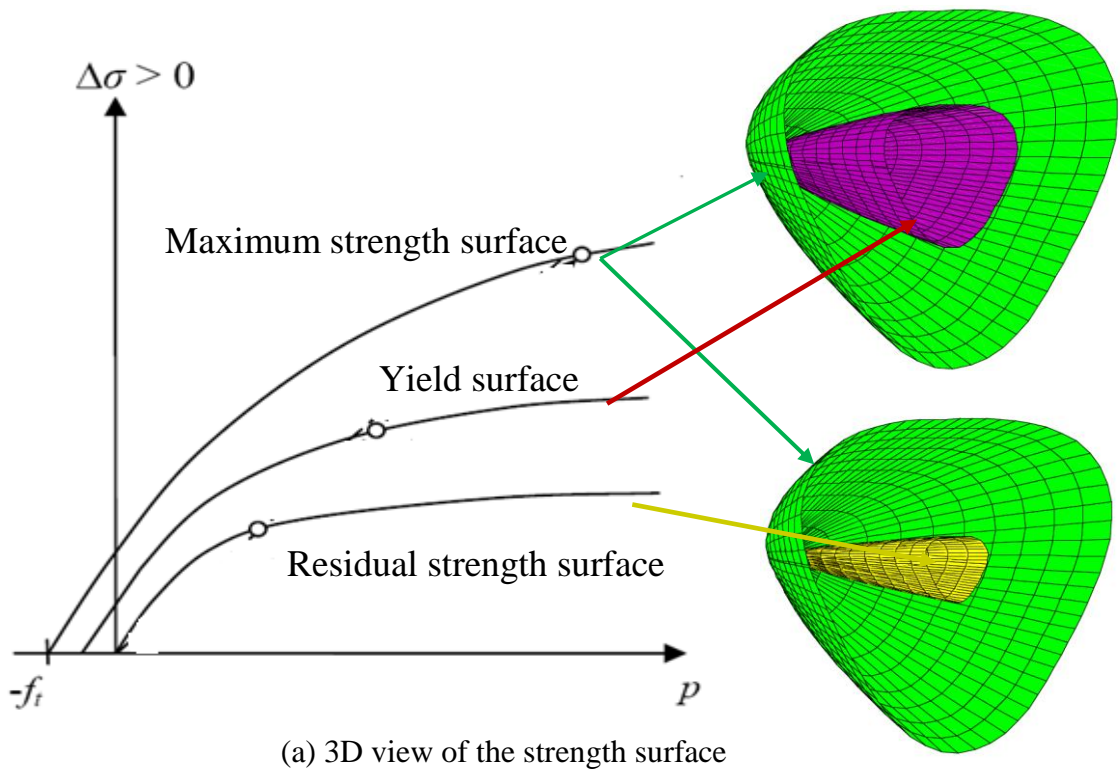
Figure 6.2 Failure surface for MAT72 R3 material model
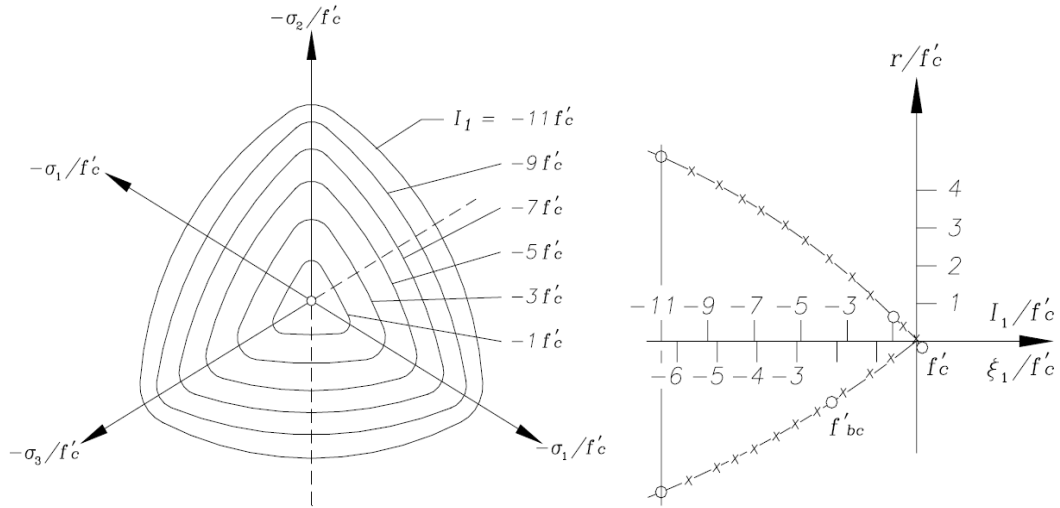
(a) Deviatoric sections for increase pressure

(b) Hydrostatic section
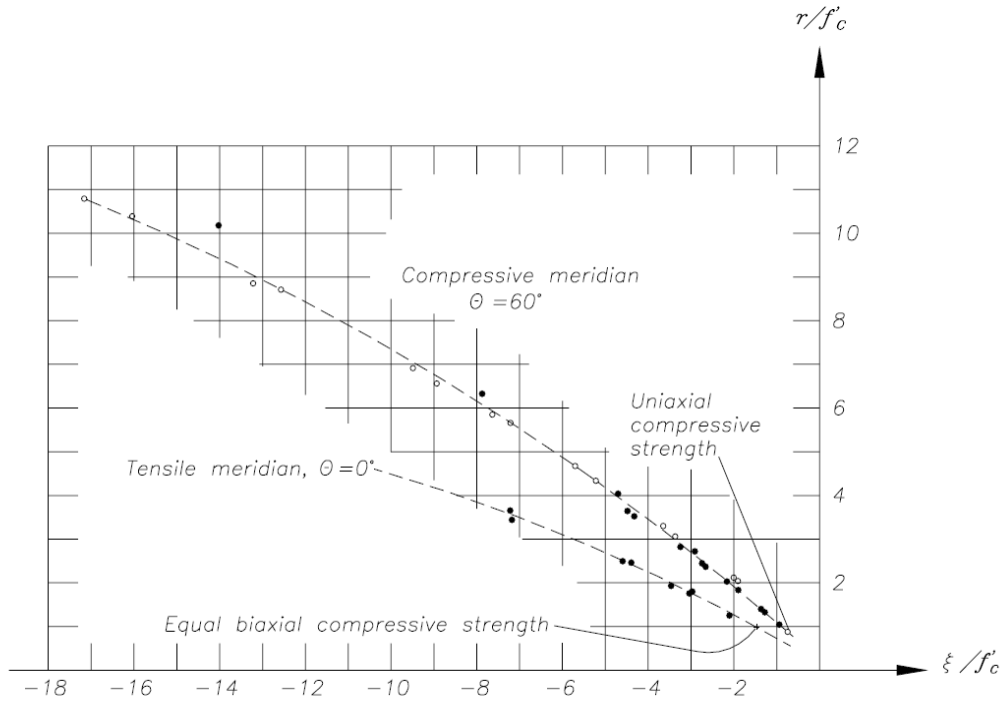
NOTE: $r = \sqrt{2 J_2}$
$\xi = I_1 / \sqrt{3}$

(c) Typical tensile and compressive meridians

Figure 6.3 Typical failure surface section for concrete (after Chen 1982)
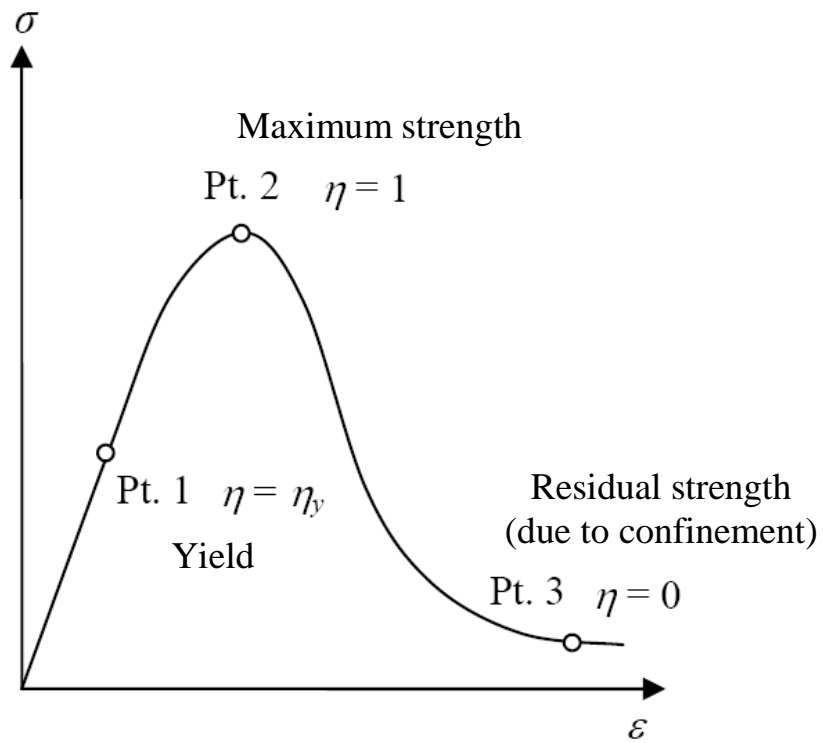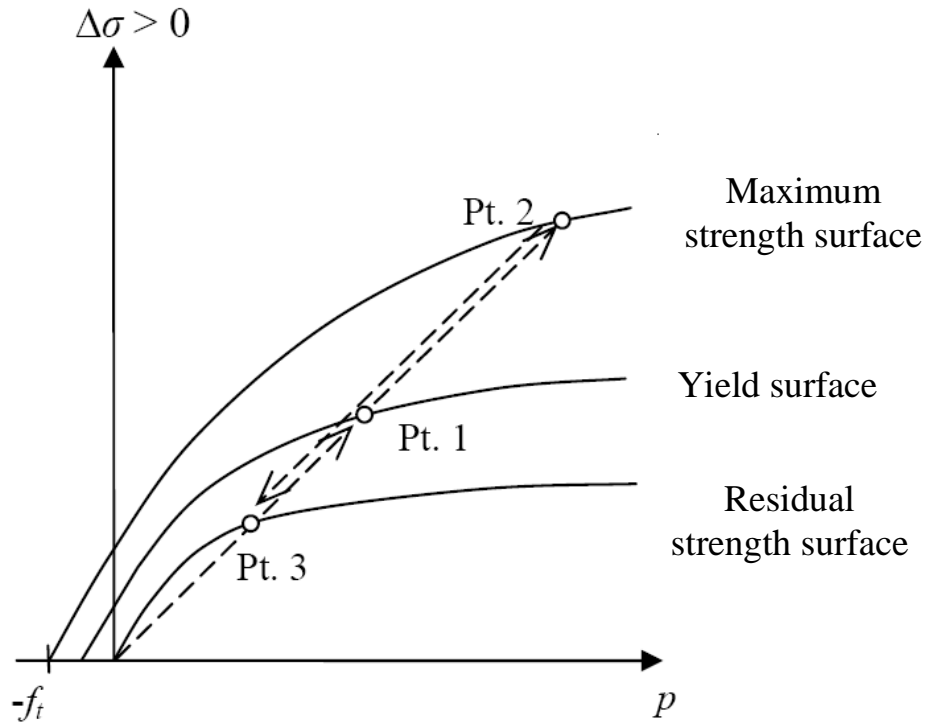
Figure 6.4 Three failure surface (after Malvar et al. 1997)
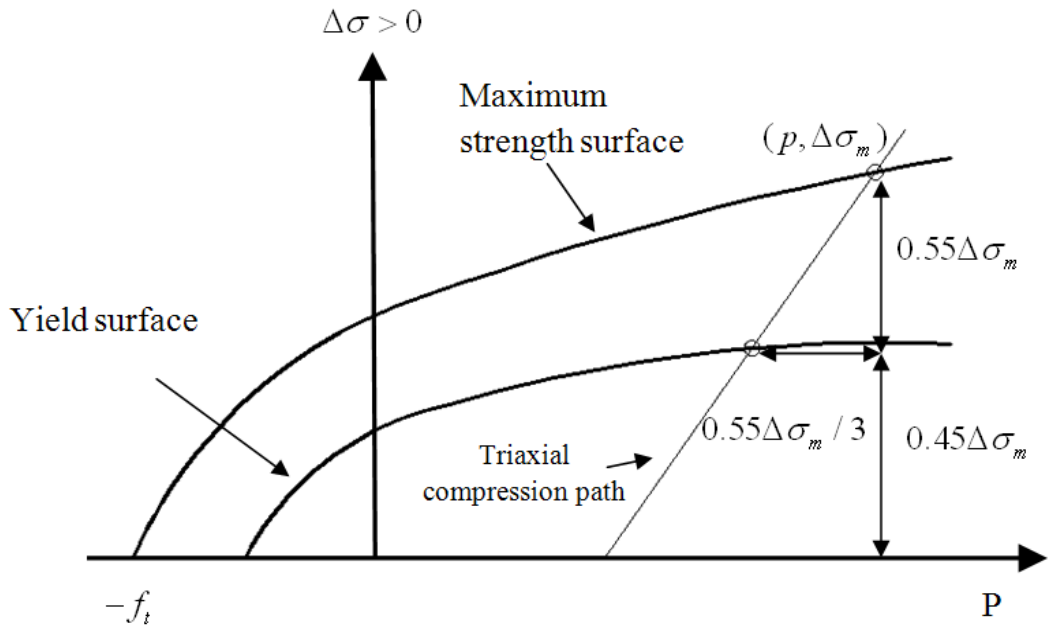
Figure 6.5 Location of yield surface (after Malvar et al.1997)
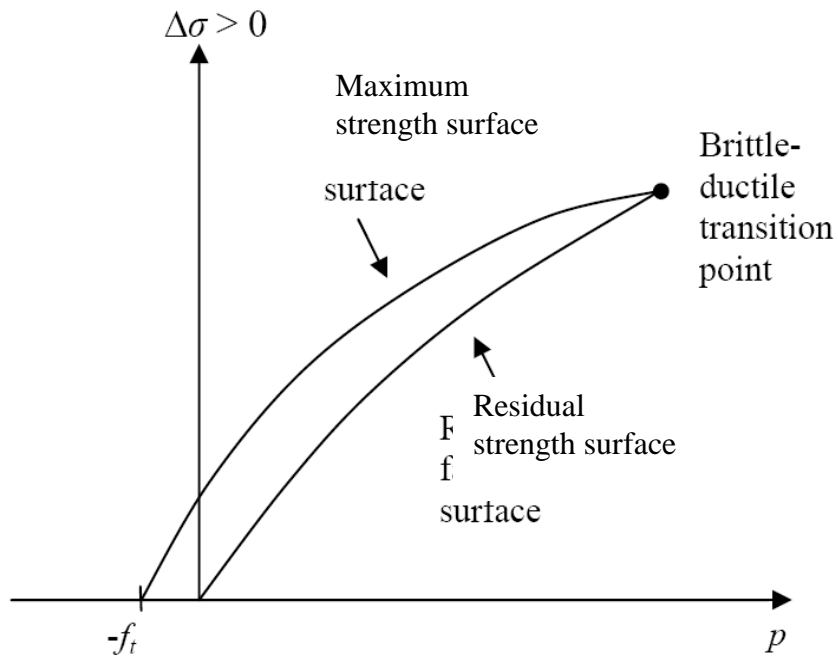
Figure 6.6 Intersection of the maximum and residual failure surface represents the brittle-ductile transition point
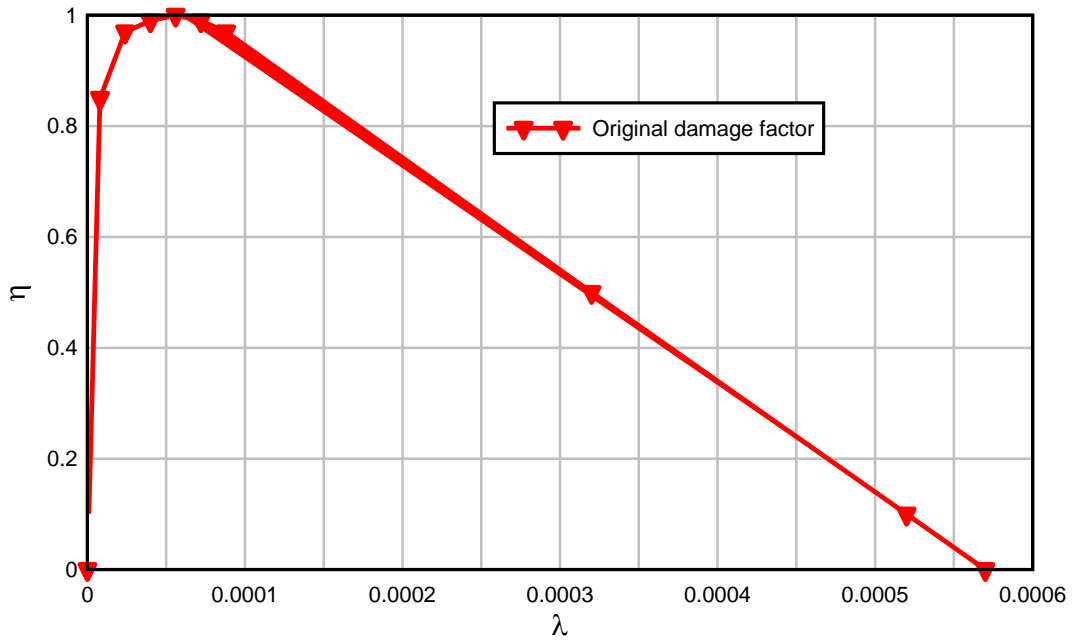
Figure 6.7 Input value of (η, λ) for concrete material
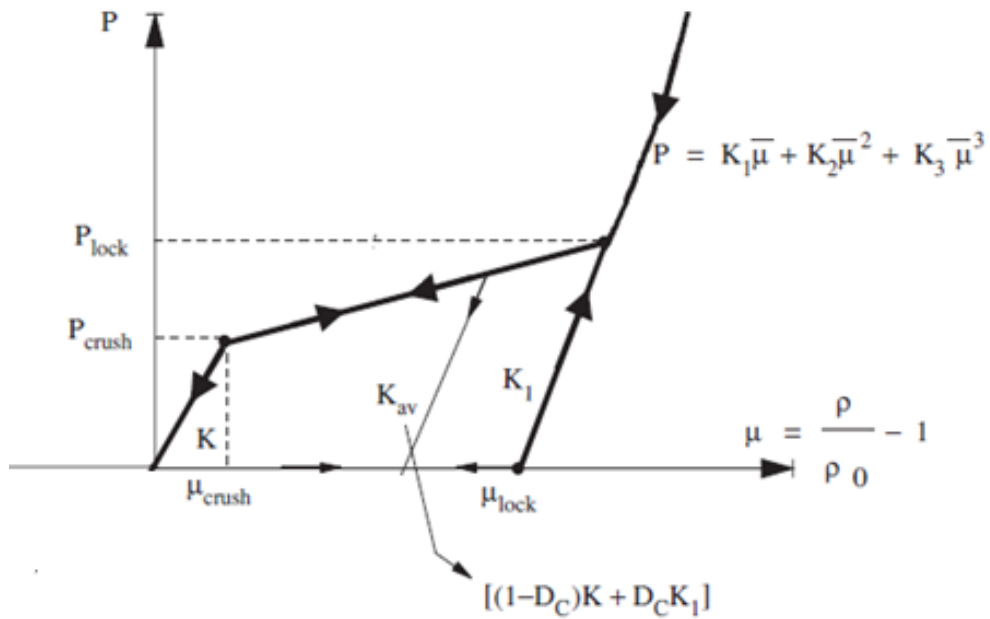
Figure 6.8 Equation of State for concrete under isotropic compression (after Loria et al. 2008)
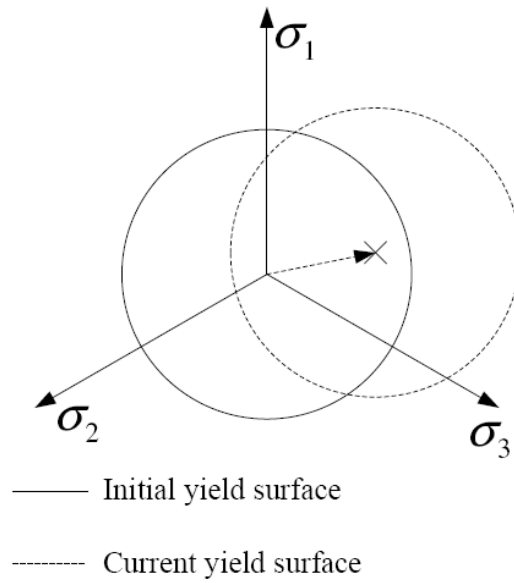
Figure 6.9 Kinematic hardening material yield surfaces in deviatoric space
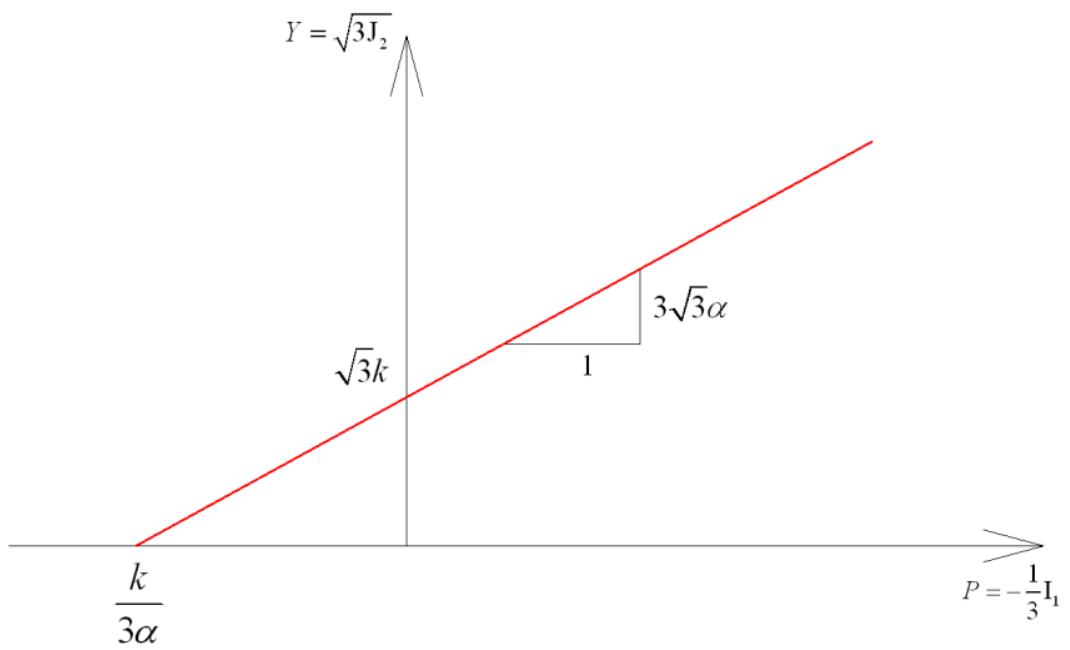
Figure 6.10 Drucker-Prager failure criteria in meridian space in LS-DYNA
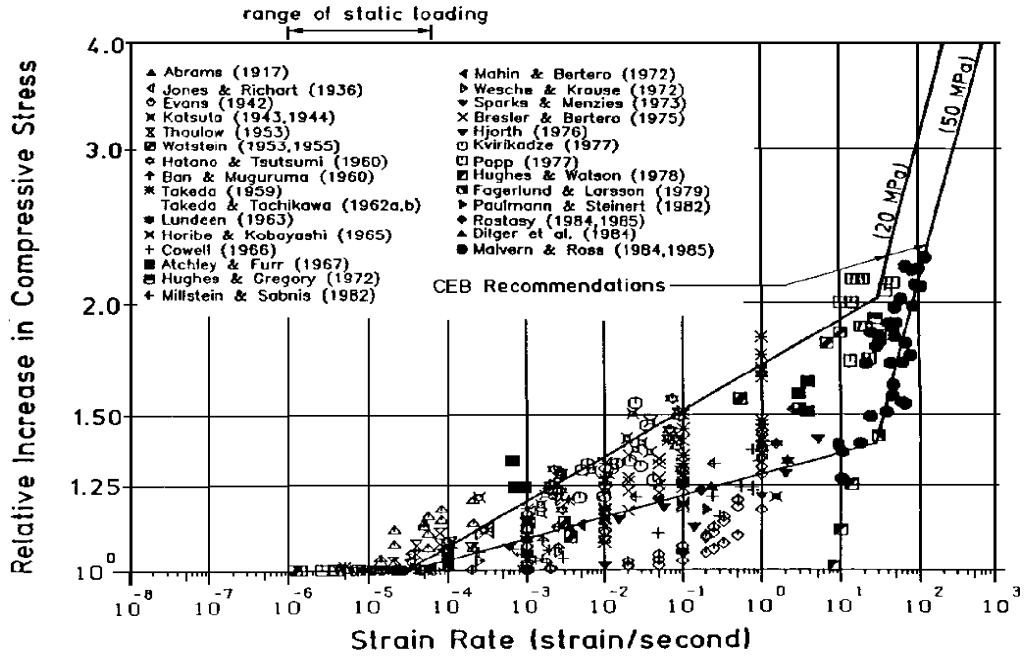
Figure 6.11 DIF data on compressive strength of concrete (after Bischoff and Perry 1991)
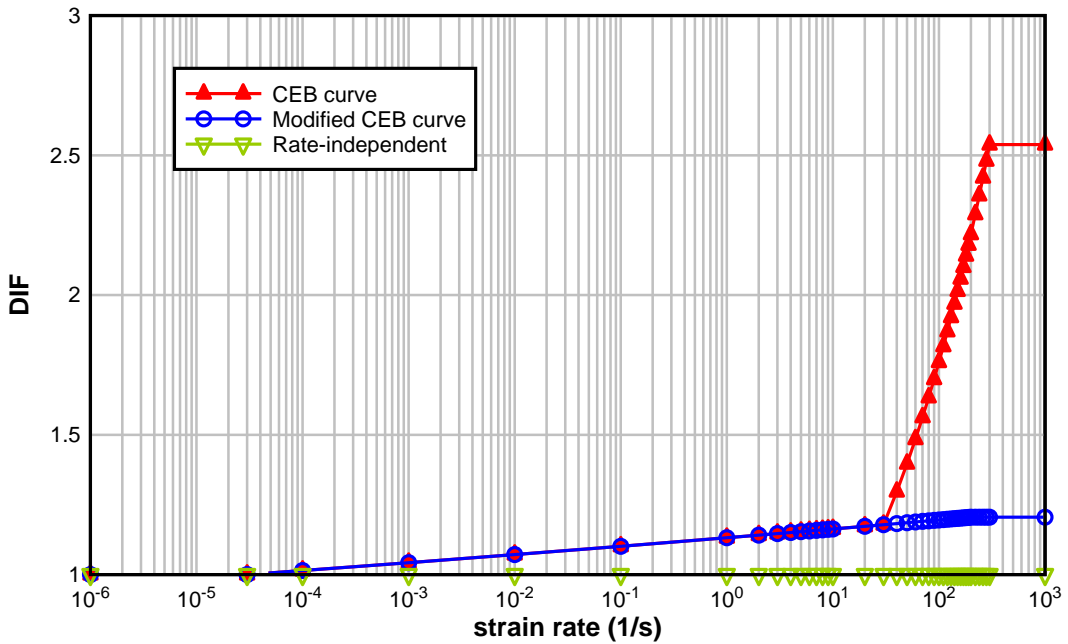
Figure 6.12 Input compressive DIF curve versus strain rate for f_c=90 MPa
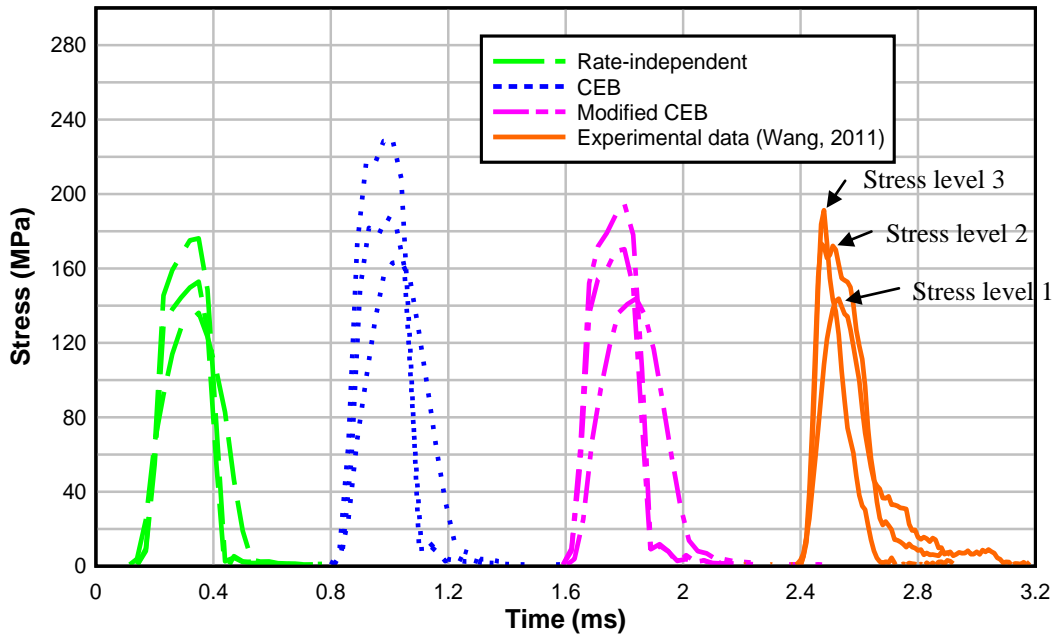
Figure 6.13 Transmitted stress pulse versus time (each curve was time shifted to be clearly compared with experimental data)
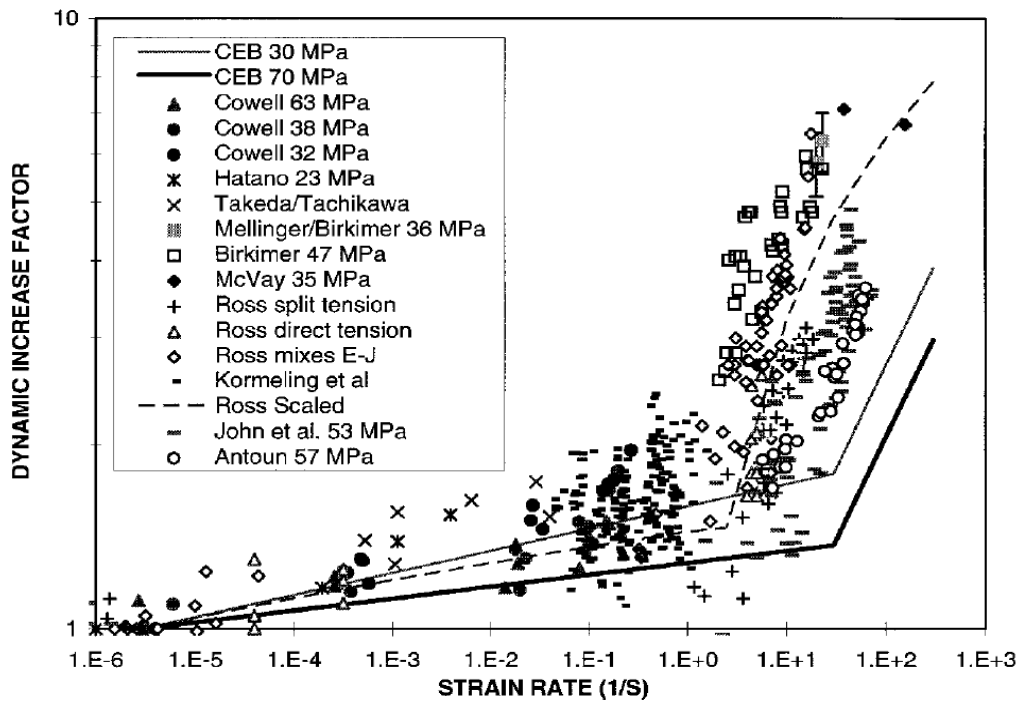
Figure 6.14 DIF data on tensile strength of concrete (after Malvar and Ross 1998)
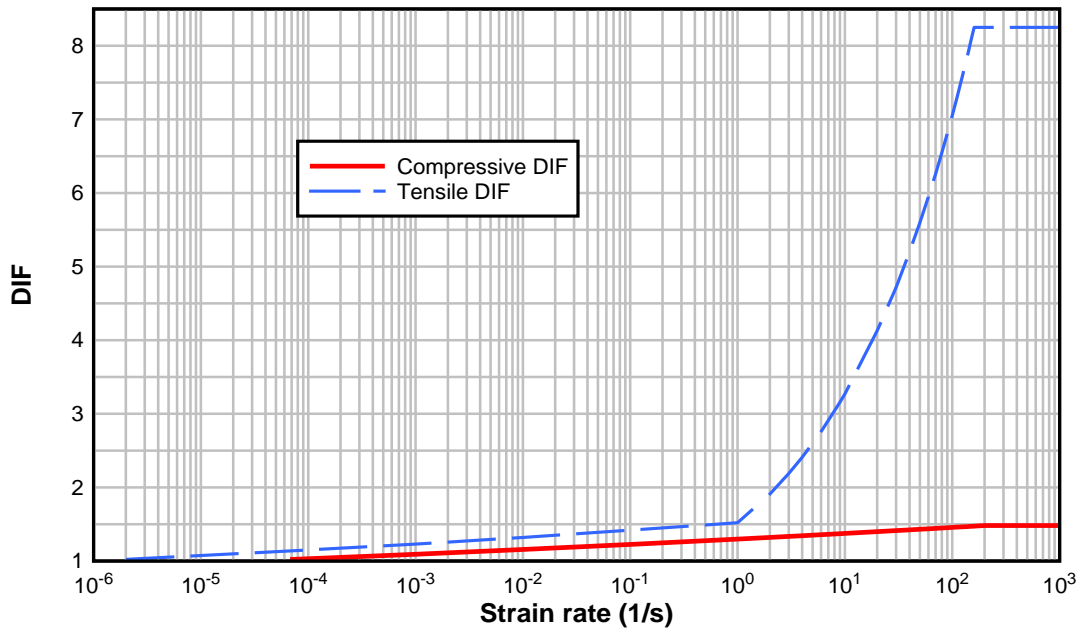
Figure 6.15 Compressive and tensile DIF curve for normal concrete with $f_c=40$ MPa
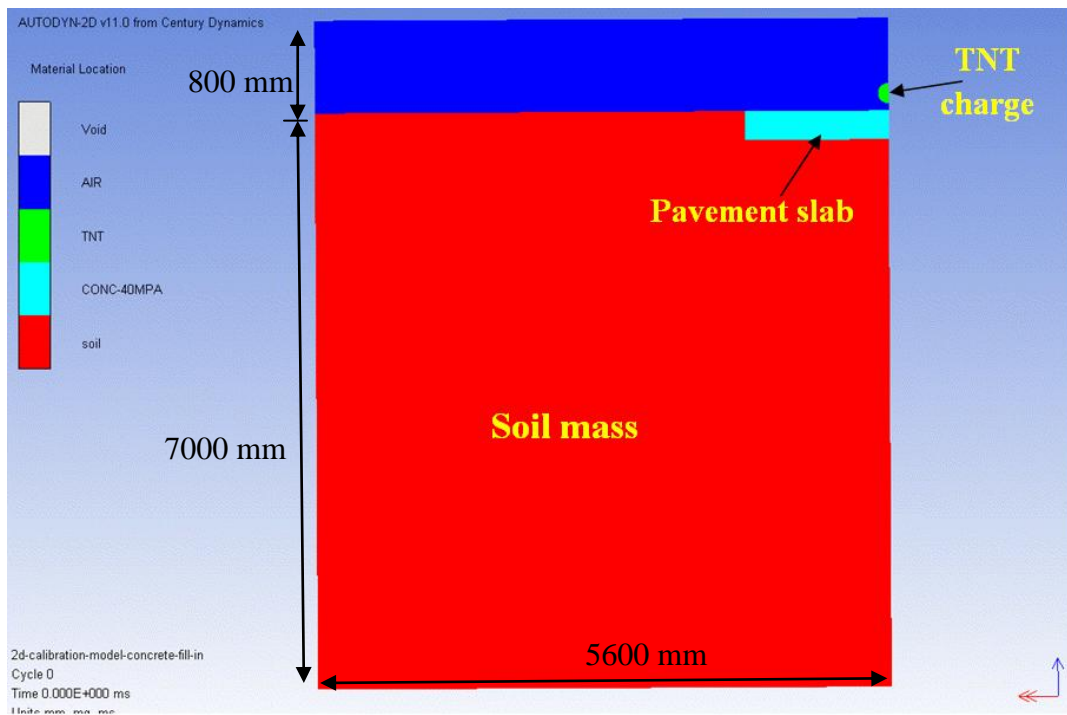
Figure 6.16 2D axsi-symetry model for pavement slab under blast loading

293
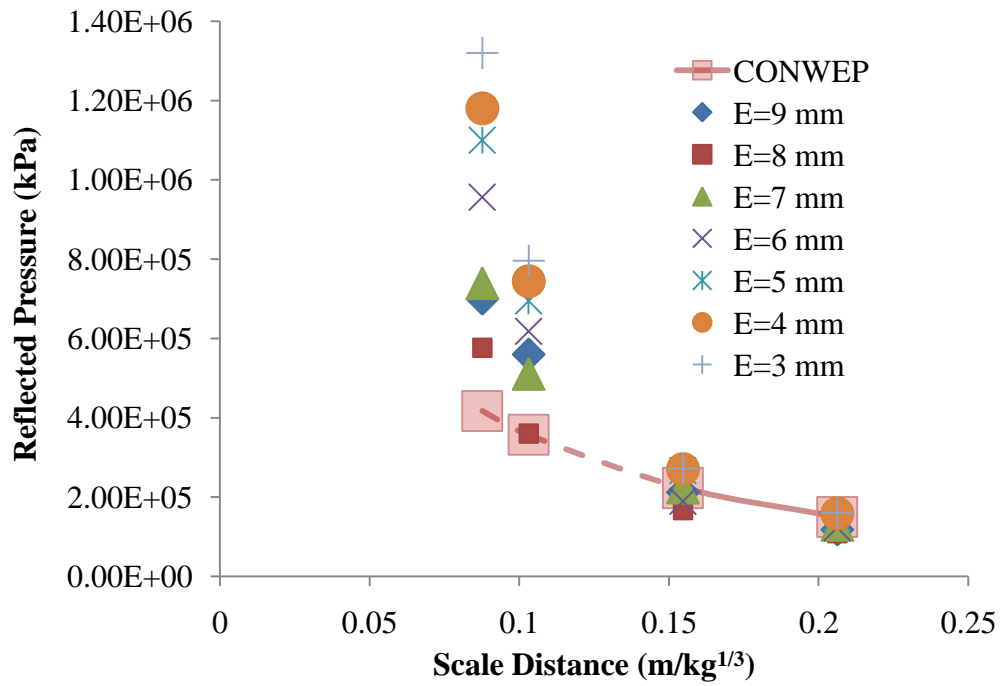
(a) Comparison of reflected pressure from AUTODYN and CONWEP
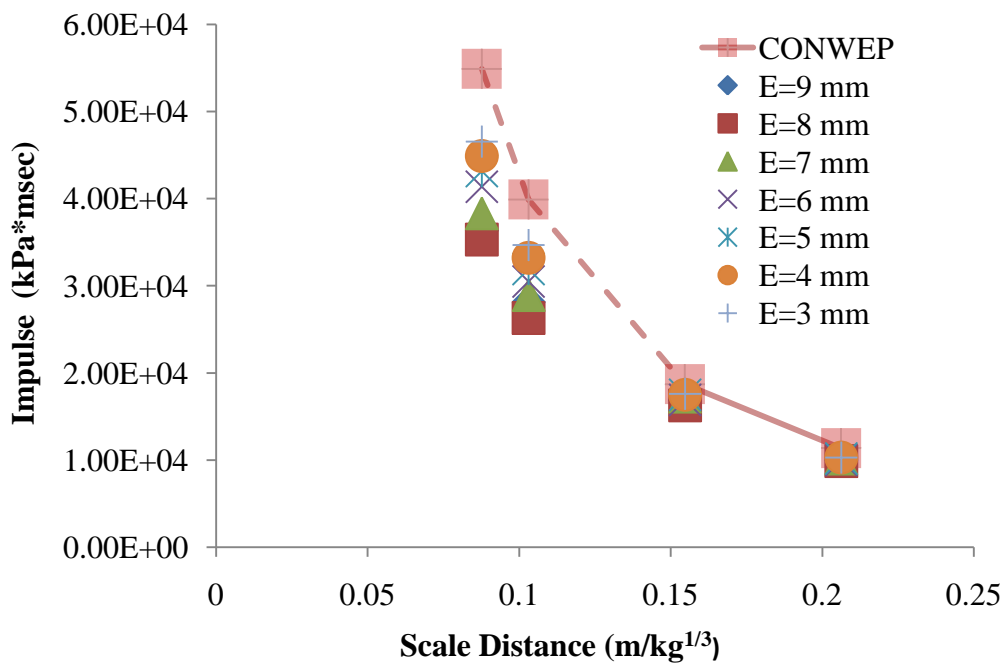
(b) Comparison of impulse from AUTODYN and CONWEP

Figure 6.17 Comparison of reflected pressure and impulse from AUTODYN and CONWEP
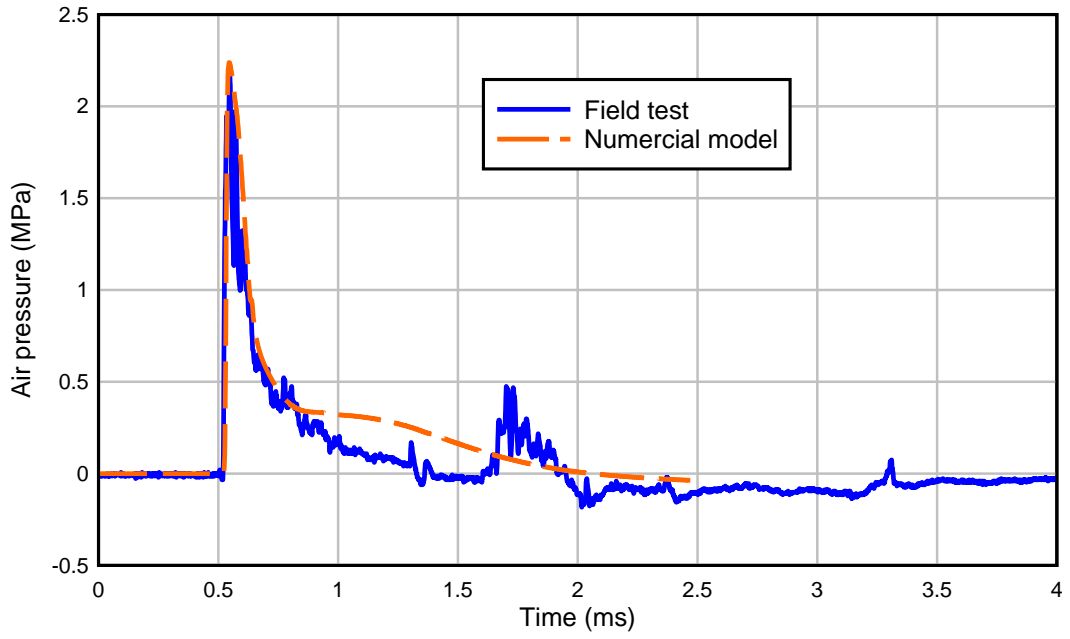
Figure 6.18 Air pressure from field test and numerical model
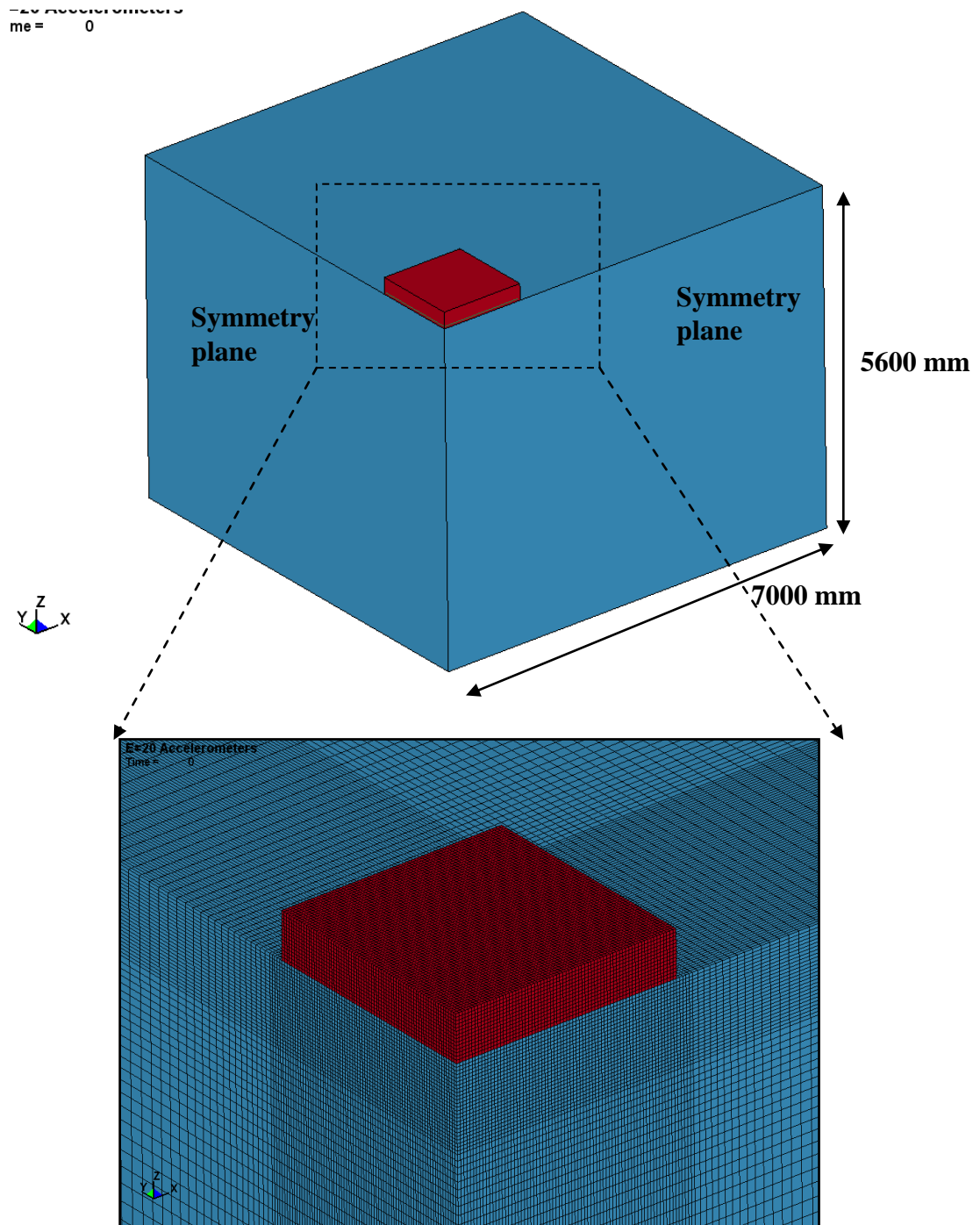
Figure 6.19 Finite element model of concrete slab sitting on soil mass
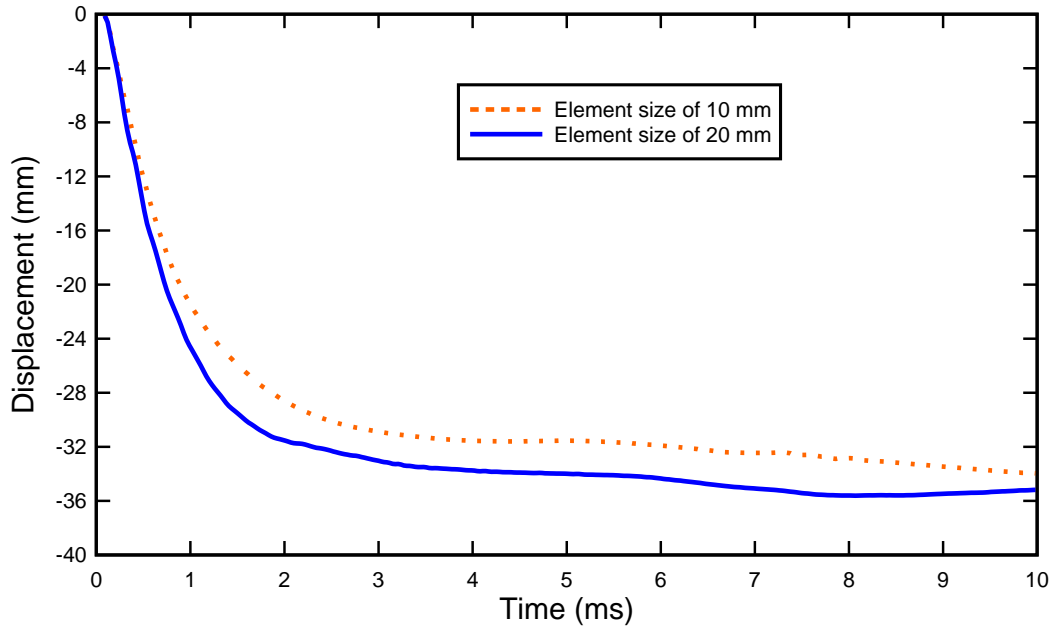
Figure 6.20 Displacement of mid-bottom for concrete slab

(a) 20 mm mesh size   (b) 10 mm mesh size
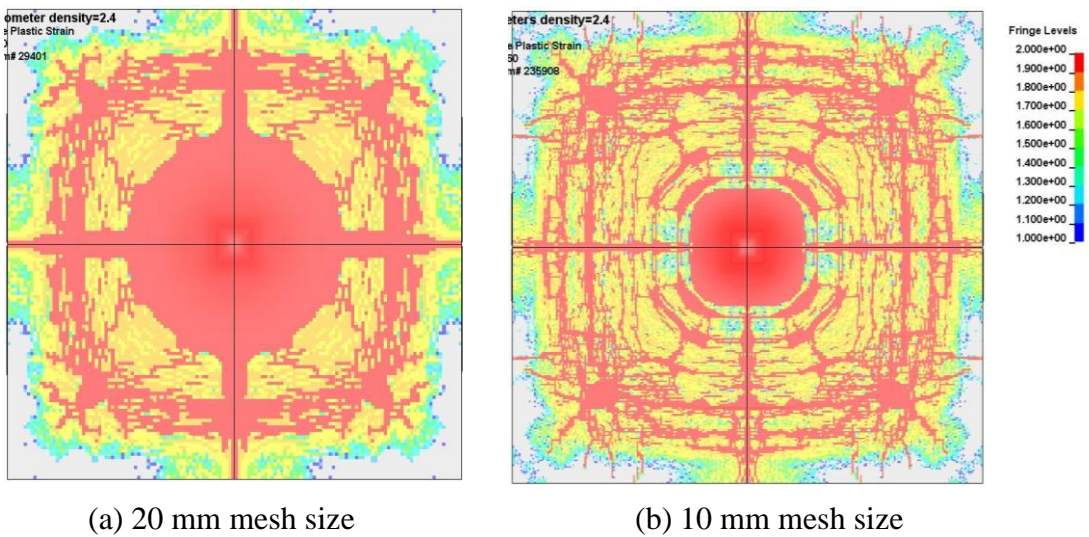
Figure 6.21 Damage contours for concrete slab using different mesh sizes
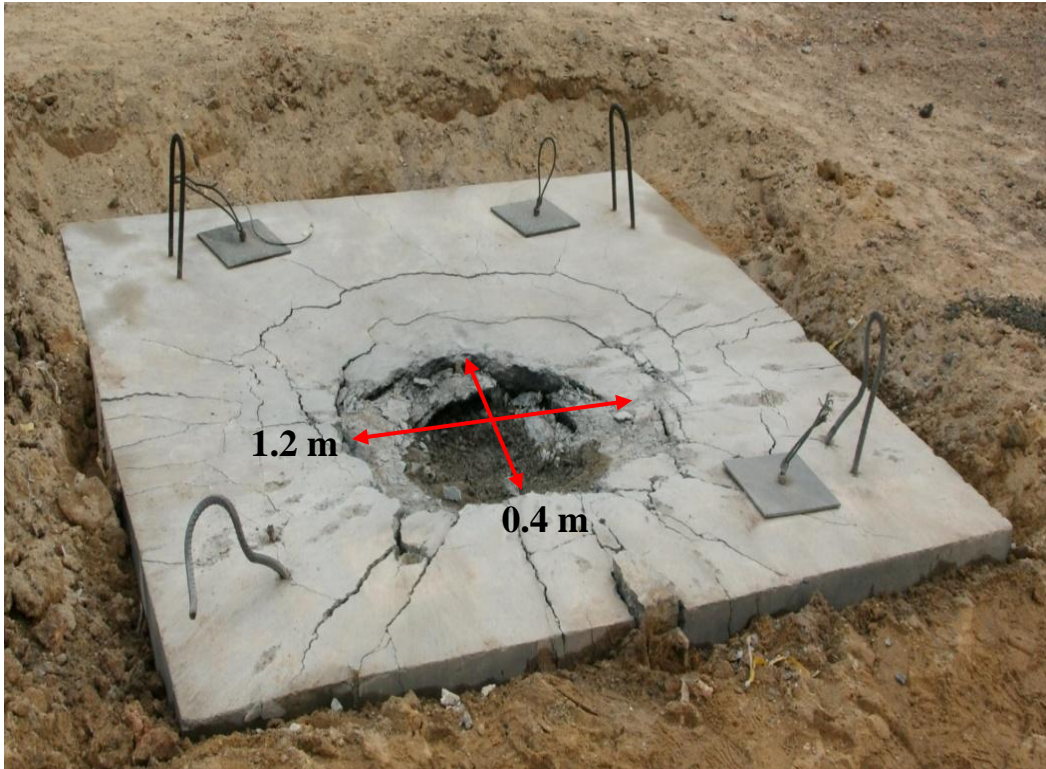
Figure 6.22 Damage pattern in field test for concrete slab

(a) Top surface   (b) Bottom surface
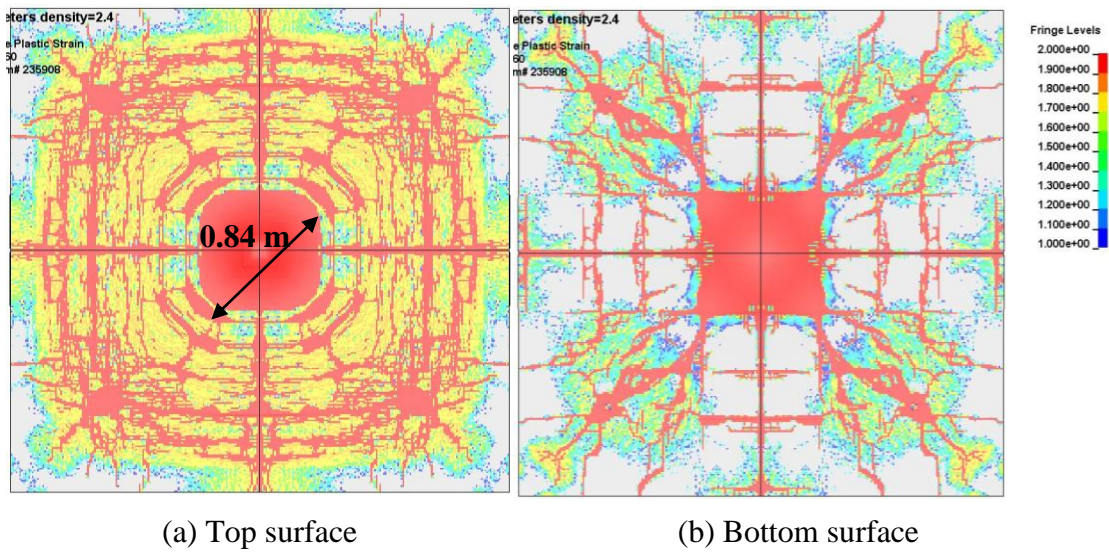
Figure 6.23 Damage pattern in numerical model for concrete slab
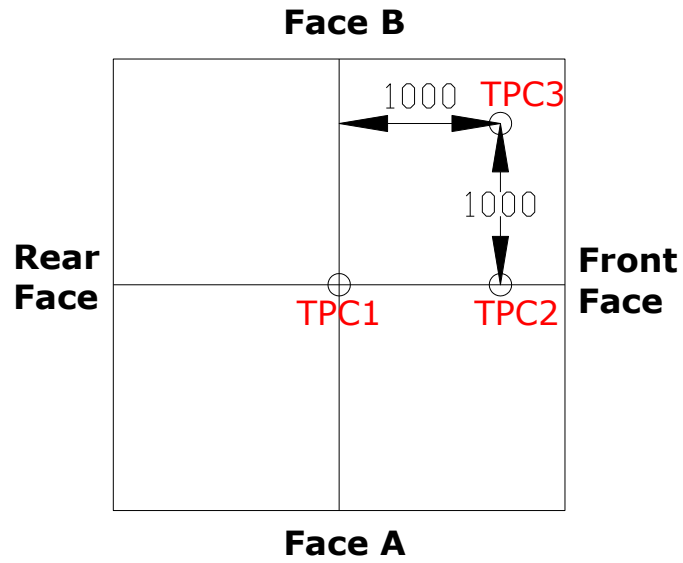
Figure 6.24 Layout of total pressure cell
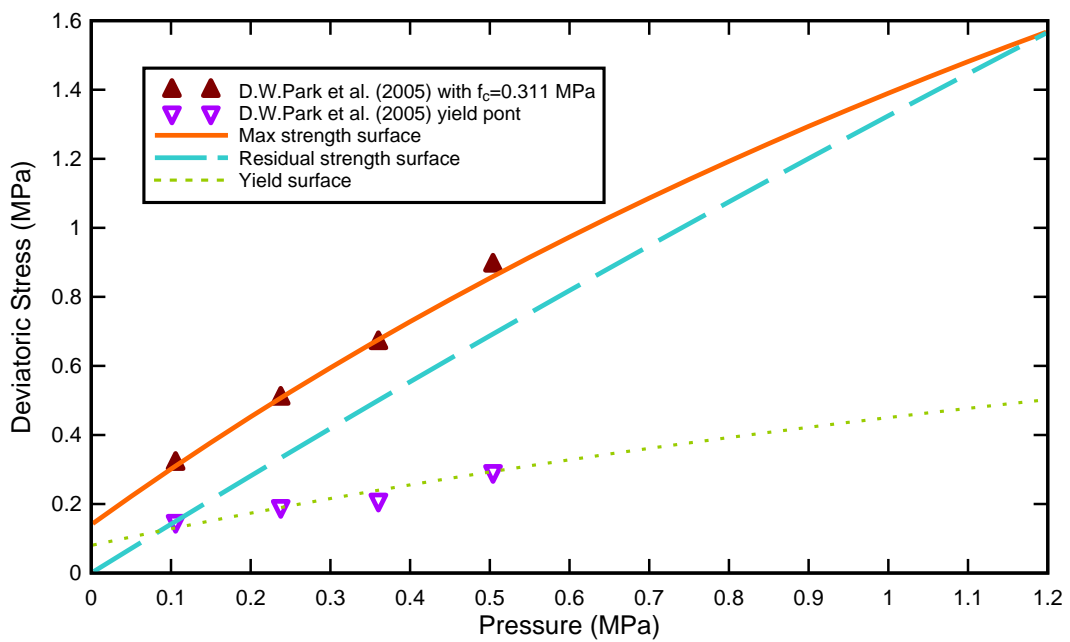
Figure 6.25 Determination of parameters from experimental data
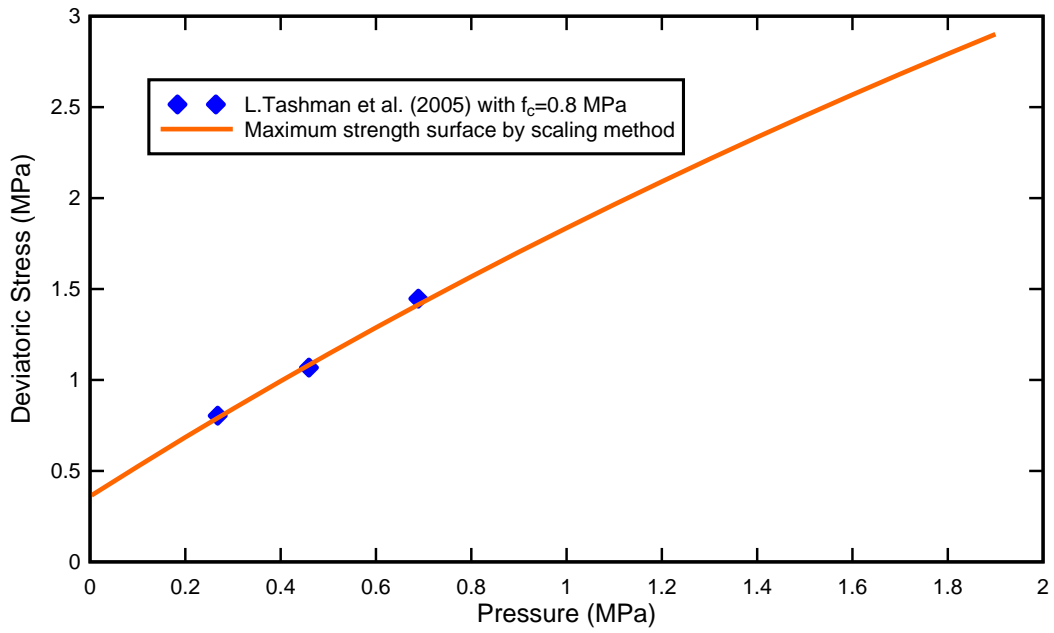
Figure 6.26 Validation of failure surface using experimental data
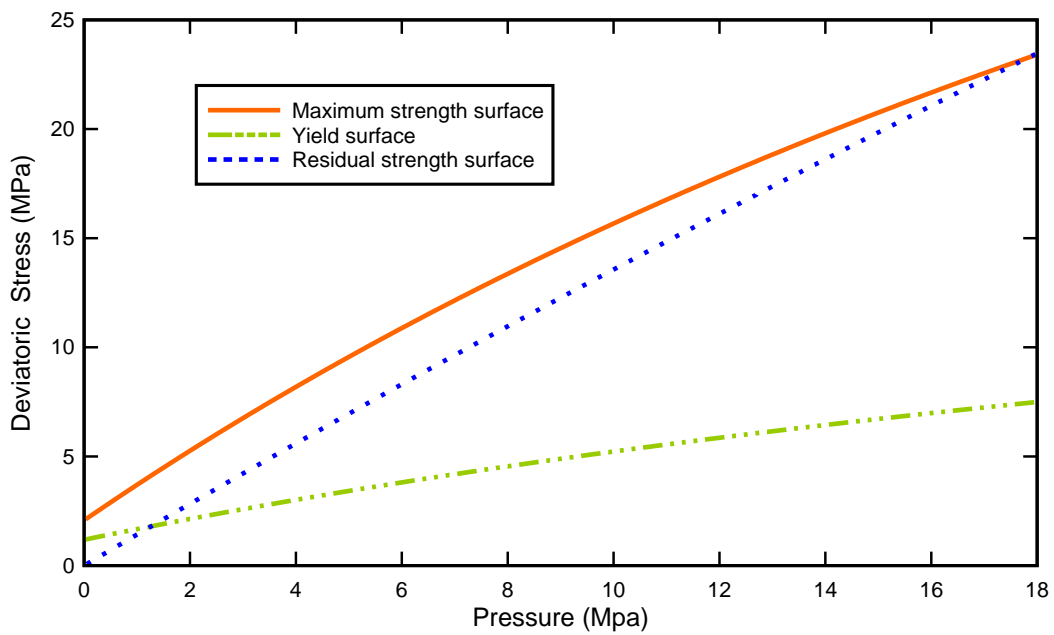
Figure 6.27 Strength surface for f_c=4.6 MPa asphalt concrete

300
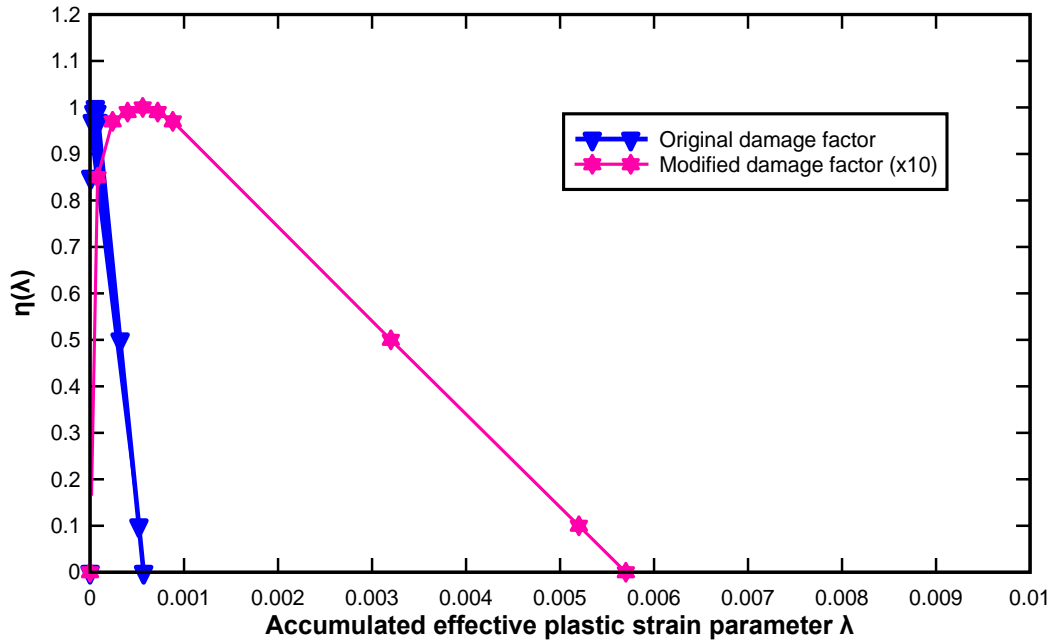
Figure 6.28 Damage factor used for asphalt concrete
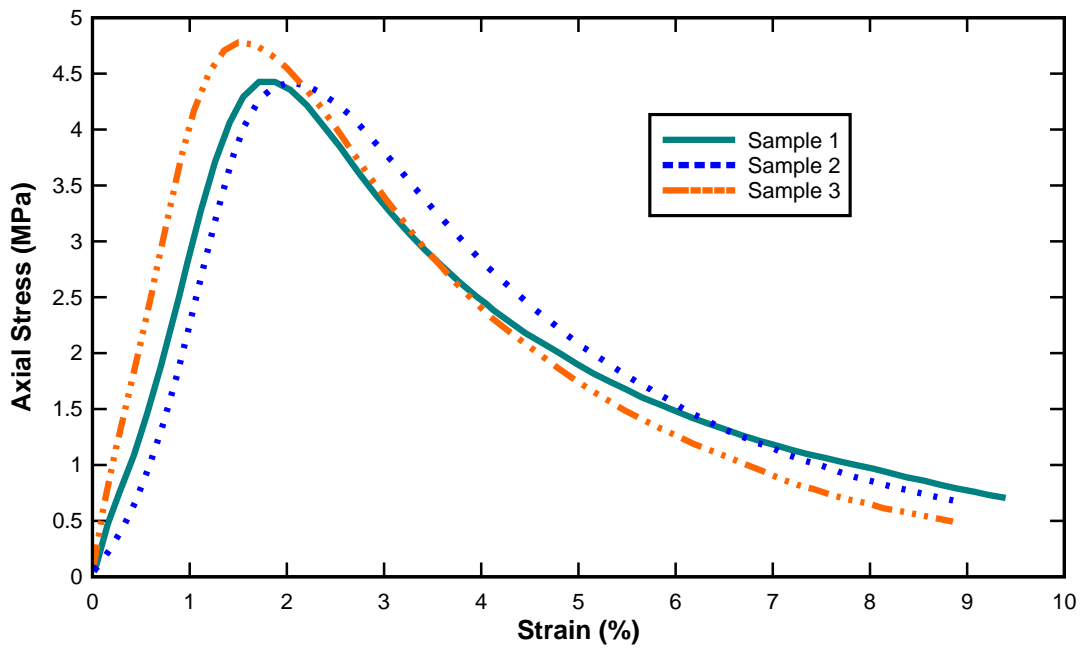
Figure 6.29 Stress strain curve of uniaxial compressive test
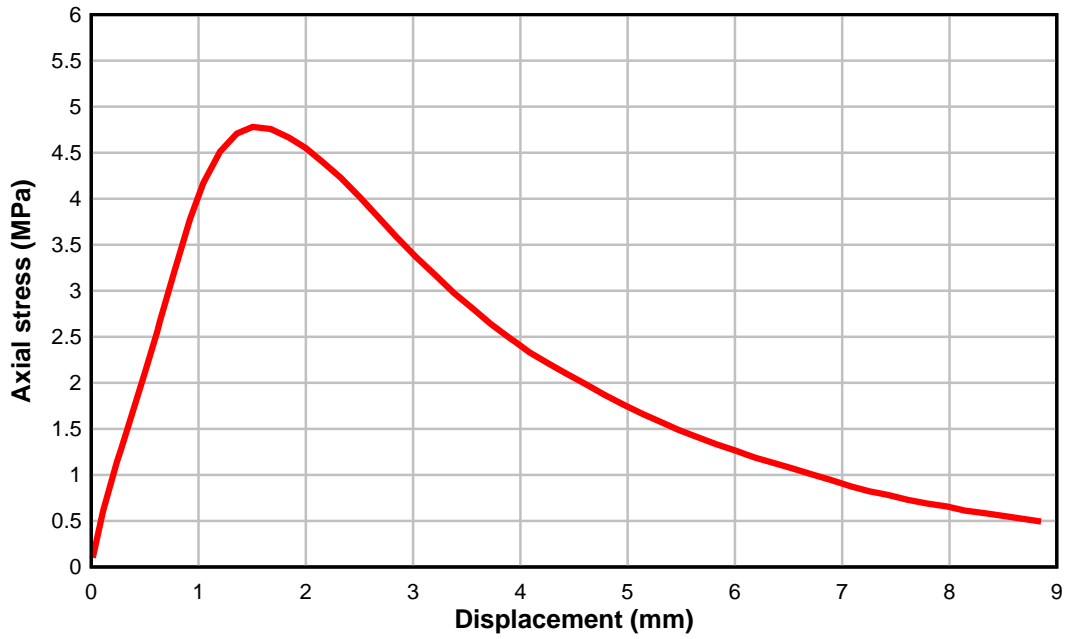
Figure 6.30 Stress displacement curve of uniaxial compressive test for asphalt concrete
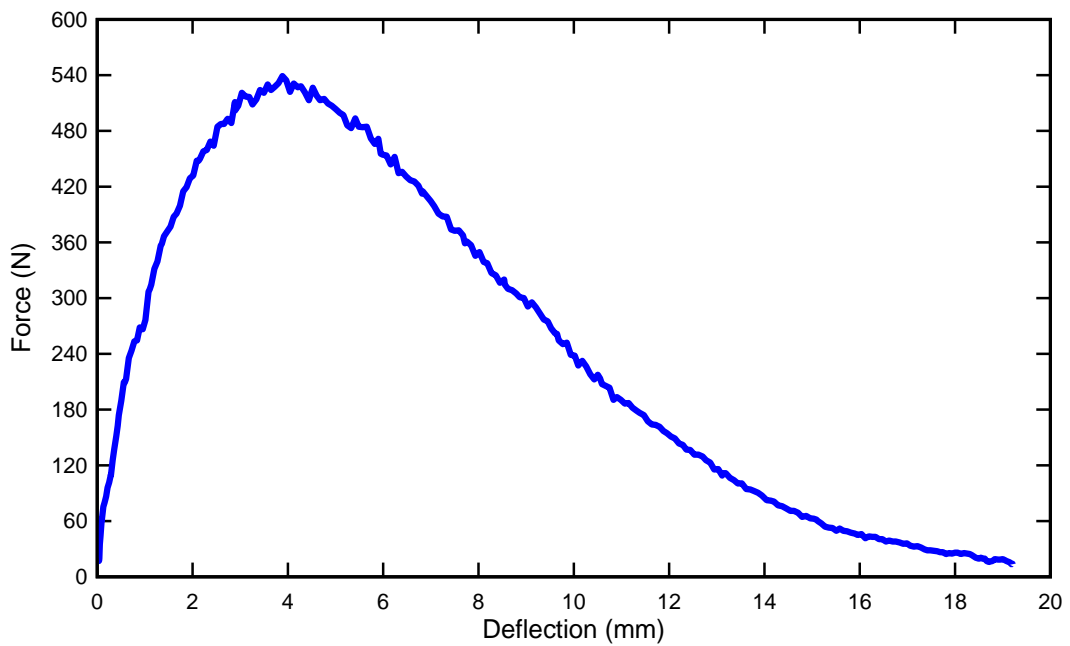
Figure 6.31 Typical load-deflection curve from SNB test
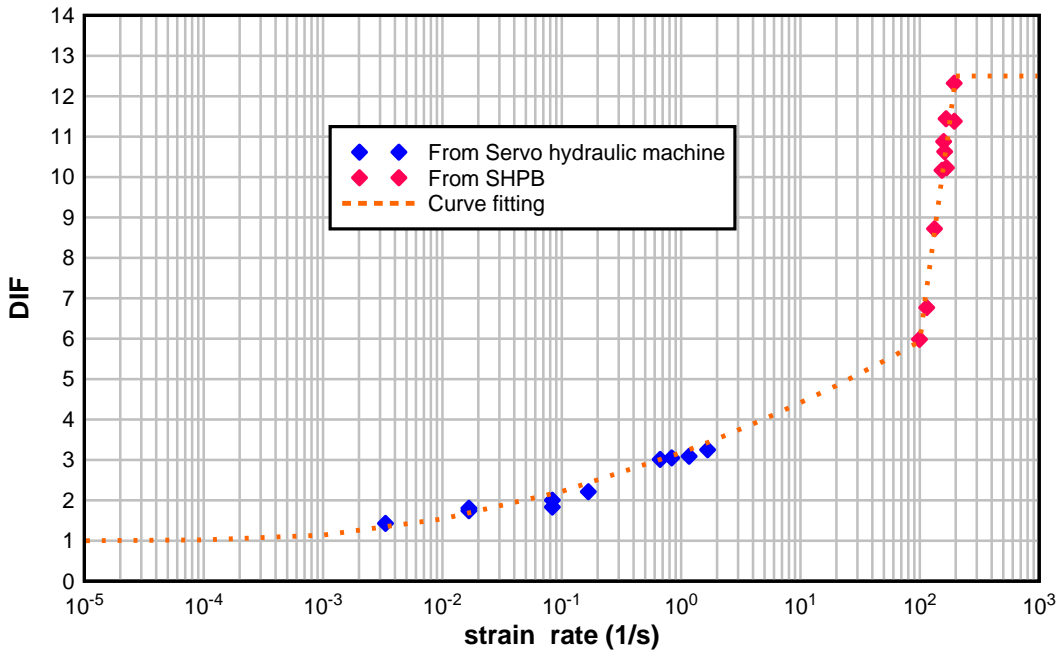
Figure 6.32 Compressive DIF curve versus different strain rate from lab test
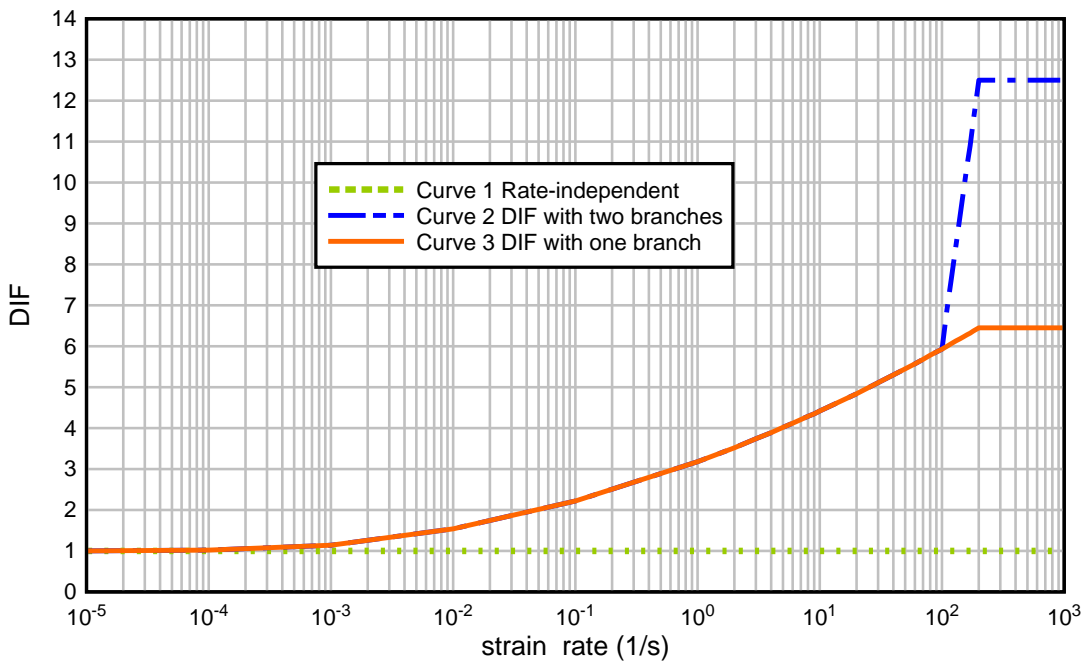
Figure 6.33 Three DIF curves used in the simulation of compressive SHPB test
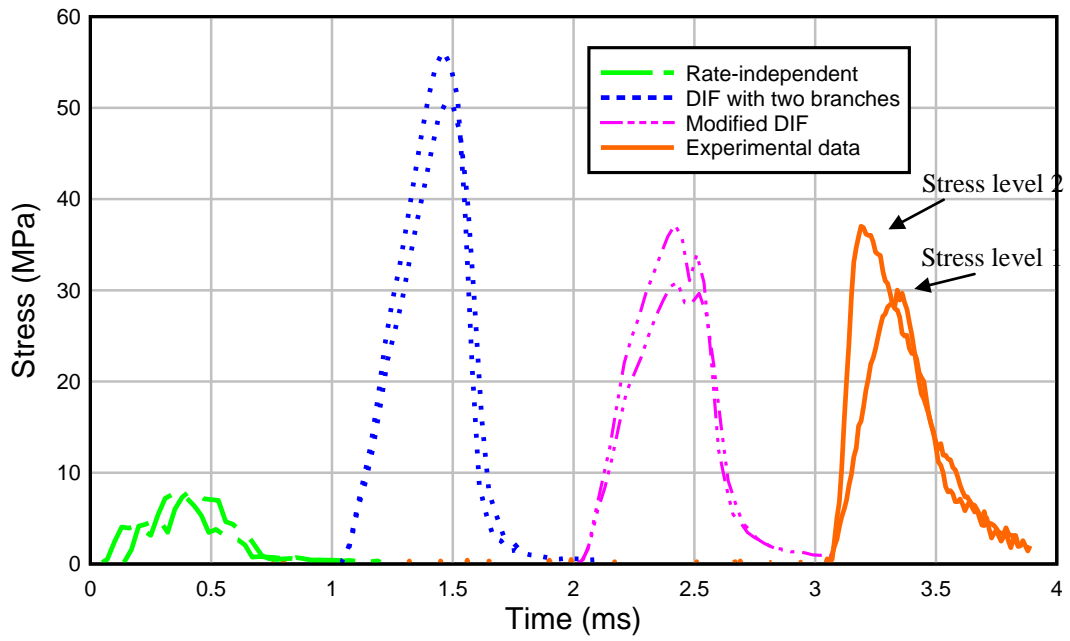
Figure 6.34 Transmitted stress pulse versus time for asphalt concrete (each curve was time shifted to be clearly compared with experimental data)
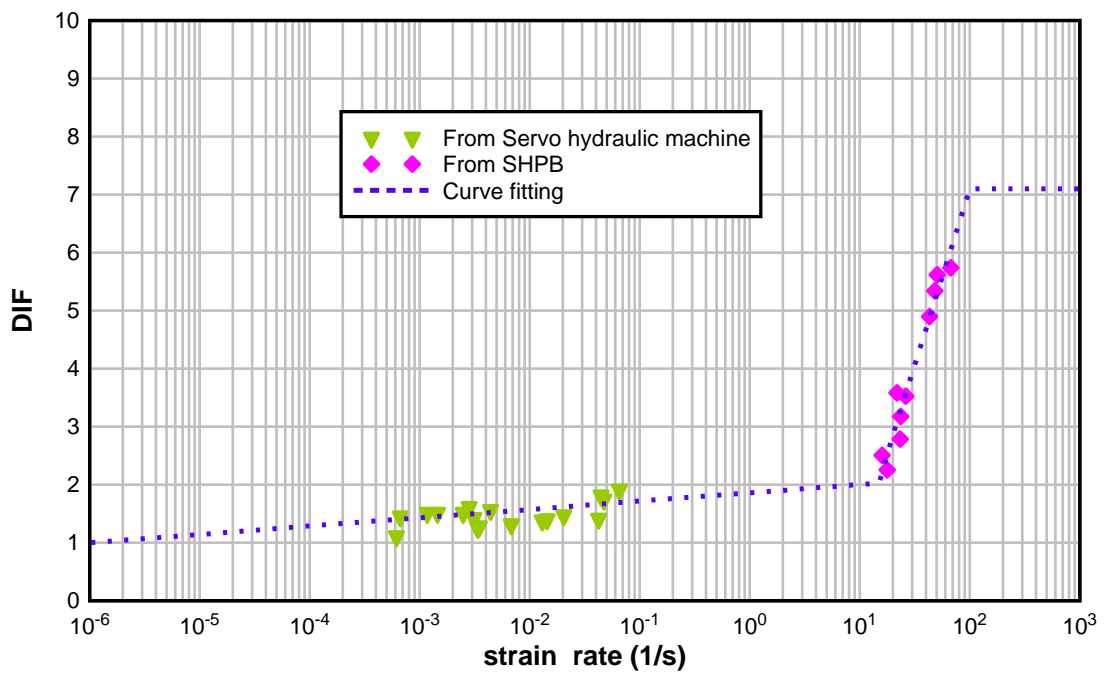
Figure 6.35 Tensile DIF curve versus different strain rate from lab test
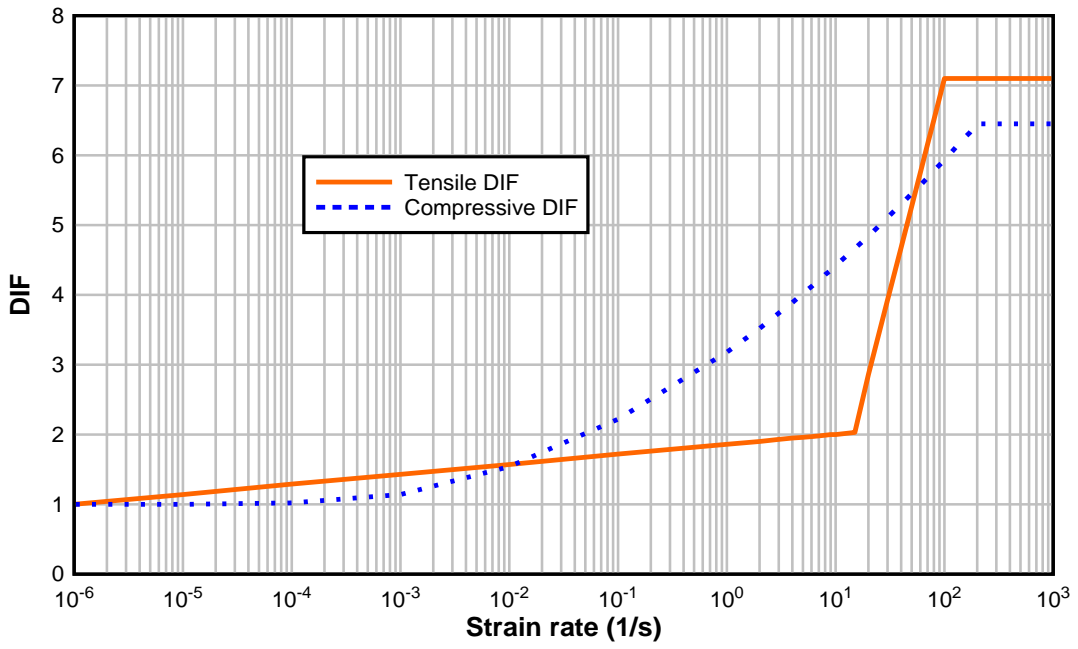
Figure 6.36 Tensile and compressive DIF curve used in numerical model for asphalt concrete
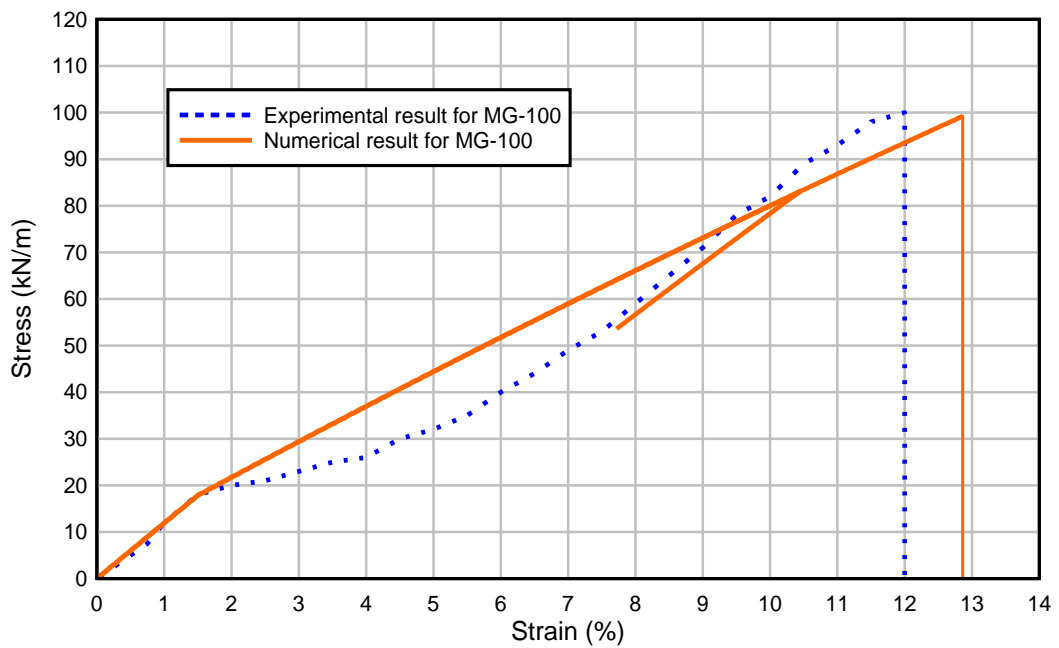
Figure 6.37 Load strain relationship of MG-100 geogrid reinforcements
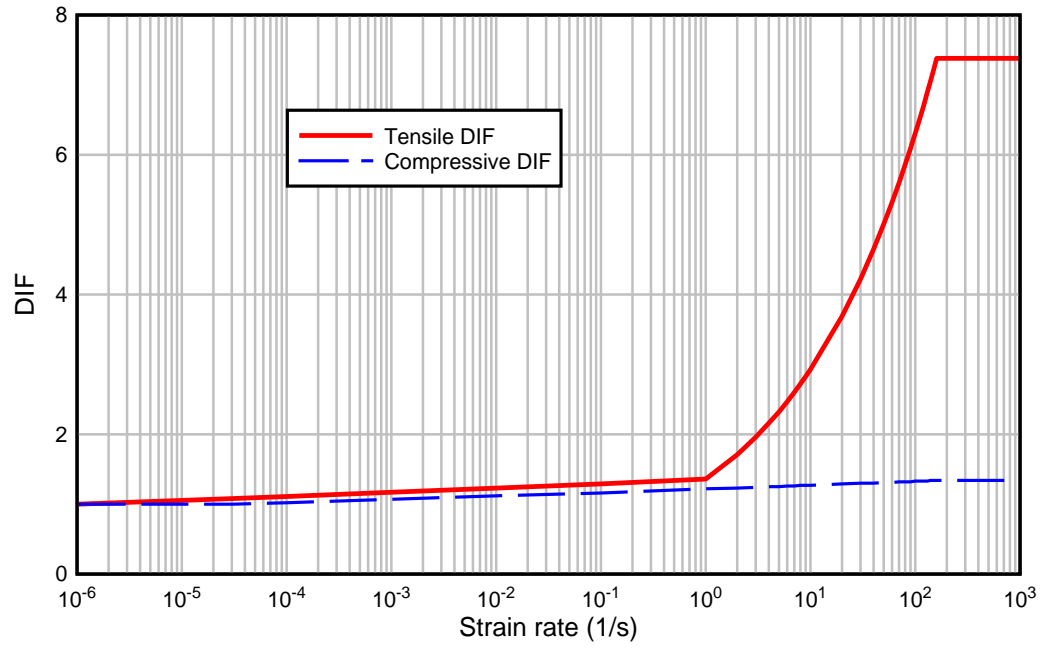
Figure 6.38 Tensile and compressive DIF curve used in numerical model for HSC with f_c=55 MPa
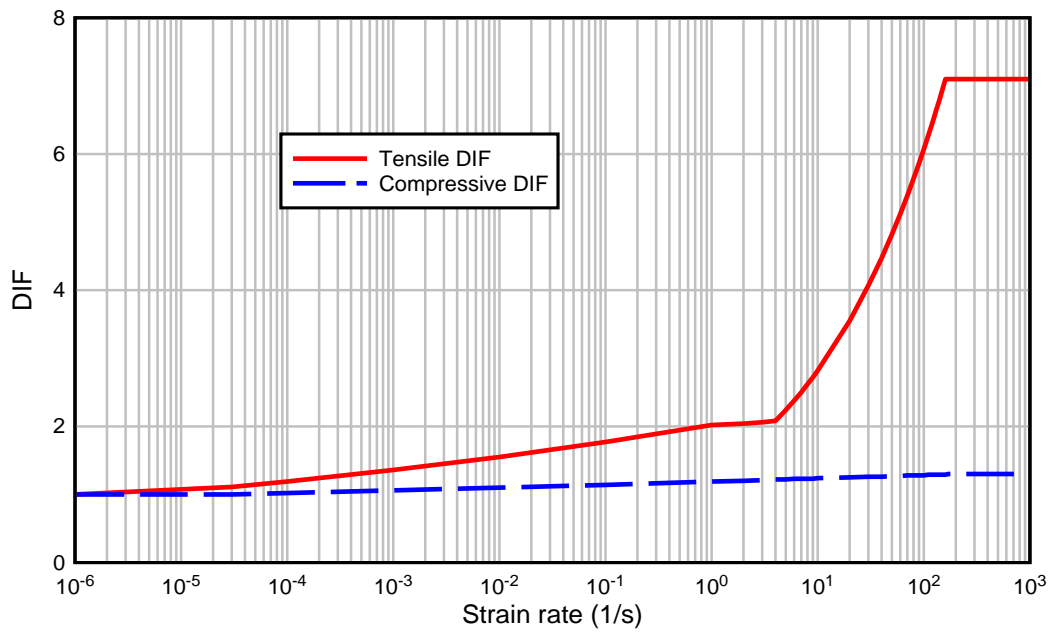
Figure 6.39 Tensile and compressive DIF curve used in numerical model for ECC with f_c=64 MPa
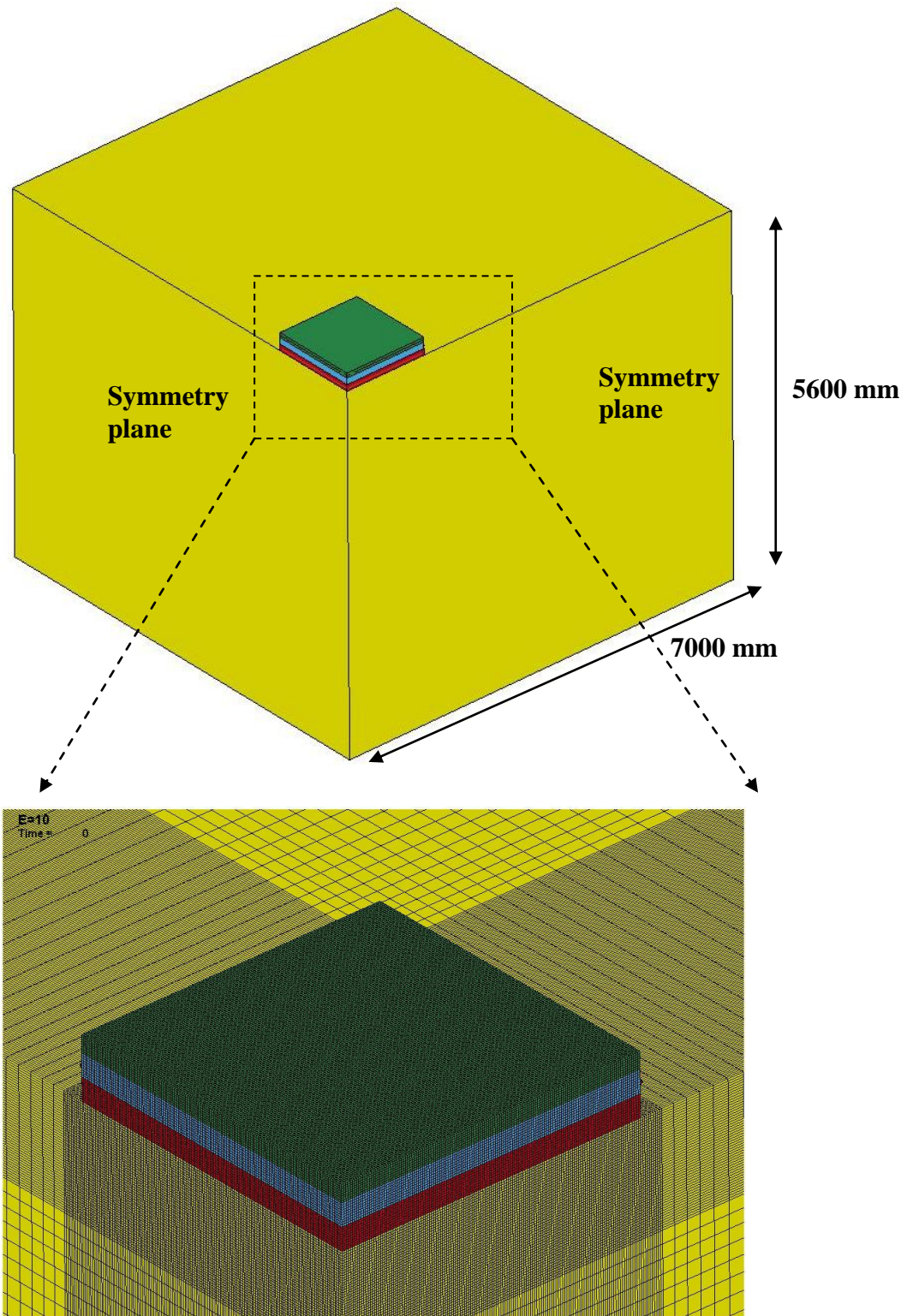
Figure 6.40 Finite element model of proposed multi-layers pavement slab sitting on soil mass

Figure 6.41 Damage of proposed multi-layers pavement after blast

0.7 m

Figure 6.42 Damage of proposed multi-layers pavement after blast (Removing asphalt layer)

Top face
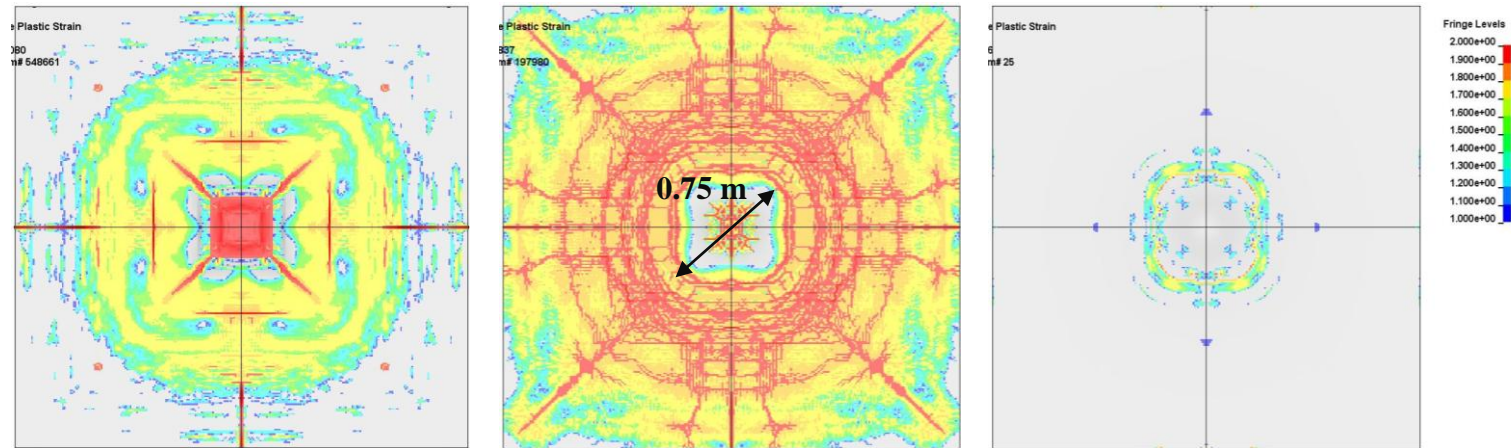
Bottom face
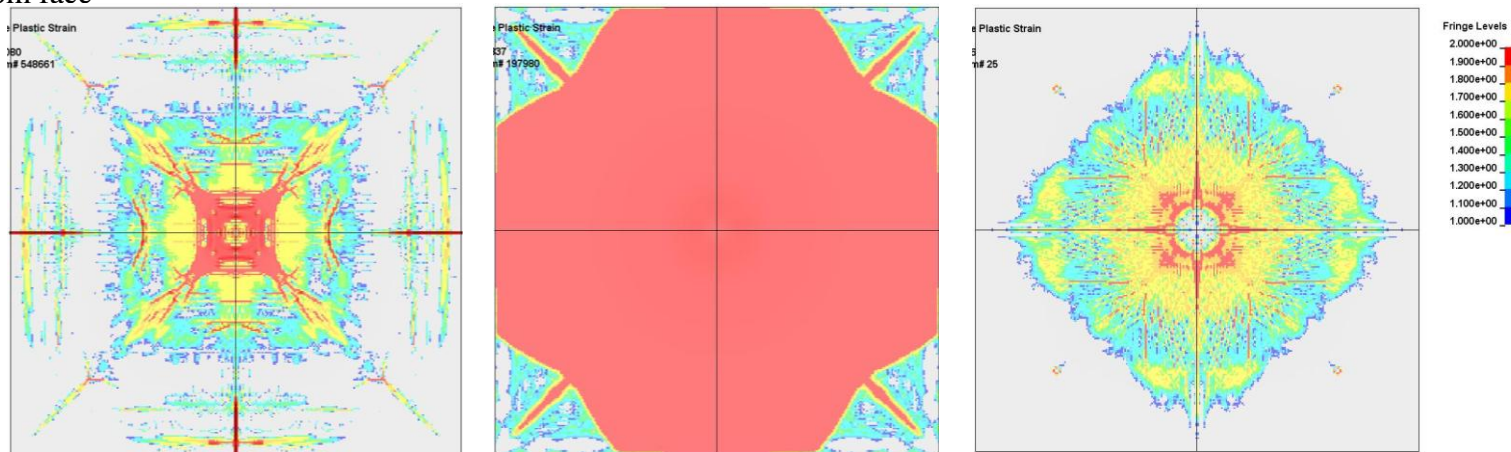
(a) Asphalt concrete layer   (b) HSC layer   (c) ECC layer

Figure 6.43 Damage pattern for each layer of proposed multi-layers pavement

Top face
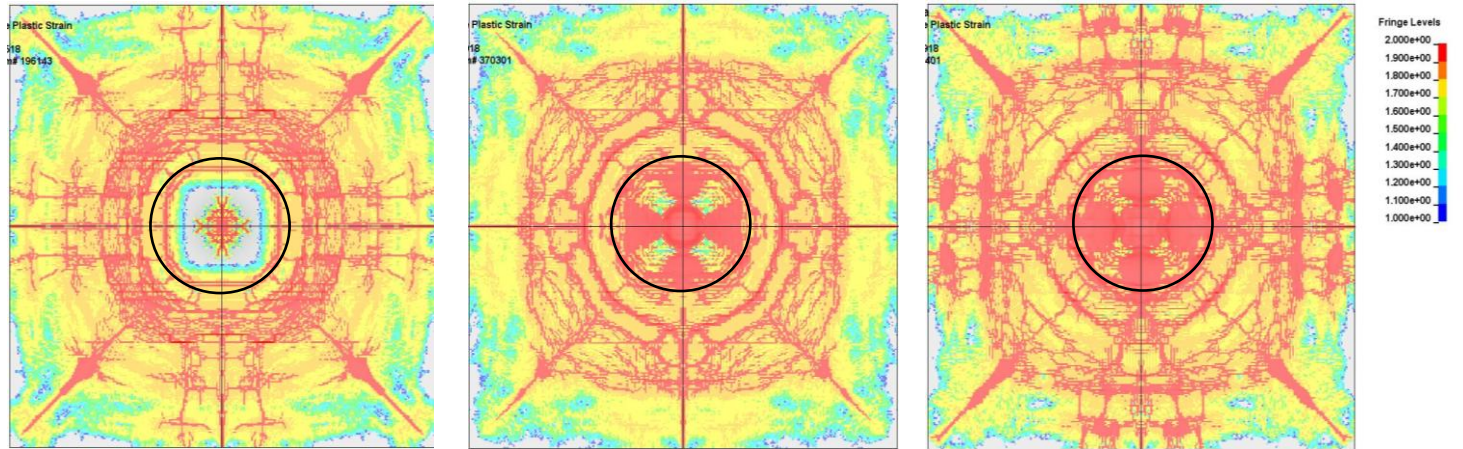
Bottom face
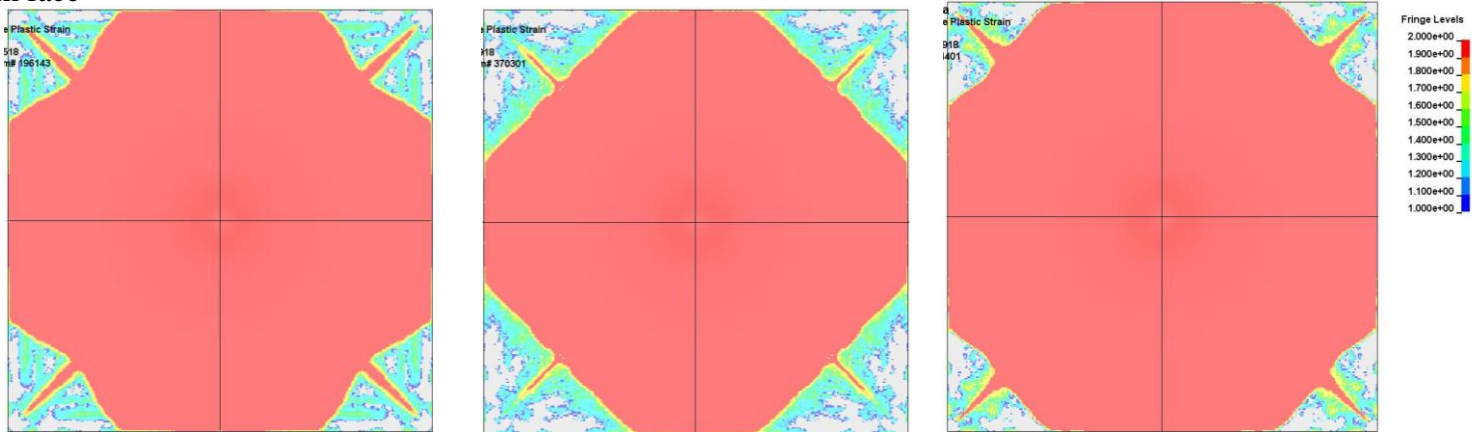
a) HSC with fc=40 MPa (b) HSC with fc=90 MPa (c) HSC with fc=110 MPa

Figure 6.44 Damage pattern for HSC layer with different compressive strength

Top face
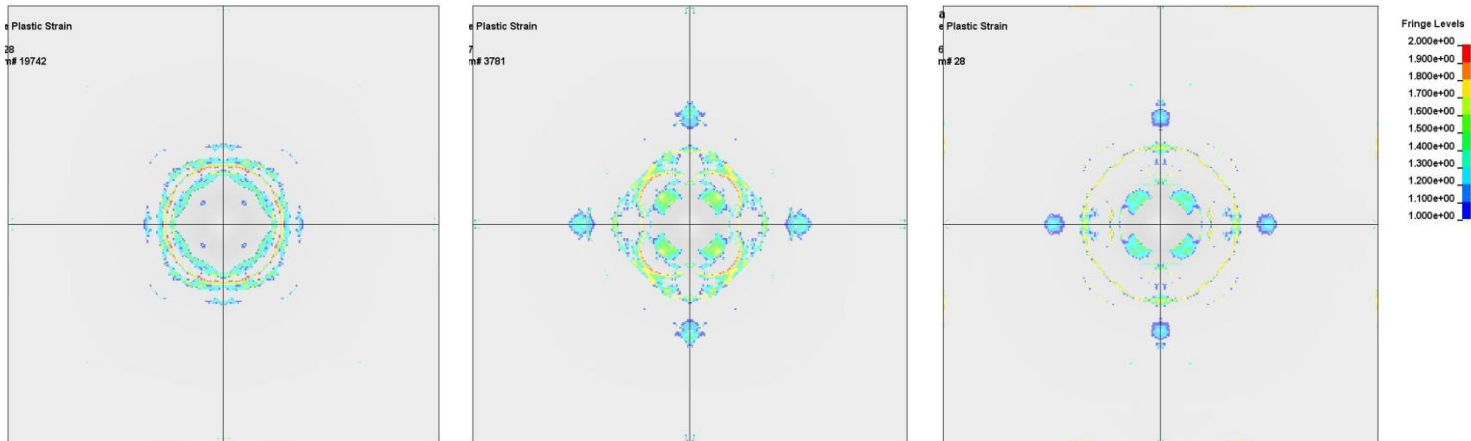
Bottom face
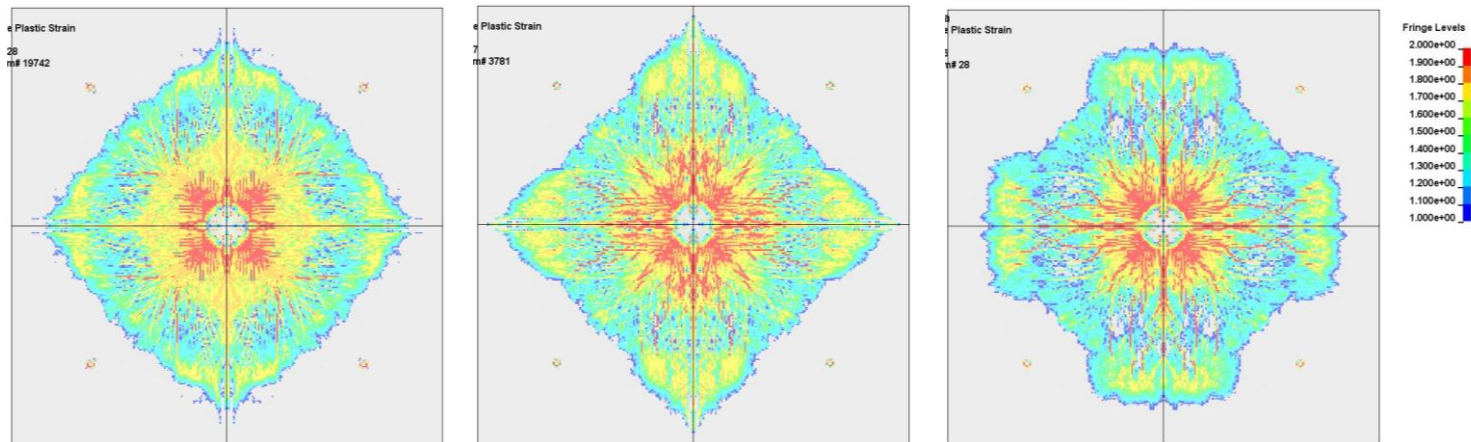
(a) HSC with fc=40 MPa   (b) HSC with fc=90 MPa   (c) HSC with fc=110 MPa

Figure 6.45 Damage pattern of ECC layer overlaid by HSC layer with different compressive strength
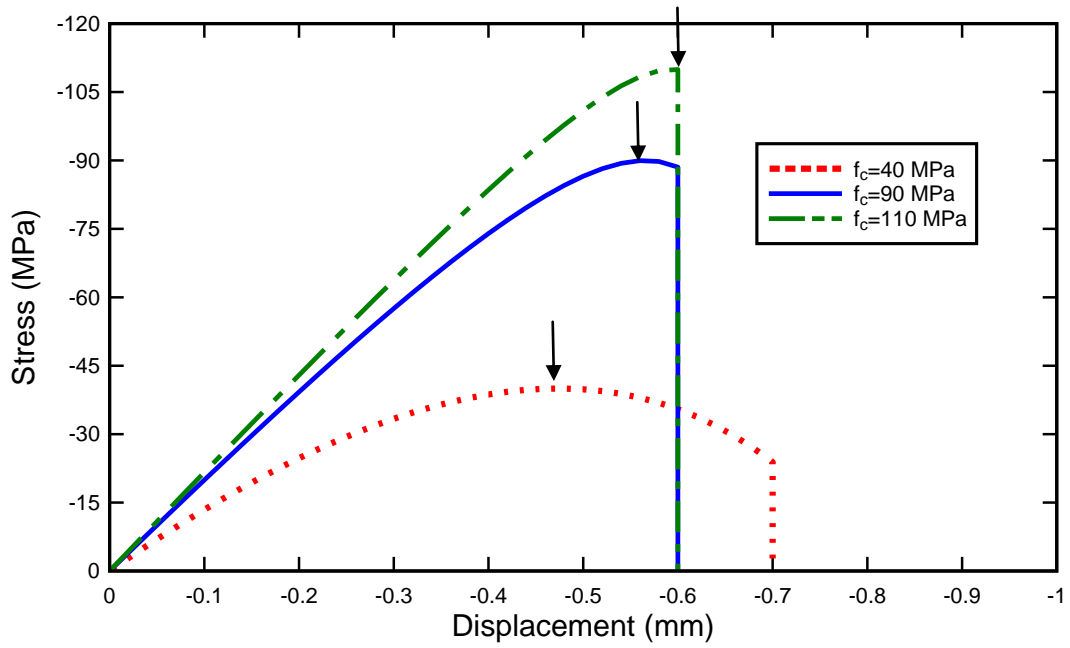
Figure 6.46 Stress-displacement curve of uniaxial compressive test
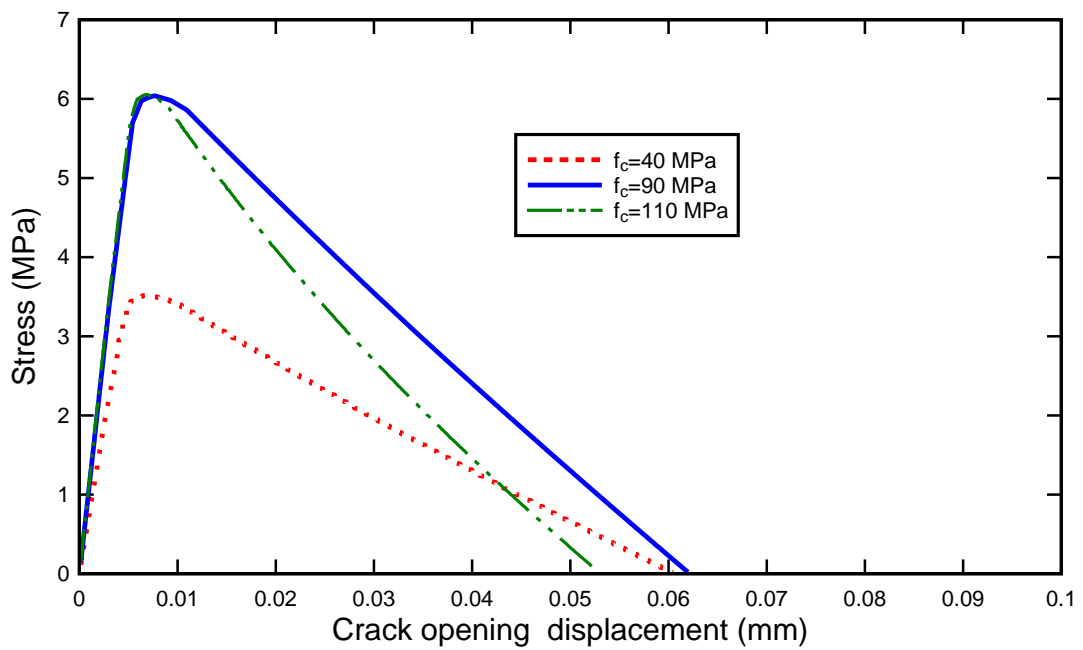
Figure 6.47 Stress-displacement curve of uniaxial tensile test

312
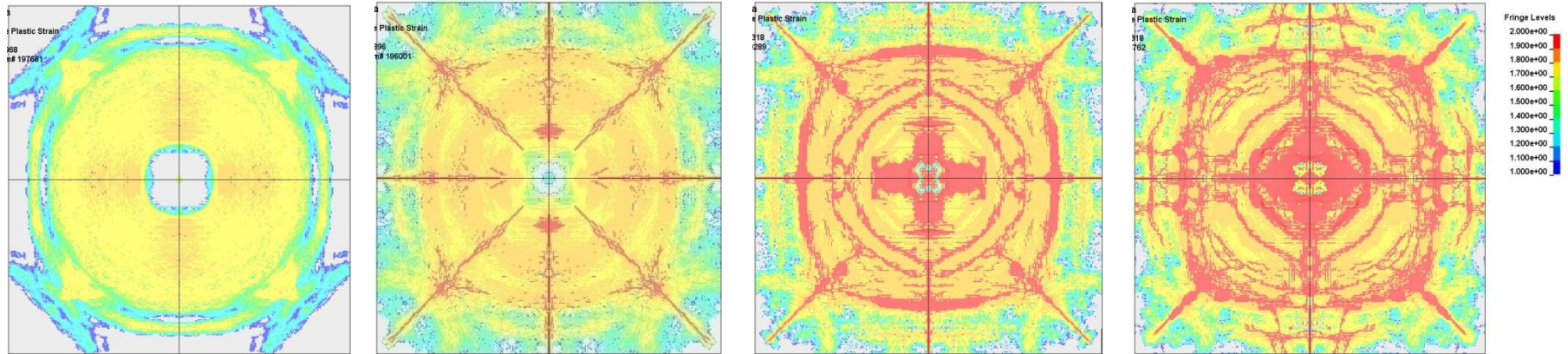
Top face
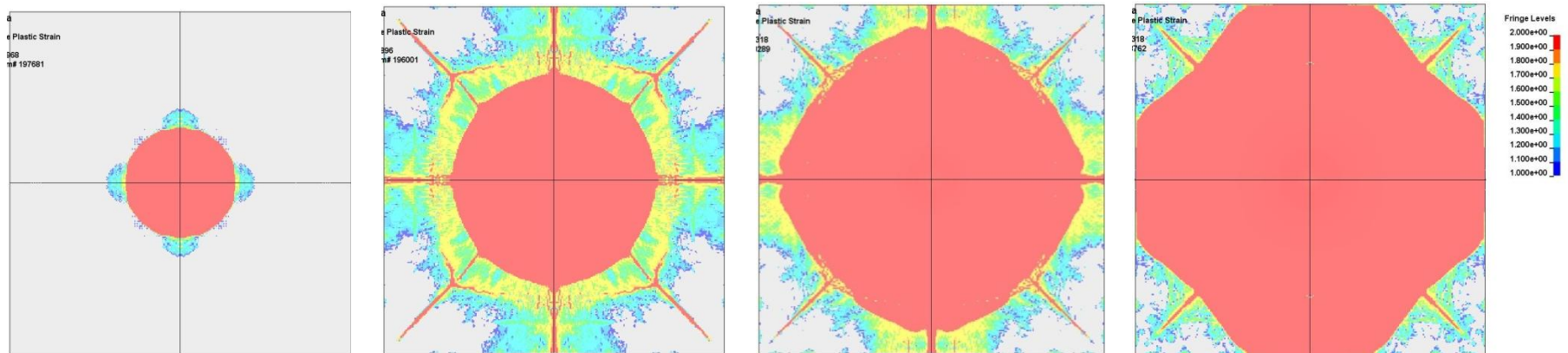
Bottom face

(a) 20% Peak pressure   (b) 40% Peak pressure   (c) 60% Peak pressure   (d) 80% Peak pressure

Figure 6.48 Damage pattern of HSC layer with compressive strength of 110 MPa under different peak pressure

313
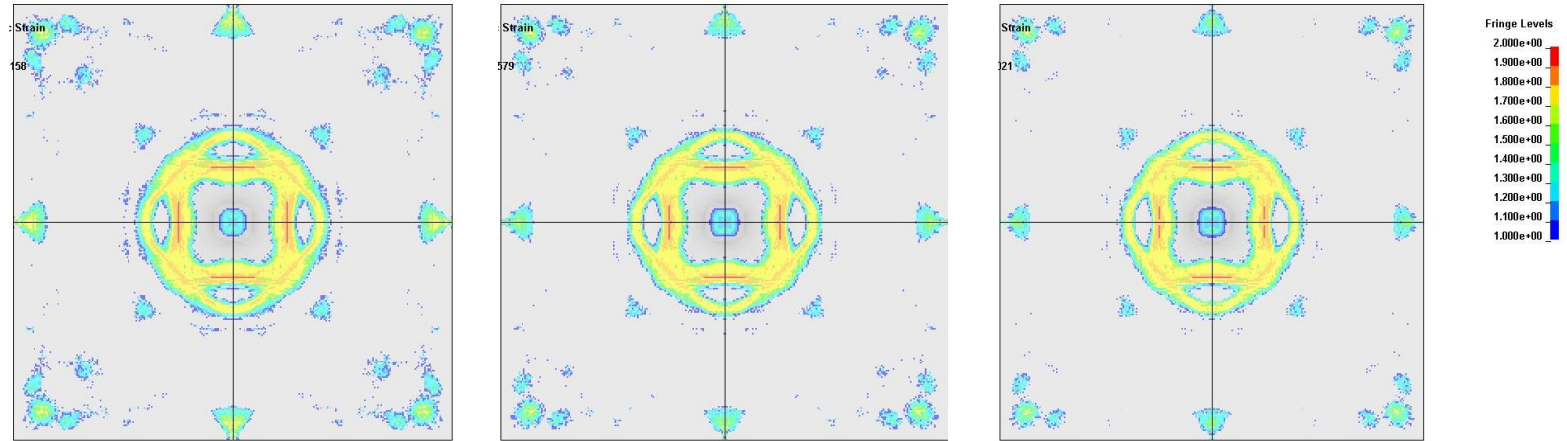
Top face
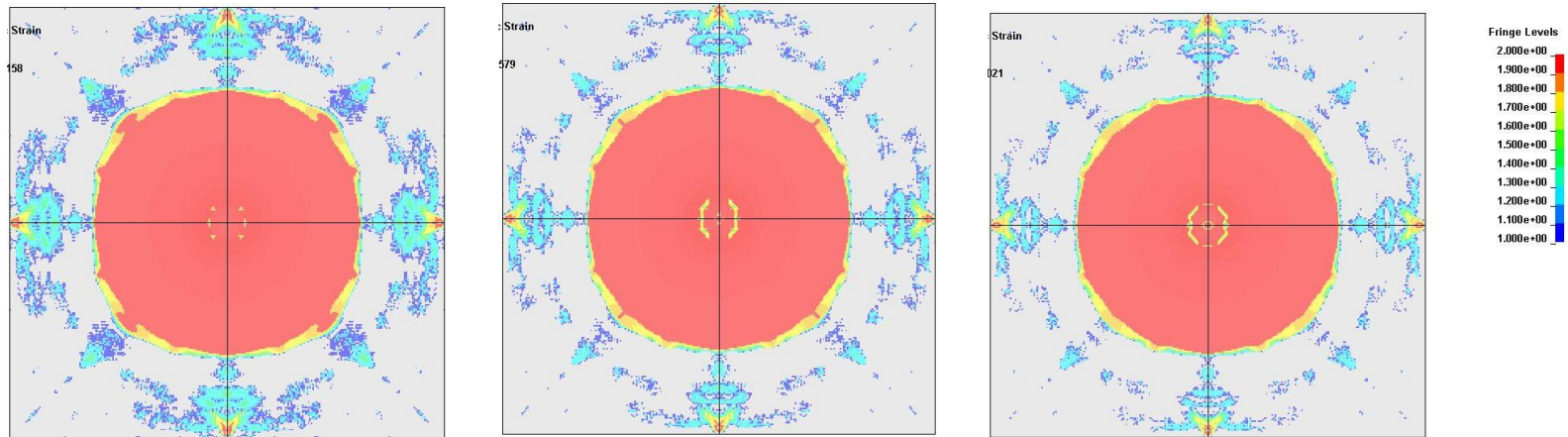
Bottom face

(a) HSC with G_f=2 N/mm   (b) HSC with G_f=4 N/mm   (c) HSC with G_f=6 N/mm

Figure 6.49 Damage pattern of HSC with different fracture energy

(a) HSC with G_f=2 N/mm

Fringe Levels

2.000e+00
1.900e+00
1.800e+00
1.700e+00
1.600e+00
1.500e+00
1.400e+00
1.300e+00
1.200e+00
1.100e+00
1.000e+00

(b) HSC with G_f=4 N/mm
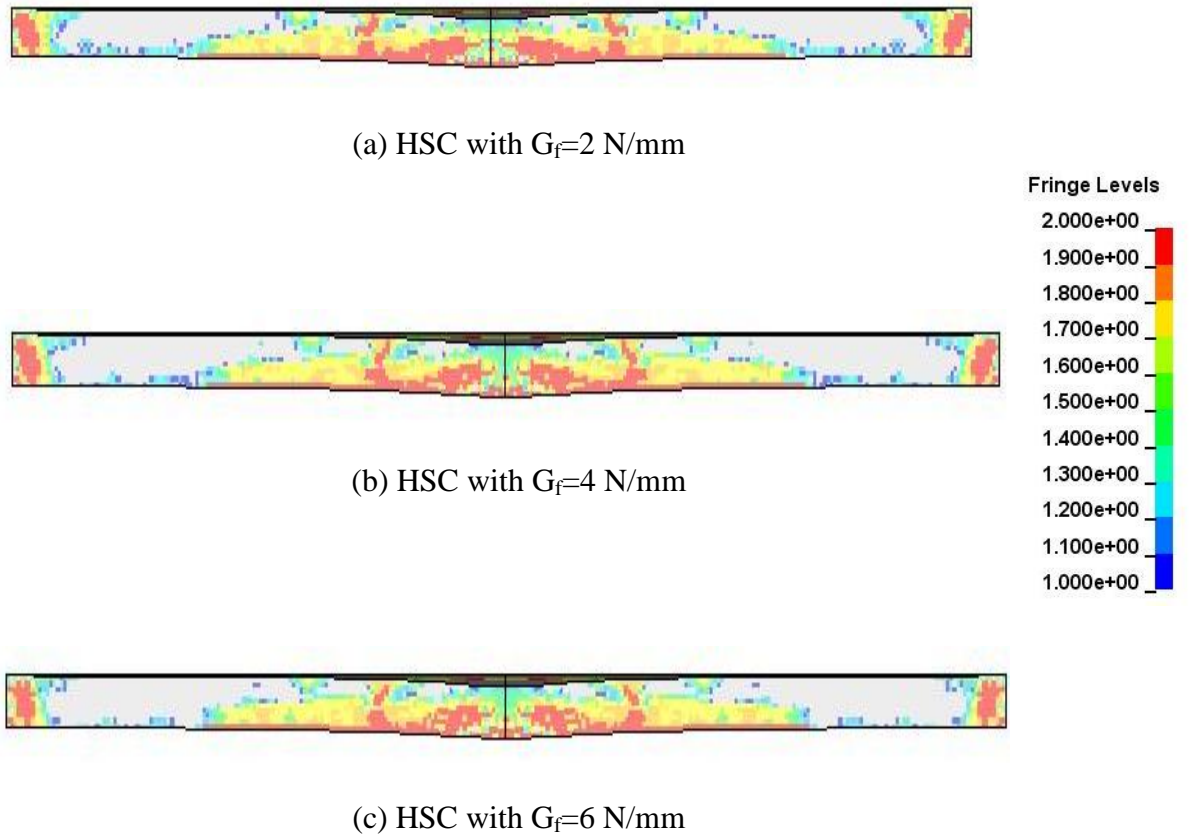
(c) HSC with G_f=6 N/mm

Figure 6.50 Damage pattern of the cross section of HSC layer

Top face
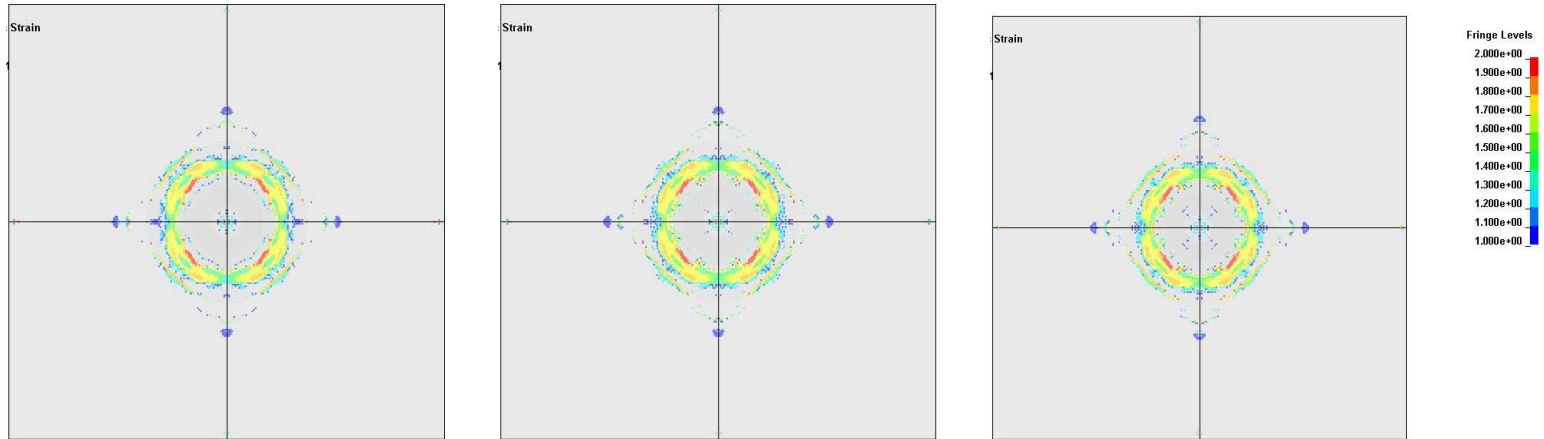
Bottom face
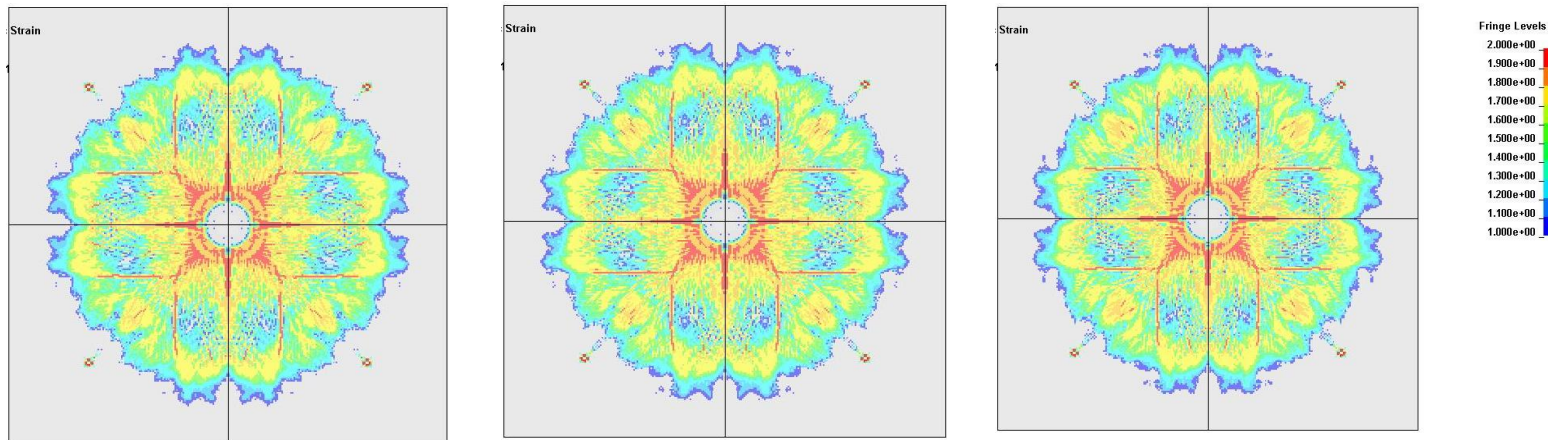
(a) Overlaid by HSC with G_f=2 N/mm   (b) Overlaid by HSC with G_f=4 N/mm   (c) Overlaid by HSC with G_f=6 N/mm

Figure 6.51 Damage pattern of ECC overlaid by HSC with different fracture energy

Top face
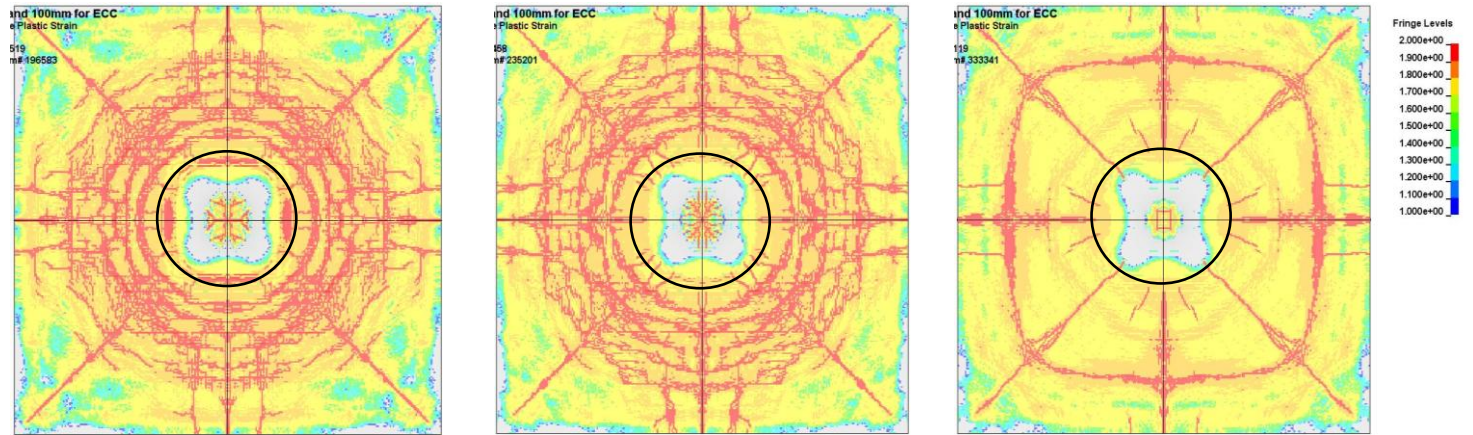
Bottom face
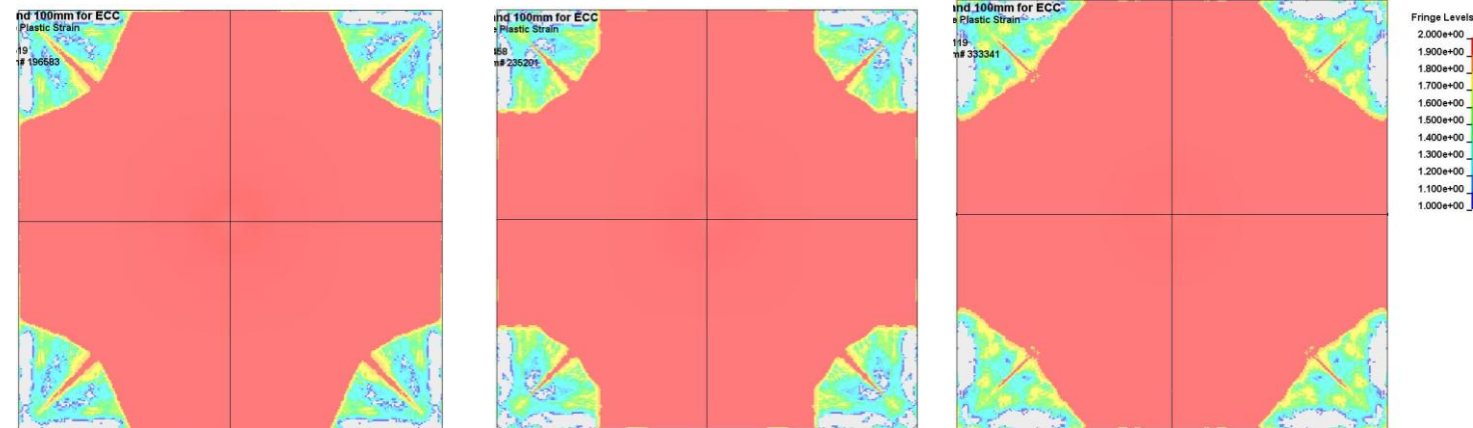
(a) HSC layer with120 mm thickness   (b) HSC layer with 140 mm thickness   (c) HSC layer with 200 mm thickness

Figure 6.52 Damage pattern for HSC layer with different thickness (Set 1)

(a) HSC with 120 mm thickness

(b) HSC with 140 mm thickness

(c) HSC with 200 mm thickness
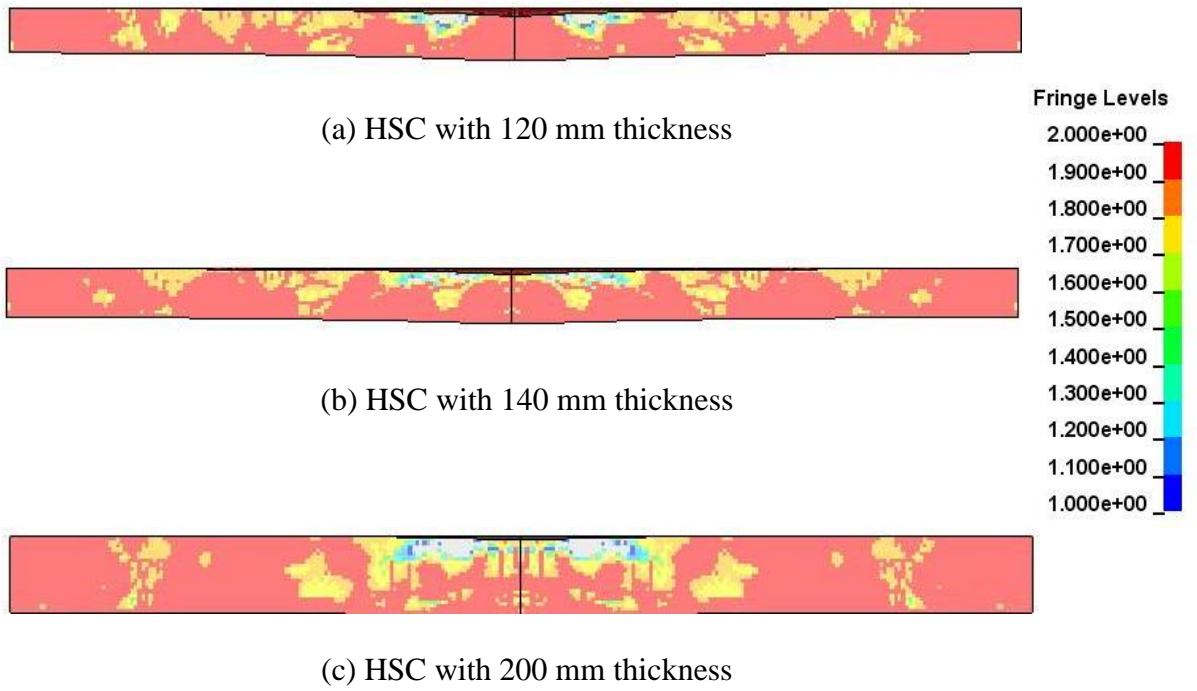
Figure 6.53 Damage pattern of the cross section of HSC layer with different thickness (Set 1)

Top face
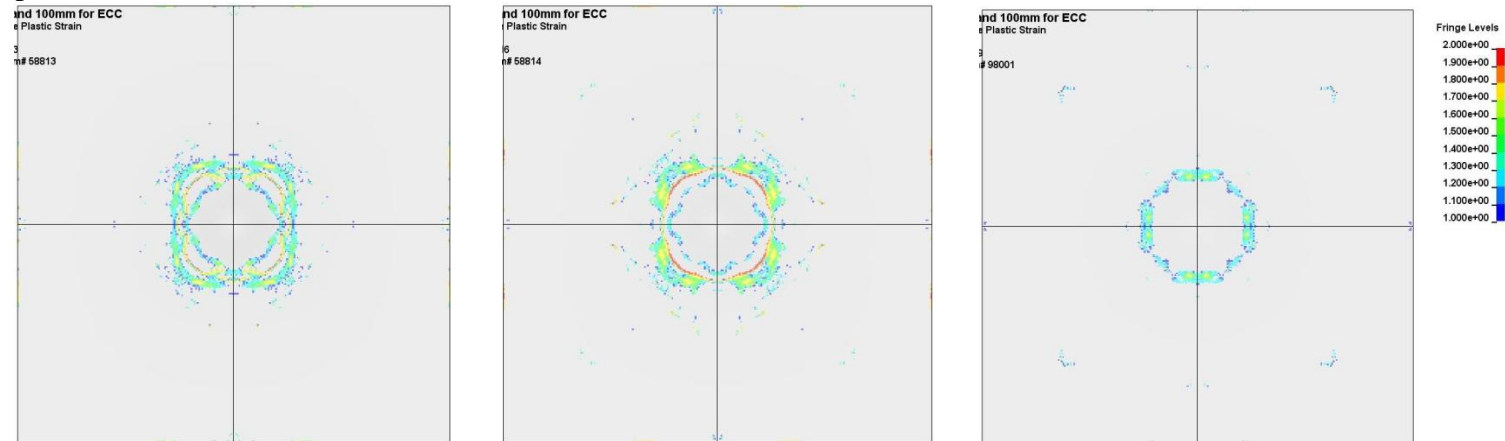
Bottom face
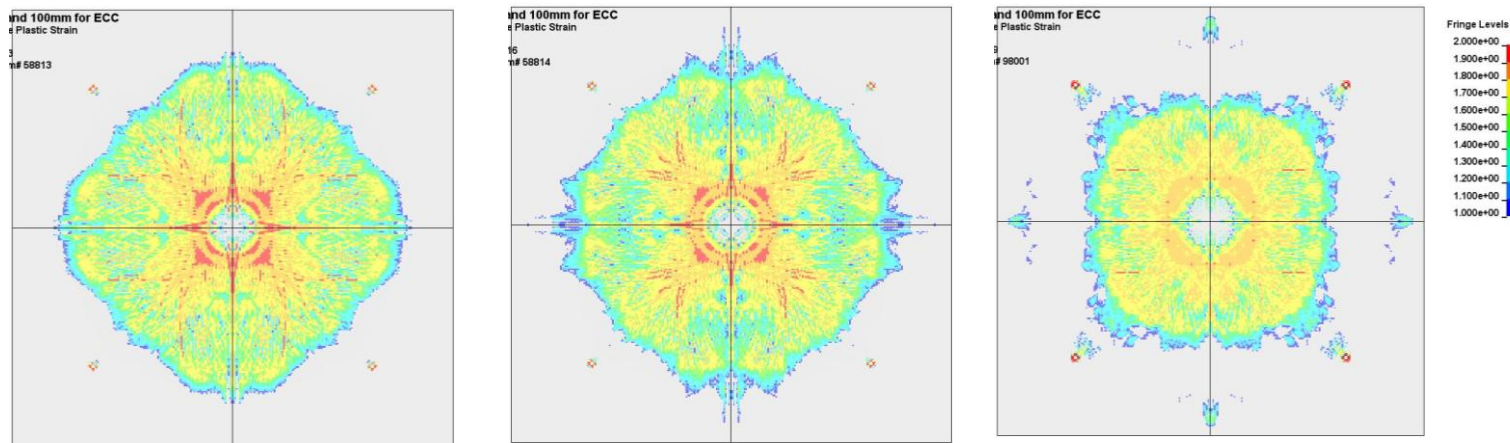
(a) Overlaid by 120 mm thickness HSC (b) Overlaid by 140 mm thickness HSC (c) Overlaid by 200 mm thickness HSC

Figure 6.54 Damage pattern for ECC layer with 100 mm thickness overlaid by different thickness of HSC layer (Set 1)

(a) ECC with 100 mm thickness overlaid by 120 mm thickness HSC

(b) ECC with 100 mm thickness overlaid by 140 mm thickness HSC

(c) ECC with 100 mm thickness overlaid by 200 mm thickness HSC
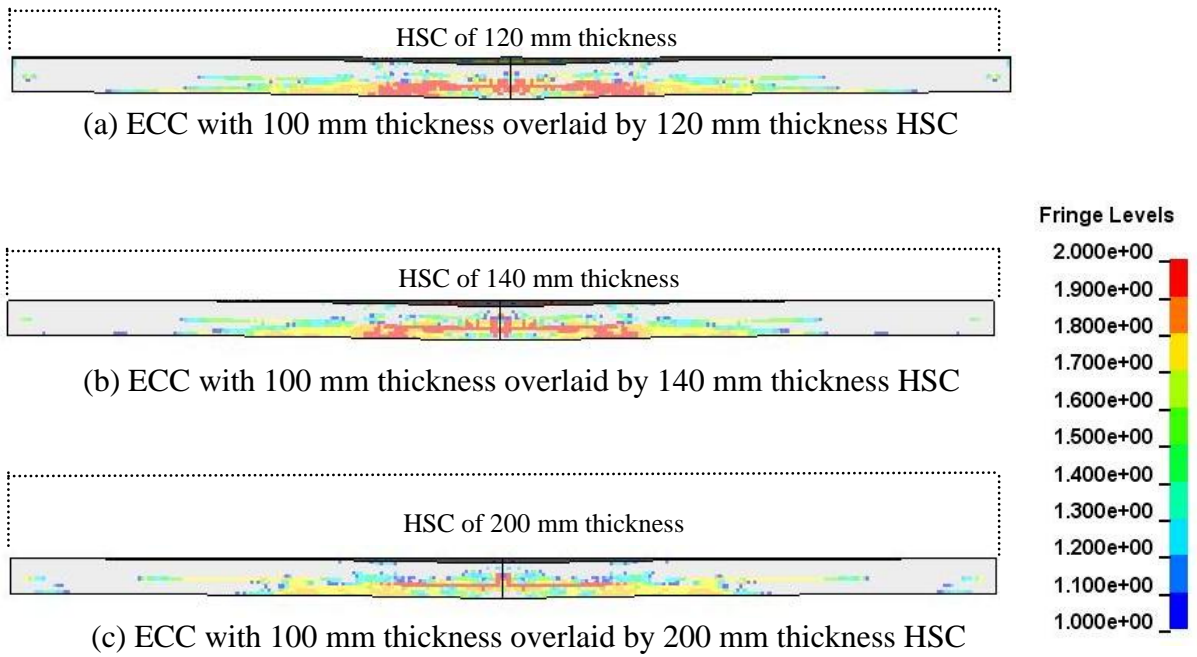
Figure 6.55 Damage pattern of the cross section of ECC layer overlaid by different thickness of HSC layer (Set 1)

Top face
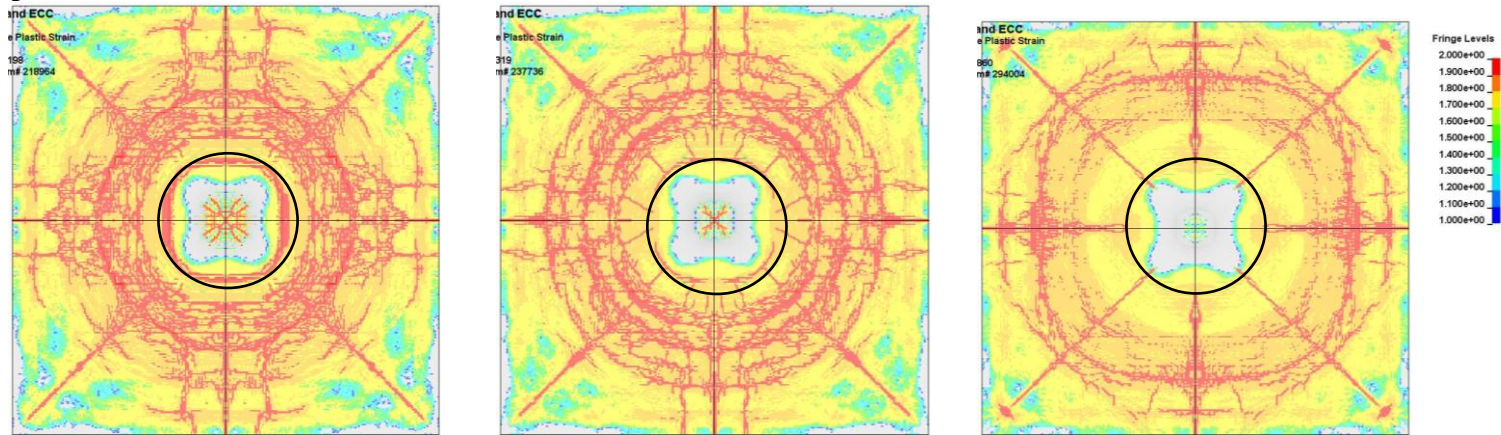
Bottom face
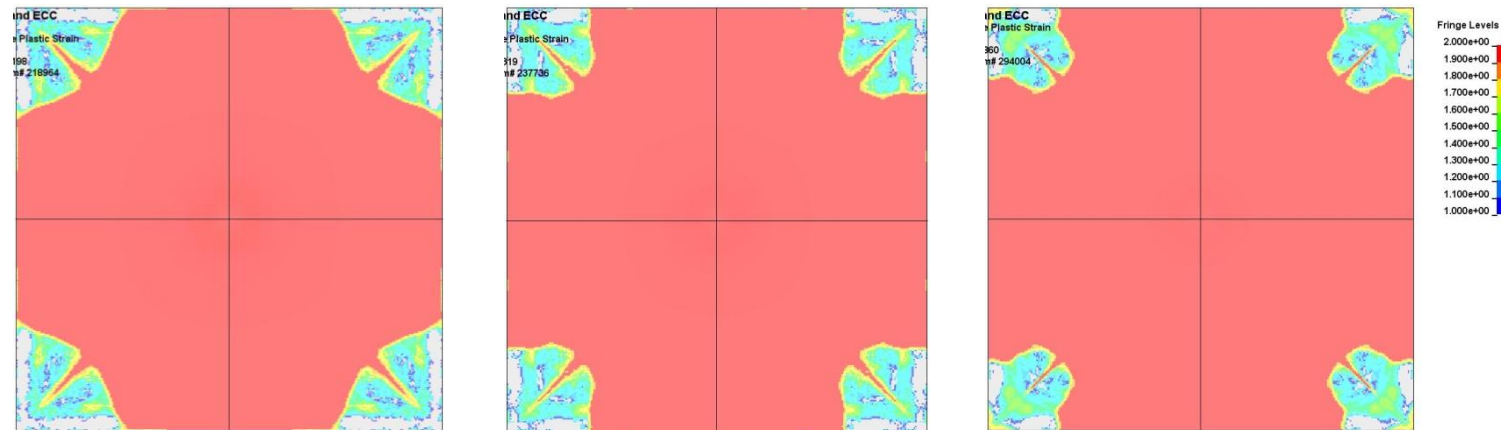
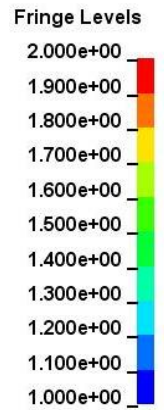(a) 110 mm thickness for HSC & ECC   (b) 120 mm thickness for HSC & ECC   (c) 150 mm thickness for HSC & ECC

Figure 6.56 Damage pattern for HSC layer with equal thickness of HSC and ECC layer (Set 2)

(a) HSC with 110 mm thickness

(b) HSC with 120 mm thickness

(c) HSC with 150 mm thickness
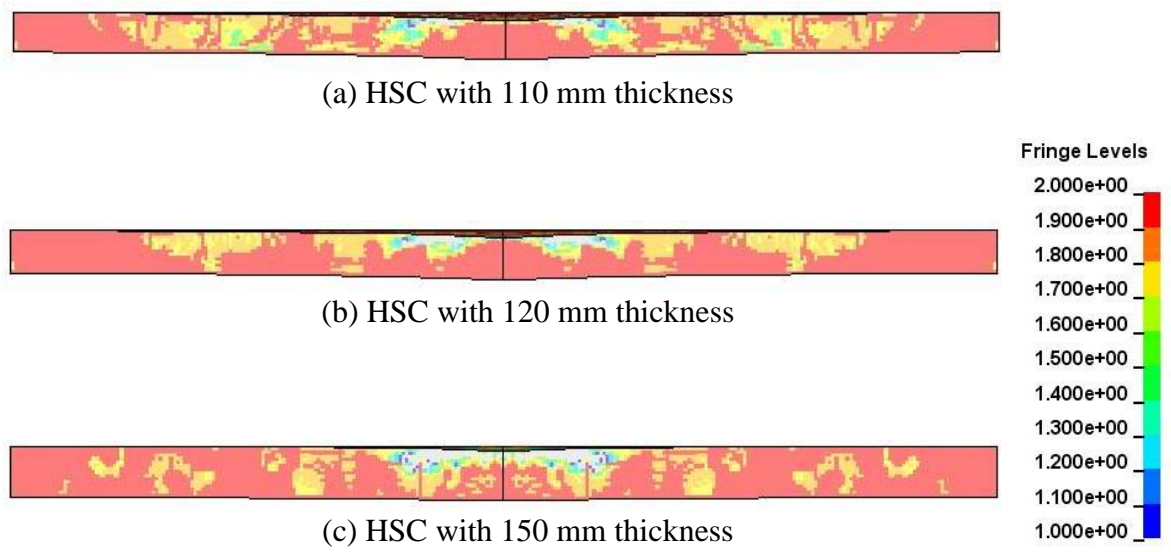
Figure 6.57 Damage pattern of the cross section of HSC layer with equal thickness of HSC and ECC layer (Set 2)

Top face
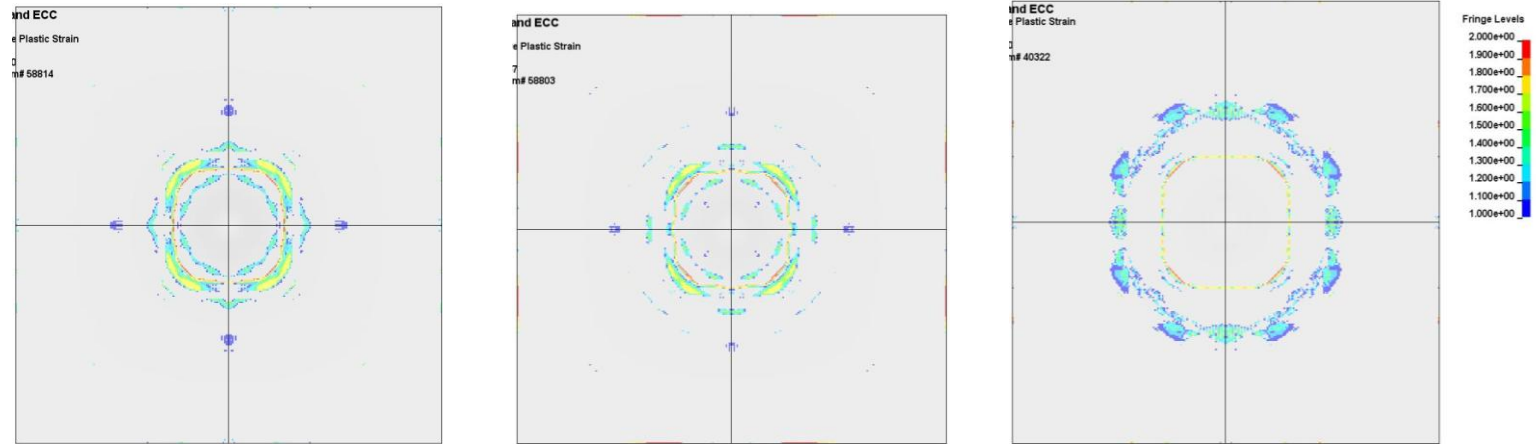
Bottom face
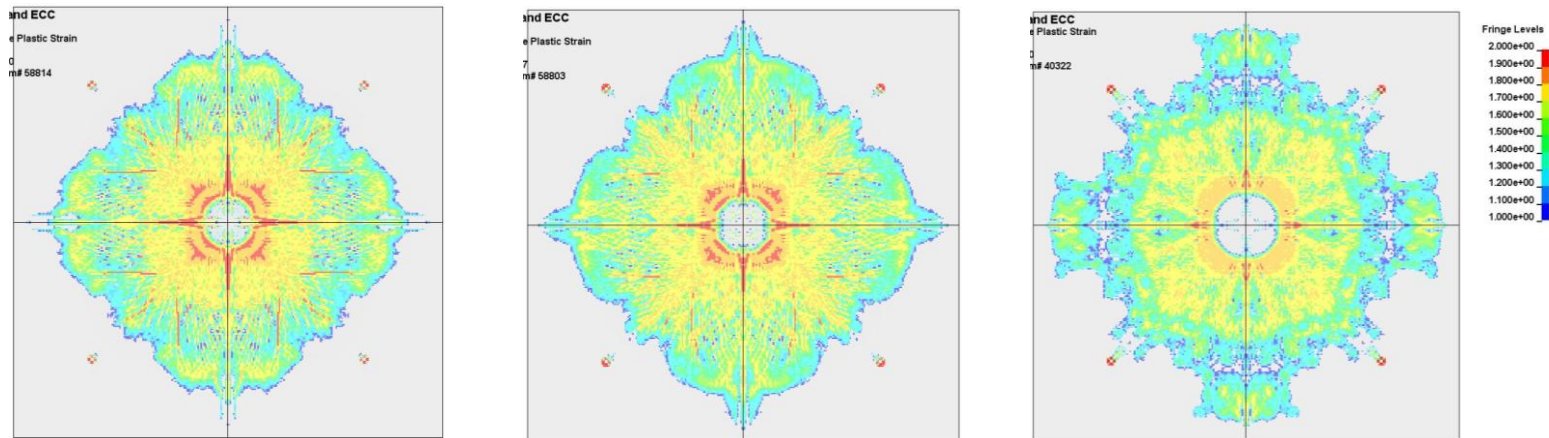
(a) 110 mm thickness for HSC & ECC   (b) 120 mm thickness for HSC & ECC   (c) 150 mm thickness for HSC & ECC

Figure 6.58 Damage pattern for ECC layer with equal thickness of HSC and ECC (Set 2)

HSC of 110 mm thickness

(a) ECC with 110 mm thickness overlaid by 110 mm thickness HSC

Fringe Levels

2.000e+00
1.900e+00
1.800e+00
1.700e+00
1.600e+00
1.500e+00
1.400e+00
1.300e+00
1.200e+00
1.100e+00
1.000e+00

HSC of 120 mm thickness
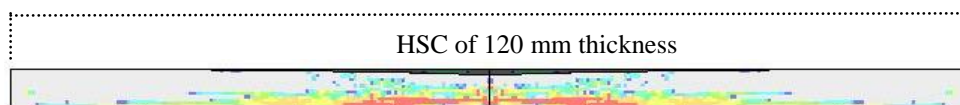
(b) ECC with 120 mm thickness overlaid by 120 mm thickness HSC

HSC of 150 mm thickness

(c) ECC with 150 mm thickness overlaid by 150 mm thickness HSC

Figure 6.59 Damage pattern of the cross section of ECC layer with same thickness of HSC and ECC (Set 2)

ECC with 100 mm thickness overlaid by 120 mm thickness HSC (Set 1)

ECC with 110 mm thickness overlaid by 110 mm thickness HSC (Set 2)
(a) Pair # 1
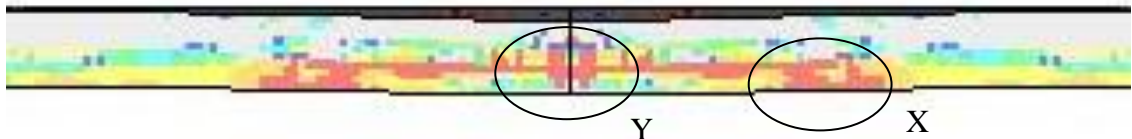
ECC with 100 mm thickness overlaid by 140 mm thickness HSC (Set 1)
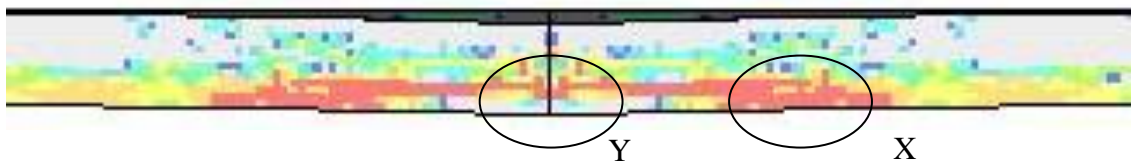
ECC with 120 mm thickness overlaid by 120 mm thickness HSC (Set 2)
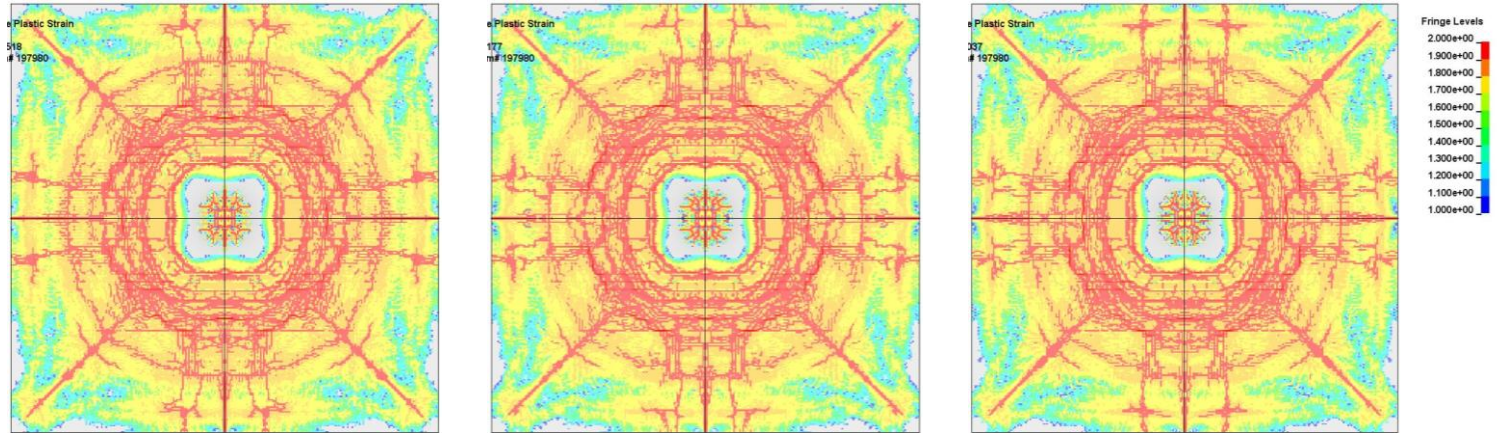(b) Pair # 2

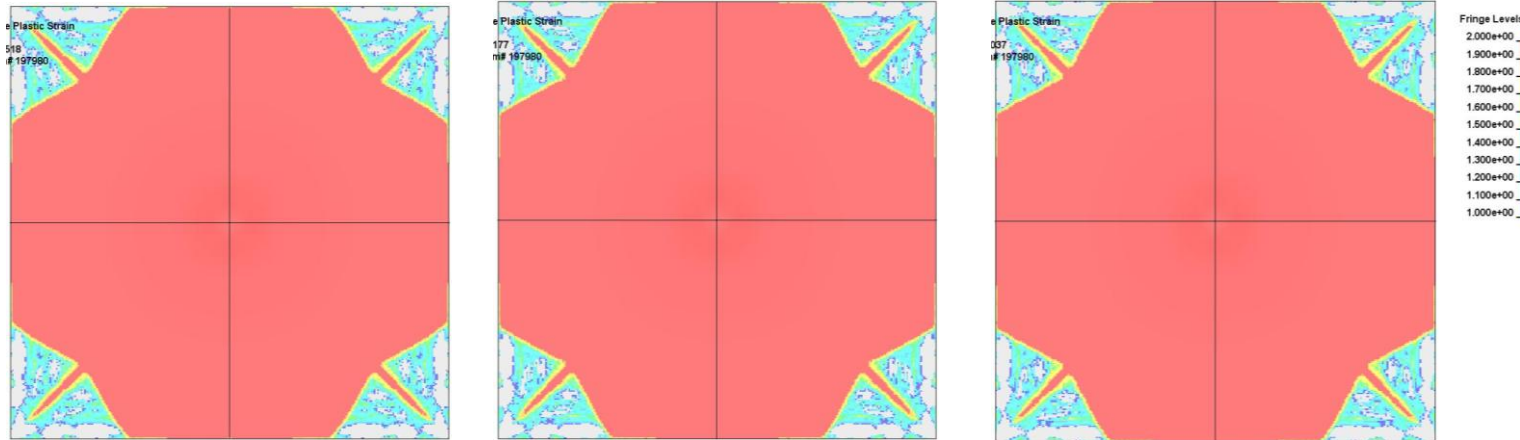ECC with 100 mm thickness overlaid by 200 mm thickness HSC (Set 1)
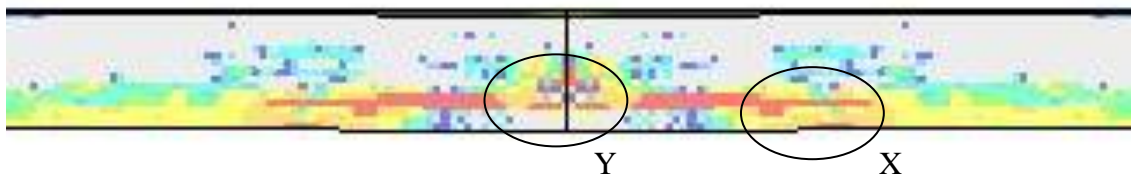
ECC with 150 mm thickness overlaid by 150 mm thickness HSC (Set 2)
(c) Pair #3

Figure 6.60 Comparison of ECC cross section in Set 1 and 2
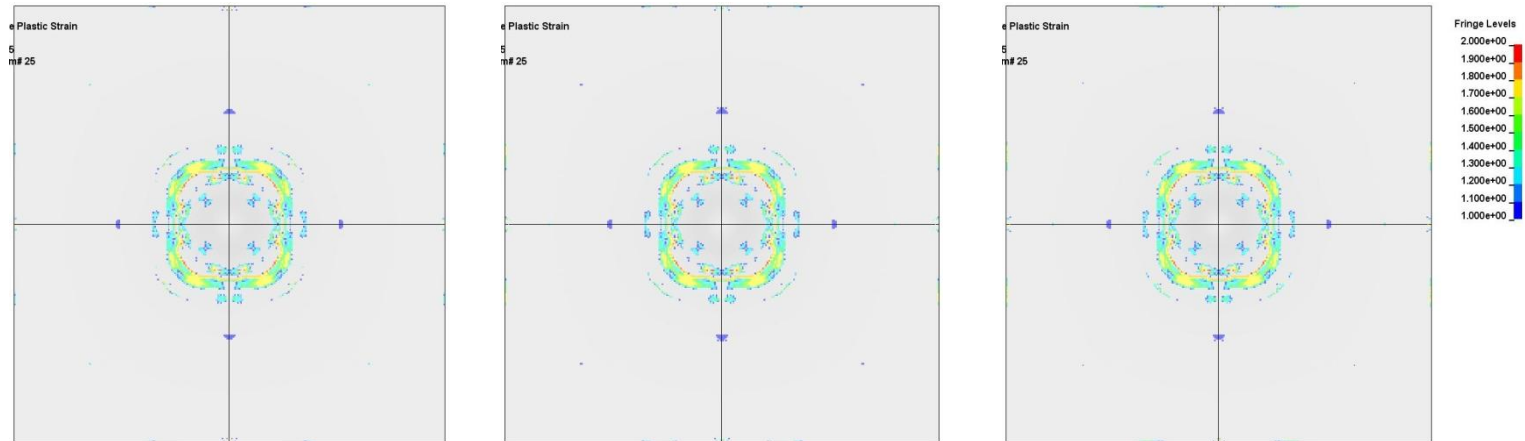
Top face

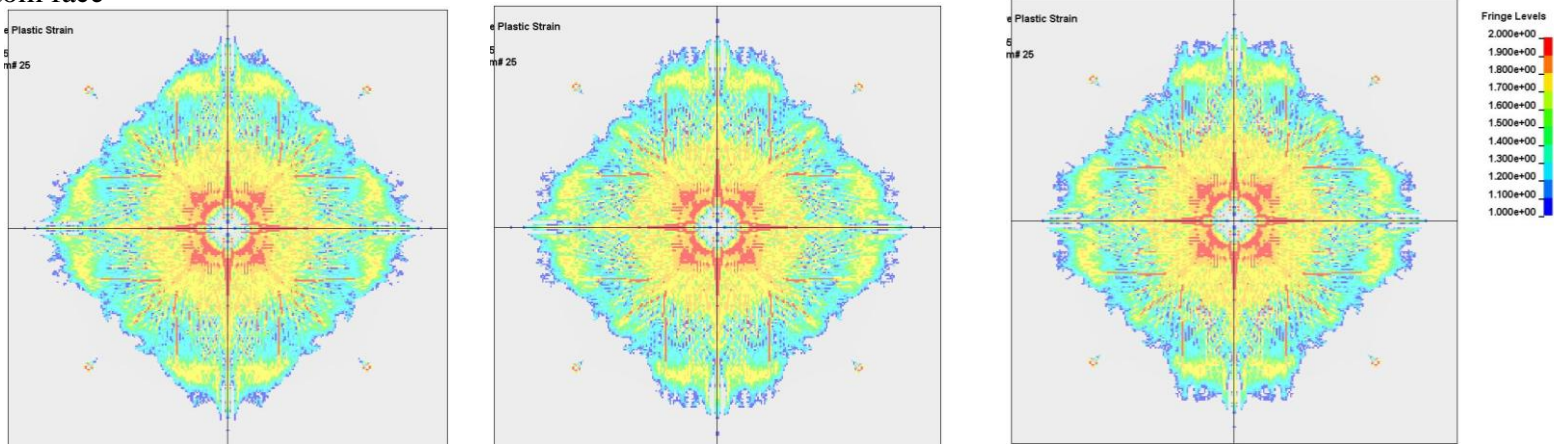Bottom face

(a) G_I=0.5 N/mm (b) G_I=1.0 N/mm (c) G_I=1.5 N/mm

Figure 6.61 Damage pattern of HSC layer for different tensile fracture energy G_I

Top face

Bottom face

(a) G_I=0.5 N/mm   (b) G_I=1.0 N/mm   (c) G_I=1.5 N/mm

Figure 6.62 Damage pattern of ECC layer for different tensile fracture energy G_I

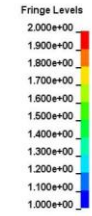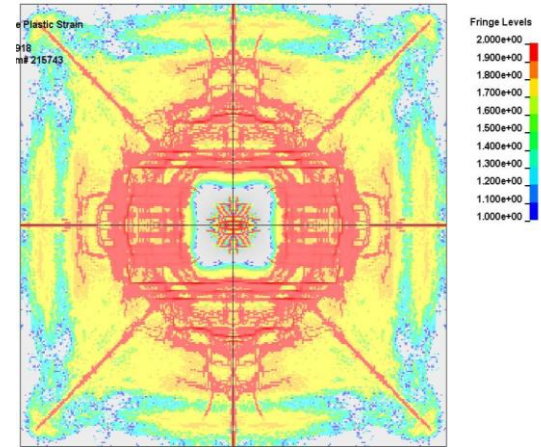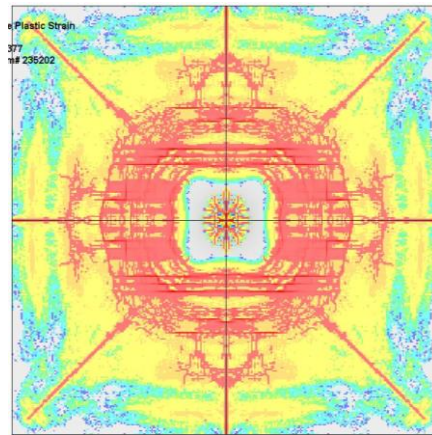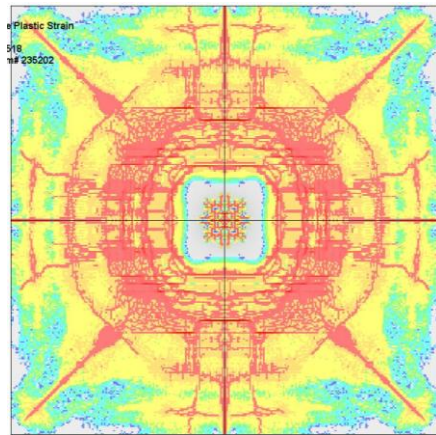Top face
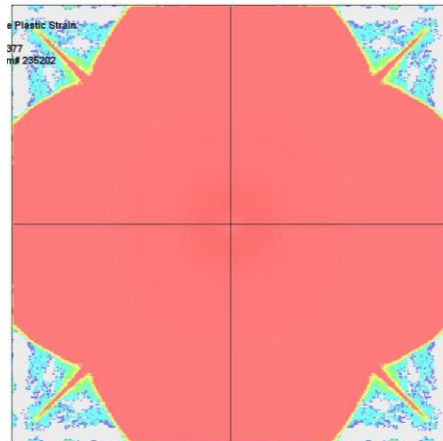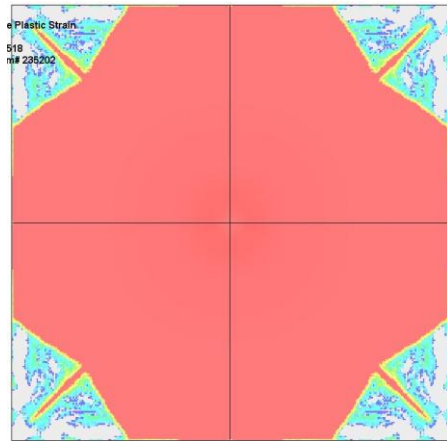
Bottom face

(a) G_{II}=10 N/mm   (b) G_{II}=20 N/mm   (c) G_{II}=30 N/mm

Figure 6.63 Damage pattern of HSC layer for different shear fracture energy G_{II}
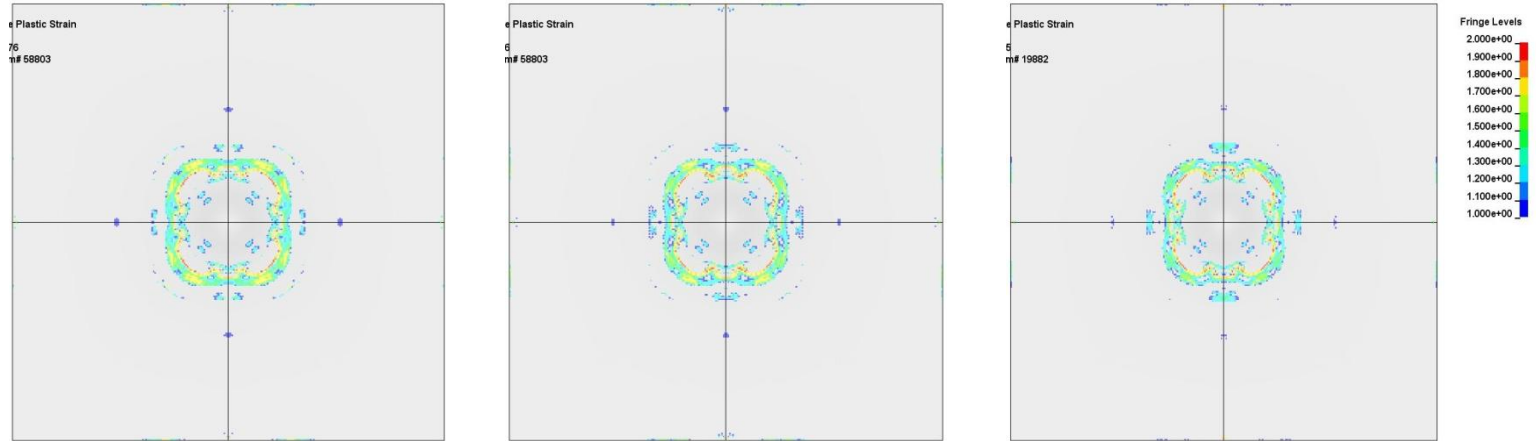
Top face
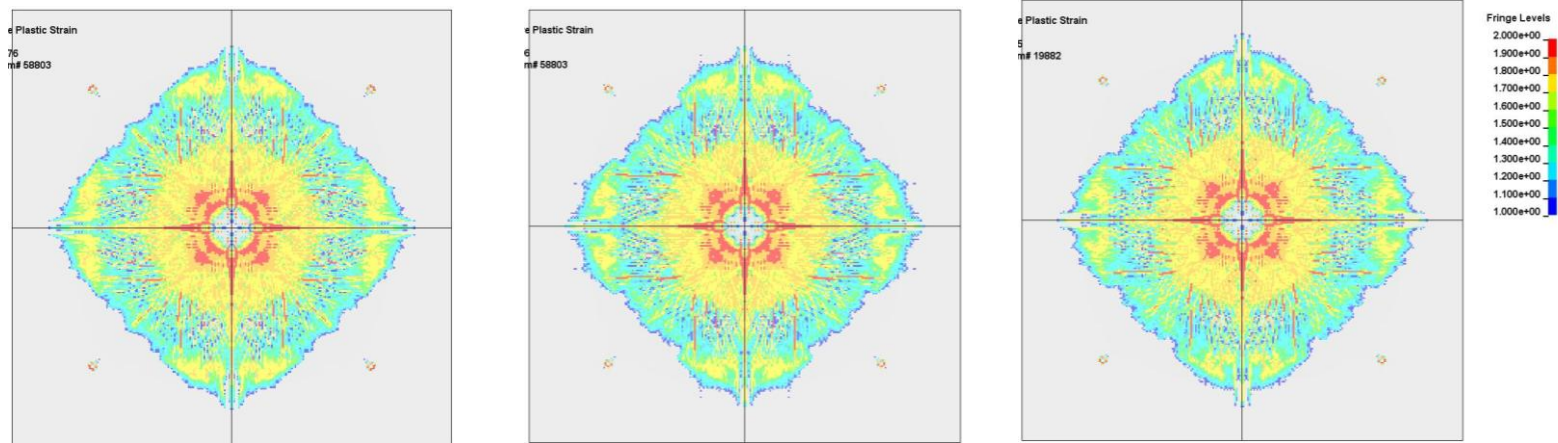
Bottom face

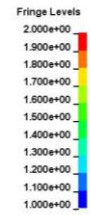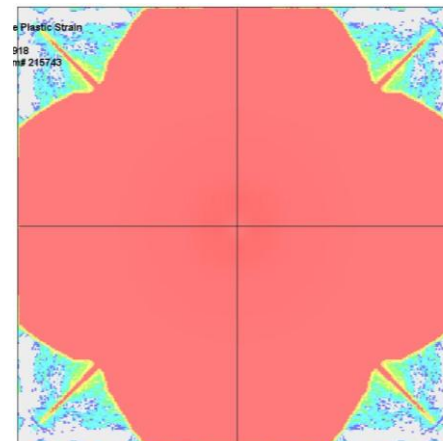(a) G_{II}=10 N/mm $\qquad$ (b) G_{II}=20 N/mm $\qquad$ (c) G_{II}=30 N/mm

Figure 6.64 Damage pattern of ECC layer for different shear fracture energy G_{II}
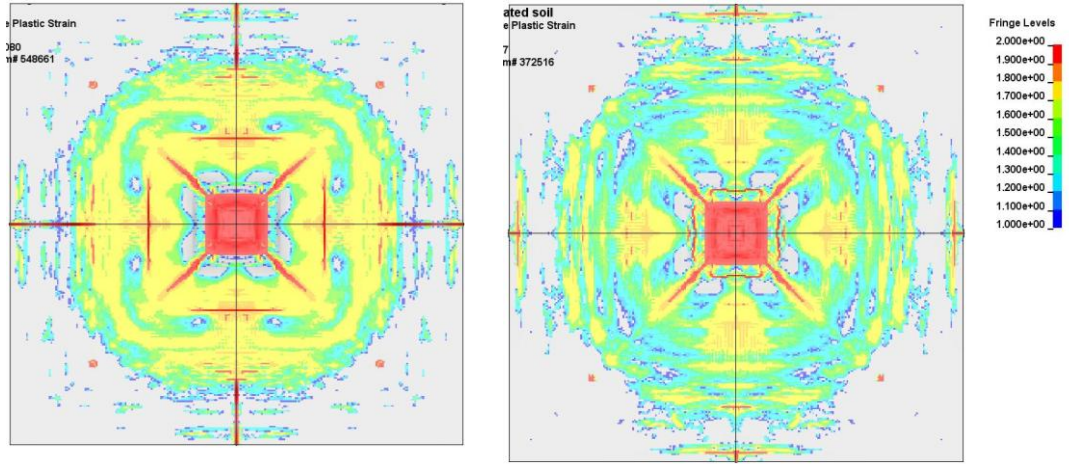
Top face
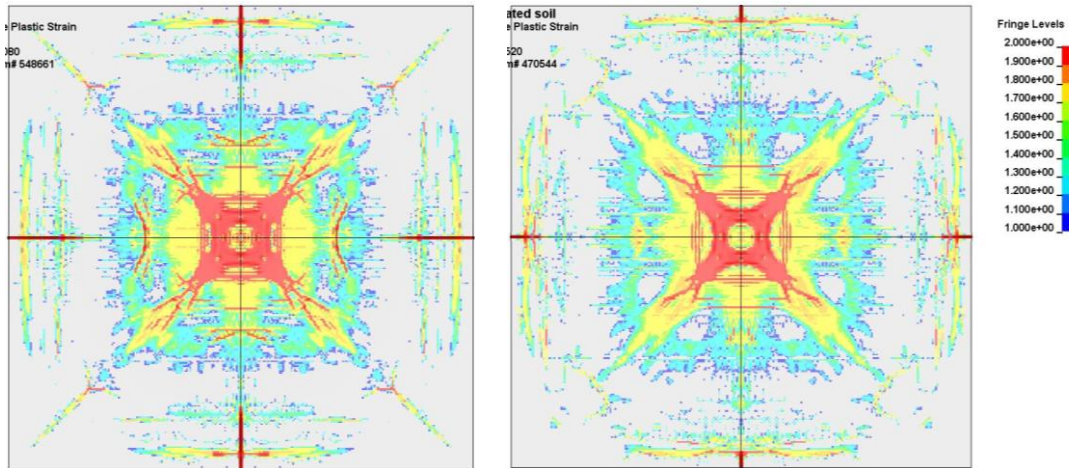
Bottom face

| (a) Untreated soil foundation | (b) Treated soil foundation |

Figure 6.65 Damage pattern of asphalt concrete layer for two types of soil foundation

Top face
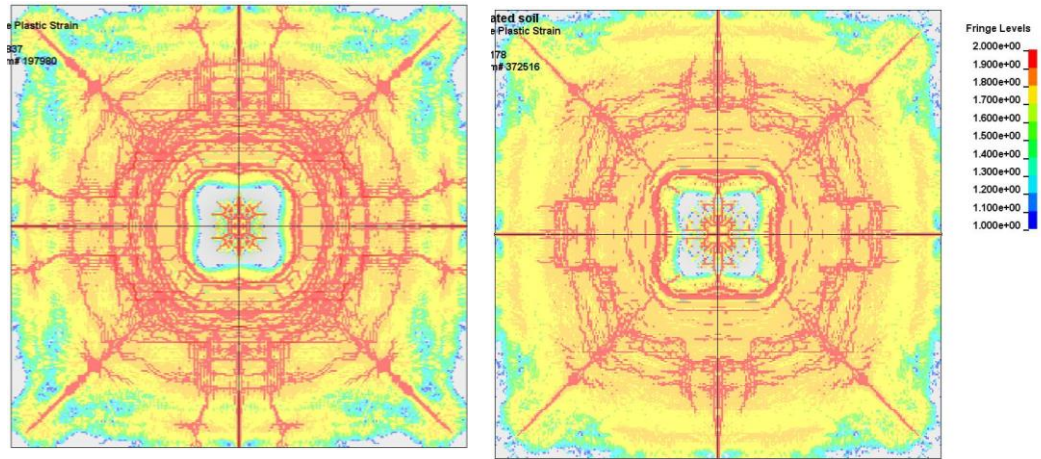
Bottom face
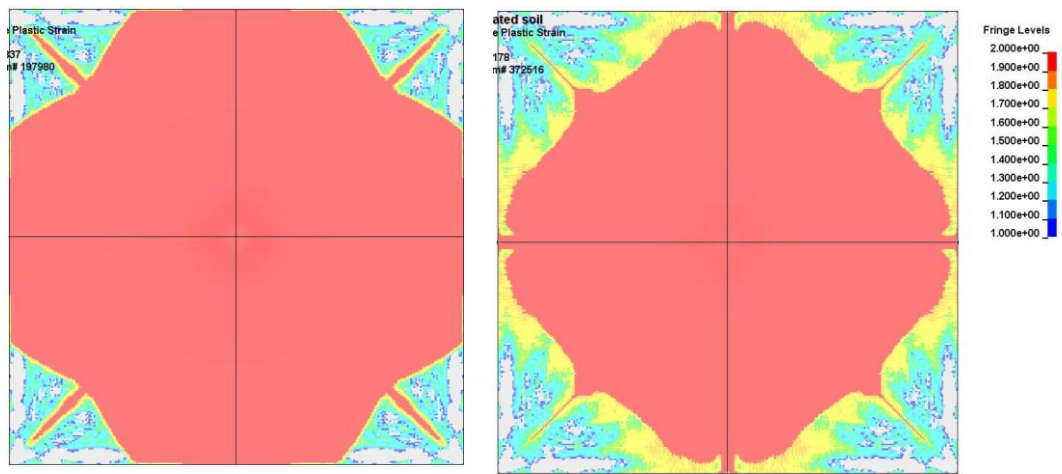
| (a) Untreated soil foundation | (b) Treated soil foundation |

Figure 6.66 Damage pattern of HSC layer for two types of soil foundation
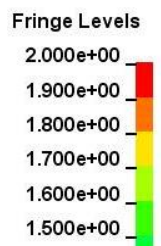
(a) Cross section of HSC layer for untreated soil foundation

(b) Cross section of HSC layer for treated soil foundation

Figure 6.67 Damage pattern of cross section of HSC layer with two types of soil foundation

Top face
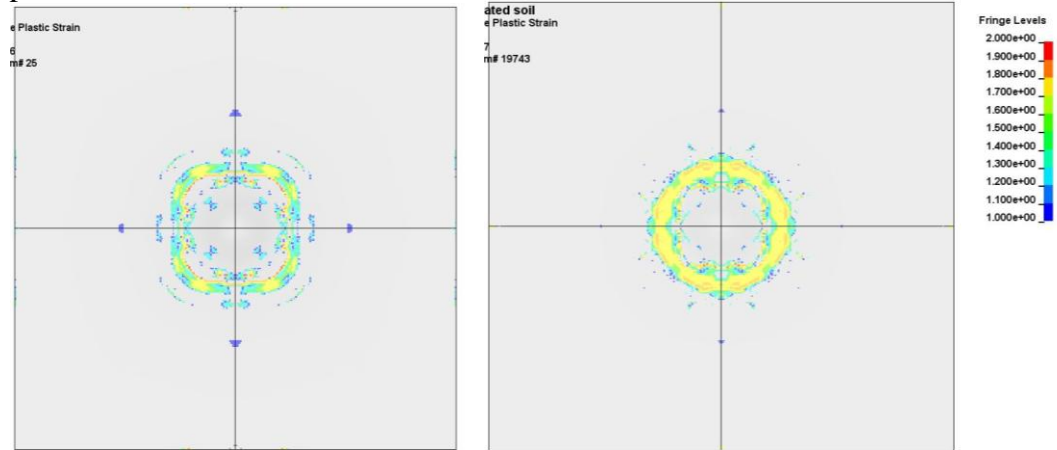
Bottom face
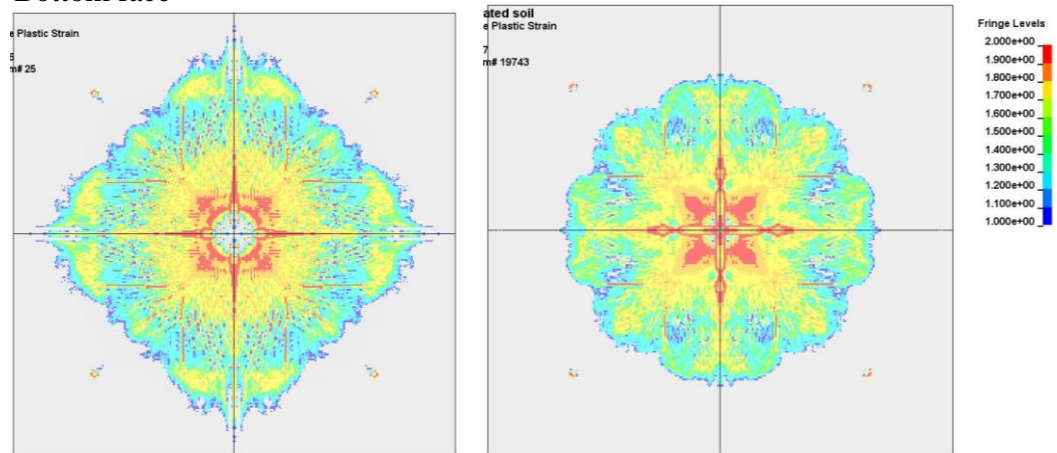
(a) Untreated soil foundation   (b) Cement treated soil foundation

Figure 6.68 Damage pattern of HSC layer under two types of soil foundation

(a) Cross section of ECC layer for untreated soil foundation

(b) Cross section of ECC layer for treated soil foundation

Figure 6.69 Damage pattern of cross section of ECC layer with two types of soil foundation
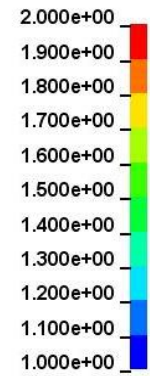
(a) Center portion of ECC cross section for untreated soil foundation
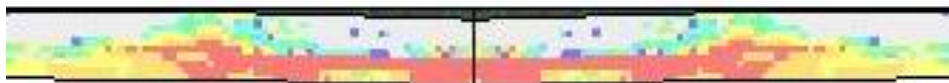
(a) Center portion of ECC cross section for treated soil foundation

Figure 6.70 Enlarge of center portion of ECC cross section with two types of soil foundation
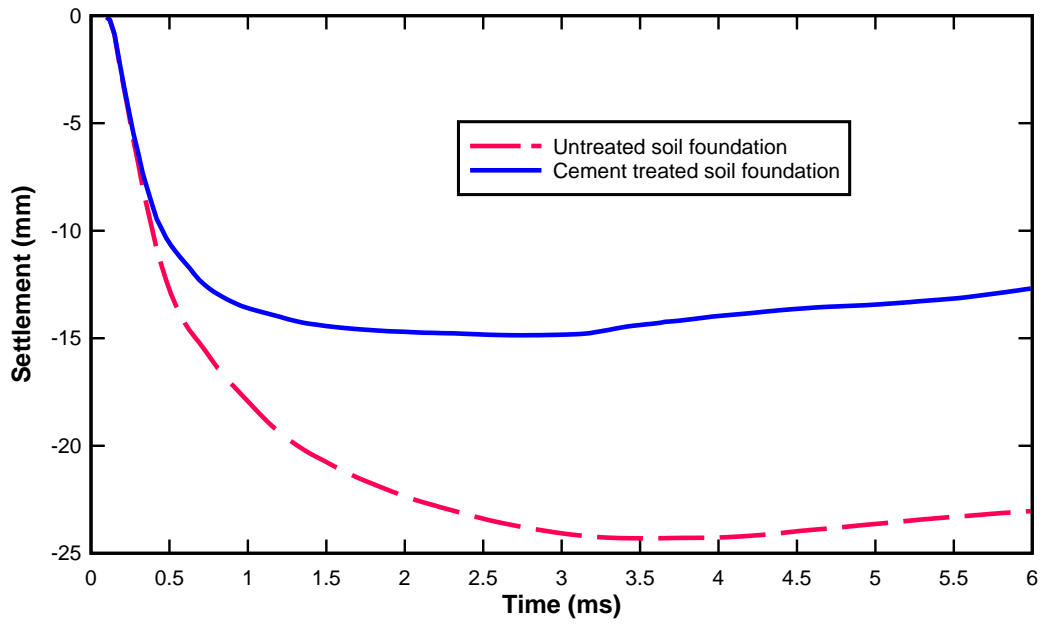
Figure 6.71 Settlement at middle point of the proposed multi-layers pavement slab
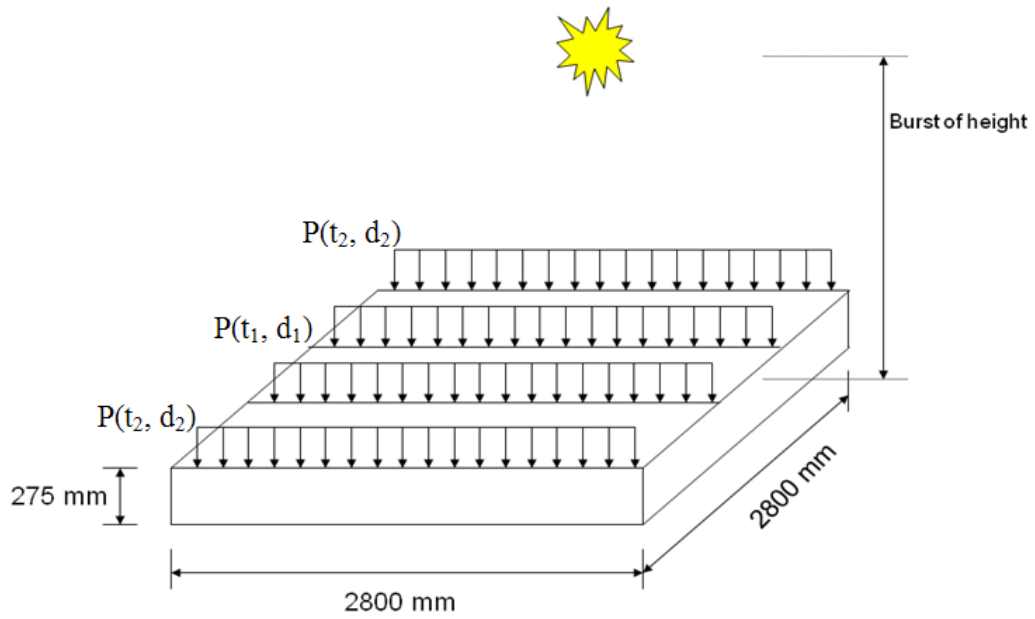
(a) Blast pressure from CONWEP
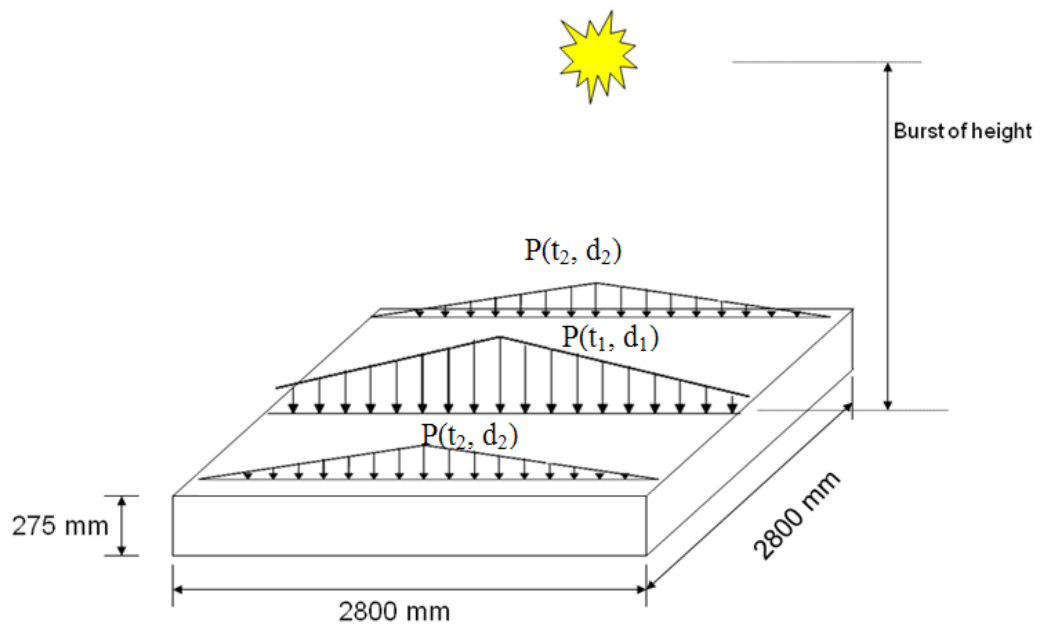
(b) Blast pressure simplified to linear decrease

Figure 6.72 Blast pressure acted on pavement surface

Top face
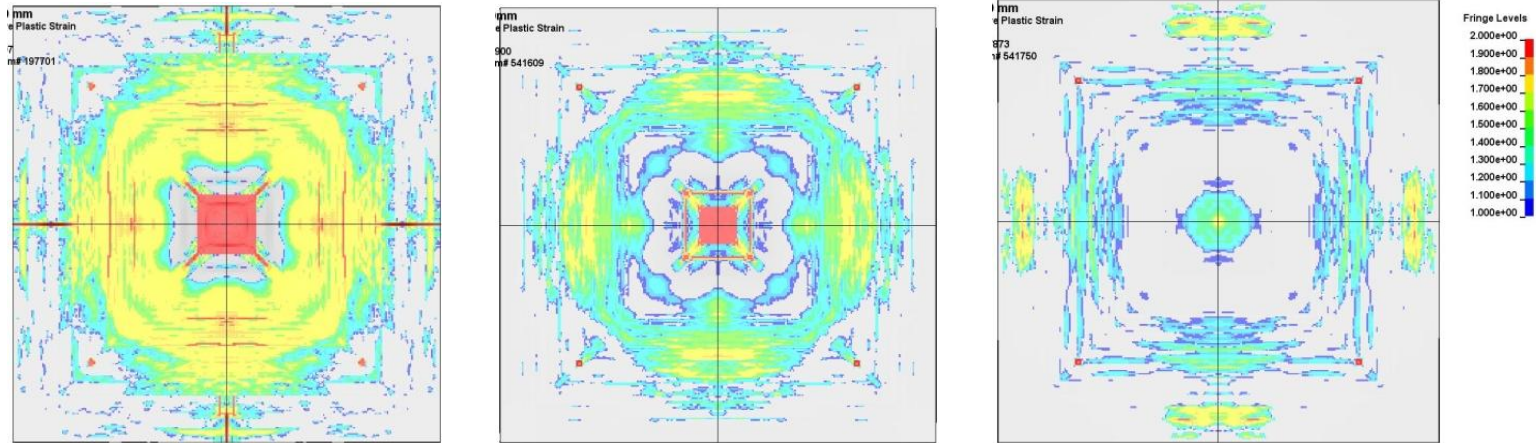
Bottom face
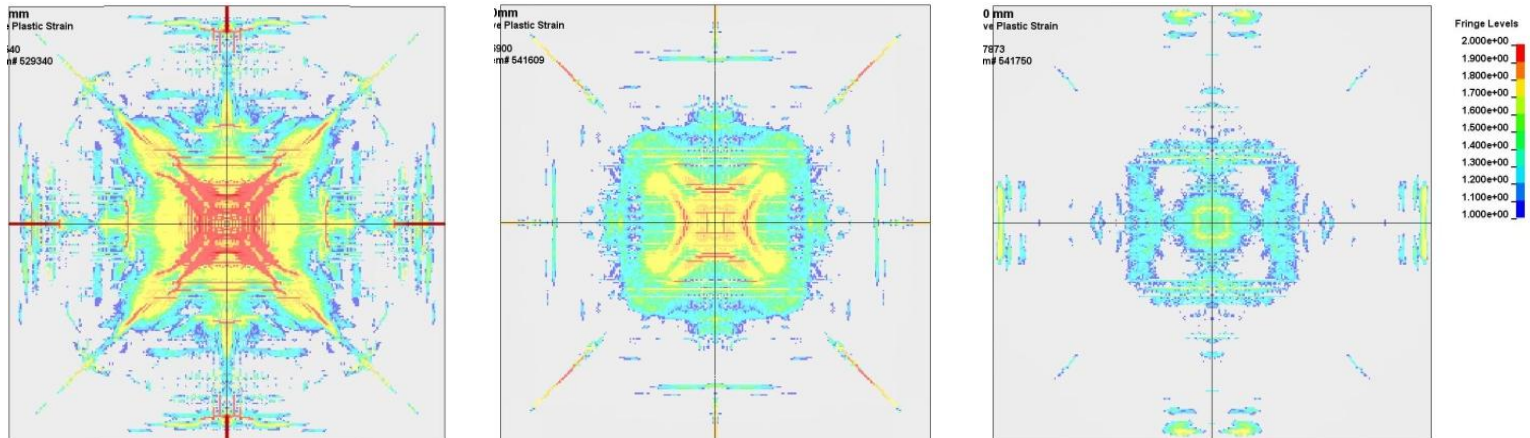
(a) 200 mm burst height   (b) 300 mm burst height   (c) 400 mm burst height

Figure 6.73 Damage pattern of asphalt concrete layer under different burst height

Top face

Bottom face

<div align="center">
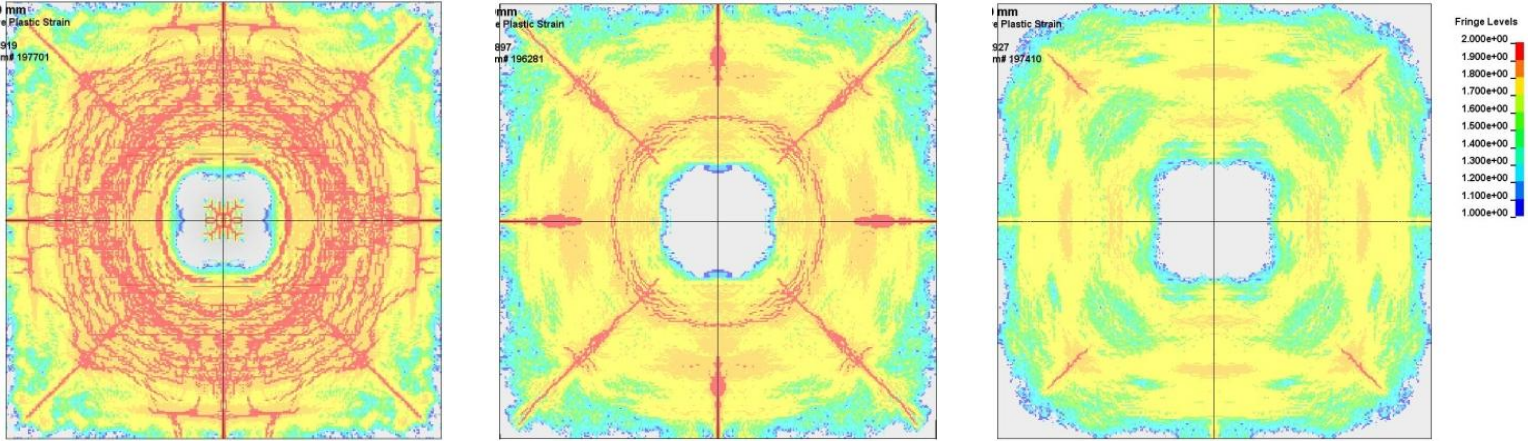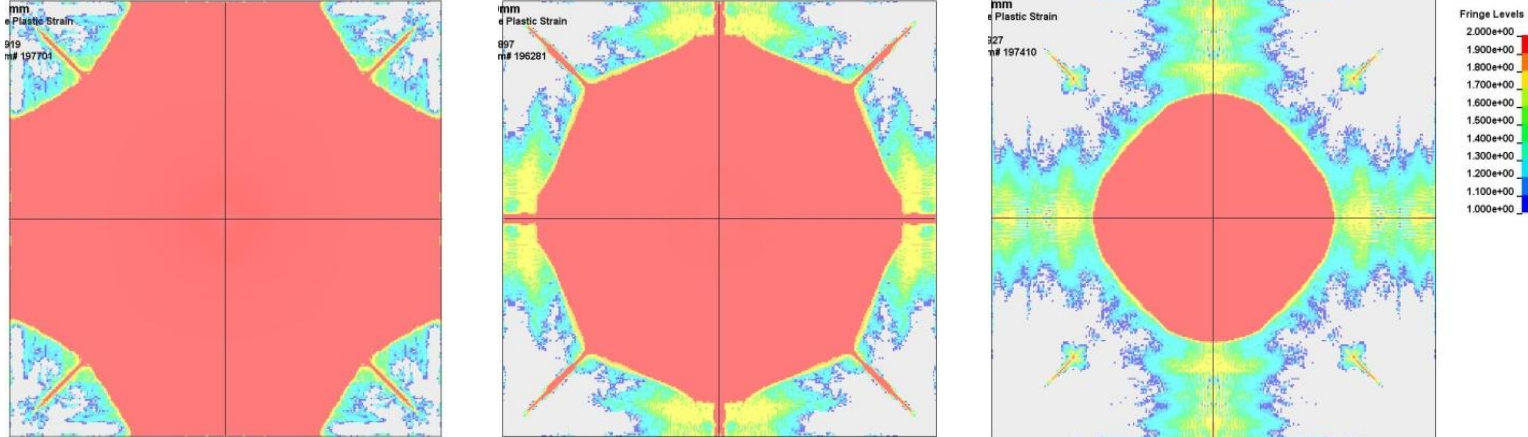
(a) 200 mm burst height   (b) 300 mm burst height   (c) 400 mm burst height

Figure 6.74 Damage pattern of HSC layer under different burst height

</div>

Top face
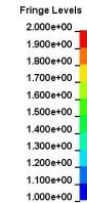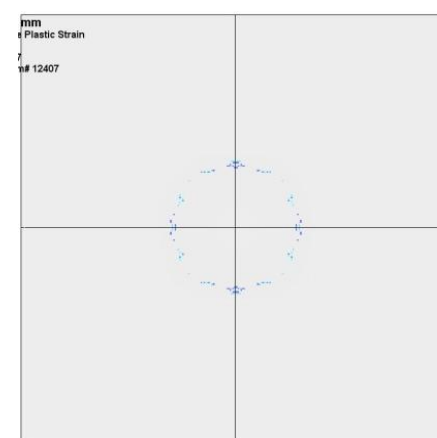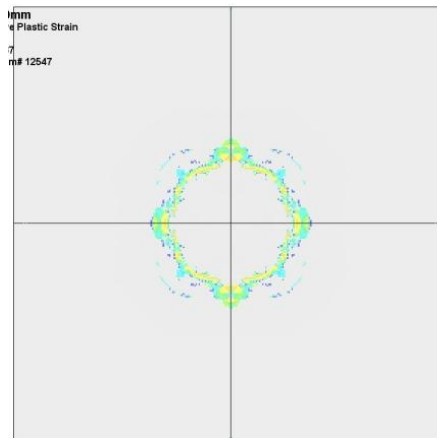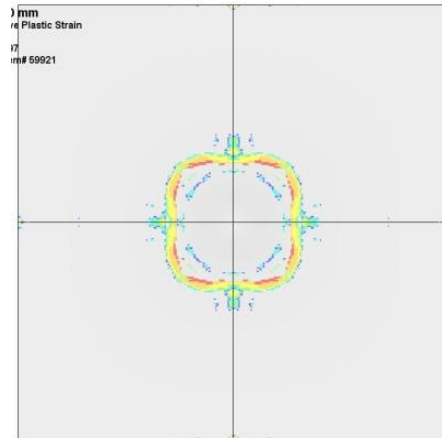
Bottom face
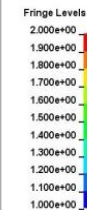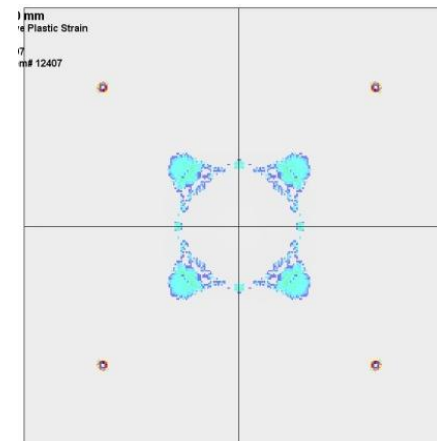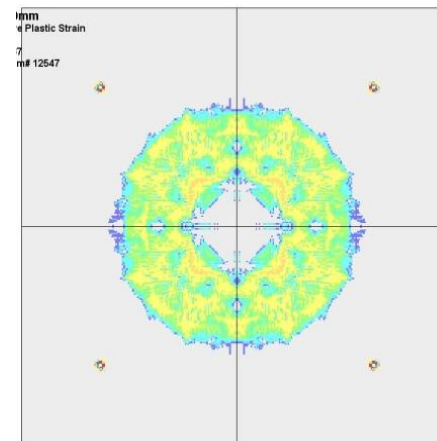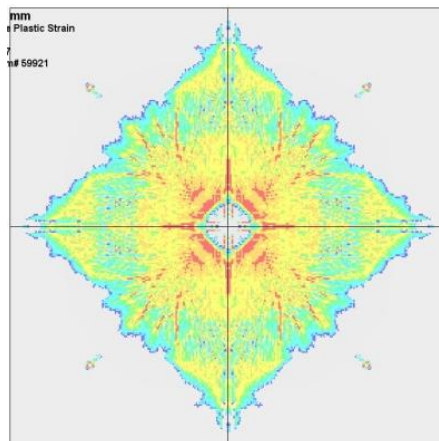
(a) 200 mm burst height　　　(b) 300 mm burst height　　　(c) 400 mm burst height

Figure 6.75 Damage pattern of ECC layer under different burst height

(a) Cross section of HSC layer under 200 mm burst height

(b) Cross section of HSC layer under 300 mm burst height

(c) Cross section of HSC layer under 400 mm burst height
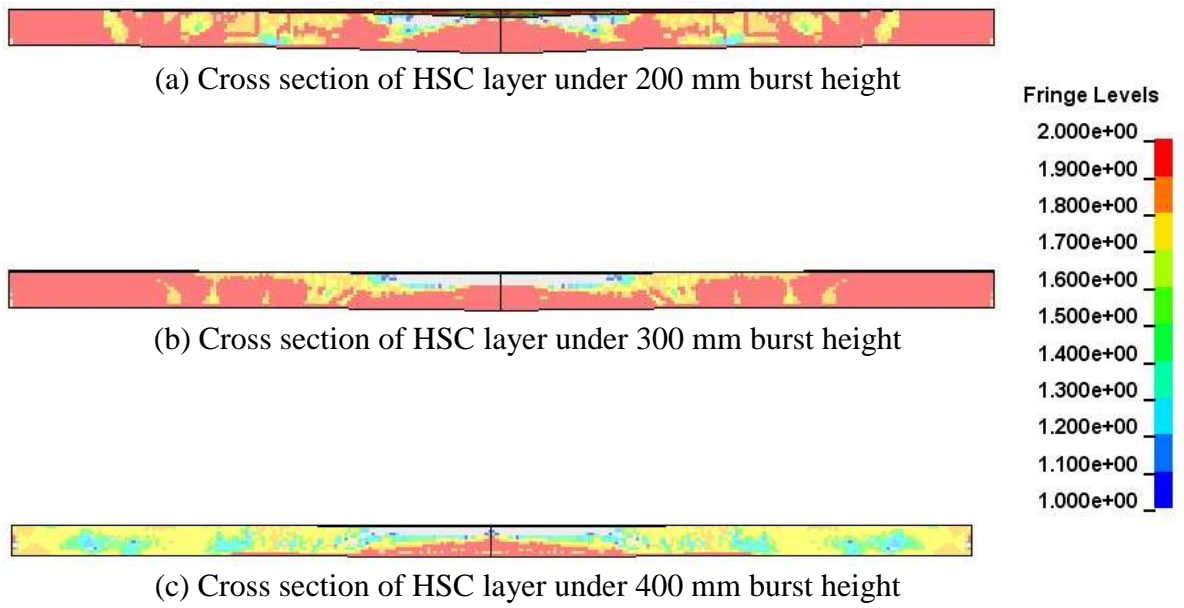
Figure 6.76 Damage pattern of cross section of HSC layer under different burst height

(a) Cross section of ECC layer under 200 mm burst height

(b) Cross section of ECC layer under 300 mm burst height

(c) Cross section of ECC layer under 400 mm burst height
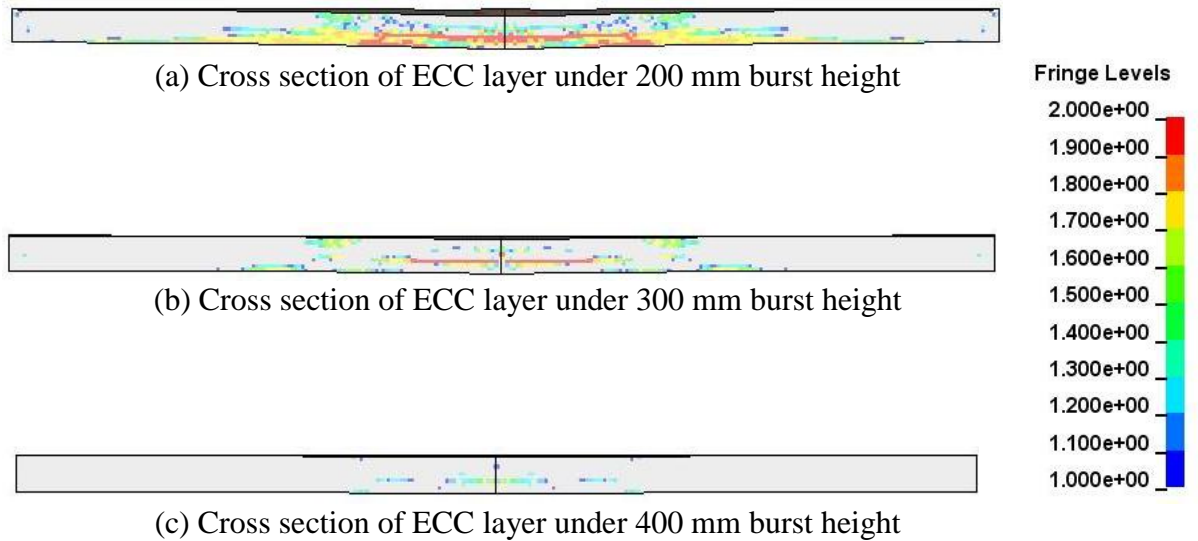
Figure 6.77 Damage pattern of cross section of ECC layer under different burst height
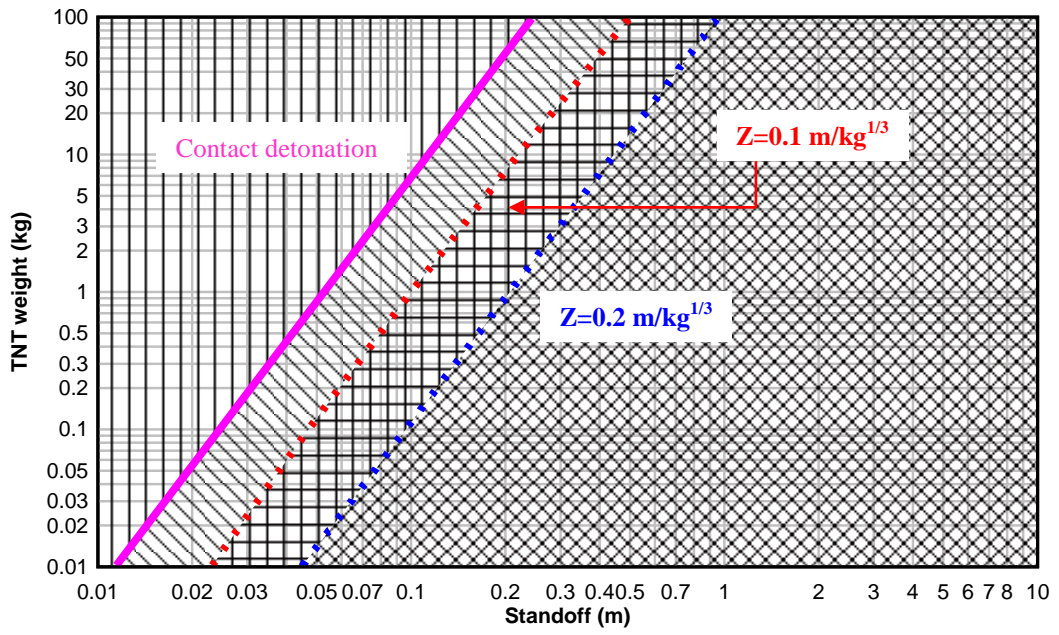
Figure 6.78 Damaged pattern for proposed multi-layers pavement under different scale distant charge

Chapter 7   Conclusions and Recommendations

7.1 Conclusions of this study

The main objective for this research is to develop and evaluate the performance of an advanced composite pavement materials for airfield runways which have better resistance to blast load. The findings and conclusions of this research are summarized in the following section.

7.1.1 Conclusions on laboratory impact test

In this study, the concept of a multi-layers system is proposed in order to achieve high blast resistance for this pavement structure. The configuration of the proposed multi-layers pavement is: (a) the asphalt concrete (AC) reinforced with Geosynthetics (GST) serviced as a top layer, and (b) followed by the High Strength Concrete (HSC) layer as the second layer, and (c) subsequently, the Engineered Cementitious Composites (ECC) as the bottom layer. A series of large scale laboratory impact tests were carried out to evaluate the efficiency of this concept and show the advantage of this proposed multi-layers pavement over other conventional pavement system.

A 1181 kg large scale impact test facility in NUS was used. The drop height of 1.5 m and 3.0 m were used in this test. After twice 1.5 m drop height, two conventional pavement slab suffered complete failure, while no complete failure was observed for the proposed multi-layers pavement slab. In the proposed multi-layers pavement slab, the top AC layer was still intact, and multiple small cracks were propagating from ECC Layer. This pavement slab kept its integrity.

For the drop height of 3.0 m, only the proposed multi-layers pavement slab was tested to evaluate its behavior under higher impact energy. After 1st 3 m height impact, the top asphalt layer was destroyed and shafted, while the HSC and ECC layer was intact. Upon 2nd 3 m height impact, the whole pavement slab was broken into 4 pieces. However, this failure was caused by 3m drop height, compared to the two conventional pavements (i.e. rigid pavement and flexible pavement) of which complete failure was caused by 1.5 m drop height.

Hence, laboratory impact test results concluded that combination of ECC, HSC and AC with GST could improve the impact resistance of the pavements system significantly. Proposed multi-layers pavement was found to perform better than conventional pavement structures (i.e. concrete rigid pavement or asphalt concrete flexible pavement). This is because the "soft" material (AC) in the proposed multi-layers pavement system functioned as the sacrificial surface layer to absorb some portion of the dynamic energy. Thereby, the energy transmitted to the following layers was greatly reduced. With the inclusion of the high strength Geosynthetic (GST) within this AC layer, the tensile strength of this layer was increased and in turn reduced the damage to the AC layer. Below the AC layer, HSC which was a "strong" material was used. This HSC layer served as the main body to sustain the dynamic load. Under the dynamic loading, the tensile stress tends to develop at the rear face of the material due to the reflection of the compressive stress propagating from the top face. However, it is well known that the concrete has low tensile strength. Furthermore, the HSC is very brittle and may develop cracks easily. Hence, another "soft" and ductile material (ECC) is deemed to be needed at the base of the "strong" HSC layer to absorb the energy. This ductile material can develop micro crack to dissipate and attenuate the

impacted dynamic energy. Thus, the multi-layer pavement system showed a very good impact resistance from the laboratory test.

7.1.2 Conclusion on full scale field blast test

A series of field blast test was conducted to evaluate the behavior of the proposed multi-layers pavement under blast load in the field condition. Two slabs of 2.8 m by 2.8 m with 275 mm thickness were cast and tested. One is a normal concrete pavement, as control, and the other is the proposed multi-layers pavement system.

Based on the field trial test results, it was found that the normal concrete pavement was severely damaged with the whole depth being punched through. Large cracks propagated through the whole depth of the slab and significant amount of debris was found throughout. It seemed to suffer brittle and sudden failure. The crater formed had a diameter of 1.2m and depth of 300mm. A pavement with this type of severe damage would need to be completely replaced as it was no longer feasible to repair.

For the proposed multi-layers pavement material, the damage was confined to the top asphalt layer and a small portion of the second layer which is the HSC layer. The crater is found to be having a diameter of 0.7 m at the plan of the top of HSC layer. The crater depth is only 10 mm in HSC layer. The debris formed from the blast mainly consisted of the softer AC rather than concrete fragments. Small cracks were evenly distributed around the crater.

Based on the field trial test results, it was concluded that during the blast event, high peak air pressure impacted the runway pavement, and the high incident pressure destroyed the top layer (i.e. AC with the inclusion of geogrid

material). It was found that the AC layer was able to dissipate a significant amount of the dynamic load in the course of being destroyed, thereby reduced the blast energy transmitted to the lower layers. It was also observed that while the blast load completely destroyed the upper section of the AC layer above the geogrid reinforcement, the AC layer was still largely intact below the geogrid level. This showed that geogrid served its purpose of increasing the tensile strength of AC layer. It was further observed that the crater was formed, and its depth was very shallow from the top of the HSC layer. Under the dynamic loading, the tensile stress tends to develop at the rear face of the material due to the reflection of the compressive stress propagating from the top face. The HSC was very brittle and may develop cracks easily with sudden failure. Regarding the ECC layer, which was provided to capture the ductile behavior, allowed material to suffer large deformation without sudden failure. During the deformation, the micro-cracks were developed to dissipate the tensile stress and energy.

7.1.3 Conclusion on laboratory interface test

The direct shear test and tilt table test were conducted to evaluate the interface strength between Asphalt Concrete (AC) and High Strength Concrete (HSC) layer in the proposed multi-layers pavement. According to the direct shear test, it was found that the under the normal loading of 2.1MPa, the shear strength was 1.5 MPa for the interface between AC and HSC. The friction coefficient is 0.71, and 0.56 for static and dynamic friction, respectively. It can also be observed that interface between HSC and AC was initially bonded together, after peak strength the interface began to move. At the failure surface, it was found that AC surface was smashed during the shear test while the HSC surface had less

damaged than that of AC. This was because that the strength of AC was much lower than that of HSC, and shear failure was mainly due to the AC failure. It might be concluded that the interface shear strength was determined by the strength of AC, and hence it is possible to enhance the interfacial strength by increasing the strength of AC and interfacial bonding strength.

7.1.4 Conclusion on material modelling

Tests were also conducted to evaluate the material model used for subsequently numerical modelling. The Split Hopkinson Pressure Bar (SHPB) and servo hydraulic test was conducted to obtain the Dynamic Increase Factor (DIF) of asphalt concrete under compressive and tensile loading with different strain-rates. It was found that the DIF was increasing with the increase of strain rates. For dynamic compressive loading, it is found that the enhancement of DIF values for asphalt concrete was higher than that of concrete-like materials at the same strain rate. This might be due to the asphalt concrete had higher content of coarse aggregates compared to concrete material. The aggregate would be rearranged under dynamic loading. It was also shown that the DIF value increased sharply at the certain strain rate, which was same as the behavior of the concrete-like material. The transmit point was found at $100s^{-1}$ for dynamic compressive loading. For dynamic tensile loading, the failure of asphalt concrete usually occurred at the weakest component (interfacial zone). Thus the dynamic tensile strength of the asphalt concrete under high strain rate would enhance due to the tensile strength of aggregate and binder. The tensile DIF value also increased sharply at the certain strain rate. The transition point was found to be $15s^{-1}$ for dynamic tensile loading. Hence, a modified DIF curve for asphalt concrete under compression and

tension with different strain rates were proposed and implemented in the numerical model.

7.1.5 Conclusion on numerical modelling

In order to investigate the effect of the different parameters of this proposed multi-layers pavement system (i.e. thickness of the HSC and ECC, strength of the HSC and ECC and the interface property) on its overall blast resisting behavior, the numerical modeling was employed. In this study, the numerical simulation of concrete pavement slab and the proposed multi-layers pavement under blast loading was conducted using AUTODYN and LSDYNA software.

For the simulation of concrete pavement slab under blast load, it was shown that the crater diameter predicted in the numerical model was 0.84 m which was very close to that in the field trial test (crater diameter=0.844 m). For the instrument results, it was found that the variation of vertical acceleration of the pavement slab between field trial test and numerical model was around 5%. However, in view of the inherent uncertainties in the field trial test, prediction of 5% deviation from field trial test results in numerical model was acceptable.

For the simulation of the proposed multi-layers pavement slab under blast load, it was found that the damaged pattern was similar with that in field trial test. The diameter of crater was about 0.75 m in numerical model which was quiet close to that in field trial test (crater diameter=0.7m). It was also found that the variation of vertical acceleration of the pavement slab between field trial test and numerical model was around 5%, which was acceptable for the numerical modelling of dynamic event.

Based on the numerical results, it was shown there were well agreement between the numerical results and field blast trial test result in terms of damage pattern, crater diameter and instrument readings. Hence, it could be concluded that the current 3D numerical model using AUTODYN and LSDYNA could model the real behavior of the pavement slab with interface under blast loading. A modified DIF curve for asphalt concrete was proposed based on the results from Split Hopkinson Pressure Bar (SHPB) and servo hydraulic test. The MAT72 R3 model with implementation of modified DIF was found to be suitable for simulating asphalt material under high strain rated loading.

After validation of the numerical model for the proposed multi-layers pavement, the parametric study was conducted for the following factors:

1) Effect of steel fiber (Fracture energy): It was found that incorporation of steel fibers in the HSC would significantly increase the fracture energy and then reduce the damaged area of the HSC layer. However, it was shown further increasing of the steel fibers in the HSC would not significantly increase the blast resistant of the HSC. In this study, after 0.5% steel fiber, no significant blast resistance was obtained.

2) Effect of higher compressive strength of HSC layer: It was shown the increase of the compressive strength of the HSC layer did not enhance the blast resistant of the material beyond certain compressive strength. In the current study, the optimum compressive strength value was 90 MPa. Further increasing the compressive strength, the HSC would show brittle behavior with a lots of crack lines.

3) Effect of HSC thickness and ECC thickness: It was shown that the thicker ECC layer would have stronger bending resistance. It was found that the

tensile wave could still propagate upwards and arrived about ¾ of the height. Based on the parametric study, it was found that the increasing of HSC thickness would make little contribution to prevent the pavement layer being penetrated though under blast load. However, the tension cracks at the bottom of ECC layer were significantly reduced. The equal thickness for the HSC and ECC layer might be better configuration for blast loading, since the bending resistance of the ECC layer would be enhanced.

4) Interface strength: It could be concluded that the increase of the released energy GI (tensile released energy) and GII (shear released energy) might not enhance the blast resistance of the proposal multi-layers pavement significantly. The HSC layer was still penetrated through irrespective to GI and GII values. This might be due to the magnitude of the tensile and shear strength of the interface material was much lower than that of blast loading. Thus, the increase of the GI and GII did not show higher blast resistance of the proposed multi-layers pavement under severe blast load.

5) Effect of subsoil: In order to reduce the settlement of the proposed multi-layers pavement under blast loading, the underneath soil could be improved to increase its stiffness and shear strength. Some treated methods, such as geosynthetic reinforced soil foundation or cement treated soil foundation, can be adopted. Moreover, the cement treated soil foundation would have higher bearing capacity which could sustain high energy from the overlaid pavement structures.

6) Effect of blast loading from different burst of height: It was shown that with the increase of the burst height, the damage pattern of the proposed

multi-layers pavement is changing. Beyond 300 mm burst of height, the HSC and ECC would suffer less damage, and then can be further used without being repaired.

7.1.6 Development of design chart

Based on the numerical modelling parametric study, according to the dynamic behavior of the proposed multi-layers pavement under blast load from different burst height, the damaged pattern chart was developed. In this chart, the blast resistance of the proposed multi-layers pavement structure can be quickly assessed under different blast event. According to different damage situation, the repair for the pavement structure can be carried out. At same time, in order to enhance the blast resistance of the proposed multi-layers pavement structure, some methods such as increasing thickness of HSC and ECC, incorporation of steel fiber in HSC and using treated subsoil ground condition are strongly recommended.

7. 2 Recommendations for future research

From the design chart, it was found that when the TNT charge weight exceed the certain level, the contact detonation will occur. In the current study, it was assumed that under this circumstance, the proposed multi-layers pavement will fail. According to the parametric study, it was found some methods such as increasing thickness of HSC and ECC, and incorporation of steel fiber in HSC will enhance the blast resistance of the proposed multi-layers pavement. However, these should be validated in the field trial test.

In current numerical model, the effect of high temperatures of bombs blast on the pavement material is not considered. Especially for the proposed multi-layers pavement system, the high temperature from the bomb blast will cause the softening of asphalt concrete and the melting of plastic geogrid, and then the pavement would suffer more damaged. Hence, in the future work, the temperature effect on pavement should be considered. The numerical model should also be developed to include the consideration of the contact detonation on the proposed multi-layers pavement. The Euler mesh might be employed to simulate the propagation of the TNT charge in the air. The Lagrange mesh will be used to model the pavement structure and underneath soil foundation. Hence, the interaction between the Euler and Lagrange mesh will be conducted to transmit the pressure from the TNT charge to the pavement structure. However, it should be noticed that for the interaction of Euler and Lagrange mesh, the mesh size should be carefully adopted to obtain proper results.

In this study, only the effect on pavement structure from TNT charge detonation was considered. In future research, the combination of impact and blast loading should be investigated. This is because in the reality, the impact from projectile will occur first, and followed by the detonation. Hence, the damage may be worse than that from blast load alone. Hence, the new methodology to test the dynamic response of pavement structure under this combination of impact and blast loading should be developed.

With the proposed multi-layers pavement design, the damage, in terms of crater size and depth, caused by impact and blast loading will be minimized and repair requirements will be kept to a minimum. However, there is still a need to look for a new rapid repair materials/methods to repair current damaged airfield

pavements or damaged proposed multi-layers pavement, since the current repaired

material were found to be inadequate in providing rapid repair with sufficient

strength.

References

AUTODYN (2003). Theory Manual, Century Dynamics, Inc.

Aymerich, F. et al. (1996). An Instrumented Drop Weight Machine for Low Velocity Impact Testing. Structures Under Shock and Impact IV: 243-253.

Bangash, M. Y. H. (1993). Impact and Explosion Analysis and Design. Oxford, Blackwell Scientific Publication.

Becham, W. K. and Mills, W. H. (1935). "Cotton-Fabric Reinforced Roads." Engineering News Record: 453-455.

Benson, D. J. (1992). "Computational Methods in Lagrangian and Eulerian Hydrocodes." Computer Methods in Applied Mechanics and Engineering **99**: 235-394.

Bessette, G. C. and Littlefield.D.L (1998). Analysis of Transverse Loading in Long-Rod Penetrations by Oblique Plates. Shock Compression of Condensed Matter. New York, American Institute of Physics Press: 937-940.

Canestrari, F. and Santagata, E. (2005). "Temperature Effects on the Shear Behavior of Tack Coat Emulsions Used in Flexible Pavements." International Journal of Pavement Engineering **6**(1): 39-46.

CEB-FIP (2008). Constitutive Modelling of High Strength/High Performance Concrete.

Chen, W. F. (1982). Constitutive Equations for Engineering Materials, John Wiley & Sons.

Chew, S. H. and Lim, A. (2006). The Use of Paving Fabrics to Prevent Reflective Cracking in Asphalt Concrete Pavement. 4th Asia Pacific Conference on Transportation and the Environment. Xian, China.

Chew, S. H., Tan.H.W and Wu, J. (2009). Development of Advanced Pavement materials and Cover System for Protection and Mitigation of Airfield Runway. Center for Protective Technology National of University of Singapore.

Clifton, J. R. (1982). Penetration resistance of Concrete - a review. Special Publication,National Bureau of Standards. Washington,DC: 480-485.

Collop, A. C. et al. (2009). "Shear Bond Strength between Asphalt Layers for Laboratory Prepared Samples and Field Cores." Construction and Building Materials **23**: 2251-2258.

Comite Euro-International du Beton (1993). CEP-FIP Model Code 1990, Redwood Books, Trowbridge, Wiltshire, UK.

CRC (1997). CRC Handbook of Physical Quantities. Boca Raton, FLorida.

Dancygier, A. N. and Yankelevsky, D. Z. (1996). "High strength concrete response to hard projectile impact." International journal of Impact Engineering **18**(6): 583-599.

Gebbeken, N., Greulich, S. and Pietzsch, A. (2006). "Hugoniot Properties for Concrete Determined by Full-Scale Detonation Experiments and Flyer-Plate-Impact Test." International journal of Impact Engineering **32**: 2017-2031.

Gupta, P., Banthia, N. and Yan, C. (2000). "Fiber Reinforced Wet-Mix Shotcrete under Impact." Journal of Materials in Civil Engineering **12**(1): 81-90.

Hanchak, S. J., Forrestal, M., J and Young, E. R. (1992). "Perforation of concrete slab with 48 MPa (7 ksi) and 140 MPa (20 ksi) unconfined compressive strengths." International Journal of Impact Engineering **12**(1): 1-7.

Hansson, H., Skoglund, P. and Unosson, M. (2001). Structural Protection for Stationary/Mobile Tactical behaviour Weapons and Protection, Tumba.

Hyde, D. (1992). Fundamentals of Protective Design for Conventonal Weapons. Vicksburg, MS, Structural Mechanics Division, Structures Laboratory, USACE Waterways Experiment Station.

Karihaloo, B. L. and Nallathambi, P. (1990). "Effective Crack Model for the Determination of Fracture Toughness (K_{ic}^{e}) of Concrete." Engineering Fracture Mechanics **35**(4/5): 637-645.

Kim, K. W. and Hussein, M. E. (1997). "Variation of Fracture Toughness of Asphalt Concrete under Low Temperature." Construction and Building Materials **11**: 403-411.

Koerner, R. M. (1998). Designing with Geosynthetics. N.J., Prentice-Hall Eaglewood.

Kuznetsov, V. A., Rebentrost, M. and Waschl, J. (2006). Strength and toughness of steel fibre reinforced reactive powder concrete under blast loading. First international conference on analysis and design of structures against explosive and impact loads. Tianjin,China, Transaction of Tianjin University. **12(Suppl.):** 70-74.

Lan, S., Lok, T. S. and Heng, L. (2005). "Composite structural panels subjected to explosive loading." Construction and Building Materials **19**: 387-395.

Lee, S. C. (2006). Finite Element Modeling of Hybrid-Fiber ECC Targets Subjected to Impact and Blast. Ph.D Thesis, National University of Singapore.

Leng, Z. et al. (2008). Interface Bonding Between Hot-Mix Asphalt and Various Portland Cement Concrete Surface: Laboratory Assessment. Transporation Research Record 2057. Washington D.C**:** 46-53.

Li, Q. M. and Meng, H. (2003). "About the dynamic strength enhancement of concrete-like materials in a split Hopkinson pressure bar test." International Journal of Solids and Structures **40**: 343-360.

Li, V. C. and Maalej, M. (1996). "Toughening in Cement Based Composites-Part II: Fiber-Reinforced Cementitious Composites." Journal of Cement and Concrete Composites **18**(4): 239-249.

Li, V. C. et al. (1994). "On the shear behavior of Engineered Cementitious Composites." Journal of Advanced Cement Based Materials **1**(3): 142-149.

Lok, T. S. and Pei, J. S. (1996). "Impact resistance and ductility of steel fibre reinforced concrete panels." Trans Hong Kong Inst Eng HK **3**(3): 7-16.

Lok, T. S. and Pei, J. S. (1997). Steel fibre reinforced concrete panels subjected to blast loading. Proceeding of 8th international symposium on interaction of the effect of munitions with structures. McLean, VA, USA. **IB:** 701-711.

LSDYNA (2007). LSDYNA Keyword User's Manual, Livermore Software Technology Corporation (LSTC).

Lu, Y. B. and Li, Q. M. (2011). "About the dynamic uniaxial tensile strength of concrete-like materials." International Journal of Impact Engineering **38**: 171-180.

Luccioni, B. M. and Luege, M. (2006). "Concrete pavement slab under blast loads." International Journal of Impact Engineering **32**: 1248-1266.

Luo, X., Sun, W. and Chan, S. Y. N. (2000). "Characteristics of high-performance steel fiber-reinforced concrete subject to high velocity impact." Cement and Concrete Research **30**: 907-914.

Maalej, M., Hashida, T. and Li, V. C. (1995). "Effect of Fiber Volume Fraction on the Off-Crack Plane Energy in Strain-hardening Engineered Cementitious Composites." Journal of the American Ceramic Society **78**(12): 3369-3375.

Maalej, M., Quek, S. T. and Zhang, J. (2005). "Behavior of Hybrid-Fiber Engineered Cementitious Composites Subjected to Dynamic Tensile Loading and Projectile Impact." Journal of Materials in Civil Engineering **17**(2): 143-152.

Magallanes, J. M. et al. (2010). Recent Improvements to Release III of the K&C Concrete Model. 11th International LSDYNA Users Conference. Detroit, USA. **3:** 37-48.

355

Maitra, S. R., Reddy, K. S. and Ramachandra, L. S. (2009). "Experimental Evaluation of Interface Friction and Study of Its Influence on Concrete Pavement Response." Journal of Transportation Engineering **135**(8): 563-571.

Malvar, L. J. and Crawford, J. E. (1998). Dynamic Increase Factors for Steel Reinforcing Bars. Twenty-Eighth Department of Defense Explosives Safety seminar Orlando, FL, USA.

Malvar, L. J., Crawford, J. E. and Wesevich, J. W. (1996). A New Concrete Material Model for DYNA3D Release II: Shear Dilation and Directional Rate Enhancements. Defense Nuclear Agency, Alexandria, VA, USA.

Malvar, L. J. et al. (1997). "A plasticity concrete material model for DYNA3D." International journal of Impact Engineering **19**(9-10): 847-873.

Malvar, L. J. and Ross, C. A. (1998). "Review of strain rate effects for concrete in tension." ACI Material Journal **95**(6): 735-739.

Methta, P. K. and Monteiro, P. (2005). Concrete: Microstructure, Properties, and Materials. New York, McGraw-Hill.

Mindness, S., Young, J. F. and Darwin, D. (2002). Concrete. Upper Saddle River, NJ, Pearson Education,Inc.

Nyström, U. and Gylltoft, K. (2011). "Comparative numerical studies of projectile impacts on plain and steel-fibre reinforced concrete." International Journal of Impact Engineering **38**: 95-105.

O'Neil, E. F., Neeley, B. D. and Cargile, J. D. (1999). "Tensile properties of very-high-strength concrete for penetration-resistant structures." Shock and Vibration **6**: 237-245.

Ong, K. K. G., Basheeerkhan, M. and Paramasivam, P. (1999). "Resistance of fibre concrete slabs to low velocity projectile impact " Cement and Concrete Composites **21**: 391-401.

Ottosen, N. S. and Ristinmaa, M. (2005). The Mechanics of Constitutive Modeling, ELSEVIER.

OW, Y. W. E. (2008). Testing of New Composite Pavement Material for Runway B.Eng Dissertation, National University of Singapore.

Park, D. W. et al. (2005). "Characterization of Permanent Deformation of an Asphalt Mixture Using a Mechanistic Approach." KSCE Journal of Civil Engineering **9**(3): 213-218.

Praveen, G. N. et al. (2008). Cohensive Contact Based Delamination Modeling with LS-DYNA Manuscript in Preparation.

Romanoschi, S. A. (1999). Characterization of Pavement Layer Interfaces Ph.D Thesis, Louisiana State University.

Ross, C. A., Jerome, D. M. and Tedesco, J. W. (1996). "Moisture and Strain Rate Effects on Concrete Strength." ACI Material Journal **93**(3): 293-300.

Ross, C. A., Thompson, P. Y. and Tedesco, J. W. (1989). "Split-Hopkinson Pressure Bar Test on Concrete Strength." ACI Material Journal **86**(5): 475-481.

Saad, B., Mitri, H. and Poorooshasb, H. (2005). "Three-Dimensional Dynamic Analysis of Flexible Conventional Pavement Foundation." Journal of Transportation Engineering **131**(6): 460-468.

Saad, B., Mitri, H. and Poorooshasb, H. (2006). "3D FE Analysis of Flexible Pavement with Geosynthetic Reinforcement." Journal of Transportation Engineering **132**(5): 402-414.

Sadd, M. H. et al. (2007). Interfacial Failure Behavior of Concrete-Asphalt Bi-materials. SEM Annual Conference and Exposition on Experimental and Applied mechanics**:** 1421-1430.

Schwer, L. E. and Day.J (1991). "Computational Techniques for Penetration of Concrete and Steel Targets by Oblique Impact of Deformable Projectiles " Nuclear Engineering and Design **125**: 215-238.

Seibi, A. C. et al. (2001). Constitutive Relations for Asphalt Concrete under High Rates of Loading. Transportation Research Record 1767. Washington D.C, National Research Council**:** 111-119.

Showichen, A. (2008). Numerical analysis of vehicle bottom structures subjected to anti-tank mine explosions. Ph.D thesis PhD, Cranfield University.

Smith, P. D. and Hetherington, J. G. (1994). Blast and Ballistic Loading of Structures. Oxford, Great Britain, Butterworth-Heinemann Ltd.

Tan, S. A., Low, B. H. and Fwa, T. F. (1994). "Behavior of Asphalt Concrete Mixtures in Triaxial Compression." Journal of Testing and Evaluation **22**(3): 195-203.

Tang, W.-H., Ding, Y.-Q. and Yuan, X.-Y. (2009). The HJC Model Parameters of an Asphalt Mixture. DYMAT 2009 - 9th International Conference on the Mechanical and Physical Behaviour of Materials under Dynamic Loading. **2:** 1419-1423.

Tashman, L. et al. (2005). "A Microstructure-Based Viscoplastic Model for Asphalt Concrete." International Journal of Plasticity **21**: 1659-1685.

Tekalur, S. A. et al. (2009). "Mechanical Characterization of a Bituminous Mix under Quasi-Static and High-Strain Rate Loading." Construction and Building Materials **23**: 1795-1802.

Tschegg, E. K. et al. (2007). "Mechanical and Fracture Mechanical Properties of Asphalt-Concrete Interface." ACI Material Journal **104**(5): 474-480.

Tschegg, E. K. and Stanzl, S. E. (1991). "Adhesive Power Measurements of Bonds between Old and New Concrete." Journal of Material Science **26**: 5189-5194.

Uzan, J., Livenh, M. and Eshed, Y. (1978). Investigatigation of Adhension Properties between Asphaltic-Concrete Layers. Proceedings of Asphalt Paving Technology, Lake Buena Vista, Florida.

Wang, F., Lim, C. H. and Soh, T. B. (2010). Explosive Testing, Numerical and Analytical Modelling of a Modular Blast Wall System. The 3rd International Conference on Design and Analysis of Protective Structures. Singapore**:** 392-401.

Wang, F. et al. (2008). Reinforced Concrete Slab Subjected to Close-in Explosion. 2008 LSDYNA German Forum Bamberg 21-28.

Wang, S. (2011). Experimental and Numercial Studies on Behavior of Plain and Fiber-Reinforced High Strength Concrete Subjected to High Strain Rate Loading. Ph.D Thesis, National University of Singapore.

Whirley, R. G. and Engelmann, B. E. (1992). Slidesurfaces with Adaptive New Definitions (SAND) for Transient Analysis. Winter annual meeting of the American Society of Mechanical Engineers Anaheim, California ASME**:** 65-71.

Wright, A. and French, M. (2008). "The Response of Carbon Fibre Composites to Blast Loading via the Europa CAFV Programme." Journal of Material Science **43**: 6619-6629.

Xiao, H. (2009). Yielding and Failure of Cement Treated Soil. Ph.D Thesis, National University of Singapore.

Yong, C. K. (2005). Road Pavement Reinforced with Geosynthetics. B.Eng Dissertation, National University of Singapore.

Zaghloul, S. and White, T. (1993). Use of a Three-Dimensional,Dynamic Finite Element Program for Analysis of Flexible Pavement. Transportation Research Record 1388. Washington D.C, National Research Council**:** 60-69.

Zaghloul, S., White, T. and Kuczek, T. (1994). Evaluation of Heavy Load Damage Effect on Concrete Pavement Using Three-Dimensional, Nonlinear Dynamic Analysis. Transportation Research Record 1449. Washington D.C, National Research Council**:** 123-133.

Zaghloul, S., White, T. and Kuczek, T. (1994). Use of Three-Dimensional,Dynamic,Nonlinear Analysis to Develop Load Equivalency Factors for Composite Pavements. Transportation Research Record 1449. Washington D.C, National Research Council**:** 199-208.

Zhang, J., Maalej, M. and Quek, S. T. (2005). Drop-weight Impact on Hybrid-Fiber ECC Blast Doors. Proceedings of The 3rd International Conference

on Construction Materials: Performance, Innovations and Structural Implication-Conmat"05. Vancouver,Canada**:** 79.

Zhang, M. H., Sharif, M. S. H. and Lu, G. (2007). Impact resistance of high strength fibre-reinforced concrete. Magaine of Concrete Research. **59:** 199-210.

Zhang, M. H. et al. (2005). "Resistance of high-strength concrete to projectile impact." International Journal of Impact Engineering **31**: 825-841.

Zhou, X. Q. and Hao, H. (2008). "Modelling of compressive behaviour of concrete-like materials." International Journal of Solids and Structures **45**: 4648-4661.

Zhou, X. Q. et al. (2008). "Numerical prediction of concrete slab response to blast loading." International journal of Impact Engineering **35**: 1186-1200.

Appendix A Split Hopkinson Pressure Bar (SHPB) test and Simulation

A.1 Theory

The Split Hopkinson Pressure Bar (SHPB) technique was first developed in 19th century and had numerous advances in experimental procedures in recent years. The SHPB was used to study the dynamic phenomena of material under high strain rate. The configuration of SHPB system was shown in Figure A.1. From the figure, it was seen that the SHPB system consisted of a launching system, striker bar, incident bar, transmitted bar, shock absorber and data acquisition system. The specimen would be sandwiched between incident and transmitted bar. During the test, a striker bar was released under high gas pressure and propelled toward the incident bar with a certain striker velocity. Upon impact, an elastic compressive wave was generated within the incident bar, and the time-dependent strain $\varepsilon_I(t)$, in the pressure bar could be measured at strain gage A (as shown in Figure A.1), which located at the midpoint of the incident bar. At the incident bar/specimen interface, this incident wave would be partially reflected and partially transmitted into the specimen. The reflected wave that travelled back along the incident bar was a tensile wave, and the strain, $\varepsilon_R(t)$ could also measured by strain gauge A. The compressive strain $\varepsilon_T(t)$, that was transmitted through the sample into the transmitted bar, was captured by strain gauge B, located at the midpoint of the transmitted bar.
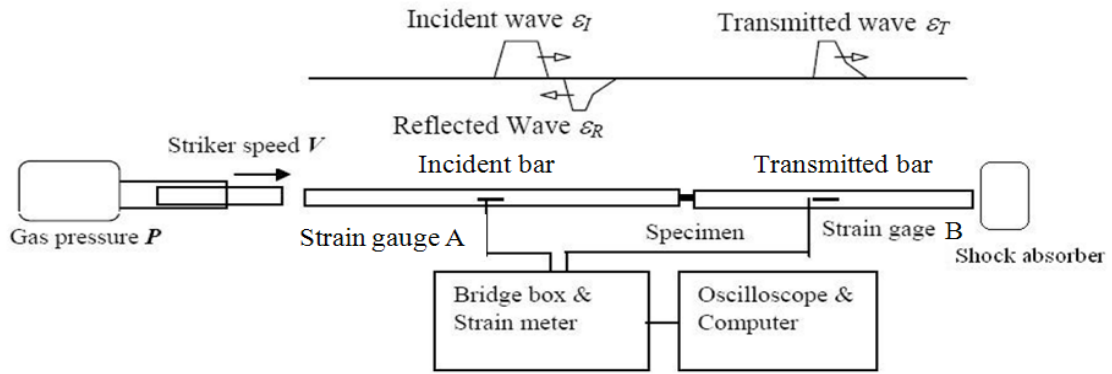
Figure A.1 Schematic setup of SHPB test (modified from SHPB User's Manual)

According to the one-dimensional wave theory, the strain rate with the specimen was directly proportional to the amplitude of the reflected wave. Likewise, the stress with the sample was directly proportional to the amplitude of the transmitted wave. Hence, through integrating the reflected wave, the strain in the specimen could be obtained. The strain rate which specimen was sustained depended on the velocity of the striker bar. Various strike bar velocity could be obtained by combination of adjusting strike length and released gas pressure. The combined two signals from two strain gauges could determine the relationship of dynamic stress-strain curve, which was described as following:

The average strain in the specimen ε_s can be determined by:

$$\varepsilon_s(t) = \frac{c_0}{l_s} \int_0^t \left[\varepsilon_I(t) - \varepsilon_R(t) - \varepsilon_T(t) \right] \qquad (A.1)$$

where l_s was the original length of the specimen and $c_0 = \sqrt{E/\rho}$, was the longitudinal sound velocity in the bar, and ρ was the mass density of the bar material. The average stress acted on the specimen is:

$$\sigma_s(t) = \frac{P_1(t) + P_1(t)}{2A_s} \qquad (A.2)$$

where P_1 and P_2 were the forces at the incident bar/specimen and specimen/transmitted bar interfaces, respectively, and A_s was the initial cross-sectional area of the specimen. Then, the forces acted at the two interfaces were expressed as:

$$P_1(t) = E\left[\varepsilon_I(t) + \varepsilon_R(t)\right]A_0 \tag{A.3}$$

$$P_2(t) = E\varepsilon_T(t)A_0 \tag{A.4}$$

where E was the Young's modulus of the bar, and A_0 was the cross-sectional area of the bar. It was assumed that when specimen is deforming uniformly, the stress at the incident bar/specimen interface equals the specimen/transmitted bar interface, and then from making A.3 equal to A.4, it could be obtained that:

$$\varepsilon_I(t) + \varepsilon_R(t) = \varepsilon_T(t) \tag{A.5}$$

Substitution of A.5 into A.1 and A.2, the strain and stress for the specimen could be expressed as:

$$\varepsilon_s(t) = -\frac{2c_0}{l_s}\int_0^t \varepsilon_R(t) \tag{A.6}$$

$$\sigma_s(t) = E\frac{A_0}{A_s}\varepsilon_T(t) \tag{A.7}$$

Thus, the stress-strain behavior of the specimen was determined simply by measuring elastic pressure bars in a SHPB test.

Above discussion was related to the dynamic compressive strength of the concrete-like material, the determination of dynamic tensile strength of these material using SHPB test would be discussed in the following part.

Usually, there were three testing methods to measure the static tensile strength of the concrete-like material, that is, the direct tensile test, the modulus of rupture test and the splitting (or Brazilian) test. Researcher had indicated that

among these three methods, the splitting test gave the most accurate measurement of the true tensile strength of the material. The detailed advantage of using splitting tensile test over other tests could be referred to Lu and Li (2011). In recent years, the splitting tensile method was further used in the SHPB test to measure the dynamic tensile strength of the concrete-like materials (Ross 1989; Hughes 1993; Tekalur 2009; Lu and Li 2011). The splitting-tensile test arrangement was illustrated in Figure A.2. The bearing strips were placed between the bars and the specimen along its length to apply the line loading. The assumption (Ross 1989) for the use of the splitting tensile test in SHPB was that the peak tensile stress of the splitting cylinder was proportional to the peak transmitted compressive stress measured at the transmitted bar through the following equations:

$$f_{td}^{'} = \frac{2P_{max}}{\pi LD} \tag{A.8}$$

where P_{max} represented the peak force that was transmitted through the specimen, and was decided by peak transmitted stress:

$$P_{max} = \pi R^2 \sigma_T \tag{A.9}$$

where R was the radius of the transmitted bar, σ_T was the peak transmitted stress, which was determined from peak transmitted strain measured from strain gauge B at transmitted bar by:

$$\sigma_T = A_0 E \varepsilon_T^{max} \tag{A.10}$$

in which, A_0 and E was defined in Equation A.4.

The strain rate may also be determined from the following expression:

$$\dot{\varepsilon} = \frac{f_{td}^{'}}{E_{s}\Delta t} \tag{A.11}$$

where E_{s} was the Young's modulus of the specimen, and Δt was the rising time between the start of the transmitted stress wave and the peak transmitted stress.
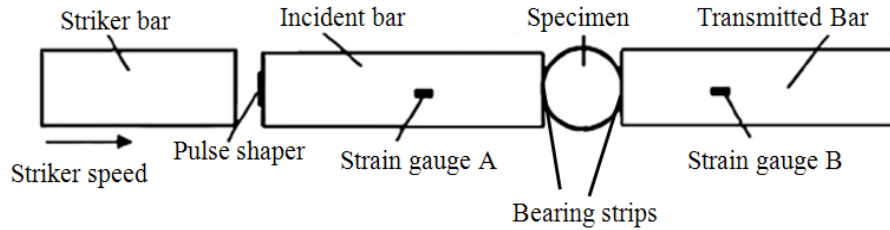

Figure A.2 Schematic setup of splitting tensile test in SHPB (Lu, 2011)

A.2 Compressive SHPB test

The diameter of the incident and transmitted bar in current study was 80mm, and both bar length were 5000 mm. For the compressive SHPB test, the asphalt concrete specimen was fabricated with 75 mm diameter and 35 mm length, which made the L/D ratio around 0.5. Both faces of the specimen were well lubricated to minimize the friction as shown in Figure A.3. The strain-time history from strain gauges A and B were recorded by DL750 acquisition system. A typical set of incident, reflected and transmitted waves recorded by the acquisition system were shown in Figure A.4. From the figure, it was shown that the rising time for incident wave was very smooth this was because a 1 mm thick aluminum disk with a diameter of 25 mm was attached on the impact surface of the incident bar to be used as pulse shaper. This method would increase the rising time of the incident wave to make the specimen deform uniformly and the stress equilibrate within the specimen.

Figure A.3 Asphalt concrete specimen with lubricating surface for SHPB test
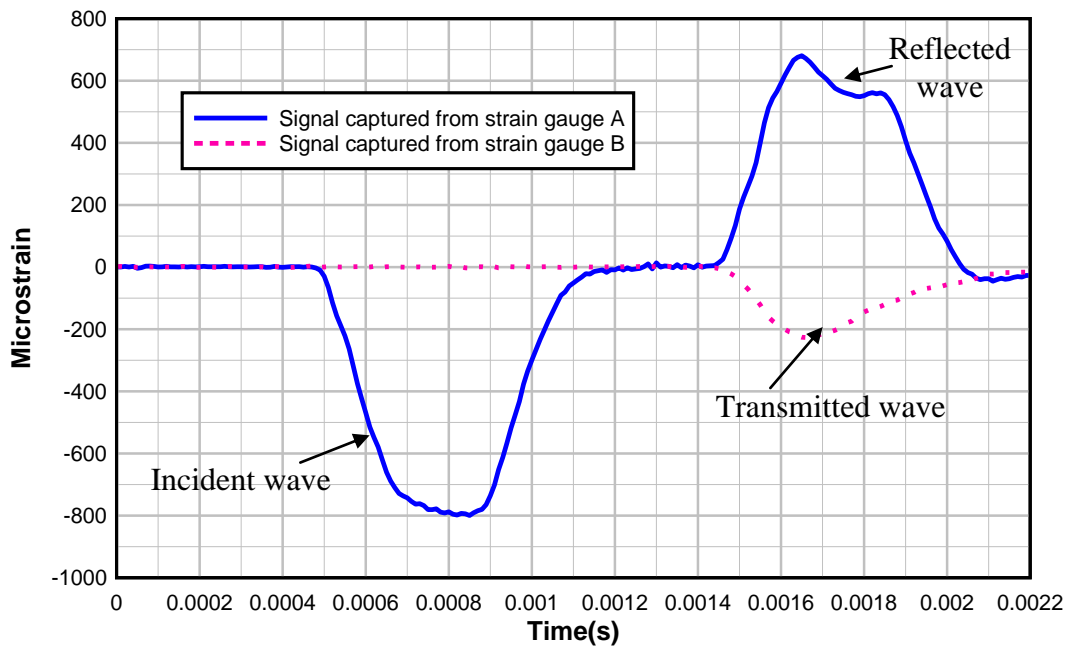
Figure A.4 Typical incident, reflected and transmitted waves for asphalt concrete

The experiment data was processed based on the 1D wave theory as expressed by equations A.1 to A.7. The static compressive strength of asphalt concrete was 4.6 MPa under 35°C. The asphalt concrete was cured in oven with 35°C at least 8 hours before shifted to the SHPB test. The SHPB test was conducted within 1mins in order to maintain the specimen within the required test temperature. The dynamic stress-stain curves of asphalt material under different strain rate were shown in Figure A.5.

Figure A.5 Dynamic stress-strain curve of asphalt concrete under high strain rate

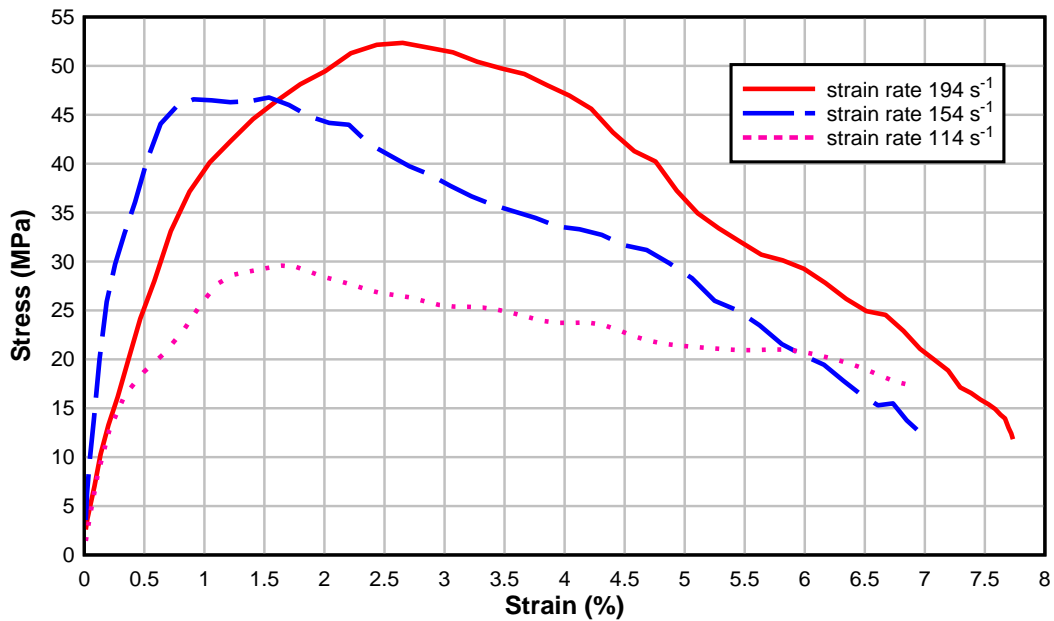The compressive SHPB test for asphalt concrete was conducted various strain rates, and the results for Dynamic Increase Factor (DIF) under different strain rates were plotted in the Figure A.6. In the figure, the red diamond represented that the DIF values was obtained through uniaxial compressive test by servo hydraulic machine, while blue one represented that the DIF values was yielded from SHPB test. It was clearly shown that the compressive strength of asphalt concrete was increasing with the increase of the strain rates. However, in the current study, the maximum strain rate from compressive SHPB test for asphalt concrete was around $200s^{-1}$. Further increasing the velocity of the striker bar would not enhance the strain rate within the specimen any more. Hence, for the current asphalt concrete, the DIF values were valid from 10^{-5} to $200s^{-1}$.
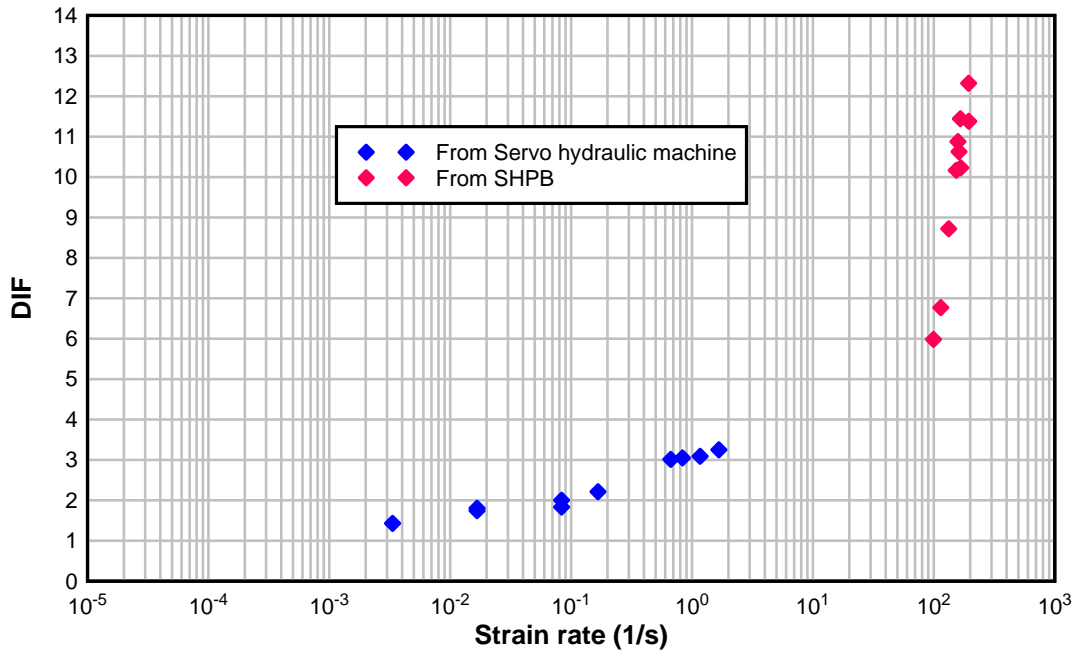
Figure A.6 Compressive DIF curve versus strain rate

A.3 Splitting tensile SHPB test

Two sizes of specimen were adopted in the splitting tensile SHPB test. One was the big size and as same as that used in Marshall Test, that is, the specimen was a cylinder having a diameter of 101.6 mm with the height of 64 mm as described in ASTM1074. Another was the specimen with a diameter of 75mm and the height of 28 mm to 35mm.. This was due to the different specimen sizes could obtain the strength for the strain rate from $10s^{-1}$ to $100s^{-1}$. At the same time, the specimen size effect was also considered. Based on Ross (1989), it was concluded that for concrete-like material, the tensile strength was size dependent, but the ratio of the dynamic to static strength was size independent. Hence, to eliminate size effect, the static strength for each specimen size should be obtained from quasi-static loading, and then the dynamic strength for each specimen size was normalized with respect to the corresponding static strength, which deduced the ratio of Dynamic increase factor (DIF) .

During the test, the rubber bearing strips were attached at the two side of the specimen to apply line loading during SHPB test as shown in Figure A.7. The width of the rubber layer was taken as 1/12 of the diameter of specimen based on the ASTM standard. In the figure, it was also illustrated the two sizes of specimen. Thus, the tensile DIF curve for the asphalt concrete under different strain rate was shown in Figure A.8. From the figure, it was shown that the SPHB test applied the strain rate from 10 to 100 s^{-1}. Further increasing the velocity of the striker bar would not enhance the strain rate within the specimen any more. Hence, for the current asphalt concrete, the tensile DIF values were valid from 10^{-6} to 100s^{-1}.

(a)   (b)

Figure A.7 Dimension of asphalt concrete specimen in split tensile SHPB test (a) 101.1 mm diameter with thickness 64 mm, (b) 75 mm diameter with thickness from 28 to 35 mm
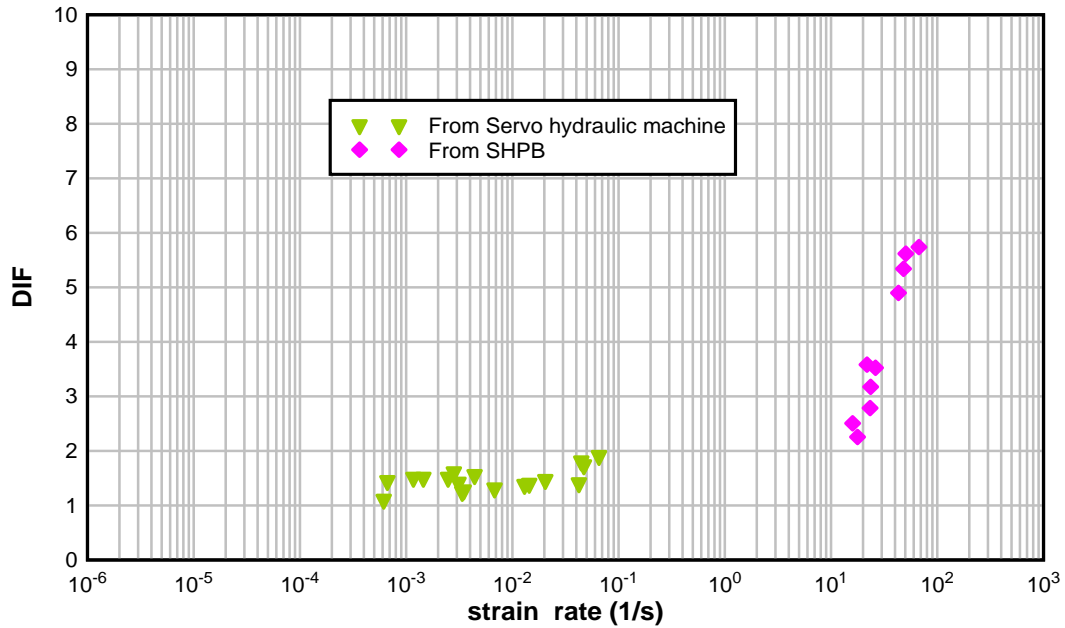
Figure A.8 Tensile DIF curve versus strain rate

A.4 Numerical simulation of the compressive SHPB test for concrete and asphalt concrete

The goal of the simulation study of the SHPB test for concrete and asphalt concrete compression was to examine the strain rate effects when it was considered in the numerical model. It was to valid that the second branch of the DIF curve recommended from CEB or derived from SHPB test could be showed up automatically in the numerical model, and input the second branch of DIF curve in the numerical model would duplicate the inertial effects and overestimate the strength of the materials.

A.4.1 Simulation model

The incident and transmitted bar used in current study was 80mm in diameter and 5000 mm in length. Both bars were made of stainless steel, and assumed to be in elastic range during the SHPB test. The typical steel parameters

used in the simulation were given in Table A.1. The material model for steel was

PLASTIC_KINEMATIC.

Table A.1 the steel properties used in SHPB test simulation

Parameters	Symbol	Units	Value
Young's modulus	E	MPa	203000
Yield stress	f_y	MPa	758
Poisson's ratio	ν	---	0.3
Density	ρ	kg/m^3	7850

In the numerical model, the simplified loading condition was employed. The striker bar was not simulated and replaced by imposing stress impulse at one end of the incident bar. This input stress impulse was determined from the strain time history measured at the strain gauge located at the middle length of the incident bar. The shape of the input stress impulse was trapezium.

For the simulation of compressive SHPB test for plain concrete, three stress levels were considered and summarized in Table A.2, which was measured by Wang (2011). The experimental results of compressive SHPB test for plain concrete was extracted from Wang (2011) as well, in which the properties of the plain concrete were listed in Table A.3, and the concrete specimen was a diameter of 77 mm with the length of 37 mm.

Table A.2 Input stress impulse in compressive SHPB test for plain concrete

No.	Stress level (MPa)	Rise time (ms)	Ramp time (ms)	Total time (ms)
1	200	0.13	0.215	0.37
2	225	0.04	0.19	0.23
3	290	0.045	0.195	0.24

Table A.3 Material properties of plain concrete used in compressive SHPB test

Parameters	Symbol	Units	Value
Young's modulus	E	GPa	44
Compressive strength	f_c	MPa	90
Tensile strength	f_t	MPa	3.5
Poisson's ratio	v	---	0.3
Density	ρ	kg/m^3	2400

In the numerical model, the input bar, transmitted bar and plain concrete samples were modelled with 8-node solid element. Only a quarter of the specimen and bars were modelled due to the symmetry. After few trials, it was found that when the specimen adopted 1mm x 1mm element size and incident and transmitted bars used 2mm x 2 mm element size, the numerical results were converged. Hence, in the current model, 1mm and 2 mm element size were adopted for the simulation of specimen and bars respectively. The numerical model for compressive SHPB test was shown in Figure A.9. From the figure, it was showed that the finer mesh was adopted in the specimen, and the ratio of the mesh was kept constant for the incident and transmitted bar in order to make stress wave propagate smoothly without reflection in the bars. The contact algorithm AUTOMATIC_SURFACE_TO_SURFACE was employed to simulate the interface between specimen and input bar, and specimen and transmitted bar. The friction between the specimen and bars was considered and set as 0.35. The three DIF curves were used in the material model as shown in Figure 6.6. The vaule recorded by gauge point at the transmitted bar in numerical model was compared with the experimental data. The results were presented and discussed in section 6.2.3.
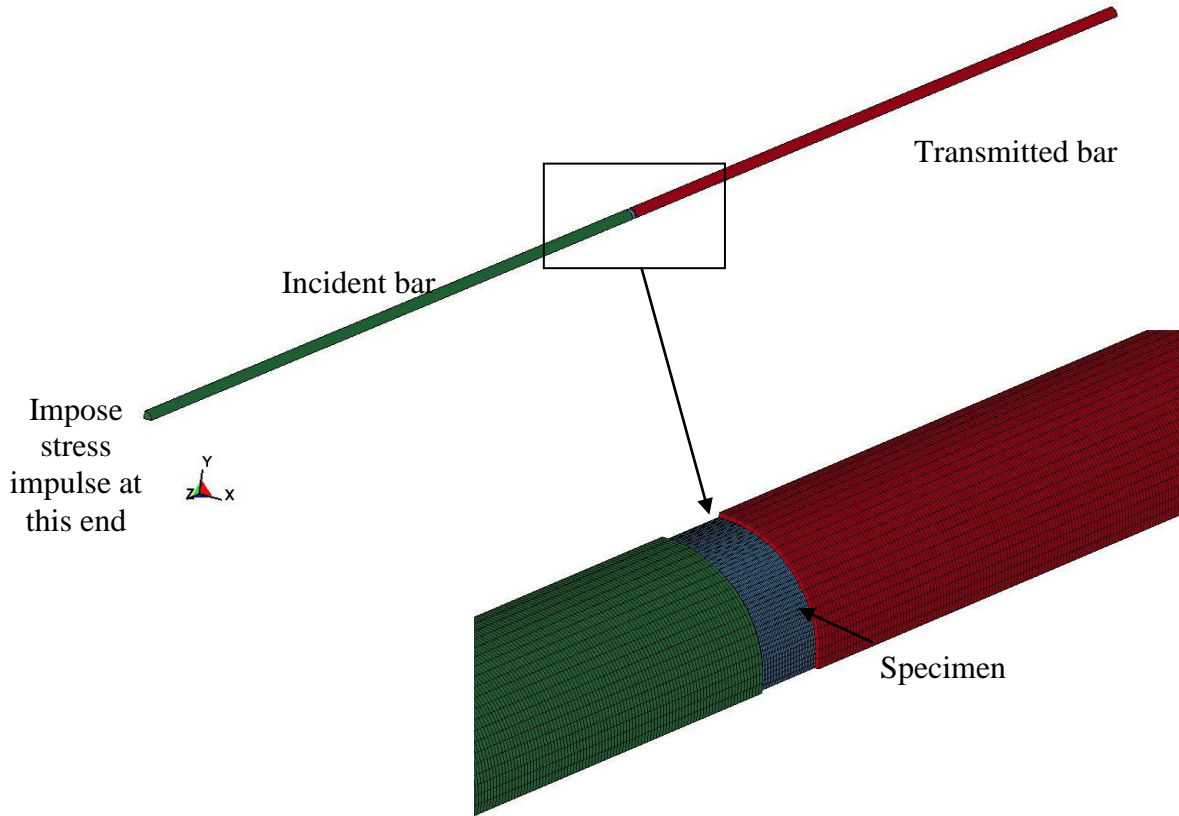
Figure A.9. Numerical model of compressive SHPB test

For the simulation of compressive SHPB test for asphalt concrete, the setting up of the SHPB test was the same as that for plain concrete, except that the specimen was a cylinder with 75 mm in diameter and 33 mm in length. The property of asphalt concrete was also introduced in Section 6.4.2, and its properties were listed in Table A.4. The loading condition and shape of the impulse was the same as that in plain concrete SHPB test, but adopting two different stress levels as shown in Table A.5. The friction coefficient for the interface between asphalt concrete and steel was taken as 0.35. In the simulation of compressive SHPB test, three DIF curves would be considered, that is, rate-dependent curve, proposed DIF curve with two branches (Equation 6.42) and the modified proposed DIF curve with only the first branch (Equation 6.43), which

was shown in Figure 6.33. The results were presented and discussed in section

6.4.2.

Table A.4: Material properties of asphalt concrete used in compressive SHPB test

Parameters	Symbol	Units	Value
Young's modulus	E	MPa	598
Compressive strength	f_c	MPa	4.6
Tensile strength	f_t	MPa	0.7
Poisson's ratio	v	---	0.35
Density	ρ	kg/m^3	2470

Table A.5 Input stress impulse in compressive SHPB test for asphalt concrete

No.	Stress level (MPa)	Rise time (ms)	Ramp time (ms)	Total time (ms)
1	170	166	400	600
2	200	160	400	560